
The stellar structure and outer disk kinematics of high-redshift galaxies from near-infrared observations

Philipp Lang



München 2016

The stellar structure and outer disk kinematics of high-redshift galaxies from near-infrared observations

Philipp Lang

Dissertation
an der Fakultät für Physik
der Ludwig–Maximilians–Universität
München

vorgelegt von
Philipp Lang
aus München

München, April 2016

Erstgutachter: Prof. Dr. Reinhard Genzel
Zweitgutachter: Prof. Dr. Andreas Burkert
Tag der mündlichen Prüfung: 21. Juli 2016

Zusammenfassung

Das Universum bei Rotverschiebung $1 < z < 3$ ist die Epoche mit dem Maximum an Sternentstehung und Massenzuwachs von Galaxien, bietet jedoch viele Herausforderungen für Beobachtungen. Diese Doktorarbeit beschäftigt sich mit dem Aufbau von Masse und dem plötzlichen Abklingen der Sternentstehung in Galaxien (auch bezeichnet als Quenching). Dazu werden neueste räumlich aufgelöste Beobachtungsdaten von Galaxien bei hoher Rotverschiebung aus erd- und weltraumgestützten Nahinfrarot (NIR)-Datensätzen genutzt.

Der erste Teil dieser Arbeit präsentiert eine Analyse der stellaren Morphologie von massereichen Galaxien ($M_* > 10^{10} M_\odot$) bei $0.5 < z < 2.5$, die sich auf den CANDELS Datensatz stützt. Dieser bietet tiefe und hochaufgelöste Ultraviolett- bis NIR-Aufnahmen des Hubble Weltraumteleskops. Diese Daten werden durch Grism-Spektroskopie des 3D-HST-Surveys ergänzt, mit der präzise Rotverschiebungen berechnet werden. Durch einfache Sérsic-Modelle und Bulge-Scheiben-Dekompositionen werden die räumlichen Verteilungen der stellaren Masse und des Lichts von 6764 Galaxien bei optischen Ruhewellenlängen quantifiziert. Die stellaren Massenverteilungen werden durch räumlich aufgelöste SED-Modellierung rekonstruiert, die sich auf die panchromatischen Aufnahmen stützt.

Die Massenverteilungen zeigen, dass inaktive Galaxien bei hoher Rotverschiebung einen größeren Bulge-Anteil als sternbildende Galaxien besitzen. Dies wurde bislang nur anhand von Aufnahmen bei optischen Ruhewellenlängen beobachtet. Darüber hinaus zeigen der Sérsic-Index und der Massenanteil des Bulges (B/T) von sternbildenden Galaxien einen Anstieg bei höheren stellaren Massen, der Median von B/T erreicht 40-50 % oberhalb von $10^{11} M_\odot$. Dies deutet auf ein signifikantes Wachstum der Bulge-Komponenten innerhalb von sternbildenden Galaxien entlang der sog. Main Sequence hin, bevor diese Quenching durchlaufen. Die Masse des Bulges einer Galaxie ist ein zuverlässigerer Indikator für Inaktivität als die totale stellare Masse oder die Masse in der Scheibe einer Galaxie. Diese empirischen Ergebnisse und ein Vergleich mit neuesten theoretischen Modellen unterstützt die Annahme, dass mögliche Quenching-Mechanismen galaxienintern wirken, und eng mit dem Wachstum von Bulges verknüpft sind.

Der zweite Teil dieser Arbeit konzentriert sich auf die Kinematik der äußeren Scheiben von sternbildenden Galaxien bei hoher Rotverschiebung. Er basiert auf großen und tiefen Datensätzen von Integralfeld (engl.: integral field unit, 'IFU') -Spektroskopie, die mittels $H\alpha$ die Kinematik des ionisierten Gases vermisst. Sowohl der laufende KMOS^{3D} Survey als auch der Teil des SINS/zc-SINF Surveys, der mithilfe adaptiver Optik beobachtet wurde, werden genutzt, um eine Stichprobe von ~ 100 massreichen sternbildenden Scheibengalaxien bei $0.7 < z < 2.6$ zusammenzustellen. Mithilfe einer neuartigen Mittelungs-Methode kann eine typische Rotationskurve bis auf mehrer Effektivradien hinaus robust bestimmt werden.

Diese mittlere Rotationskurve zeigt einen signifikanten Geschwindigkeitsabfall jenseits des Maximums. Dieses Ergebnis bestätigt anhand einer größeren Stichprobe einen solchen Abfall, wie er bei hoher Rotverschiebung bisher nur bei wenigen einzelnen Scheibengalaxien bei hervorragender Datenqualität und hohem Signal-zu-Rausch-Verhältnis beobachtet wurde. Ein Vergleich mit Modellen zeigt, dass die abfallende Rotationskurve durch einen hohen Anteil baryonischer Masse in der Scheibe an der Gesamtmasse des Halos dunkler Materie ($m_d = 0.05 - 0.1$) erklärt werden kann. Zusätzlich muss die äußere Scheibe signifikant druckgestützt sein ($\sigma_0 = 35 \text{ km s}^{-1}$). Die Resultate bestätigen die bisher durch den Vergleich von dynamischer, stellarer und Gasmasse gemessenen hohen baryonischen Anteile in Scheibengalaxien bei hoher Rotverschiebung, sind jedoch unabhängig von Annahmen über die Umrechnung von Licht zu Masse und die Ursprüngliche stellaren Massenfunktion (engl.: 'Initial stellar Mass Function', IMF). Der steil abfallende Verlauf der mittleren Rotationskurve kann zudem durch Druckgradienten erklärt werden, die in gasreichen, turbulenten Scheibengalaxien bei hoher Rotverschiebung signifikant sind. Dies deutet auf ein druckbedingtes Abschneiden der äußeren Scheibe hin.

Schließlich werden Korrekturen für die räumliche Verschmierung (engl.: 'beam smearing') präsentiert, mit denen man die intrinsische Rotationsgeschwindigkeit und Geschwindigkeitsdispersion wiederherstellen kann, und die auf IFU-Datensätze von Galaxien bei hoher Rotverschiebung anwendbar sind. Diese Korrekturen basieren auf simulierten Datenkuben, die reale IFU-Beobachtungen für einen weiten Bereich von intrinsischen Galaxienparametern imitieren und exponentielle Scheiben voraussetzen. Die Korrekturen für die Rotationsgeschwindigkeit hängen lediglich von der Größe der Galaxie im Vergleich zur Breite der instrumentellen Punktspreizfunktion ab. Um die Korrekturen einfach auf Datensätze anwenden zu können, werden parametrisch angepasste Funktionen präsentiert. Die Korrekturen für die Geschwindigkeitsdispersion hängen von mehreren zusätzlichen Galaxieparametern wie Inklinationwinkel und dynamischer Masse ab. Basierend auf dem Gitter dieser Modelle, die einen großen Bereich von Galaxienparametern abdecken, könne die Korrekturen für die Geschwindigkeitsdispersion auf beliebige Quellen angewandt werden.

Abstract

The universe at redshift $1 < z < 3$ represents the peak epoch of rapid galaxy mass assembly and very active star-formation in galaxies, but also poses many observational challenges. This thesis addresses the buildup of galaxy mass as well as the shut-down of star formation in galaxies (referred to as 'quenching') using state-of-the-art spatially resolved observations of galaxies at high redshift from ground- and space based near-infrared (NIR) datasets.

The first part of this thesis presents an analysis of the stellar morphology of massive galaxies ($M_* > 10^{10} M_\odot$) at $0.5 < z < 2.5$ on the basis of the CANDELS dataset, providing deep rest-frame Ultraviolet(UV)-to-NIR imaging from the Hubble Space Telescope (HST) at high angular resolution. This is complemented by grism spectroscopy from the 3D-HST survey used to derive accurate redshift information. Both stellar mass and rest-frame optical light distributions of 6764 galaxies are quantified by performing single Sérsic fits as well as bulge-to-disk decompositions. The stellar mass distributions are reconstructed through resolved stellar population modeling on the panchromatic imaging dataset. The results show that quiescent galaxies at high redshift possess increased bulge fractions compared to their star-forming counterparts as seen in their mass distribution, previously only observed in rest-frame optical light. Moreover, the Sérsic index and bulge-to-total ratio (B/T) among star-forming galaxies show an increase towards higher stellar masses (with the median B/T reaching 40-50% above $10^{11} M_\odot$), hinting at significant bulge growth of star-forming galaxies along the main sequence before quenching. The bulge mass of a galaxy appears to be a more reliable predictor of quiescence than total stellar mass or disk mass. These empirical results and a further comparison to state-of-the-art theoretical models support that possible quenching mechanisms are internal to galaxies and closely associated with bulge growth.

The second part of this work focuses on the outer disk kinematics of star-forming galaxies at high redshift on the basis of large and deep Integral-Field-Unit (IFU) datasets tracing the resolved ionized gas kinematics from $H\alpha$. Both the ongoing KMOS^{3D} survey and the subset of the SINS/zc-SINF survey observed in adaptive optics assisted mode, are exploited to build a sample of ~ 100 massive star forming disk galaxies at $0.7 < z < 2.6$. Employing a novel stacking approach, a representative rotation curve reaching out to several effective radii can be robustly constrained. The stacked rotation curve exhibits a significant decrease in rotation velocity beyond the turnover. This result confirms, and extends to a larger sam-

ple, the falloff that had so far been observed in a handful of individual high- z disks with best data quality and signal-to-noise ratio. A comparison with models shows that the falling outer rotation curve can be explained by a high mass fraction of baryons in the disk relative to the dark matter halo ($m_d = 0.05 - 0.1$) in combination with a significant level of pressure support in the outer disk ($\sigma_0 = 35 \text{ km s}^{-1}$). These findings confirm the high baryon fractions found by comparing the stellar, gas and dynamical masses of high redshift galaxies independently of assumptions on the light-to-mass conversion and Initial stellar Mass Function (IMF). The rapid falloff of the stacked rotation curve can be explained by pressure gradients, which are significant in the gas-rich, turbulent high- z disks and suggests a possible pressure-driven truncation of the outer disk.

Lastly, a derivation of beam smearing corrections is presented that is applicable to high-redshift IFU datasets to recover the intrinsic values of rotation velocity and velocity dispersion. The corrections are based on simulated mock datacubes to mimic real IFU observations for a wide range of various intrinsic galaxy parameters assuming exponential disks. The correction for rotation velocity only depends on the size of the galaxy versus the size of the instrumental spatial point spread function (PSF), and fitting functions for the corrections to be easily applied to large datasets are presented. The corrections for velocity dispersion depend on several additional intrinsic galaxy parameters such as the inclination angle and dynamical mass. Based on the grid of models spanning a wide range in these galaxy parameters, the correction for velocity dispersion can be applied to any observed source.

Contents

Zusammenfassung	v
Abstract	vii
1 Introduction	1
1.1 Galaxy evolution in the context of Λ CDM	1
1.1.1 The current paradigm of modern cosmology	1
1.1.2 Dark Matter halos as the seeds for galaxies	3
1.2 Properties of galaxy populations	5
1.2.1 The local galaxy bimodality	5
1.2.2 The structure of local disk galaxies	6
1.3 Properties of high redshift galaxies	14
1.3.1 Star formation properties	14
1.3.2 Structural properties	17
1.3.3 Kinematics	20
1.3.4 Dark matter fractions	25
1.3.5 The need for quenching	26
1.4 This thesis	30
1.4.1 Motivation and structure	30
2 Bulge growth and Quenching since $z = 2.5$ in CANDELS/3D-HST	31
2.1 Aims	32
2.2 Data and Sample selection	32
2.2.1 The HST CANDELS and 3D-HST datasets	33
2.2.2 Sample definition	35
2.3 Methodology	36
2.3.1 Resolved SED Modeling	36
2.3.2 Structural Parameters	37
2.4 Results on Galaxy Structure	41
2.4.1 The Evolving Mass Budget of Disks and Bulges	41
2.4.2 Profile shape	42

2.4.3	Fraction of Quenched galaxies	45
2.5	Comparison with SAMs	48
2.5.1	The Somerville model	48
2.5.2	Fraction of Quenched Galaxies in the SAM	49
2.5.3	The agent of quenching	52
2.6	Comparison with Measurements on H-band	54
2.7	Discussion	56
2.7.1	Structural change	56
2.7.2	AGN as the driver of quenching ?	57
2.8	Conclusions	58
3	Outer disk kinematics of high-redshift star-forming galaxies	61
3.1	Aims	61
3.2	Data and sample selection	62
3.2.1	The KMOS ^{3D} and SINS/zc-SINF datasets	62
3.2.2	Ancillary data	63
3.2.3	The stacking sample	64
3.3	Methodology	70
3.3.1	Extraction and normalization of RCs	70
3.3.2	Final stacking and error estimation	74
3.3.3	Using R_e to calibrate R_{turn}	76
3.3.4	Sample properties at different radii	78
3.3.5	Potential biases due to sample selection and normalization	81
3.4	Results	86
3.4.1	Shape of the stacked rotation curve	86
3.4.2	Comparison to local rotation curves	91
3.4.3	Comparison to baryonic plus dark matter rotation curves	92
3.4.4	The effects of pressure support to outer disk rotation	97
3.4.5	Effect of adiabatic contraction	101
3.4.6	Impact of deviations from exponential distributions	105
3.4.7	Exploring variations in the concentration parameter	106
3.5	Conclusions	108
4	Beam smearing corrections	109
4.1	Aims	109
4.2	Simulations and setup	111
4.3	Results	112
4.3.1	Corrections for velocity	112
4.3.2	Corrections for velocity dispersion	114
4.4	Summary	118

Table of contents **xi**

5	Conclusions and outlook	119
5.1	Summary of this work	119
5.2	Future work	121
A	The meaning of a Sérsic index measurement	127
B	Comparison to the Guo et al. (2013) Semi-analytic model	129
	Bibliography	132
	Acknowledgements	157

List of Figures

1.1	Hubble classification scheme	7
1.2	Rotation curve decomposition of NGC2403	11
1.3	Local dark matter fractions	13
1.4	Cosmic star formation rate density	14
1.5	Main sequence up to redshift 2.5	16
1.6	UV imaging of high-z galaxies	17
1.7	Rest-frame optical Sérsic indices	19
1.8	SINFONI H α observations	21
1.9	The KMOS instrument	23
1.10	Velocity dispersion across redshift	24
1.11	Stellar-to-halo mass fractions at high redshift	26
1.12	Abundance matching results	28
2.1	Imaging exposure coverage in the CANDELS fields	34
2.2	Grism exposure coverage in the CANDELS fields	35
2.3	CANDELS morphologies at different wavelengths	37
2.4	GALFIT fitting examples	40
2.5	Sérsic index and B/T vs. M_*	43
2.6	$R_e, R_{Bulge}, R_{e,Disk}$ vs. M_*	45
2.7	f_q vs. M_*, M_{Bulge}, M_{Disk}	46
2.8	f_q vs. M_*, M_{Bulge}, M_{Disk} predicted by the SAM	50
2.9	f_q vs. M_{Halo}, M_{BH}	53
2.10	Sérsic index and B/T vs. M_* measured on H -band	54
2.11	f_q vs. M_*, M_{Bulge}, M_{Disk} measured on H -band	55
3.1	Stacked sample in the $R_e - M_*, SFR - M_*$ planes	66
3.2	Distributions of galaxy parameters	68
3.3	Apertures used for extraction	71
3.4	Spectral extraction and the normalization of rotation curves	72
3.5	Stacked pv diagram	75
3.6	Modeled RCs with varying R_e/R_{beam}	77
3.7	Modeled RCs with varying Sérsic index	78

3.8	Stacked sample in the $R_e - M_*$, $SFR - M_*$ planes for different radii	80
3.9	Distribution of H -band n for stacked sample for different radii	81
3.10	Examples of simulated Mock rotation curves	83
3.11	Selection fractions and recovered outer slopes of mock rotation curves	85
3.12	Stacked rotation curve	87
3.13	Gaussian fits of stacked spectra	88
3.14	Stacked rotation curves from R_{turn}^{meas} and R_{turn}^{morph}	90
3.15	Template RCs at low redshift	92
3.16	Stacked RC with baryonic + DM models	94
3.17	Stacked RC with baryonic + DM models including pressure support	99
3.18	Stacked RC in bins of V_{rot}/σ_0	100
3.19	Modeled RCs with and without adiabatic contraction	103
3.20	RC with baryonic + DM models including adiabatic contraction	104
3.21	Stacked RC with baryonic + DM models including bulge components	106
3.22	RC with baryonic + DM models with varying c	107
4.1	Simulated profiles of velocity and velocity dispersion	110
4.2	Beam smearing corrections for velocity	113
4.3	Beam smearing corrections for velocity dispersion at $z \sim 1$	116
4.4	Beam smearing corrections for velocity dispersion at $z \sim 1.5$	117
4.5	Beam smearing corrections for velocity dispersion at $z \sim 2$	117
A.1	$R_{e,B}/R_{e,D}$ vs. B/T and n vs. B/T	128
B.1	f_q vs. M_* , M_{Bulge} , M_{Disk} in the Guo et al. (2013) SAM	130
B.2	f_q vs. M_{Halo} , M_{BH} in the Guo et al. (2013) SAM	131

List of Tables

3.1	Properties of the stacking and full KMOS ^{3D} + SINS/zc-SINF sample	67
4.1	Parameters for velocity correction factors for a single Gaussian PSF	114
4.2	Parameters for velocity correction factors for double component AO PSF .	114

Chapter 1

Introduction

This introductory chapter outlines the broad framework and open questions in galaxy evolution that are addressed in this thesis work. I start with the modern paradigm of cosmology and the large-scale structure formation as the basis for galaxy formation and evolution and as mostly driven by the non-luminous dark matter component of the universe. Then I proceed to the properties of the baryons observed in local galaxy populations. In particular, I will discuss the bimodality in structure and kinematics of local galaxies and the processes thought to be responsible for these properties. Finally, I will elaborate on look-back studies trying to extend our picture of galaxy evolution to higher redshifts when galaxies appeared to most actively forming stars. I will especially focus on studies of kinematics and structure of galaxies at redshifts $z \sim 1 - 3$ enabled by recent developments in observational instrumentation. I close with a discussion on open questions about galaxy evolution at high redshift as a motivation for this thesis.

1.1 Galaxy evolution in the context of Λ CDM

1.1.1 The current paradigm of modern cosmology

The Λ CDM model is currently the standard paradigm that has emerged over the last decades in modern cosmology. Within this picture, the two main constituents of the universe are dark energy and dark matter (DM), both of which are non-luminous components of the universe (e.g. Riess et al. 1998; Perlmutter et al. 1999; Dunkley et al. 2009). In contrast, the baryonic component, making up all visible matter such as stars and gas, only contributes $\sim 5\%$ of the total energy budget of the universe (e.g. Yang et al. 1984; Iocco et al. 2009). According to Λ CDM, we live in a homogeneous and isotropic universe on large scales ($\gtrsim 100$ Mpc) that is continuously expanding. The latter fact is motivated by the discovery that galaxies are receding away from us at a rate linearly increasing with their distance (Hubble 1929). The 'drift' of galaxies away from us is measured by the shift in wavelength that light undergoes while it is traveling from its distant source to earth. It is called 'cosmological redshift' and

is defined as

$$1 + z = \frac{\lambda_o}{\lambda_e}, \quad (1.1)$$

where λ_e is the wavelength of the light when emitted from the source and λ_o is the observed wavelength. As the age of the universe approaches $t = 0$ (thus z reaches infinity), the energy density and temperature approach infinite values and our laws of physics break down. At cosmic times earlier than 10^{-43} seconds, the so called 'Planck time', gravitational interactions are believed to have been as strong as interactions due to quantum effects and there is currently no proper description for this period. Thus we can only correctly describe the universe at cosmic ages higher than the Planck time.

With the aid of General Relativity developed by Einstein (1916), the space-time structure of the universe can be related to its total energy budget, described by the Friedmann equations (Friedmann 1922):

$$H(t)^2 = \frac{\dot{a}^2(t)}{a^2(t)} = H_0^2[\Omega_r(1+z)^4 + \Omega_m(1+z)^3 + \Omega_k(1+z)^2 + \Omega_\Lambda], \quad (1.2)$$

where $H(t)$ is the Hubble parameter (i.e. the expansion rate of the universe at time t), and a is the scale factor. The density parameters Ω_r , Ω_m , and Ω_Λ denote the present-day energy densities of radiation, non-relativistic matter, and dark energy, respectively, compared to the critical density ρ_{crit} :

$$\rho_{crit}(t) = \frac{3H^2(t)}{8\pi G}. \quad (1.3)$$

Ω_k represents the contribution due to space-time curvature; and current observations suggest that this term is zero, i.e. the universe appears to be flat.

At early cosmic times ($z \gtrsim 3000$), the universe was dominated by radiation density Ω_r , until radiation and matter decoupled, which is believed to have happened at $z \sim 1000$, when the radiation density became too low to keep H and He fully ionized. The Cosmic Microwave Background (CMB) originated as an imprint of the density fluctuations during the decoupling of radiation and matter. These density fluctuations are believed to stem from tiny quantum fluctuations in the very early stages of the universe. The CMB was discovered by Penzias & Wilson (1965) and serves until today as a valuable source of information about the structural development of the universe since the initial density perturbations appear to be the seed for further structure formation driven by dark matter. This non-baryonic component of the universe appears to dominate the overall gravitational interaction of matter in the universe, but there is currently no direct evidence for an elementary particle or other phenomena that could explain the dm component. However, the existence of dark matter is supported by several independent lines of evidence. Historically, the first hint at a non-luminous component came from observations of the Coma cluster which exhibits random

motions at a level that cannot be explained by the gravitational force of the baryons measured by stellar light alone (Zwicky 1933). Further observations of galaxy clusters such as the Bullet cluster (Clowe et al. 2004; Markevitch et al. 2004) have confirmed this conclusion. Another argument for the existence of dark matter on galactic scales comes from the ubiquitous rising or flat outer rotation curves of spiral galaxies, which will be discussed in more detail in this chapter. Alternative explanations exist that are able to explain flat rotation curves, with the most successful being the Modified Newtonian Dynamics (MOND, Milgrom 1983), which is, however, not further discussed in the framework of this thesis. The need for a dark matter component dominating Ω_m also comes from the fact that the universe is observed to be flat in curvature, as well as from the amplitude of structure in the universe today compared to the CMB anisotropies.

The most recent measurements of the cosmological parameters are (Planck Collaboration 2013):

$$\begin{aligned}
 H_0 &= 67.8 \pm 0.77 \text{ km s}^{-1} \text{ Mpc}^{-1} \\
 \Omega_\Lambda &= 0.692 \pm 0.010 \\
 \Omega_{DM} &= 0.262 \pm 0.0038 \\
 \Omega_{bar} &= 0.0489 \pm 0.00053.
 \end{aligned}
 \tag{1.4}$$

Together, the dark matter component Ω_{DM} and the baryonic matter component Ω_{bar} add up to the total matter density $\Omega_m = 0.311$. These numbers already point out that the dark matter is strongly dominating the matter budget averaged over the entire space ($\Omega_{DM}/\Omega_{bar} \sim 0.8$). However, this ratio is significantly smaller on scales of galaxies as discussed further in this chapter.

1.1.2 Dark Matter halos as the seeds for galaxies

The structure of the universe seen today from the densest regions like galaxy clusters to the least dense voids are believed to have formed through the initial perturbations seen in the CMB, which are on the order of $\frac{\Delta T}{T} = 10^{-5}$. These fluctuations represent anisotropies in the baryons at the time of recombination and are by large too small to explain the growth of structures seen in the universe today, considering that perturbations in baryonic density are able to grow only after $z \sim 1000$ due to scattering of photons in the hot plasma before recombination. However, perturbations in the dark matter density were able to grow since the epoch of inflation ($t \lesssim 10^{-32}$ s) due to the absence of radiation pressure, allowing much higher density anisotropies of the dark matter component relative to that of the baryons at the time of recombination.

Regions that exceeded a certain threshold in the resulting overdensity underwent a spherical collapse into virialized objects known as dark matter halos. Those are characterized by their virial radius r_{200} , i.e. the region in which the average density is 200 times the cosmic

mean density, and the correspondingly enclosed mass M_{vir} . Dark matter halos are mainly pressure-supported systems. Their angular momenta are acquired through tidal torques, resulting in a small centrifugal support (Hoyle 1951; Peebles 1969; White 1984), often expressed by the dimensionless spin parameter λ , which indicates the fraction of the actual specific angular momentum of a halo compared to its theoretical maximum.

In N-body simulations, where collisionless dark matter particles can be simulated, the growth of large-scale structure and halos has been confirmed. Moreover, the radial structure of halos have been found to be universal and independent of mass. Navarro et al. (1997) showed that the radial density profile of halos can be well described by:

$$\rho(r) = \frac{\rho_0}{(r/r_s)(1 + r/r_s)^2}, \quad (1.5)$$

where ρ_0 is the central density of the halo, and r_s is the scale radius. It is related to the halo's virial radius, r_{200} via $r_s = r_{200}/c$ where c is the concentration parameter. Once dark matter halos have formed, they function as seeds for the formation of galaxies by accretion of matter through the filamentary 'cosmic web' structure. When gas is entering the halo, it is shock heated to the virial temperature ($T \sim 10^6 K$, Rees & Ostriker 1977). From this stage, the heated material has to subsequently cool through radiative processes, then segregate from the dark matter to build-up the Interstellar Medium (ISM) in the disk of the galaxy in the center of the halo to enable star formation (SF). The details of the cooling of gas onto the disk is strongly dependent on the halo properties, since the virial temperature increases with virial mass which in turn decreases the cooling rate of the gas. Recent hydrodynamical simulations have revealed that at least for smaller halos with masses below $M_{vir} \lesssim 10^{12} M_\odot$, the gas is accreted via 'cold streams' along filaments, whereas for massive halos this cold mode accretion is suppressed due to shock heating (e.g. Silk 1977; Rees & Ostriker 1977; Kereš et al. 2005; Dekel & Birnboim 2006). However, at higher redshift, cold streams are possible even in massive halos (e.g. Dekel et al. 2009). Once gas has cooled to the center of the halo, it is predicted to settle onto a centrifugally supported disk configuration (e.g. Fall & Efstathiou 1980; Mo et al. 1998). Mo et al. (1998) presented a model in which the size of the resulting disk is dependent on the properties of the host halo:

$$R_{disk} \propto \lambda \cdot r_{200} \quad (1.6)$$

This model is able to explain many of the observed properties of local spiral galaxies and damped Ly α absorbers (i.e. galaxies observable at redshifts $z \sim 2 - 4$, rich in neutral hydrogen causing absorption lines in spectra of bright background sources) such as their stellar densities and rotation curves, suggesting that the angular momentum of the host dark matter halo has a strong influence on the final baryonic structure of disk galaxies. One important parameter in this model is m_d , the fraction of baryonic mass of the disk compared to the virial mass of the halo, which has a large influence on the predicted properties of disk galaxies and therefore represents a key ingredient for constraining such models.

In addition to the above mentioned processes of gas inflow and settling in a disk configuration, there are more complex baryonic processes such as feedback from star formation or Active Galactic Nuclei (AGN) containing a super massive black hole (SMBH) that, once a sufficient accretion rate is reached, can drive powerful outflows. Also secular processes internal to galaxies, and galaxy mergers, are potentially acting to redistribute baryons inside galaxies. These processes lead to the morphological variety observed among galaxies. Additionally, the condensation of baryons in the center of halos might also in turn affect the structure of the halo itself. In this context, the scenario of adiabatic contraction has been proposed as a simple prescription of how the dark matter halo reacts to the infall and condensation of baryons onto its central region. Blumenthal et al. (1986) suggested a simple model in which the baryonic disk forms in the center of a dark matter halo so slowly that the orbital period of a dark matter particle is short compared to the build-up time of the disk, leading to an effective contraction of the dark matter halo. However, the effect of rapid outflowing gas due to supernova or AGN feedback might lead to a reduction of contraction or even act to expand dark matter halos (Navarro et al. 1996; Gnedin & Zhao 2002; Read & Gillmore 2005).

Thus, in the context of galaxy evolution models, it is important to determine the baryonic structure of galaxies, also relative to that of the dark matter, in order to understand the build-up history of galaxies in the context of gas accretion onto dark matter halos and to understand further baryonic processes inside galaxies.

1.2 Properties of galaxy populations

1.2.1 The local galaxy bimodality

Observations of local galaxies have shown that there is clear bimodality in the local galaxy population which is reflected in several fundamental galaxy parameters. This bimodality was first classified by Hubble (1926) who put galaxies in a sequence shown in Figure 1.1. In his classification scheme, the so called 'Hubble sequence', the population of galaxies are separated into spirals (or late-type galaxies) on the right part of the diagram and ellipticals (or early-type galaxies, ETGs) on the left part.

Spiral galaxies are observed to be geometrically flat systems in which most of the starlight is coming from the disk which also has spiral arm features. The Hubble sequence sub-divides spirals into two groups depending on whether a central bar structure is observed or not. In contrast, the population of ETGs are flattened elliptical systems and are found to have a smooth appearance with strongly peaked central light emission.

These distinct shapes reflect a sequence of dynamical support along the Hubble sequence. In spiral galaxies, stars and gas inside their disks move along regular circular orbits with only little amount of random motions. In contrast, ETGs represent systems which are dominated by random motions. Extensive kinematical analysis of local ETGs in the framework of the SAURON and ATLAS-3D surveys (Emsellem et al. 2004; Cappellari et al.

2011) have revealed that a significant fraction of ETGs also exhibit rotational signatures as well as nuclear rotating disks, especially in Lenticular galaxies (i.e. galaxies which are of intermediate type containing disk components but no spiral arms). However, the overall spheroidal appearance of galaxies anti-correlates well with their amount of rotation or equivalently with their angular momentum.

The bimodality in structure is furthermore observed to be linked to a color bimodality of galaxies, which is connected to their star formation properties (e.g. Strateva et al. 2001; Kauffmann et al. 2003b). Spirals have blue optical colors indicative of significant ongoing star formation activity. That is since current star formation produces a high abundance of short-lived massive and hot stars emitting light at short optical wavelengths. The presence of star formation in spiral galaxies is known to be connected to the presence of gas acting as fuel (Kennicutt 1998). In contrast, ETGs seem to be almost devoid of star formation, resulting in their red colors dominated by long-lived smaller and colder stars. In particular, the spectral properties of the stellar component in ETGs suggest the presence of older stellar populations that formed early and evolved 'passively' with no further star formation (e.g. Kelson et al. 2001; Bell et al. 2004), suggesting a shut-down of star formation on short time scales, also referred to as 'quenching'. However, it is currently not fully understood which group of galaxies represent the progenitors of today's massive ETGs and which physical processes lead to quenching in those galaxies.

1.2.2 The structure of local disk galaxies

Spiral galaxies show a complex structure with several distinct components that each have different properties in terms of their kinematics and stellar populations. As mentioned above, the component mostly dominating the morphology of local spirals is their disk, which is the main site of ongoing star formation. They are also geometrically thin, since their extent in the vertical direction is many times smaller than their extent in radial direction. The thickness (i.e. ratio of vertical to radial scale-height) of spirals in bulgeless systems (also referred to as 'simple disks') is found to be $\lesssim 0.15$ (e.g. Kautsch 2009 and references therein). Studies exploiting local imaging surveys have shown that the average thickness of disk galaxies also including early-type spirals is larger ($\sim 1/5 - 1/4$ based on axial ratio measurements, Padilla & Strauss 2008), likely caused by the light contribution from the central, more spheroidal bulge component. Moreover, in most spiral galaxies including the Milky Way, also thicker disk components are found surrounding the thin disk.

In contrast to the presence of young stellar populations in thin disks, thick disks contain mostly older stellar populations, suggesting a formation at earlier times. In the central parts of galaxies, also spheroidal components containing older stellar populations are observed, which are referred to as 'bulges'. Those are, similar to ETGs, mostly dispersion dominated components.

In order to understand the underlying structure of baryons, the surface brightness distributions of disk galaxies have been extensively analyzed. To first order, Surface Brightness

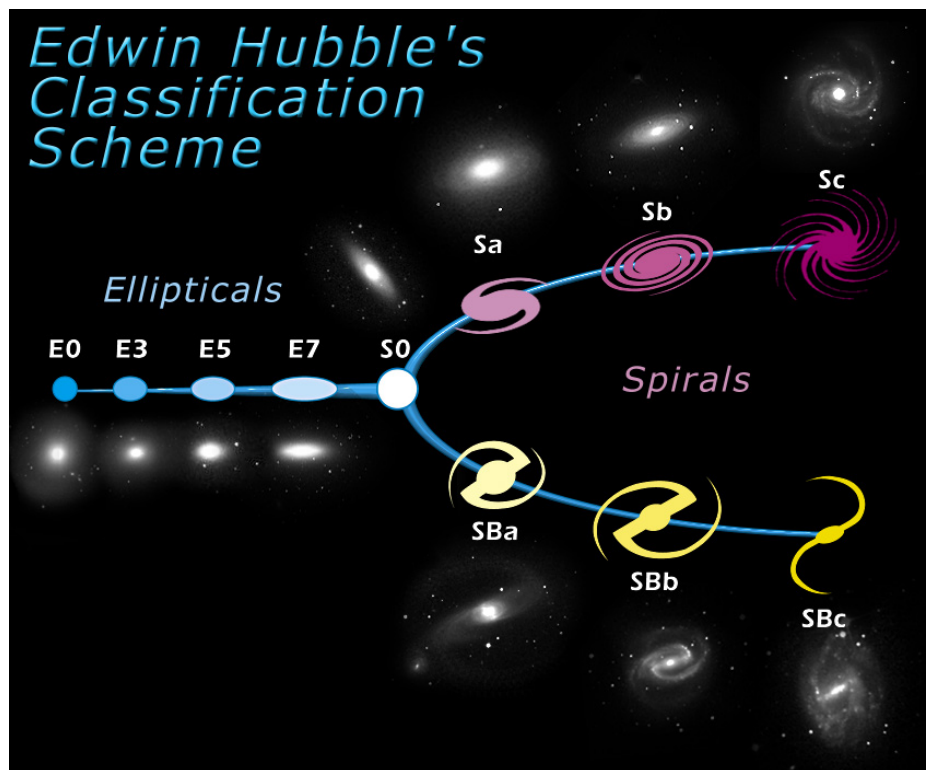


Figure 1.1: The Hubble classification scheme of galaxies. Image credits: '<http://skyserver.sdss.org/dr1/en/proj/advanced/galaxies/images/TuningFork.jpg>'

Profiles (SBPs) traced by e.g. the rest-frame optical light based on galaxy images reflects the stellar mass structure of galaxies representing most of the (inner) baryons. In this context, using SBPs derived from Near-Infrared (NIR) images are most suitable since the effects of dust extinction decrease at longer wavelengths, and variations of the stellar mass-to-light ratio (M_*/L) inside and among galaxies also decrease (e.g. Kauffmann et al. 2003a). The surface brightness distribution of galaxies is often parametrized by Sérsic profiles (Sérsic 1968), which have the form :

$$I(R) = I_0 \times \exp(-b_n \cdot (\frac{R}{R_e})^{1/n}), \quad (1.7)$$

where I_0 is the central intensity, R_e is the effective radius (enclosing 50 % of the total integrated luminosity) and n is the Sérsic index. The normalizing factor b_n ensures that the total integrated profile corresponds to the total luminosity of the galaxy. Spiral galaxies are well fit by exponential intensity profiles (corresponding to $n = 1$) and thus have exponential stellar disks. In their inner parts, their SBPs are well fit by a second central component with $n > 1$ representing the bulge. In contrast, ETGs are well fit $n \sim 4$ profiles (also referred to as 'de Vaucouleurs' profiles, de Vaucouleurs 1948) representing a more centrally peaked mass distribution.

In their outer parts, stellar disks are often observed to deviate from the extrapolated exponential surface brightness distributions in the form of radial truncations. Those were first found in edge-on galaxies where the signal is most clear. It was first noted by van der Kruit & Searle (1981a,b) that the radially extended light profiles of a few disks in deep photographic exposures did not continue further than some galactocentric radius. Further systematic studies using CCD surface photometry of edge-on systems confirmed that the frequency of such truncations is at least 60 % (e.g. Kregel et al. 2002; see also van der Kruit & Freeman 2011 and references therein). The truncations appear to be quite sharp, with radial e-folding length scales of only about 1 kpc. Detecting truncations in disks with lower inclination is more challenging due to line-of-sight integration of stellar light. However, they have also been detected in less inclined galaxies in deep photometric studies (e.g. Florido et al. 2006; Pohlen & Trujillo 2006) confirming that radial truncations are common among disk galaxies irrespective of their orientation. The galactocentric radii at which truncations are found (R_{max}) typically correspond to $3.5 - 4 \cdot r_d$, where r_d is the radial scale length of the disk (i.e. the radius at which the density of an exponential disk drops to $1/e$ of the central value; r_d corresponds to $\sim 1.68 \cdot R_e$). The ratio $\frac{R_{max}}{r_d}$ shows correlation with the face-on central surface brightness indicating that truncations happen at roughly constant disk surface density (Kregel & van der Kruit (2004). In the Milky Way, the stellar disk is also observed to be truncated at a radius of $\sim 14 - 15$ kpc (e.g. Ruphy et al. 1996). The origin of such radial truncations are still under debate. In one proposed scenario, the gas surface density in the outer disk drops to a level at which it falls below the threshold for local stability such that gas does not collapse and form stars (Kennicutt 1998; Schaye et al. 2004). The latter could also be the consequence of gravitational shear acting to stabilize the outer

disk (Fall & Efstathiou 1980). On the other hand, the truncation radius could also represent the border at which the star formation currently propagated considering inside-out growth scenarios of disk galaxies (Larson 1976). Since the truncation of the disk corresponds to a maximum of a galaxy's current specific angular momentum, it would correspond to that in the protogalaxy assuming conservation of angular momentum (Fall & Efstathiou 1980). In addition, further processes might lead to a redistribution of angular momentum such as bars (e.g. Erwin et al. 2008), dark matter sub-halos (de Jong et al. 2007), radial migration of stars or galaxy interactions.

Complementary information about the mass distribution especially for disk galaxies can be obtained by analyzing velocity profiles representing the maximum orbital velocity of stars or gas in a galaxy as a function of galactic radius, also referred to as rotation curves (RCs). Those trace the dynamical mass, which is the sum of the baryonic components and the dark matter halo component.

Very early observations of rotation curves were obtained for nearby spiral galaxies, including M31, based on nebular emission lines. Oort (1940) and Babcock (1939) found unexpectedly high rotation velocities, suggesting the presence of large amounts of unseen matter (which can be similarly expressed as a very high dynamical M/L ratio). With the advance of improved detectors especially at radio frequencies tracing the neutral hydrogen component, it could be confirmed that the rotation of M31 is flat out to even ~ 38 kpc (Rubin & Ford 1970; Roberts & Winterhust 1975). Flat rotation curves are now known to be a ubiquitous feature among local spiral galaxies (Sofue & Rubin 2001 and references therein). This is not expected when considering an exponential mass distribution with constant M/L (e.g. Freeman 1970), and there is large consensus today that this observational fact can be firmly interpreted in terms of non-luminous dark matter dominating the kinematics of disk galaxies in their outer parts.

In general, dynamical mass estimates in disk galaxies are available through rotation curves that can be extracted from several emission lines. For instance, commonly used diagnostics include the $H\alpha$ emission line, which is a Balmer recombination line created by the ionized phase of hydrogen. The rotational transitions of Carbon monoxide (CO) (e.g. $J = 1 - 0$ and $J = 3 - 2$) can be used to trace the molecular phase, and the 21 centimeter line due to the hyperfine structure transition of hydrogen is tracing HI, the neutral hydrogen component. While the former two lines are mostly detected within the optical radius of the disk given the general (decreasing) surface brightness distribution within disks, HI provides a more extended sampling of RCs at the expense of spatial resolution. Integrated line widths can also provide information about the amplitude of large-scale kinematics especially in unresolved galaxies. The dynamical mass of a system can be derived from the velocity at radius r , $V(r)$, by solving the Poisson equation for the potential $\Phi(r)$:

$$V^2(r) = r \frac{d\Phi(r)}{dr}. \quad (1.8)$$

Assuming a simple spherical mass distribution $M(r)$ yields $V(r)^2 = G \frac{M(r)}{r}$ (Binney & Tremaine 2008), where G is the gravitational constant. However, for oblate systems such as galactic disks, equation 1.8 has to be solved accounting for the geometry of the mass distribution. Freeman (1970) provided a solution assuming an infinitely thin exponential disk, yielding

$$V_{disk}(r) = \sqrt{4\pi G \Sigma_0 r_d x [I_0(x)K_0(x) - I_1(x)K_1(x)]}, \quad (1.9)$$

with $x = r/(2r_d)$, where r_d the radial scale-length of the exponential disk, corresponding to $r_d \sim R_e/1.68$. Σ_0 is the central stellar surface density of the disk, and I_n and K_n denote the modified Bessel functions of the first and second kind. This model predicts the radial velocity profile of a thin exponential disk appropriate for spiral galaxies, in the absence of a bulge or dark matter. The resulting profile peaks at $\sim 2.2r_d$, where the peak rotation velocity V_{rot} is reached and drops at larger radii. As mentioned above, the presence of dark matter in the outer parts of disks causes a flattened behavior of RCs deviating from the expected shape of this model. Moreover, due to the presence of central stellar mass concentrations as well as bar structures, the inner as well as outer parts of rotation curves of galaxies significantly deviate from these simple rotation curves. In particular, early-type spirals with massive central stellar bulges have RCs with very steep inner gradients leading to an inner peak in cases of well resolved RCs. Concentrated inner (baryonic) mass distributions also lead to declining outer rotation curves (see Kent 1986; Corradi & Capaccioli 1990; Casertano & van Gorkum 1991; Noordermeer et al. 2007; Noordermeer 2008). Also kinematic signatures in form of a drop in extended rotation curves of disks at their photometric truncation radius have been found that hint at a truncation of the underlying mass distributions (e.g. Casertano 1983).

One goal of dynamical mass studies is decomposing the velocity profile into the main contributing components which are bulge, (gaseous + stellar) disk and dark matter halo in order to quantify the relative contribution of dark matter and even trace its mass profile. The RC of a galaxy can be expressed as combination of the individual components all contributing to the full gravitational potential. For an axisymmetric matter distribution equation 1.8 yields to (e.g. Casertano 1983; Courteau et al. 2014) :

$$V(r) = \sqrt{V_{baryons}^2(r) + V_{DM}^2(r)} = \sqrt{V_{disk}^2(r) + V_{bulge}^2(r) + V_{gas}^2(r) + V_{DM}^2(r)}. \quad (1.10)$$

The most common method for a decomposition of a rotation curve into these components is a mass modeling approach in which prior knowledge of the baryonic distribution is used as a constraint. The baryonic distribution is usually derived by converting observed light profiles into mass distributions using estimates on the stellar M_*/L , and furthermore adding gas components from independent gas measurements. Photometric decompositions of light and mass profiles are often used to determine the $V_{disk}(r)$ and $V_{bulge}(r)$ components.

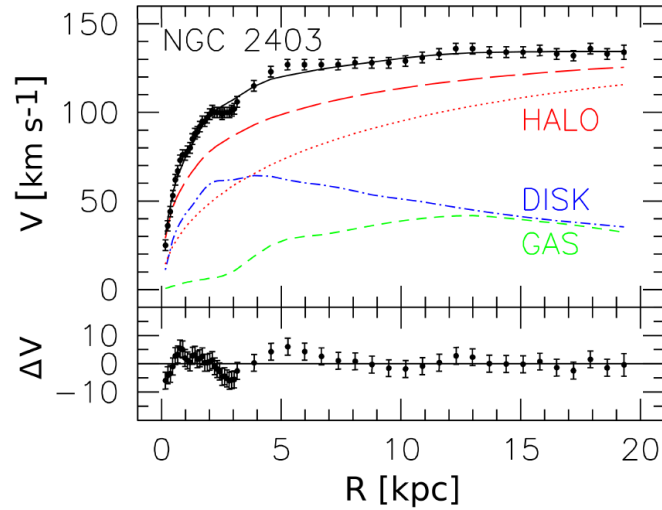


Figure 1.2: RC decomposition for the spiral galaxy NGC 2403 into disk (blue), gas (green) and dark halo (red) components. Residuals to the fit are shown in the lower part of the figure. This Figure is taken from Courteau et al. (2014).

Unknown parameters in the modeling are therefore mainly the properties of the dark matter halo, such as the virial mass, radius, and the concentration parameter of the halo. An example of such a decomposition is shown in Figure 1.2 representing a typical RC and mass profile of local spiral galaxies.

From Figure 1.2 it is clear that the dark matter halo mass distribution roughly similarly contributes to the inner baryonic mass budget but dominates in the outer parts of the example case. While on large scales the dark matter mass is clearly dominant over the baryons, the inner baryonic contribution is clearly more significant and varies among different galaxy types. In principle, such decompositions are suitable to derive mass profiles of baryonic and dark matter components for disk galaxies, provided that observed RCs are extended enough and especially trace the flat regime of the RC.

One technique to estimate the stellar M_*/L needed for such decompositions is employing stellar population modeling. However, uncertainties associated with these models are unfortunately large since they require assumptions on the detailed star formation history (SFH), chemical enrichment, dust extinction, the initial stellar mass function (IMF) and detailed descriptions of late stellar evolution phases. From merely varying the choice of the IMF, resulting systematic uncertainties on the stellar M_*/L are a factor of two (e.g. Kauffmann et al. 2003a). Moreover, RC decompositions suffer from degeneracies that introduce further uncertainties on the resulting dark matter halo profiles. These uncertainties together allow a wide range in dark matter fractions in mass modeling approaches (see e.g. van Albada et al. 1985; Dutton et al. 2005; Courteau et al. 2014). Observationally, mass mod-

eling techniques applied to local rotation curves have been used to quantify the dark matter contribution within the peak of the rotation curve at $\sim 2.2r_d$, f_{dm} , with $f_{dm} = V_{DM}^2/V_{tot}^2$.

In order to overcome uncertainties in the stellar M_*/L , it has been proposed that the bulge and disk components contribute maximally to the total rotation curve (Carignan & Freeman 1985; van Albada et al. 1985). Through the assumption of disk maximality, the stellar M_*/L can set such that the inner rotation curve approximates the rotation curve of the baryonic component. In such a situation, f_{dm} inside $2.2 r_d$ should not exceed a value of ~ 0.28 . If the dark matter contributes more than this value, disks are referred to as 'sub-maximal'. In the literature there is currently no consensus whether disks are truly maximal. Instead, dark matter fractions seem to strongly depend on galaxy type (see discussion below).

In order to circumvent these uncertainties and break the disk-halo degeneracy, it is possible to use the vertical stellar velocity dispersion as an additional constraint to estimate the dynamical $M/L(dyn)$ (Martinsson et al. 2013):

$$M/L(dyn) = \frac{\sigma_z^2}{\pi G k h_z I}, \quad (1.11)$$

where I is the surface brightness, σ_z the vertical velocity dispersion, h_z the disk scale height, and k a geometry-dependent constant. Assuming an exponential disk surface density, $M/L(dyn)$ can be estimated through measuring the surface brightness and z-velocity dispersion. Using this technique, f_{dm} has been measured to lie in the sub-maximal regime for local face-on disk galaxies (Kregel et al. 2005). Recently, f_{dm} has also been determined for galaxies observed within the DiskMass survey (Bershady et al. 2010, 2011; Martinsson et al. 2013) targeting 46 almost face-on local galaxies. They show that their average dark matter fractions inside $2.2r_d$ point indeed to sub-maximal disks with $f_{dm} \sim 0.68$. The authors furthermore report positive correlations of the inferred baryonic fractions with surface brightness and total luminosity. Through detailed mass modeling using measurements of line-of-sight velocities and proper motions of stars in the Galactic disk, Bovy & Rix (2013) demonstrated that the dark matter fraction of the Milky Way is, however, in agreement with maximal disks.

There are other techniques to infer dark matter fractions, such as inspecting deviations from the Tully-Fisher relation (Tully & Fisher 1977) with surface brightness. The Tully-Fisher relation is an empirical relationship between the intrinsic luminosity and rotational velocity for spiral galaxies. Due to the lack of correlation between the surface brightness of galaxies and their offset from the velocity-luminosity relation, it has been shown that dark matter contributes roughly equal mass compared to baryons inside $2.2r_d$, supporting that bright spirals are sub-maximal disks (Courteau et al. 2007; Dutton et al. 2007).

The measurement of dark matter fractions in ETGs is more challenging but has been also made possible through surveys such as ATLAS-3D. In this case, inferred f_{dm} rely on velocity dispersion measurements and indicate that baryons in massive ETGs are strongly dominant within $2.2r_d$, in contrast to spiral galaxies (Cappellari et al. 2013). Furthermore,

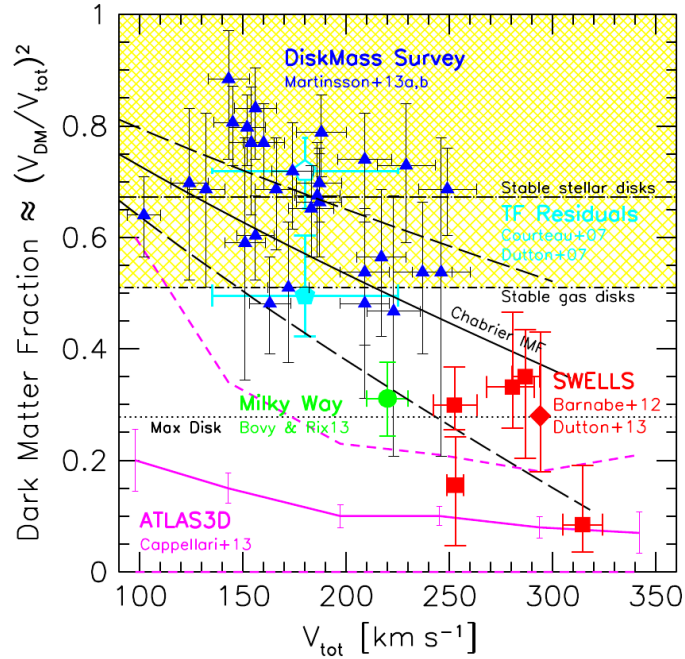


Figure 1.3: Dark matter fractions f_{dm} inside $2.2r_d$ as a function of total rotation velocity V_{tot} measured from various samples. This Figure is taken from Courteau & Dutton (2015).

strong gravitationally lensing can be used to break the baryon-dark matter halo degeneracy for deriving dark matter fractions. The deflection of light by the lens (i.e. the deflector) is sensible to its gravitational potential and thus a total matter distribution can be recovered when reconstructing the lens with aid of imaging data. If the lens is furthermore observed to trace the system's kinematics, a self-consistent mass model can be obtained, which can be decomposed into the baryonic and dark matter components. In this respect, surveys such as SWELLS, focusing on high-mass systems, have enabled the study of dark matter fractions and yield f_{dm} in agreement with disk maximality (e.g. Barnabè et al. 2012).

A compilation of the aforementioned measurements of f_{dm} across various galaxy types is shown in Figure 1.3 taken from Courteau & Dutton (2015). Low-mass spiral galaxies seem to be more dominated by dark matter than higher-mass systems or more massive ETGs. Despite the currently significant uncertainties in these measurements, the trends as well as the scatter in Figure 1.3 might reflect size variations (and equivalently variations in the morphology) among galaxies that are affecting the relative contribution of dark matter at a given scale radius. Possible variations among the underlying dark matter profiles could be also imprinted in these trends, which could be associated with a potential adiabatic contraction of the halo.

A discussion on the expansion of these studies to high redshift galaxies can be found in Section 1.3.4.

1.3 Properties of high redshift galaxies

1.3.1 Star formation properties

Until the advent of recent instrumental technologies during the last decades, our understanding of galaxy populations at higher redshift was very limited. However, since the discovery of redshifted Quasi-stellar objects (QSOs) detected at $z > 1$, our knowledge about the populations of 'normal' galaxies at higher redshift has been enormously improved. In our current understanding, the universe at $z \sim 1 - 4$ was the most active cosmic epoch in the galaxy assembly as seen by tracing the cosmic star formation rate density (cSFRD). Figure 1.4 shows the evolution of the globally averaged cSFRD in galaxies as a function of redshift measured by large look-back surveys, from a compilation of Madau & Dickinson (2014).

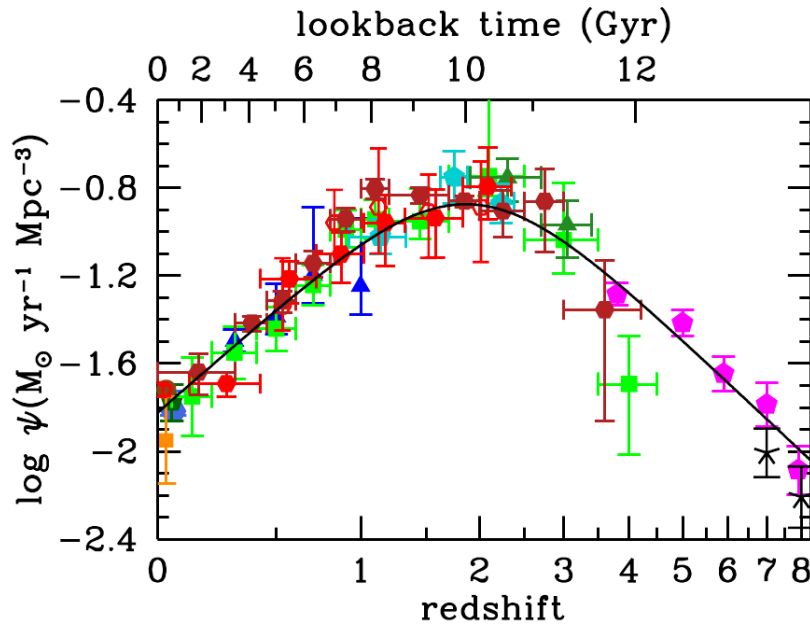


Figure 1.4: Compilation of the measured cosmic star formation rate density as a function of redshift. This figure is taken from Madau & Dickinson (2014).

As apparent in Figure 1.4, the cSFRD is rapidly increasing with look-back time and peaks at $z \sim 2$. At this epoch, the universe thus experienced the most rapid assembly of galaxies, which went alongside with a rapid accretion of black holes in QSO and high galaxy merger rates (e.g. Fan et al. 2001; Conselice et al. 2009; Kartaltepe et al. 2007; Lotz et al. 2011).

It is furthermore found that the vast majority of actively star-forming galaxies are aligned on a tight relation of 0.2 - 0.3 dex scatter, between their amount of assembled stars and the currently ongoing Star Formation Rate (SFR). This relation is dubbed the 'Main sequence'

(MS) and is found to have existed at least until $z \sim 4$ (Noeske et al. 2007; Daddi et al. 2007; Elbaz et al. 2007; Magdis et al. 2010; Whitaker et al. 2012, 2014). Figure 1.5 shows the $SFR - M_*$ relation for a sample of galaxies at $z \sim 0 - 2.5$ observed within the NEWFIRM Medium-Band Survey (NMBS), measured by Whitaker et al. (2012). The normalization of the MS, i.e. the specific star formation rate (sSFR) with $sSFR = \frac{SFR}{M_*}$, as also obvious from Figure 1.5, increases strongly with look-back time ($sSFR \propto (1+z)^3$, Lilly et al. 2013), such that at $z \sim 2$, the SFR in galaxies was higher by a factor of $\sim 10 - 20$ compared to their local counterparts at the same stellar mass. This increase reflects the evolution of cSFRD as shown in Figure 1.4.

The current interpretation of the existence and the observed tightness of the MS is that star-forming galaxies evolve along the MS when building up their stellar material, keeping their sSFR at an equilibrium level. This fast but 'continuous' growth of galaxies at higher redshifts seems to be triggered by efficient feeding through minor mergers and cold accretion streams from the surrounding cosmic web as suggested by recent numerical simulations. Moreover, the disk-like light profiles as well as the regular gas kinematics observed for the majority of star-forming galaxies (see discussion in the next two sections) both give independent evidence that the bulk of star formation in galaxies on the MS at least until $z \sim 2.5$ is occurring in a continuous mode rather than being triggered by major mergers.

As known in the local universe, the level of star-formation is tightly linked to the available reservoir of molecular gas. Observations quantifying the level of star formation as well as measuring the amount of hydrogen in local galaxies led to findings that both quantities are tightly correlated, which has been expressed by the Kennicutt-Schmidt (K-S) relation (Kennicutt 1998):

$$\Sigma_{SFR} = \Sigma_{gas}^n, \quad (1.12)$$

where Σ_{SFR} is the surface density of star formation and Σ_{gas} is the gas surface density. The zero point of this relation, e.g. the overall efficiency of star formation is set by the depletion timescale $t_{depl} = M_{gas}/SFR$, where SFR is the star formation rate and M_{gas} is the amount of gas in a galaxy. Equivalently, the often used star formation efficiency (SFE) is then $SFE = \frac{1}{t_{depl}}$. Studies quantifying both the neutral and molecular gas content of local spiral galaxies found that the K-S relation yields a linear relation (i.e. $n = 1$) over many orders of magnitude on galaxy-integrated as well as on resolved scales, when considering the molecular gas phase only, with typical t_{depl} of ~ 2 Gyrs (e.g. Bigiel et al. 2008). Studies of the molecular gas content of high- z star forming galaxies were enabled through deep CO observations, where the CO luminosity is converted into a molecular gas mass. Surveys such as PHIBSS (Tacconi et al. 2010, 2013) observing the CO 3 – 2 transition at a rest-frame frequency of 345.998 GHz using the IRAM Plateau de Bure Millimeter Interferometer have revealed that the molecular gas fraction f_g (i.e. the fraction of molecular gas mass to total baryonic mass) is significantly enhanced for star-forming galaxies (SFGs) at higher redshift compared to local spiral galaxies. Gas fractions at $z \sim 2$ are ~ 0.5 for typical main sequence galaxies and are decreasing to a local value of ~ 0.1 , which seems to explain the evolution of sSFR with redshift to a great extent (see also e.g. Daddi et al. 2010; Genzel et al. 2015).

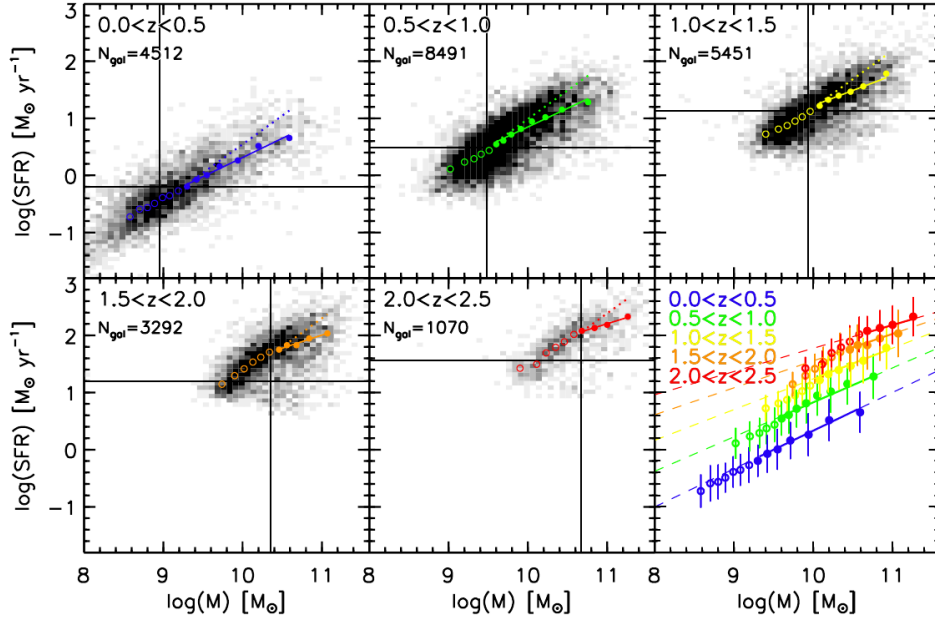


Figure 1.5: The relation between SFR and stellar Mass M_* for galaxies at $z \sim 0 - 2.5$ as measured within the NEWFIRM Medium-Band Survey. Each panel shows a different redshift range. The filled colored symbols denote the running medians above the mass completeness limit for the different redshift ranges, and the dashed lines in the last panel indicate the best-fit power law to the filled symbols. This Figure is taken from Whitaker et al. (2012).

By combining the systematic measurements of molecular gas through CO and dust mass observations of ~ 500 SFGs at redshifts $0 < z < 3$, Genzel et al. (2015) established scaling relations that allow estimates of gas masses for individual main-sequence galaxies based on their stellar mass and SFRs. Those scaling relations are based on inverting the K-S relation, where depletion timescales are calibrated based on observations.

The cause for these high gas fractions is plausibly attributed to elevated accretion rates of gas from the cosmic web onto galaxies at higher redshift, and has been qualitatively and quantitatively demonstrated with the aid of toy models, invoking a 'baryonic cycle' (e.g. Lilly et al. 2013). Within this 'gas regulator model', only part of the accreted gas resides in galaxies whereas frequent and rapid outflows expel the gas that is later partly re-accreted onto the disk. It is also observed that the conversion rate of molecular gas into stars is increased at higher redshifts, with depletion timescales of ~ 700 Myrs at $z \sim 2$ (Tacconi et al. 2013), which also implies an increased SFR compared to local galaxies at a given molecular gas mass. The high gas fractions at $1 < z < 3$ are observed to possibly be imprinted on the kinematical and morphological properties of star-forming galaxies on the MS, which will be discussed in detail in the remainder of this introduction.

1.3.2 Structural properties

Studying the morphology and therefore the baryonic structure of galaxies at higher redshift is challenging due to the limited resolution of ground-based telescopes as well as the rapidly decreasing surface brightness with redshift from the 'cosmological dimming', where the surface brightness decreases $\propto (1+z)^4$. Studies of morphologies of galaxies at high redshift were facilitated once space-borne missions such as the Hubble Space Telescope (HST) became available. Compared to facilities operating from the ground, space-based telescopes such as the HST do not suffer from atmospheric absorption and turbulence, allowing imaging with better sensitivity and at \sim kpc resolution. The first systematic imaging observations of high redshift systems with the HST were done at rest-frame UV wavelengths, based on deep integrations e.g. in the Hubble Deep Fields (Williams et al 1996), revealing peculiar morphologies of 'normal' SFGs at $z \sim 1-2$ (e.g. Schade et al. 1995; Abraham et al. 1996; Dickinson 2000). Figure 1.6 displays one of these imaging results from Elmegreen et al. (2004a). Those studies report irregular appearance, that do not resemble the regular pattern of local spirals (Elmegreen et al. 2004a, 2004b, 2005). Overall, the UV morphologies are dominated by bright clumpy, off-centered features that appear to have intrinsic sizes of typically ~ 1 kpc. Even when viewed edge-on, the clumps are aligned in an elongated structure. The interpretation of these morphologies is that a significant fraction of star formation in these galaxies resides in large star-forming clumps, and high dust columns further lead to a disturbed and irregular appearance.

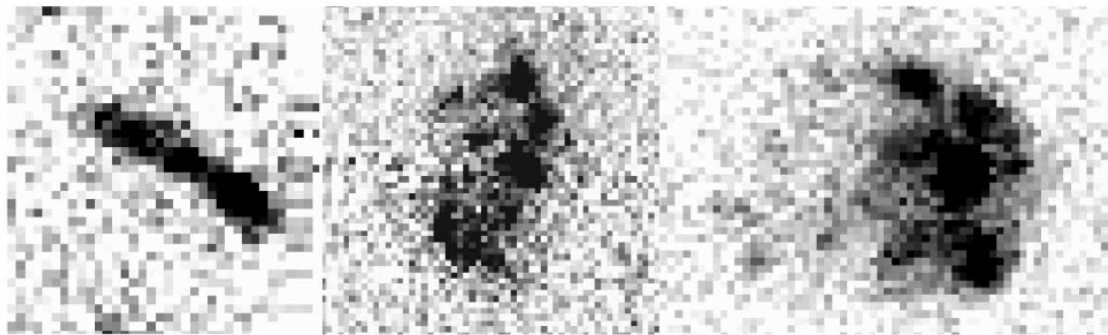


Figure 1.6: Rest-frame UV images of SFGs at $z \sim 1$ taken from the HST. This Figure is taken from Elmegreen et al. (2004a).

Several lines of evidence suggest that the star-forming clumps seen in high redshift galaxies originate from disk fragmentation rather than from accreted material in the context of mergers. E.g., the size distribution of SF clumps are to first order in agreement with the typical spatial scale on which gas is collapsing according to the Toomre instability criterion given the high gas fractions of high redshift disks. However, their time evolution still remains quite uncertain. Some hydrodynamical simulations suggest that they rapidly migrate

inward due to dynamical friction inside the disk and then finally coalesce in the central regions to form a stellar bulge (e.g. Bournaud et al. 2011). However, strong stellar feedback might disrupt the clumps on short timescales (e.g. Genzel et al. 2011). The photometric properties of clumps extracted in larger samples of galaxies observed with multi-wavelength imaging revealed radial optical color gradients too strong to be explained by extinction gradients, supporting the scenario of inward-migration (e.g. Förster Schreiber et al. 2011b, Guo et al. 2012).

The recent advent of high-resolution imaging instruments on board HST operating in the NIR regime at wavelengths $\sim 0.7 - 1.8\mu m$ have allowed us to trace the morphologies of high-redshift galaxies in the rest-frame optical regime, where the structure of the underlying bulk of stars can be seen, providing a more comprehensive picture of galaxy structure at high redshift. Deep panchromatic imaging surveys such as the COSMIC ASSEMBLY NEAR INFRARED DEEP EXTRAGALACTIC LEGACY SURVEY (CANDELS, Grogin et al. 2011; Koekemoer et al. 2011) allowed the systematic study of surface brightness distributions of star-forming as well as quiescent galaxies at early cosmic times.

CANDELS also enabled a more robust determination of the stellar mass - size relation for both SFGs and QGs separately, determined by van der Wel et al. (2014a) on the basis of size-measurements from Sérsic - profile fitting using the CANDELS rest-optical imaging dataset at redshifts $0 < z < 3$. The authors find that the radial extent of SFGs as characterized by their effective radius becomes smaller with increasing redshift: $R_e \propto (1 + z)^{-0.75}$. At all redshifts, the effective size correlates positively with increasing stellar mass, with a shallow slope of $M_*^{0.22}$. Beyond the quantification of their radial sizes, the 3D geometry of SFGs are reconstructed by modeling their distribution of projected axial ratios. While nearby SFGs appear to be really oblate thin disks, their counterparts at $z \gtrsim 1$ are a mixture of disky and triaxial (mainly elongated) systems, most noticeable at low ($M_* < 10^{10} M_\odot$) masses, suggesting that low-mass galaxies at high redshift have not yet developed a regular rotating disk (Law et al. 2012; Yuma et al. 2012; van der Wel et al. 2014b).

Another striking result of these studies using sufficiently large samples of galaxies is that the surface brightness distributions of star-forming galaxies on the MS are well approximated by exponential profiles, whereas Quiescent Galaxies (QGs) are better described with de Vaucouleurs profiles (e.g. Wuyts et al. 2011b). Figure 1.7 illustrates these measurements.

Clearly, a bimodality in star formation activity (i.e. the position relative to the MS) and morphology is apparent at $z > 1$, reflecting the existence of a Hubble sequence since at least $z \sim 2.5$ (see also Bell et al. 2012). This result confirms earlier studies based on smaller samples with HST imaging stating a correlation between galaxy color and morphology (Bell et al. 2004; Weiner et al. 2005; Koo et al. 2005). Utilizing photometric bulge-to-disk decompositions of light profiles for massive galaxies ($M_* > 10^{11} M_\odot$) at $1 < z < 3$, Bruce et al. (2012) showed that SFGs have disk-dominated profiles and QGs are bulge dominated. However, it should be noted that they also find a significant fraction ($\sim 30\%$) of passive disk-dominated galaxies and star-forming bulge-dominated systems in this high-mass regime (see also van der Wel et al. 2011).

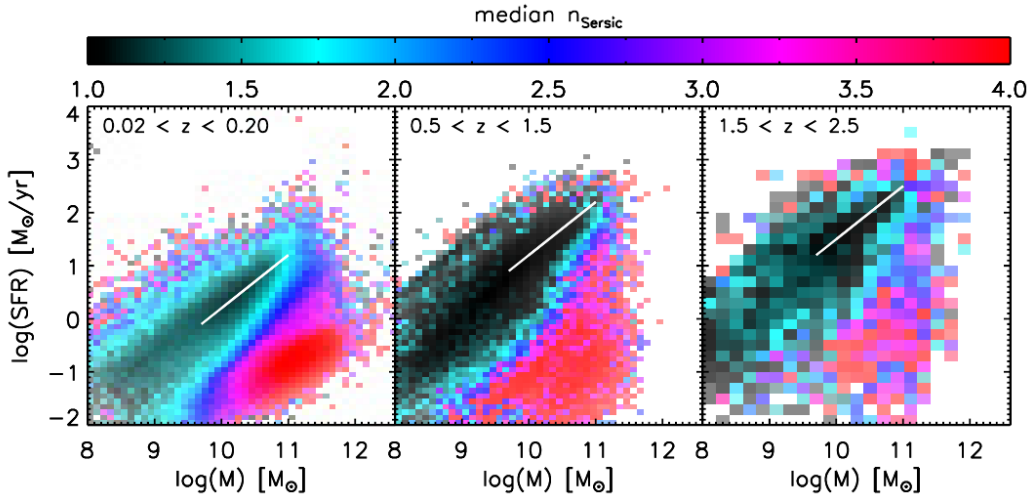


Figure 1.7: Rest-frame optical sersic indices of galaxies on the SFR - M_* plane up to redshift 2.5. This Figure is taken from Wuyts et al. (2011b).

All the above mentioned studies are currently based mostly on rest-frame optical and ultraviolet imaging approximating the stellar distributions. This assumes that the M_*/L does not vary significantly within galaxies which, however, does not need to be the case. As known from the detailed photometric analysis of resolved stellar populations in nearby galaxies, the M_*/L shows significant variations with the detailed SFH and extinction (e.g. Walcher et al. 2011; Conroy 2013 and references therein). At high redshift, the deep panchromatic imaging enabled us to go beyond the measurements of structure based on light profiles alone, and reconstructions of the stellar mass distributions became possible by determining the M_*/L through resolved Spectral Energy Distribution (SED) fitting. With this technique, described in detail by e.g. Zibetti et al. (2009), the M_*/L ratio is reconstructed by fitting SEDs to the multi-wavelength imaging. At high redshift, this technique was first employed by pioneering work using high-resolution imaging datasets from the HST/NICMOS camera on smaller sample sizes (e.g. Elmegreen et al. 2009; Förster Schreiber et al. 2011a). These authors demonstrated that the M_*/L and inferred stellar surface mass density Σ_* for their high- z SFGs can be reliably determined based on the information from one optical color index alone. This is possible since the chosen color index, covering the age-sensitive Balmer break, shows a tight correlation with the stellar M_*/L , largely independent of the details of SFH, metallicity and extinction (see also Tacchella et al. 2015). Utilizing the full available 7-band multi-wavelength imaging in the CANDELS/GOODS fields, Wuyts et al. (2012) employed resolved SED-modeling on a pixel-to-pixel basis for a large sample of ~ 600 massive ($> 10^{10} M_\odot$) SFGs at $0.5 < z < 2.5$. The resulting reconstructed stellar mass distributions show overall smooth structure since clumpy features seen in the

rest-frame optical light distributions large disappear in stellar mass. This finding confirms that the clumpy features represent young regions with copious amounts of SF, with a lower M_*/L than the underlying disk. As so far assessed only with non-parametric measurements, SFGs are more centrally concentrated in stellar mass than in light due to systematic positive rest-frame optical color gradients. These variations in M_*/L likely originate from a combination of internal varying SFHs and extinction, which possibly both contribute significantly (Guo et al. 2012; Lanyon-Forster 2012; Szomoru 2013; Wuyts et al. 2012, 2013). The color gradients appear to be most strongly pronounced for the most massive galaxies. Guo et al. (2011) have furthermore shown that also QGs at higher redshifts feature significant radial M_*/L gradients. The existence of such variations in M_*/L across galaxies at high redshift emphasizes the importance of measuring the underlying structure on reconstructed stellar mass maps rather than only on rest-frame optical imaging.

1.3.3 Kinematics

Complementary information about the evolution of galaxies at high redshift can be also obtained by analyzing their kinematics. This was first done by long-slit spectroscopy tracing optical emission lines, where the slit is placed along the morphological major axis of the targeted galaxy since no prior knowledge about the 2-dimensional velocity field is known. Observing galaxies at $0.1 \leq z \leq 3$ in this fashion, studies were able to give evidence for significant velocity gradients of the ionized gas component across star-forming galaxies, that even show regular disk-like rotation curves (e.g. Vogt et al. 1996, 1997; Moorwood et al. 2000; Pettini et al. 2001; Erb et al. 2003, 2004). The advent of sensitive Integral Field Unit (IFU) spectrographs on 8-10m class telescopes operating in the NIR enabled the study of resolved 2-dimensional velocity fields of star-forming galaxies, enabling a more comprehensive insight into their internal dynamics. One of the first pioneering IFU studies of high redshift SFGs were undertaken with the SINFONI instrument (Eisenhauer et al. 2003) mounted on the Very Large Telescope (VLT), using a set of 14 optically selected SFGs at $z \sim 2$ (Förster Schreiber et al. 2006). The seeing limited resolution of $0''.5$ revealed extended $H\alpha$ emission, with spatially resolved velocity gradients for most of the sources. For a significant fraction of their sample, the authors found 2D velocity fields that are well described by rotating disks, albeit with large velocity dispersions. The use of adaptive-optics (AO) assisted IFU observations have further facilitated the study of high- z kinematics at even higher spatial resolution. Genzel et al. (2006) employed AO observations with SINFONI to study the luminous SFG 'D3a15504' at ~ 1.2 kpc resolution, revealing interesting features such as radial gas motions hinting at gas inflows into the central regions. Further IFU surveys of the $H\alpha$ kinematics at redshifts $1 < z < 3$ with moderate sample sizes operating both in seeing-limited and AO mode, such as SINS/zc-SINF (Förster Schreiber et al. 2009; Mancini et al. 2011; Förster Schreiber et al. 2016 in preparation), MASSIV (Epinat et al. 2009, 2012; Contini et al. 2012; Vergani et al. 2012), WiggleZ (Wisnioski et al. 2011), HiZELS (Swinbank et al. 2012; see also Law et al. 2009), have largely improved our

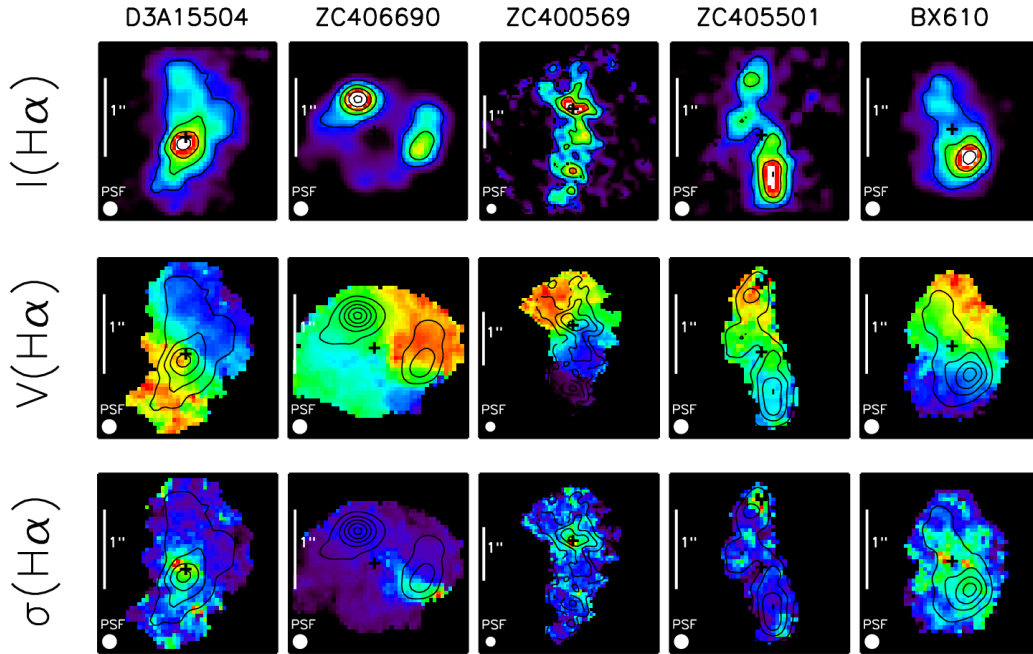


Figure 1.8: Surface brightness distributions, velocity fields, velocity dispersion fields of $H\alpha$ for a few massive star-forming galaxies in the SINS/zc-SINF AO survey.

knowledge of the dynamical state of high- z SFGs and confirmed that the majority of those are rotation dominated (i.e. systems with a ratio of inclination-corrected rotation velocity to the intrinsic velocity dispersion, $\frac{V_{rot}}{\sigma_0} > 1$). The largest among these surveys is the SINS/zc-SINF survey containing ~ 100 main sequence galaxies at $z \sim 1.5 - 2.5$ focused on massive ($M_* > 10^{10} M_\odot$) systems, with a large fraction of targets (35) followed up with AO-assisted observations. The survey also profits from the available ancillary data such as space-based multi-wavelength imaging and ground-based photometry.

Figure 1.8 displays example cases of $H\alpha$ surface brightness distributions, velocity fields, velocity dispersion fields for targets as part of the AO sample of the SINS/zc-SINF survey. Typical $H\alpha$ morphologies, reflecting the distribution of current ongoing star formation, are irregular and often with off-centered clumpy features, in agreement with the morphologies seen in rest-frame UV imaging. Despite the high angular resolution, the clumps are only marginally resolved, which confirms that those are extended, but possible substructures cannot yet be resolved. The $H\alpha$ morphologies often reveal a lack of ongoing star formation in the center, most importantly seen at high stellar masses, giving the impression of ring-like galaxies. This might stem from high dust columns towards the central regions or the absence of central star formation in those galaxies.

Despite the irregular $H\alpha$ morphologies, the $H\alpha$ velocity fields in SINS/zc-SINF show on average smooth underlying kinematics, as seen in Figure 1.8. In particular, the velocity

fields show spider-diagram like signatures (van der Kruit & Allen 1978) and the velocity dispersion maps are centrally concentrated, both of which can be well fit with rotating underlying disk models. Galaxies that appear to be most rotation-dominated (i.e. with the largest ratios of $\frac{V_{rot}}{\sigma_0}$) are most common among the larger and more massive systems, whereas smaller galaxies are more dominated by their random motions. Part of the large dispersion in smaller objects might arise through unresolved rotation due to their small angular sizes (e.g. Newman et al. 2013). Also the fact that dispersion dominated galaxies exhibit smaller stellar and dynamical masses hint at an early evolutionary stage of galaxies building up their stellar disk. Another third group of kinematic signatures are visible, which feature merger-like kinematics often alongside with counterparts seen in the HST imaging, which are however not dominating.

Recently, the K-band Multi Object Spectrograph (KMOS, Sharples et al. 2004, 2013) instrument at the VLT has started operations, further facilitating the systematic analysis of high redshift galaxy kinematics by highly multiplexed observations. KMOS is an instrument with 24 configurable arms that position pick-off mirrors in the focal plane (see Figure 1.9), each to feed a separate IFU simultaneously. Each of these IFU units have a $2''.8 \times 2''.8$ FOV with a spatial sampling of $0''.2$. The IFU units can be placed in a patrol field that is 7.2 arcmin in diameter. Equipped with these multiplexing capabilities, KMOS is able to increase the efficiency of previous single IFU surveys increasing previous sample sizes up to several hundred galaxies with deep integrations needed for measuring kinematics of SFGs at high redshift. The ongoing KMOS^{3D} survey (Wisnioski et al. 2015) utilizes the capabilities of KMOS in synergy with existing space - and ground based spectroscopic and photometric data in the deep fields GOODS-South, EGS and COSMOS, all of which have been observed as part of the CANDELS and 3D-HST Treasury Programs (Grogin et al. 2001; Koekemoer et al. 2012; Brammer et al. 2012; Skelton et al. 2014; Momcheva et al. 2015). KMOS^{3D} also profits from the available accurate redshift information from the 3D-HST grism survey providing the parent sample for the mass selected KMOS^{3D} sample at redshifts $0.7 < z < 2.7$. The KMOS^{3D} sample covers the main sequence population homogeneously, focusing at stellar masses $M_* > 10^{10} M_\odot$. Observations within the first year of the entire KMOS^{3D} program have confirmed that the vast majority of star-forming galaxies are rotating disks (Wisnioski et al. 2015). The fraction of disks is found to be 59% even when applying strict criteria to select rotating disk (such as $\frac{V_{rot}}{\sigma_0} > 1$, alignment of photometric and kinematic axis, a continuous velocity gradient across the 2D velocity field, and a kinematic center coinciding with the peak in the observed stellar continuum). Galaxies that do not show signs of rotation are found mainly at low stellar masses. Galaxies in the KMOS^{3D} sample that lie significantly below the MS, if detected, feature signatures of rotation as well, hinting at a significant population of rotating disks below the MS, albeit typically more compact (Wisnioski et al. 2016 in preparation).

The KMOS^{3D} dataset is also an excellent basis to infer the level of intrinsic velocity dispersion, σ_0 , and its evolution with redshift. The resolved dispersion distributions for galaxies within KMOS^{3D} are typically centrally peaked due to beam smearing which is

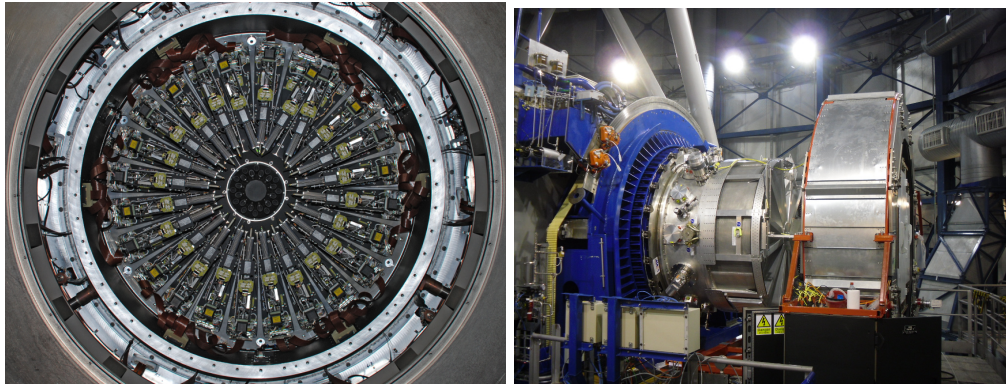


Figure 1.9: Left: Robotic pick-off arms positioned around the Nasmyth focal plane feeding the KMOS IFUs. Right: The KMOS instrument installed at the Nasmyth focus at the ESO VLT UT1. Image credits: '<http://www.ukatc.stfc.ac.uk/projects/kmos/35340.aspx>'

strongest near the kinematic center where velocity gradients are highest. Towards the outer regions, the dispersion profiles asymptotically decrease towards the outer constant level of intrinsic velocity dispersion. Thus, the measurements of σ_0 are done in regions where the beam smearing is minimal, when the rotation curve reaches the turnover in velocity. The resulting σ_0 distributions reveal a significant evolution within the observed redshift range, from $\sim 25 \text{ kms}^{-1}$ at $z \sim 1$ to $\sim 55 \text{ kms}^{-1}$ at $z \sim 2$ for the MS population. Figure 1.10 illustrates the evolution of σ_0 combining measurements from KMOS^{3D} and other IFU studies of ionized and molecular gas as compiled by Wisnioski et al. (2015). Included are measurements at high redshift from the SINS/zC-SINF survey (Förster Schreiber et al. 2009, 2014), the MASSIV survey (Epinat et al. 2012; Vergani et al. 2012), the AMAZE-LSD surveys (Gnerucci et al. 2011), the OSIRIS survey from Law et al. (2009), the DEEP2 long-slit survey (Kassin et al. 2012), the GHASP sample (Epinat et al. 2010), and molecular gas velocity dispersion measurements from the PHIBSS survey (Tacconi et al. 2013). Locally, measurements from the 'main sequence' subset of the DYNAMO sample (Green et al. 2014) and the HERACLES survey (Leroy et al. 2008, 2009) are added.

The overlap of the different measurements is large and indicates that gas velocity dispersions of SFGs at high redshift are significantly elevated compared to their local counterparts. The origin of these large velocity dispersions reflecting a more turbulent ISM in high redshift disks is not yet fully understood. Proposed explanations include e.g. feedback (e.g. Dib et al. 2006; Green et al. 2010) or the release of gravitational energy from gas accretion onto the disk (Förster Schreiber et al. 2006; Genzel et al. 2006, 2008; Cacciato et al. 2012). Both of these processes are indeed expected for high-redshift galaxies since outflows from both star formation and AGN are observed (e.g. Genzel et al. 2011; Newman et al. 2013; Förster Schreiber et al. 2014; Genzel et al. 2014b). Accretion of gas onto high redshift galaxies can be inferred from the observed gas fractions (e.g. Tacconi et al. 2010, 2013; Daddi et al. 2010; Genzel et al. 2015). These effects can be all interlinked which each

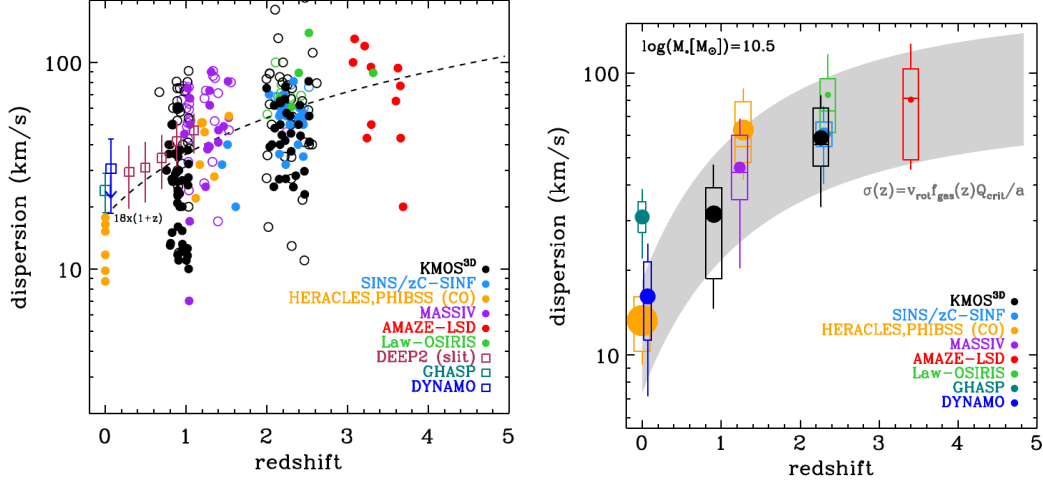


Figure 1.10: Left: Measurements of galaxy velocity dispersion at $z \sim 1-4$ based on ionized molecular gas emission, taken from the literature as well as from KMOS^{3D} for the $z \sim 1$ and $z \sim 2$ samples (black symbols), compiled by Wisnioski et al. (2015). The dashed lines denotes a linear redshift evolution of $(z + 1)$ scaled to overlap with the observations. Right: Same as the left panel but with binned measurements of the high-resolution IFU measurements, together with their 50 and 90 percent scatter (boxes and vertical lines, respectively). The grey shaded area indicates the expected evolution of dispersion on the basis of equation 1.13, and 1.14 for the evolution of gas fractions for MS galaxies, $a = \sqrt{2}$, and a constant rotation velocity according to $\log(M_*) = 10.5$. These Figures are taken from Wisnioski et al. (2015).

other as shown by the gas regulator models mentioned in Section 1.3.1 which connect the evolution of gas accretion rates with gas fractions, sSFR, and outflow properties of the gas within a baryonic cycle that keeps galaxies in an self-regulated equilibrium state.

The compilation of data in Figure 1.10, despite difference in details of measurement, is consistent with an evolution of $\propto (1 + z)$. In fact, the level of intrinsic velocity dispersion can be connected with the gas fraction via rewriting the Toomre stability criterion (Toomre 1964) for a rotating disk:

$$\frac{V_{rot}}{\sigma_0} = \frac{a}{f_{gas}Q} \quad (1.13)$$

Assuming that $a = \sqrt{2}$ and $Q \sim 1$ for quasi-stable disks (Förster Schreiber et al. 2006; Genzel et al. 2011; Wisnioski et al. 2015), the expected dispersion can be expressed as

$$\sigma_0 = \frac{1}{\sqrt{2}} V_{rot} f_{gas}(z). \quad (1.14)$$

To first order, this trend matches the observations shown in Figure 1.10 remarkably well.

Thus the observed evolution of σ_0 is consistent with being a consequence of the evolution of galaxy properties such as the gas fraction, depletion time scales and sSFR, in turn reflecting a higher accretion rate of gas onto galaxies at higher redshift in the context of gas regulator models. However, the scatter in the σ_0 measurements at a given redshift is large, and may reflect real intrinsic variations but also stem from measurement uncertainties. The latter might be increased for galaxies where the dispersion profile cannot be traced out far enough into the regime where the rotation curve flattens, thus overestimating σ_0 .

1.3.4 Dark matter fractions

Since ionized gas kinematics for star-forming disks are available also at high redshift, the methodologies described in Section 1.2.2 are also applicable to access the dark matter versus baryon mass budget at higher redshifts, albeit with more limitations. These include notably the vastly decreased angular size and surface brightness compared to local galaxies and the significant uncertainties of stellar and gas mass estimates. Furthermore, rotation curves of SFGs at high redshift are currently well probed only in their inner parts whereas their profiles in the outer, fainter parts of disks are largely unconstrained. Thus estimates of the dark matter fractions merely rely on measurements of the kinematics and baryon masses inside the turnover radius. Using the measurements of rotation velocities on individual RCs reaching out to the turnover radius, in combination with estimates of integrated stellar masses from SED modeling with added gas mass estimates (from e.g. gas mass scaling relations) available for high redshift disks, their dynamical mass budget can be split into dark matter and baryon components.

On the basis of the SINS IFU sample, Förster Schreiber et al. (2009) estimated dark matter fractions of $\sim 0.2 - 0.3$ inside ~ 10 kpc, hinting at strong baryon dominance within the inner regions of massive SFGs at $z \sim 2$. Complementary measurements based on larger IFU datasets have confirmed these high baryon fractions for SFGs at $1 < z < 3$, with the aid of KMOS^{3D} (Burkert et al. 2015; Wuyts et al. 2016) estimating $f_{dm} = 0.25 - 0.33$. Based on long-slit spectroscopy with the MOSIFRE instrument, Price et al. (2015) even estimate $f_{dm} = 0.08$ inside the effective radius.

The above findings might be on the one hand a result of a more compact baryonic configuration in disk galaxies at high redshift compared to their local counterparts. On the other hand numerical simulations show that also the underlying dark matter halos are expected to be less concentrated at higher redshifts (e.g. Neto et al. 2007; Zhao et al. 2009; Prada et al. 2012), leading to an increase of the inner baryonic fraction for a galaxy at a given baryon density.

Extrapolating the measured kinematics plus baryon distributions in the inner parts, employing the MMW Model (Mo et al. 1998) based on the currently largest compilation of IFU datasets, Burkert et al. (2015) determined the stellar and baryonic fractions in the disk compared to the whole halo for SFGs at $0.5 < z < 2.5$. The authors find a stellar disk mass fraction $\frac{M_*}{M_{DM}}$ of ~ 0.022 and $m_d = \frac{M_* + M_{gas}}{M_{DM}}$ of ~ 0.05 when accounting for the signifi-

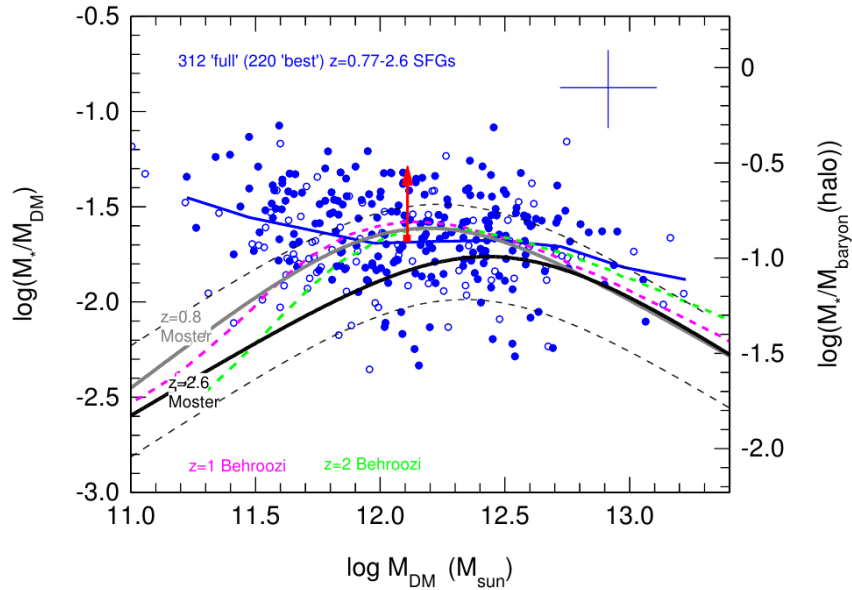


Figure 1.11: Ratio of stellar to total halo mass as a function of halo mass based on the sample of Burkert et al. (2015). Measurements of single galaxies are in blue, the median is plotted as the red square, and the red arrow indicates the change when including the contribution of molecular gas mass. Typical uncertainties are indicated by the blue cross. The right vertical axis indicates the ratio between the disk mass and the total amount of available baryons inside a halo assuming a cosmic baryon fraction of 0.17. The lines display the results of abundance matching for different redshifts from Moster et al. (2013) and Behroozi et al. (2013). This Figure is taken from Burkert et al. (2015).

cant molecular gas contribution of $f_{gas} \sim 0.58$. The determined fractions show only little dependence on halo mass. Despite significant uncertainties, these findings are in reasonable agreement with the findings determined independently by abundance matching techniques such as by Moster et al. (2013) and Behroozi et al. (2013). The measurements of m_d from Burkert et al. (2015) for the sample is plotted in Figure 1.11, also in comparison with predictions from from abundance matching. Extending observations of strong gravitationally lensed early-type galaxies up to redshifts of ~ 1 so far hint at the existence of extended a significant dark matter component in the galaxies with $f_{dm} = 0.15 - 0.65$ (Treu & Koopmans 2004).

1.3.5 The need for quenching

The fact that ETGs exhibit no or very little SF activity has been interpreted as an evolutionary sequence, in which one or several quenching processes lead to a significant shut-down of star formation on short timescales (see e.g. Bell et al. 2004; Faber et al. 2007). However,

quenching remains still not fully understood in terms of its underlying physical mechanism.

A crucial element providing information about the evolution of galaxies comes from their relative abundance distribution as a function of luminosity or stellar mass. First measurements that were based on counting bright nearby galaxies showed that their distribution of number densities as a function of luminosity, dubbed the 'luminosity function', can be fit by the so-called 'Schechter function' (Schechter 1976):

$$\Phi(L)dL = \Phi^* \left(\frac{L}{L_*}\right)^\alpha \exp(-L/L_*) \frac{dL}{L_*}, \quad (1.15)$$

where $\Phi(L)$ is the number density of galaxies at luminosity L , L_* is the characteristic luminosity, α is the faint-end slope, and Φ^* is the normalization of the distribution. With the aid of estimates on the stellar M/L , also the abundance of galaxies as a function of their stellar mass could be established (e.g. Salucci & Persic 1999; Balogh et al. 2001; Cole et al. 2001), which can also be parametrized equivalently by the Schechter function. Then, the characteristic mass at which the number density of galaxies drops rapidly, is referred to as the 'Schechter Mass'.

The relative abundance and number densities of SFGs and QGs at different cosmic epochs have been studied with the aid of large surveys employing number counts. Surveys such as the SLOAN DIGITAL SKY SURVEY (SDSS), NMBS, zCOSMOS, and ULTRA-Vista have characterized the mass functions of the two galaxies populations and found that the number density of SFGs at redshifts $\lesssim 4$ is rapidly dropping above the Schechter Mass at $\log M_* \sim 10.8$, whereas passive galaxies become more abundant at these high stellar masses (e.g. Brammer et al. 2011; Ilbert et al. 2013; Muzzin et al. 2013; Woo et al. 2013; Tomczak et al. 2014). Peng et al. (2010) find that the fraction of quenched systems, f_q , is exponentially increasing with mass and interpret f_q as a probability of a galaxy to be quenched.

Another independent evidence for the need for quenching comes from numerical simulations. The mass function of dark matter halos from N-body simulations reveal a very different shape than the observed mass functions of stellar material in galaxies (e.g. Mo et al. 2010). Specifically, the overall efficiency of star formation must be highly suppressed depending on halo mass to explain these measurements, hinting at efficient quenching mechanisms at high and low stellar masses. These effects can be quantified by employing abundance matching. Within this technique, the cumulative abundance of galaxies constrained from observed mass functions are matched with those of dark matter halos from simulations. One of the results are shown in Figure 1.12, adopted from Moster et al. (2013).

The left panel displays the dependence of stellar mass of central galaxies (i.e. galaxies located in the center of dark matter halos, representing the most massive galaxy in a given halo) m_{cen} on the underlying dark halo mass M_h , for redshifts $0 < z < 4$.

In the right panel, the ratio between the baryons that have been converted into stars, and the total available baryons in a halo (with the latter being $M_h \times \frac{\Omega_{bar}}{\Omega_{DM}}$) is shown. As apparent in Figure 1.12, in halos above $M_h \sim 10^{12} - 10^{13} M_\odot$, the conversion of baryons

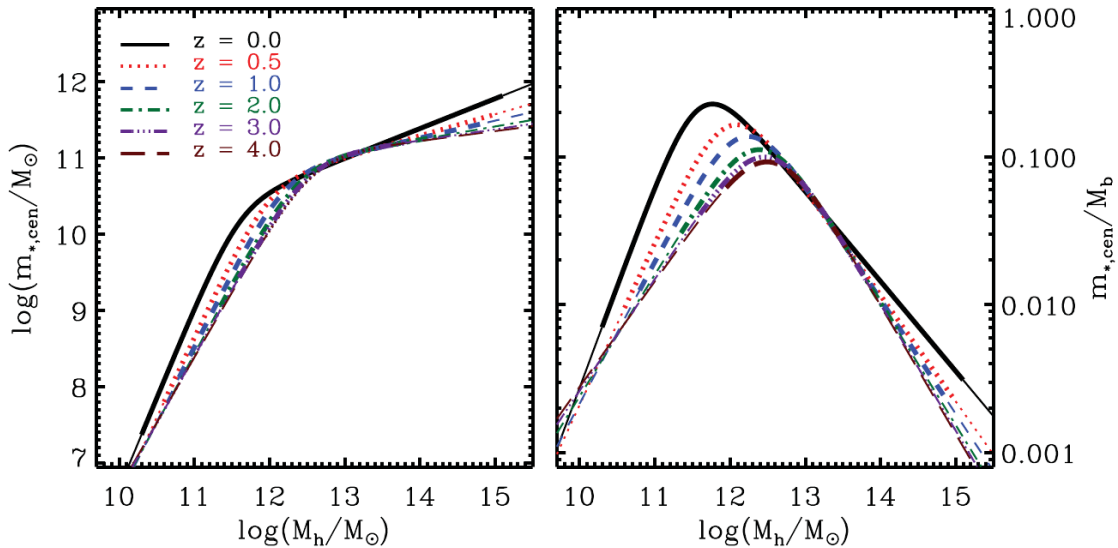


Figure 1.12: Abundance matching results showing the stellar mass of the central galaxy (left) and the mass ratio between the central galaxy and the total baryons inside the halo (right), plotted as a function of underlying dark matter halo mass and redshift. This Figure is taken from Moster et al. (2013).

into a stellar disk is more and more suppressed. As halos grow in mass beyond $10^{12} M_{\odot}$, the baryonic fraction decreases, and the stellar mass of central galaxies does not show significant increase. These findings hint at an efficient suppression of conversion of baryons into stars for high-mass galaxies, which is also the case for low-mass galaxies. Moreover, the overall efficiency of galaxy formation can be determined, which seems to be fairly low and at most $\sim 10\%$ in a given dark matter halo. The ratio between stars in the disk and the total dark matter halo mass, m_d , yields a ratio of $\sim 2 - 3\%$, which does mildly vary with redshift (see also Behroozi et al. 2013).

Several mechanisms have been proposed as agents of quenching, which either remove gas from galaxies, hinder the inflow of gas, or prevent existing gas from forming stars. For the high-mass regime of galaxies, one possible quenching mechanism is feedback from the central AGN as a power source that can drive powerful outflows once a sufficient accretion rate onto the central SMBH is reached. Such feedback mechanisms might be triggered by galaxy mergers (e.g. Hopkins et al. 2006) that lead to compression of gas and high accretion rates onto the central black hole. Also, internal secular processes in disk galaxies such as disk instabilities might lead to dissipation and inflow of gas onto the central black hole. Moreover, slow accretion rates may suppress the cooling of gas onto galaxies via heating the gas in the halo over a larger timespan (Croton et al. 2006).

Another possible process is morphological quenching (e.g. Martig et al. 2009). This

effect reduces the efficiency of star formation significantly by stabilizing the gas in the disk of galaxies against collapse through increased gravitational shear caused by a central stellar mass concentration. In the local universe, t_{depl} is indeed found to be correlated with Hubble type and to be increased for ETGs by a factor of a few, based on molecular gas measurements (e.g. Saintonge et al. 2012; Crocker et al. 2012). However, estimates of t_{depl} in ETGs are still rare since they are observationally challenging, and it is yet unclear if the observed increase in t_{depl} is sufficient to explain quenching. At higher redshifts, Genzel et al. (2014a) found that the central regions of massive SFGs with pronounced stellar mass concentrations seem to be stabilized against gravitational collapse suggesting that morphological quenching is acting inside high redshift galaxies.

Moreover, quenching might be caused by the fact that massive halos of galaxies are able to hinder the inflow of cold gas onto the galaxy due to shock heating at the virial radius (see Section 1.1.2). Simulations indicate that dark matter halos exceeding a critical mass of $M_{vir} \sim 10^{12} M_{\odot}$ can cause significant quenching (Birnboim & Dekel 2003; Kereš et al. 2005).

In the case of feedback and morphological quenching, a correlation between the quenching in galaxies (as traced by e.g. stellar population properties) and galaxy morphology is expected. Empirically, the mass of SMBHs in the local universe is observed to be correlated with the mass of a stellar bulge (e.g. Magorrian et al. 1998; Häring & Rix 2004). Furthermore, local galaxy surveys have indeed provided evidence for a strong correlation between the stellar population properties and morphological parameters such as the Sérsic index, stellar mass density or central velocity dispersion (Kauffmann et al. 2003b, 2006; Schiminovich et al. 2007; Bell 2008; Fang et al. 2013; Cheung et al. 2012). However, these correlations still lack a conclusive interpretation about the underlying mechanism of quenching that directly or indirectly causes such observed trends.

1.4 This thesis

1.4.1 Motivation and structure

Vast progress has been made in high redshift galaxy evolution studies on the basis of exquisite ground and space-based datasets, but many open questions about the processes driving the assembly and quenching of galaxies remain poorly understood. On the one hand, it is still not clear what structural changes star-forming galaxies undergo during their lifetime and how these are possibly connected to the shut-down of star formation. Although various correlations of stellar population properties with galaxy structure are found at higher redshift extending our paradigm of the Hubble Sequence to at least $z \sim 2.5$, we still lack a consistent picture of how underlying physical processes drive the quenching of galaxies. On the other hand, also the relative contribution of baryonic and dark matter components inside galaxies at high redshift is currently unconstrained, although its quantification is important to understand the assembly of disk galaxies inside dark matter halos.

In this work, I will address some of these open questions on the basis of two novel approaches. In the first part of this thesis (Chapter 2), I will turn to a project that focused on characterizing the inner stellar structure of galaxies at $0.5 < z < 2.5$ on the basis of deep panchromatic high-resolution imaging. Those are related to their star formation properties in order to elucidate how structural growth within high redshift galaxies can be connected to possible underlying quenching mechanisms. The second part of this thesis (Chapter 3) focuses on constraining the outer kinematics of high-redshift disk galaxies on the basis of deep and large IFU datasets. By constraining a representative extended rotation curve, I will discuss important implications on the baryonic mass fractions as well as outer disk structure of high-redshift disks. Chapter 4 contains an additional discussion about corrections used to determine beam-smearing corrected intrinsic kinematical properties based on IFU measurements of high-redshift galaxies.

Chapter 2

Bulge growth and Quenching since $z = 2.5$ in CANDELS/3D-HST

In this chapter I will present an analysis of the inner stellar mass distributions of galaxies to shed light on the connection between galaxy structure and the quenching process of star-forming galaxies at high redshift. This analysis is based on the deep multi-wavelength HST imaging dataset from the CANDELS survey offering the needed depth and spatial resolution to conduct measurements of structure on galaxy samples of statistically significant sizes. The star-forming properties of the sample galaxies are obtained with the aid of the comprehensive set of UV to far-IR ancillary data also available in these well-studied extragalactic fields. This chapter has been published in Lang et al. (2014); Figures 2.5 - 2.11 and most of the text in this chapter are borrowed from this paper.

First, I will discuss the motivation and aims of this analysis. In Section 2.2, I give an overview of the CANDELS imaging and 3D-HST redshift grism information and available ancillary data, as well as the selection of the sample used for this analysis. This is then followed by a description of the construction technique of stellar mass maps through resolved stellar population modeling in Section 2.3. I will then proceed to the methodology of deriving structural parameters including single Sérsic fits and bulge-to-disk decompositions. The resulting profile shapes are presented and discussed in Section 2.4, followed by a discussion of their relation to the galaxy-integrated star-forming properties. In Section 2.5, these findings are compared to predictions from state-of-the-art semi analytic models to make statements on possible quenching mechanisms at high redshift that can explain the observed trends. The observational results inferred from the structural analysis on stellar mass maps are furthermore compared with those inferred from H -band light images in Section 2.6. Finally, I summarize and discuss the implications of the findings in Section 2.7.

2.1 Aims

As mentioned in Chapter 1, current measurements of galaxy structure indicate the existence of a Hubble sequence since at least $z \sim 2.5$, on the basis of rest-frame optical light profiles. This has been shown on the basis of Sérsic profile parametrizations using large samples including parts of the CANDELS imaging datasets, as well as on bulge-to-disk decompositions on smaller samples (e.g. Wuyts et al. 2011b; van der Wel et al. 2011; Bruce et al. 2012; Bell et al. 2012). Despite these observational findings that demonstrate this correlation of star-formation properties and galaxy morphology, we still lack a conclusive interpretation of the underlying physical mechanisms responsible for quenching. Moreover, reconstructions of stellar mass distributions for star-forming galaxies as well as passive galaxies indicate the presence of significant M_*/L gradients within galaxies, that affect the interpretation of structural measurements of rest-frame optical imaging at high redshift. In order to further shed light on the connection between galaxy structure and quenching, we reconstruct stellar mass maps of a large mass-selected sample ($> 10^{10} M_\odot$) of galaxies at $0.5 < z < 2.5$ and subject those to a detailed structural analysis. For this purpose, we exploit the available multi-wavelength data in all 5 CANDELS/3D-HST fields with accurate redshifts from the 3D-HST survey offering a unique combination of sample size and depth. We do not restrict the structural measurements to one-component (Sérsic) fits, but rather also explore two-component (bulge + disk) decompositions. The latter fits allow us to carry out a more direct comparison to semi-analytic models (SAMs; specifically those by Somerville et al. 2008, 2012, further developed by Porter et al. 2014), whose prescriptions are formulated in terms of disk and bulge components. Since the agent of quenching built in the SAM is known, we are able to interpret our observed trends in the context of possible quenching mechanisms acting at high redshift.

2.2 Data and Sample selection

The core dataset used for this work is the deep space-based HST imaging from the CANDELS multi-cycle treasury program (Grogin et al 2011; Koekemoer et al 2011), complemented with redshift information from the 3D-HST grism survey (van Dokkum et al. 2011; Brammer et al. 2012; Skelton et al. 2014; Momcheva et al. 2015)¹. The properties of both datasets are described in the following sections.

In order to determine galaxy-integrated masses and SFRs, we use additional multi-wavelength data in the CANDELS/3D-HST fields including space-based photometry from *Spitzer*/IRAC, *Spitzer*/MIPS and *Herschel*/PACS and an array of ground-based facilities (see Skelton et al. 2014 for a detailed description of the *H*-selected multi-wavelength catalogs produced by the 3D-HST team).

¹The AGHAST G141 grism observations within GOODS-North from the GO-11600 program (PI: B. Weiner) are included in the analysis under ‘3D-HST’ (Brammer et al. 2012).

The galaxy-integrated properties are derived following identical procedures as Wuyts et al. (2011b). These include stellar masses, based on U - to $-8\mu\text{m}$ broad-band SED modeling using population synthesis models from Bruzual & Charlot (2003) and SFRs derived from a ‘ladder of SFR indicators’ (see also Wuyts et al. 2011a). The latter method uses detected emission in either UV + PACS for PACS-detected galaxies (Lutz et al. 2011; Magnelli et al. 2013) or UV + MIPS $24\mu\text{m}$ for MIPS-detected galaxies to compute the sum of the dust obscured and unobscured SFR. For galaxies lacking an IR detection, the SFR is adopted from the best-fit SED model.

2.2.1 The HST CANDELS and 3D-HST datasets

The CANDELS survey is a multi-orbit imaging survey using several cameras on the Hubble Space Telescope, covering the wavelength range from the ultraviolet to the NIR, imaging over 250,000 distant galaxies over a wide redshift range. The areas selected for the survey are five distinct sky regions with extensive available ancillary data: GOODS-South, GOODS-North, COSMOS, UDS, and EGS, covering a total area of 800 arcmin². The GOODS fields represent a natural choice for CANDELS since they represent regions with some of the deepest observations taken from various telescopes from space and ground covering a wide range in wavelength from the X-ray to the far-IR and radio regime. CANDELS is therefore focused on obtaining deep exposures in these fields, but also to extend its imaging capabilities to three other well-studied extragalactic fields in order to minimize the effects of cosmic variance and further gain from follow-up observations from ground-based telescopes. The unique combination of depth and covered sky area has been mainly made possible through the installation of the WFC3 instrument that strongly improves the previous NIR imaging cameras on the HST, such as NICMOS, in terms of FOV and sensitivity. CANDELS is subdivided into CANDELS/deep and CANDELS/wide. The deep part of the survey is focused merely on obtaining long exposures in the GOODS fields (covering ~ 125 arcmin²), whereas the wide part extends to all five CANDELS fields covering a larger survey area with shallower exposures. The observations within the survey are made through mosaicked exposures with the WFC3 camera as well as complementary overlapping exposures with the ACS instrument. The ACS camera covers the optical-to-UV spectral range, supplementing the WFC3 observations through greater sensitivity, with cost of angular resolution through somewhat coarser pixel sampling. Figure 2.1 shows a compilation taken from several figures in Grogin et al. (2011) and outlines the exposures made in the five CANDELS fields, arranged in mosaicked tiles. Each of the tiles contain $\sim 2 - 3$ HST orbits for CANDELS/wide and ~ 13 orbits in CANDELS/deep fields. The WFC3 camera features observing capabilities in separate UV and NIR wavelengths (dubbed ‘UVIS’ and ‘IR’ channels, respectively) with a FOV of 162×162 arcseconds and 136×123 arcseconds.

The available passbands within CANDELS that are used for this study are B_{435} , V_{606} , i_{775} , z_{850} , J_{125} , H_{160} for the GOODS fields and V_{606} , I_{814} , J_{125} , H_{160} for the remaining fields. Typical limiting depths in H_{160} are 27.0 mag for CANDELS/wide and 27.7 mag for

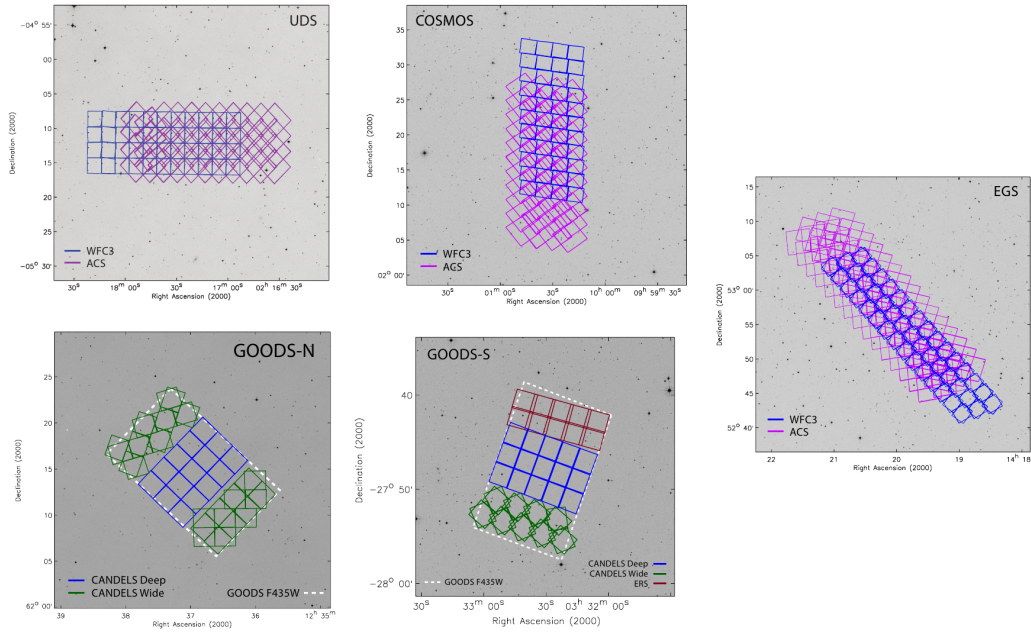


Figure 2.1: Footprints of exposures taken in the five CANDELS fields. In the fields COSMOS, UDS and EGS, as part of CANDELS/wide, observations were done using the ACS camera in parallel with WFC3, as outlined by the purple and blue boxes, respectively. In the GOODS fields, additional observations as part of CANDELS/deep are outlined as blue boxes compared to the CANDELS/wide observations indicated by green boxes. The WFC3 imaging from ERS in GOODS-South is outlined as red boxes. This figure is taken from Grogin et al. (2011).

CANDELS/deep (the central halves of the GOODS fields), respectively. Additional data used for this work include pre-existing ACS imaging in the GOODS, EGS, and COSMOS fields (Giavalisco et al. 2004; Davis et al. 2007; Koekemoer et al. 2007), plus WFC3 imaging in ERS (Windhorst et al. 2011). Additionally, Y_{098} imaging was available for ERS as part of GOODS-South and Y_{105} for the regions with CANDELS/Deep coverage. All imaging used in our analysis was drizzled to a $0''.06$ pixel scale. For further details on the observations and data reduction, we refer the reader to Koekemoer et al. (2011) and Grogin et al (2011). The CANDELS dataset used for this study comprise observations that overlap with the supplementary 3D-HST dataset, making up total area of 625 arcmin^2 within the CANDELS fields.

The 3D-HST survey is a HST Treasury program of 248 orbits covering a large portion (625 arcmin^2) of the five CANDELS fields. The observations comprise mosaicked exposures within the CANDELS fields as displayed in Figure 2.2, taken from Brammer et al. (2012). The survey utilize the WFC3/G141 and ACS/G800L grisms obtaining low-resolution ($R \sim 130$) slitless spectroscopy. The grism observations allow to trace the nebular emissions lines $H\alpha$, [OIII] and, [OII] within the redshift range $0.7 < z < 3.4$ mapping

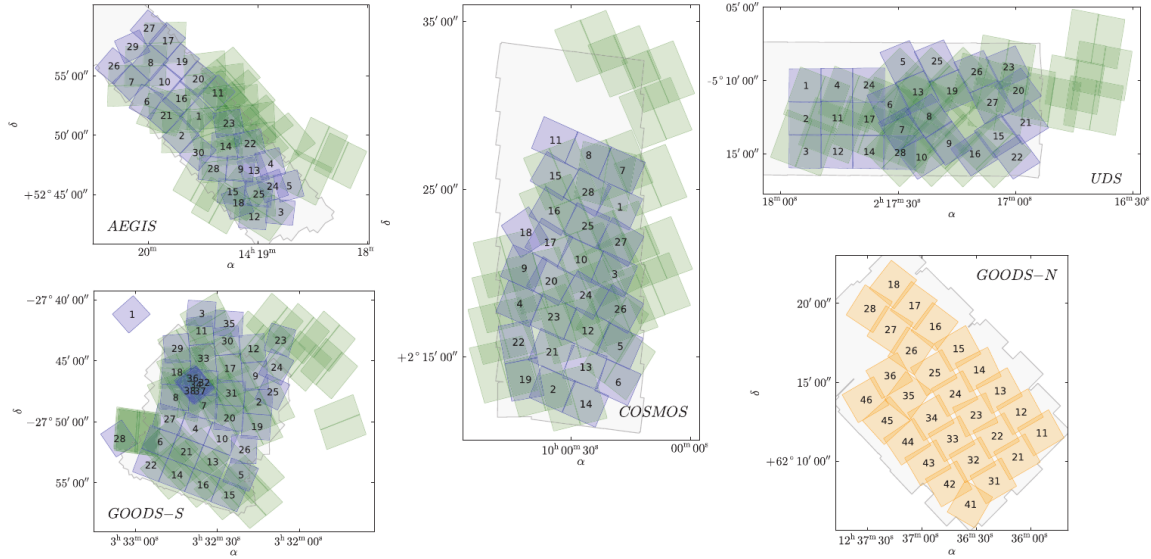


Figure 2.2: Outline of 3D-HST coverage in the five CANDELS fields shown by the blue and green polygons. Supplementing observations from the GO-11600 program covering the GOODS-North field are furthermore outlined as yellow polygons. The footprint of the CANDELS WFC3 observations are displayed as underlying grey polygons. This Figure is taken from Brammer et al. (2012).

out their spatial distribution. However, within the framework of this study, we utilize the integrated grism spectra to determine accurate grism-redshift information.

2.2.2 Sample definition

The main focus of this analysis is on the structural shape of stellar mass distributions in a mass-selected sample of galaxies in the redshift range $0.5 < z < 2.5$. For this purpose, we apply a stellar mass cut $M_* > 10^{10} M_\odot$ to select our galaxies, well above the mass completeness limit of the H_{160} -selected catalogs for all five fields. Our sample consequently spans a wide range of SFRs, from normal SFGs on the main sequence to quiescent galaxies (QGs) below, that already formed the bulk of their stars. For selection, we use the SED modeled galaxy-integrated stellar mass estimates, but note that they match well the masses obtained by summing the resolved stellar mass distributions (see also Wuyts et al. 2012). The redshift of the galaxies are taken from ground-based spectroscopy whenever available, and otherwise from fits to the combination of 3D-HST grism data and broad-band photometry, taken from the catalogs produced by the 3D-HST survey team (see Brammer et al. 2011; Momcheva et al. 2015). We define a galaxy as quiescent if its specific SFR ($sSFR$) satisfied $sSFR < 1/(3 \cdot t_{Hubble})$, where t_{Hubble} is the Hubble time at the redshift of the galaxy, and as star-forming otherwise. We tested that a definition of quiescence based on the location of

a galaxy in the UVJ diagnostic diagram (Wuyts et al. 2007; Williams et al. 2009) yields effectively identical results. The total sample comprises 6764 galaxies, of which 3839 and 2925 lie within the redshift range $0.5 < z < 1.5$ and $1.5 < z < 2.5$, respectively. In the following, these two redshift ranges are referred to as $z \sim 1$ and $z \sim 2$, respectively.

2.3 Methodology

2.3.1 Resolved SED Modeling

A detailed description of the resolved SED modeling can be found in Wuyts et al. (2012). Here, we review only the key steps involved and additional processing steps.

First, all images in the available wavelength bands are brought to the WFC3 H_{160} resolution ($0''.18$) by using the IRAF PSFMATCH algorithm. This step is necessary to ensure that no artificial color gradients are created due to the difference in PSF shapes among the different bands used. Next, the Voronoi-binning scheme from Cappellari et al. (2003) is applied in order to ensure a minimum S/N level of 10 for each bin in the corresponding H -band image. The Voronoi algorithm bins pixels together to create a tessellated image, in which all bins have at least a minimum S/N level. Due to this requirement, the area of the bins increase with galactocentric radius. After the tessellation is defined on the basis of the H -band image, the frame for each wavelength is binned according to this tessellation. Each binned multi-wavelength image is then fit simultaneously with stellar population synthesis models from Bruzual & Charlot (2003), assuming a Chabrier (2003) IMF, a uniform solar metallicity, and a Calzetti et al. (2000) reddening law with visual extinctions in the range $0 < A_v < 4$. The adopted SFHs are exponentially declining, allowing for e-folding timescales down to 300 Myr. This choice is simplistic and may not be representative of the real SFHs (e.g., for SFGs see Maraston et al. 2010). However, we are here interested in the stellar mass, which, among SED-derived properties, is most robust against variations (and uncertainties) in model assumptions (e.g., Papovich et al. 2001; Shapley et al. 2005; Maraston et al. 2010). In order to conduct further structural analysis using the (binned) output of this SED modeling technique, we constructed pixelized (instead of Voronoi binned) images of the stellar mass surface density distribution in the following way. First, we construct a M_*/L map which, within the galaxy's H_{160} segmentation map (i.e. the region in the image covering the extent of the galaxy), has uniform values for pixels belonging to the same Voronoi bins. Pixels outside the segmentation map (i.e., containing sky noise and possibly faint wings of the galaxy extending below the signal-to-noise threshold) are assigned the average M_*/L of the nearest three Voronoi bins. The resulting expanded M_*/L map is then combined with the H_{160} image to construct a final mass map at full H_{160} resolution. This ensures a smooth transition of the galaxy's mass profile from the brighter central parts to the faintest regions.

Figure 2.3 illustrates the rest-frame optical morphologies, M_*/L maps derived from resolved SED-modeling, and the reconstructed pixelized mass maps for 4 example galax-

ies. The i -band images show spatially extended and often clumpy star-formation, whereas the redder H_{160} band image exhibits smoother albeit still somewhat clumpy morphologies. However, the underlying stellar distributions are evidently in all cases smooth, and clumpy features largely disappear due to their lower M_*/L ratios.

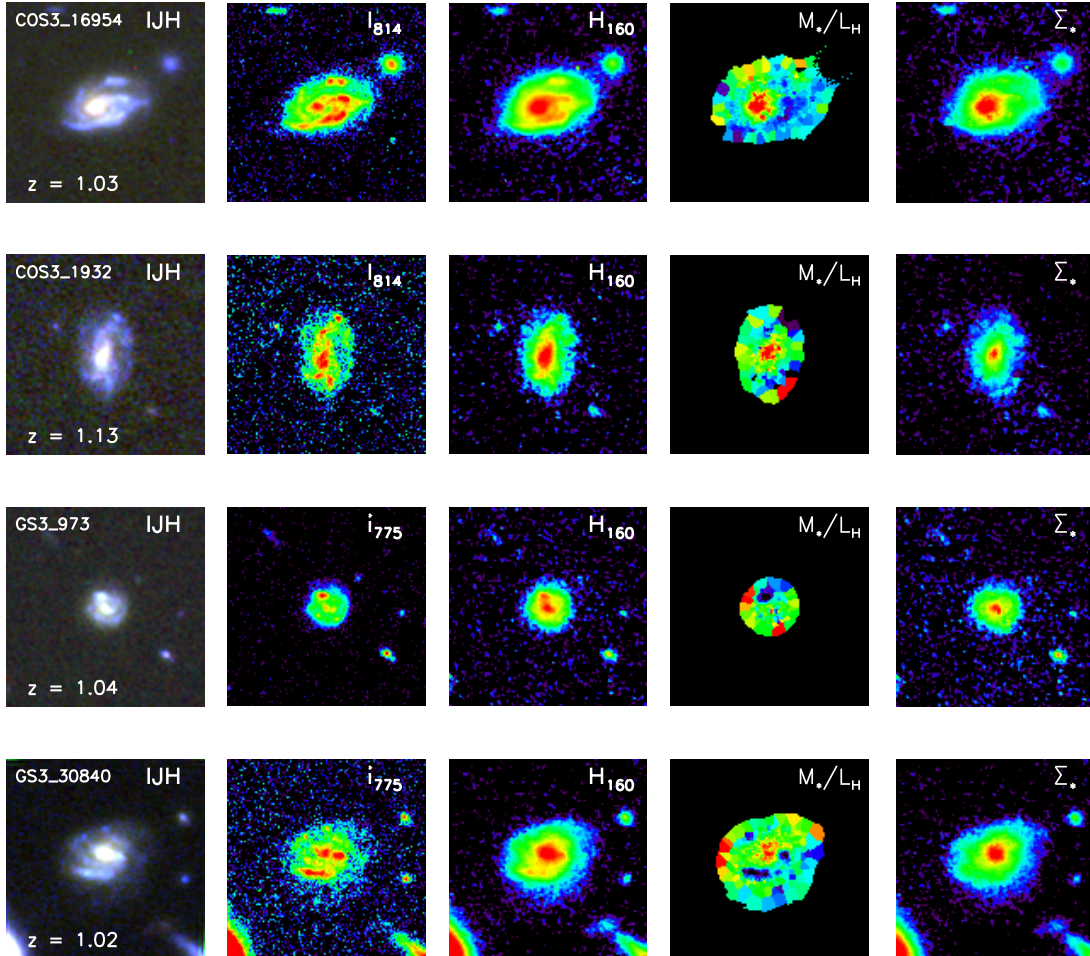


Figure 2.3: Examples for the morphologies at different wavelength bands, and in stellar mass. The different columns show, from left to right: IJH color composite, I -band image, H -band image, stellar M_*/L ratio, and reconstructed stellar mass map.

2.3.2 Structural Parameters

In order to conduct a structural analysis of our galaxy sample, we employed the GALFIT (Peng et al. 2010) morphology fitting code to fit 2-dimensional parametric models to the

stellar mass distribution. For comparison purposes, we modeled the 2D H_{160} surface brightness distributions as well, following identical procedures.

GALFIT is a code to fit 2-dimensional images with galaxy models to extract intrinsic structural parameters of galaxies. The code uses axisymmetric models with a given surface brightness distribution of various input shapes such as a Sérsic profile (Sérsic 1986). The model is fit to the observed image via a least square fitting technique on the basis of the Levenberg - Markwardt algorithm. GALFIT also takes into account the convolution of the model with the point-spread-function (PSF), such that the intrinsic surface brightness distribution can be recovered. Both for fitting light and mass, we used a PSF which is a combination of stacked stars and a Tiny-Tim (Krist et al. 1995) model PSF. For a more detailed description of the PSF used, see van der Wel et al. (2012).

For all our fitting as described below, we used an automated scheme which pre-determines neighboring sources that need to be masked out or fitted simultaneously, and passes initial guesses of fitting parameters to GALFIT. Those include estimates on size, total magnitude and the center. The initial guess on size is based on the distance from the center to the radius at which the curve of growth reaches 50% of the galaxy's total flux. The mass-weighted center of the galaxy derived within its segmentation map is adopted as initial estimate for the center.

We fitted single-component Sérsic models, and in addition two component disk+bulge models. For the single-component models, the R_e , n , the axial ratio b/a , and the total light (or mass) were set as free parameters. We allow n to vary within the range $0.2 < n < 8$. In addition, we also performed one-component pure disk and pure bulge fits by forcing $n = 1$ and $n = 4$, respectively.

While the Sérsic index n is often used as an approximate measure of the contribution of the bulge, it is important to note that n does not translate one to one to the bulge-to-total ratio B/T (see Appendix A of this thesis, also Andredakis et al. 1995; de Jong et al. 2004; Cibinel et al. 2013; Bruce et al. 2012; Bruce et al. 2014). For a given bulge + disk composite profile, the best-fit Sérsic index can be increased both by increasing its B/T , and by leaving B/T constant while growing the extent of the disk relative to that of the bulge (i.e., lowering $R_{e,B}/R_{e,D}$, where $R_{e,B}$ and $R_{e,D}$ is the size of the bulge and the disk, respectively). For the bulge-to-disk decomposition, we adopted a procedure similar to that implemented in Bruce et al. (2012) for the bulge+disk decomposition of H_{160} light profiles, where we fixed the Sérsic indices to $n = 1$ for the disk and to $n = 4$ for the bulge.² The centers are left free, but we restrict the relative distance between the bulge and disk centers to be less than 2 pixels. All other parameters defining the two components (R_e , the axial ratio b/a , and the

²Since the choice of a Sérsic index value for the bulge profile has long been debated in the literature (see Kormendy & Kennicutt 2004 and references therein), we repeated our two-component fits, with the only change fixing $n = 2$ for the bulge component to address the impact on the derived B/T values. We find a median difference of $B_{n=4}/T - B_{n=2}/T = 0.03_{-0.11}^{+0.15}$ for quiescent galaxies and $0.01_{-0.12}^{+0.09}$ for SFGs, with the errors marking the 1σ scatter. Any systematic trends are small, and our results are therefore robust against the precise value of n_{bulge} adopted.

total magnitude/mass of both components) are allowed to vary independently.

Figure 2.4 shows examples for the GALFIT modeling for three different galaxies. For each galaxy, the H_{160} and stellar mass maps are plotted together their best-fit 1-component Sérsic model with residuals, as well as the best-fit bulge+disk 2-component model with residuals.

In 2-component modeling, the higher number of degrees of freedom increases the odds of the fit being trapped in a local χ^2 minimum. In order to mitigate this risk, we ran GALFIT using a grid of initial starting values. Our grid was constructed by using a range of size ratios between bulge and disk ($R_{e,B}/R_{e,D}$) ranging from 0.1 to 1, in steps of 0.1. For each initial guess of $R_{e,B}/R_{e,D}$, the corresponding initial guess on B/T was then set such that the Sérsic index matching this initial configuration matches the one measured in the single-component fit (see Appendix A of this thesis). Likewise, the initial magnitudes and absolute values of the initial size guesses for bulge and disk were set such that the total magnitude and half-light/mass radius of the composite profile matches the respective values determined from Sérsic fitting.

In cases where GALFIT yields solutions with implausibly small bulge sizes (< 0.1 pixel, corresponding to $\lesssim 1/30$ of the resolution, or $\lesssim 50$ pc at $z \sim 2$) and flags the outcome as potentially not converged and unphysical, we excluded the respective run from the grid. Also, solutions yielding a disk smaller in size than the bulge (i.e., $R_{e,B}/R_{e,D} > 1$) were not included.³

After performing the fits for each point of the grid with initial guesses, we assigned a final B/T ratio for each object as the solution of the fit with the lowest χ_{red}^2 . Here, the pure disk and pure bulge fits were also included. Their solutions generally show higher χ_{red}^2 than the 2-component fits, but are occasionally preferred over those in a χ_{red}^2 sense (oftentimes, these are bulgeless systems with $n < 1$). The two-component decompositions are statistically preferred over the single Sérsic models (as based on both their χ_{red}^2 values and the Akaike information criterion, AIC⁴) for $\sim 2/3$ of the total sample. Those systems for which the single Sérsic model yields a lower value of χ_{red}^2 and AIC typically feature shallow profiles with $n < 1$.

We emphasize that throughout this analysis our working definition adopted for bulge and disk components is based on the above bulge+disk modeling of stellar mass or light maps, as empirical constraints on whether or not stars assigned to a bulge/disk component are dynamically hot/cold are currently lacking. As the SINS survey of $z \sim 2$ galaxy kinematics demonstrated that high-redshift SFGs are dynamically (Förster Schreiber et al. 2009) and morphologically (Förster Schreiber et al. 2011; Tacchella et al. 2015) distinct from local spiral galaxies, we caution that bulge fractions as derived by our decompositions may have a somewhat different meaning than they would have in the local universe.

³We note that nuclear stellar disks in early-type galaxies do exist (e.g., Jaffe et al. 1994; van den Bosch et al. 1994; Ferrarese et al. 1994), but they are impossible to resolve at the HST resolution for $z \sim 2$ galaxies.

⁴In evaluating models with the AIC, the preferred model is the one that minimizes $\chi^2 + 2p + \frac{2p(p+1)}{N-p-1}$, where p is the number of free parameters in the fit and N is the number of data points used in the fit.

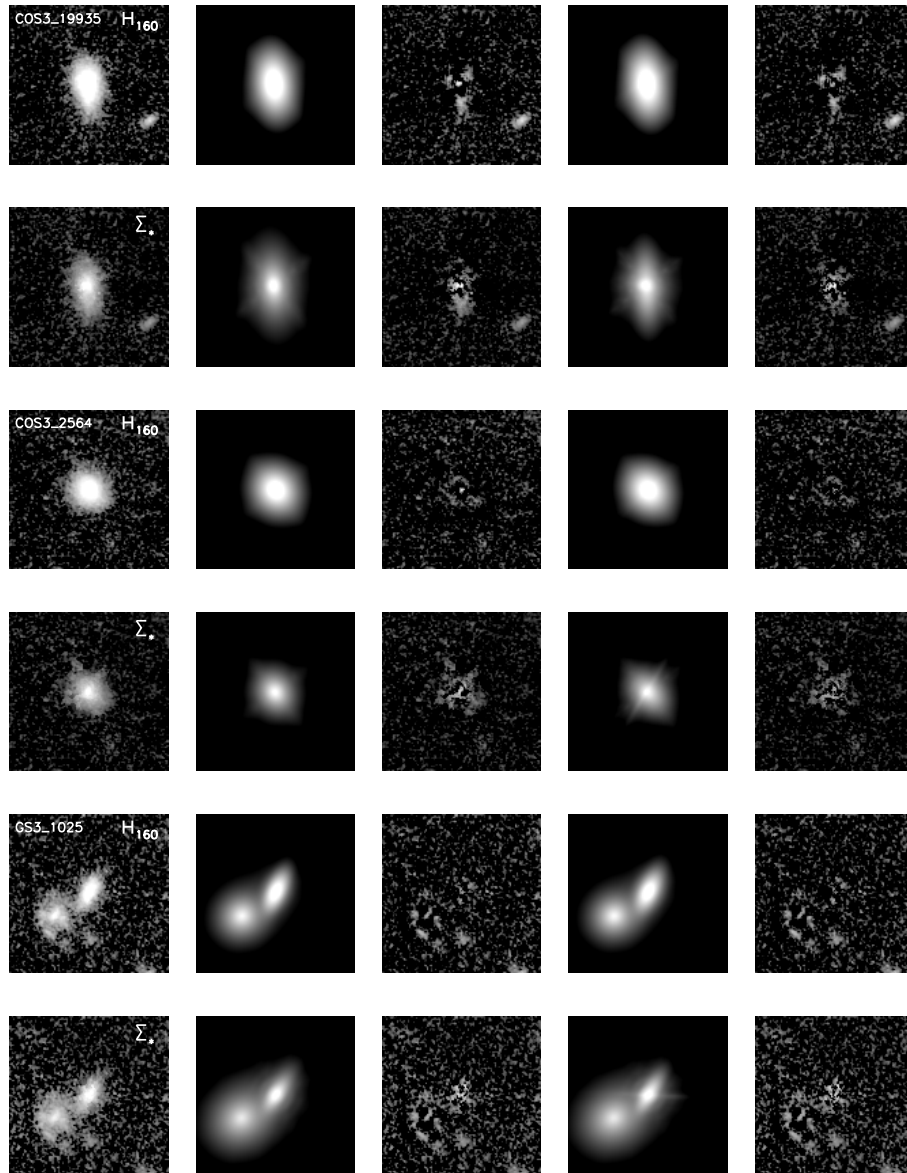


Figure 2.4: Examples for the 2D morphological fitting employed with GALFIT. There are fits for three example targets shown, each containing two rows that represent the fits to the H -band images and reconstructed mass maps. The columns show, from left to right: H -band image / stellar mass map, best-fit Sérsic model and corresponding residuals, best-fit bulge+disk model and corresponding residuals.

In addition, we estimated a typical measurement uncertainty on B/T by setting up an array of model galaxies with a range of mass, size, B/T ratio, and $R_{e,B}/R_{e,D}$, which is similar to our data. The grid of model galaxies consisted of 5, 3, 11, and 10 grid points in mass, R_e , B/T and $R_{e,B}/R_{e,D}$ respectively. These were then inserted in multiple empty sky regions of the CANDELS UDS field to mimic the typical background noise⁵. We next ran GALFIT on all 8250 mock galaxies using our 2-component fitting scheme. The measurement error on B/T of each galaxy in our sample given its mass, radius, and profile shape is then finally assigned as the scatter among the recovered B/T ratios of the corresponding model galaxy.

Typical measurement errors in B/T for star-forming and quiescent galaxies are on average ~ 0.05 and ~ 0.06 at $z \sim 1$ and ~ 0.1 and ~ 0.13 at $z \sim 2$, respectively. The distribution of errors peaks below the median ($\lesssim 0.05$), and shows a tail towards higher B/T errors. Two alternative methods to estimate the uncertainty in B/T , namely the formal random uncertainty reported by GALFIT and re-fitting the observed galaxies after applying additional background and Poisson noise, generally lead to lower estimated uncertainties (by a factor of ~ 2 in the case of GALFIT). In the remainder of this chapter, we therefore adopt the most conservative error estimates inferred from our analysis of the inserted mock galaxies.

2.4 Results on Galaxy Structure

2.4.1 The Evolving Mass Budget of Disks and Bulges

Exploiting the bulge-disk decompositions of the stellar mass maps derived for our sample of massive galaxies, we first evaluate the average mass budget of disks and bulges. Let us consider picking a random star out of our sample of massive galaxies above $10^{10} M_\odot$. At $1.5 < z < 2.5$, the probability that this star belongs to a bulge component is 46%. Increasing the mass limit to $\log(M_*) = 10.5$ or 11 yields a higher probability for the star to be associated to the bulge, of 49% and 54%, respectively. Perhaps somewhat surprisingly, the fraction of stars residing in a bulge component rises only slightly to $0.5 < z < 1.5$, to 47%, 50%, and 56% for galaxies more massive than $\log(M_*) = 10, 10.5$, and 11 respectively.

The formal uncertainties to the above stated probabilities including sample variance and typical measurement errors on B/T are limited to a few percent. The total error budget is likely dominated by systematics, for example related to the assumptions made in stellar population modeling (see Section 2.3.2). We note, however, that only M_*/L uncertainties with a differential impact on bulges and disks will affect the above numbers. Even if the

⁵UDS is part of CANDELS-Wide, which was exposed for two HST orbits divided over F125W and F160W. Part of our data set comes from the CANDELS-Deep regions (the central halves of the GOODS fields), which received 4 orbits per pointing in F125W and F160W each. The inferred uncertainties from our analysis of mock galaxies can therefore be considered as conservative estimates.

M_*/L ratio of bulges were systematically under- or overestimated by 0.2 (0.3) dex with respect to those of disks, the change in the above numbers would be limited to $\sim 7(10)\%$.

As bulges, unlike stellar disks, can be considered sinks in the continuous assembly of a galaxy's stellar component, the rising mass density of stars in bulges (by a factor of ~ 1.8 from the higher to the lower redshift bin) therefore seems to be compensated largely by the continuing assembly of new disks. Splitting our sample in finer redshift bins, we do find the fraction of stellar mass in bulges to increase more significantly, by a factor ~ 1.5 over the entire 6 Gyr timespan sampled by our study.

Overall, the bulge mass fractions are higher than what would be inferred from fits to the H -band surface brightness profiles, as the median mass-to-light ratio of disk components is 0.2 dex lower than that of bulge components. The above numbers address the evolving mass budget of disks and bulges for a mass-limited sample including both star-forming and quiescent galaxies. In the remainder of this chapter, we will break down our sample by star formation activity.

2.4.2 Profile shape

In recent years, several HST-based studies have investigated the structural differences between star-forming and quiescent galaxies at high redshift. In common to all of these analyses, star-forming systems are found to have significantly larger rest-optical sizes than their quiescent counterparts at the same mass and redshift (e.g., Toft et al. 2009; van der Wel et al. 2014a). In addition, their surface brightness profile shapes tend to be shallow ($n \sim 1$), while quiescent galaxies feature cuspiest light profiles (e.g., Wuyts et al. 2011b, Bell et al. 2012; Cheung et al. 2012; although see also Bruce et al. 2012 for decomposed light profiles at high stellar masses and redshifts).

At the same time, the same multi-wavelength high-resolution lookback surveys have also established that substantial mass-to-light ratio variations in the rest-optical can occur, not only between but also within galaxies (see, e.g., Wuyts et al. 2012; Guo et al. 2012; Boada et al. 2015). Typically, as new stars tend to form from gas settled in a disk configuration, such M_*/L ratio variations are anticipated to give rise to a composite light profile in which the disk component has a relatively larger weight (per unit mass) than the bulge. It is therefore important to address to which degree the above structural distinction between the two classes of galaxies is intrinsic to their distribution of stellar mass, or, conversely, can be attributed to stellar population and dust extinction effects. The answer to this question is of immediate relevance to our understanding of quenching, as in principle the latter scenario could imply that compact quiescent systems can evolve from the star-forming main sequence by simple fading, without invoking an associated morphological transition. Kriek et al. (2009) investigate this scenario for a spectroscopically confirmed sample of massive $z \sim 2$ galaxies, finding that 3 out of 6 massive star-forming systems have dense cores, and thus may passively evolve into compact galaxies due to fading of the outer star-forming regions. Szomoru et al. (2010), on the other hand, exploit the exquisite depth of the Hub-

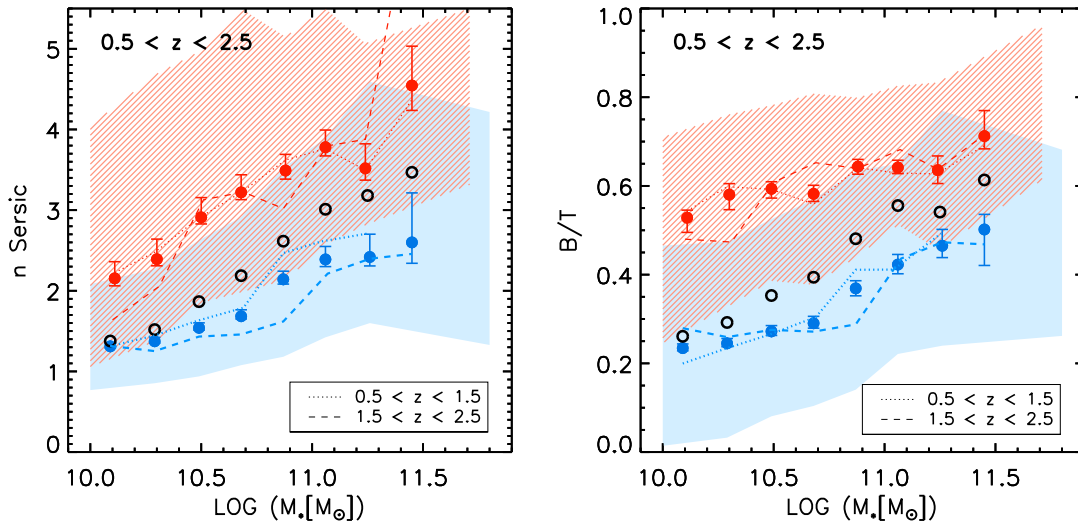


Figure 2.5: Sérsic index and B/T ratio as a function of total stellar mass of our galaxy sample spanning the redshift range $0.5 < z < 2.5$. The whole sample (black non-filled symbols) is divided in star-forming (blue symbols) and quiescent galaxies (red symbols). The respective shaded areas mark the 50th percentile scatter of the distributions within one bin, while the error bars indicate the uncertainty on the median value. Results for the lower and upper halves of the redshift interval are marked with dotted and dashed lines, respectively. The bins contain (from left to right) 1439, 1091, 886, 693, 484, 259, 114, 35 star-forming systems and 227, 267, 298, 369, 280, 214, 83, 25 quiescent systems within the whole redshift range. SFGs show a clear trend of increasing Sérsic index and B/T with increasing stellar mass, reaching $B/T \sim 0.4 - 0.5$ above $10^{11} M_{\odot}$, reflecting the build-up of central mass concentrations in main-sequence SFG up to $z \sim 2.5$.

ble Ultra Deep Field to probe the surface brightness profile of a massive compact quiescent galaxy at $z = 1.91$, ruling out the existence of a faint extended envelope or disk around the observed galaxy. Another argument against fading comes from Cheung et al. (2012), who derived the stellar masses of bulges for both star-forming and quiescent galaxies at $0.5 \leq z < 0.8$. They found that bulges of SFGs are half as massive as those of similar-mass quiescent galaxies, implying they cannot simply fade onto the red sequence without structural evolution.

Using the stellar mass maps reconstructed for our mass-selected sample of 6764 galaxies at $0.5 < z < 2.5$ with $\log(M_*) > 10$, we are now able to draw statistically significant conclusions on the structural distinction between high- z galaxies prior to and after quenching. In Figure 2.5, we compare the shape of the stellar mass distributions (i.e., corrected for spatial M_*/L variations) of star-forming and quiescent galaxies, and study their dependence on the total galaxy stellar mass. We consider profile parameters based on single-component

(i.e., Sérsic) fits as well as two-component (bulge + disk) decompositions, and show the results for two separate redshift intervals: $0.5 < z < 1.5$ and $1.5 < z < 2.5$.

Figure 2.5 immediately highlights that the distinct structural appearance of star-forming and quiescent galaxies is intrinsic to its internal distribution of stellar mass, and not just driven by stellar population or obscuration effects. In fact, a comparison to the equivalent plots based on H -band surface brightness profiles rather than mass maps (see Section 2.6) indicates that stellar population effects (when measuring at rest-optical wavelengths) only induce a modest, albeit non-negligible shift. At all masses, quiescent galaxies feature cuspier stellar mass distributions (i.e., higher n) than star-forming systems. Their typical best-fit Sérsic index is furthermore an increasing function of galaxy mass. Interestingly, also among SFGs the profile shape is not independent of stellar mass. An increase in n is apparent above $10^{11} M_{\odot}$, both at $z \sim 1$ and at $z \sim 2$. A similar trend of increasing cuspieness at the tip of the MS was noted by Wuyts et al. (2011b, Figure 1, see also Nelson et al. 2015).

Next, it is worthwhile reflecting on what it is that we measure when fitting Sérsic profiles. Appendix A illustrates that, when considering galaxies as superpositions of bulge and disk components, a given best-fit Sérsic index does not necessarily correspond one-to-one to a unique B/T value, even though it is often interpreted as such. Given a bulge+disk system with associated best-fit n , one can increase its n either by boosting B/T , or, alternatively, by growing the extent of the disk with respect to that of the bulge without any change to B/T .

Turning to the right-hand panel of Figure 2.5, we now explore the B/T ratio as a function of galaxy mass, for SFGs and quiescent galaxies separately. Again, we find a clear anti-correlation between star formation activity and bulge prominence. Focussing on the star-forming population, the median B/T is limited to below 30% for intermediate mass SFGs ($10 < \log(M_*) < 11$), while typical bulge mass fractions rise to 40-50% above $10^{11} M_{\odot}$. We note that there is a significant scatter in the distribution of individual B/T values around the median for both quiescent and star-forming galaxies. We investigated the variation in median trends when varying the binning intervals, finding negligible changes at lower masses, while the median B/T of the most massive ($\log(M_*) \sim 11.3$) SFG bin changes by ± 0.1 , depending on the applied binning intervals⁶.

We note that measurements on the H -band yield bulge mass fractions among SFGs that are lower by on average $\sim 30\%$, as can be understood from a disk component composed of a younger, lower M_*/L stellar population than the bulge.

From the two-component fits, we infer a typical $R_{e,B}/R_{e,D}$ size ratio of ~ 0.2 , albeit with significant scatter (see Figure A.1). The median size ratio shows little dependence on star formation activity or mass, over the range probed by our sample. Given the enhanced B/T values in quiescent galaxies, and the fact that bulges have smaller half-mass radii than disks, one may wonder if the difference in total size between SFGs and quiescent galaxies can be accounted for completely by a redistribution of stellar material from the

⁶The binning scheme applied in Figure 2.5 is such that the most massive bin still contains more than 10 galaxies, allowing a robust estimation of the median.

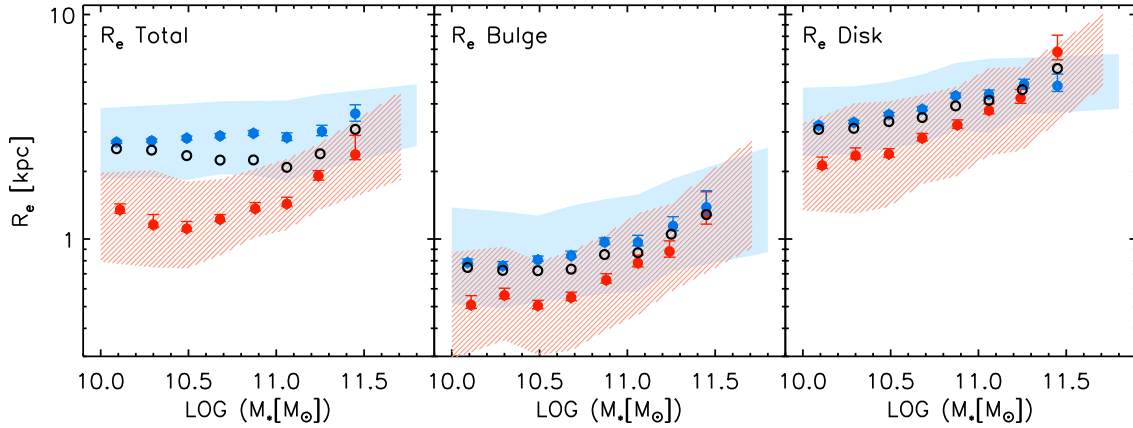


Figure 2.6: Effective total size, bulge size and disk size as a function of total stellar mass in the redshift range $0.5 < z < 2.5$. The total sizes are derived from single Sérsic fits, bulge and disk sizes are inferred from the bulge-disk decompositions. The whole sample (black symbols) is divided into star-forming (blue symbols) and quiescent galaxies (red symbols). The respective shade areas mark the 50th percentile scatter of the distributions, while the error bars indicate the uncertainty on the median value. There is a clear difference in total size between SFGs and QGs over the whole mass range. Also the bulge and disk components individually appear to be smaller for the star-forming population up to masses of $\log(M_*) \sim 11.3$.

disk to the bulge, without changing the extent of each of the components individually. Our analysis confirms that the change in B/T of SFGs prior or during quenching is to a large extent responsible for the size difference between the quiescent and star-forming population. However, some fraction of the shrinking size is still attributed to the individual components being smaller. In Figure 2.6, we show the total sizes as well as the sizes of the individual components for star-forming and quiescent galaxies, as measured on the mass maps. While the total sizes of SFGs and QGs are noticeably different (by a factor ~ 3 at $\log(M_*) \sim 10.5$), the difference in size of bulge and disk components between SFGs and QGs respectively is smaller, typically by a factor ~ 1.5 .

2.4.3 Fraction of Quenched galaxies

With the morphological parameters of the mass maps for our entire galaxy sample in hand, we now proceed to relate those with galaxy-integrated star formation properties.

The three panels of Figure 2.7 show, from left to right, the fraction f_{quench} of quenched galaxies as a function of total stellar mass, bulge mass, and disk mass, respectively. Here, we again define galaxies as quenched/quiescent when $sSFR < 1/(3 \cdot t_{Hubble})$, and as star-forming otherwise.

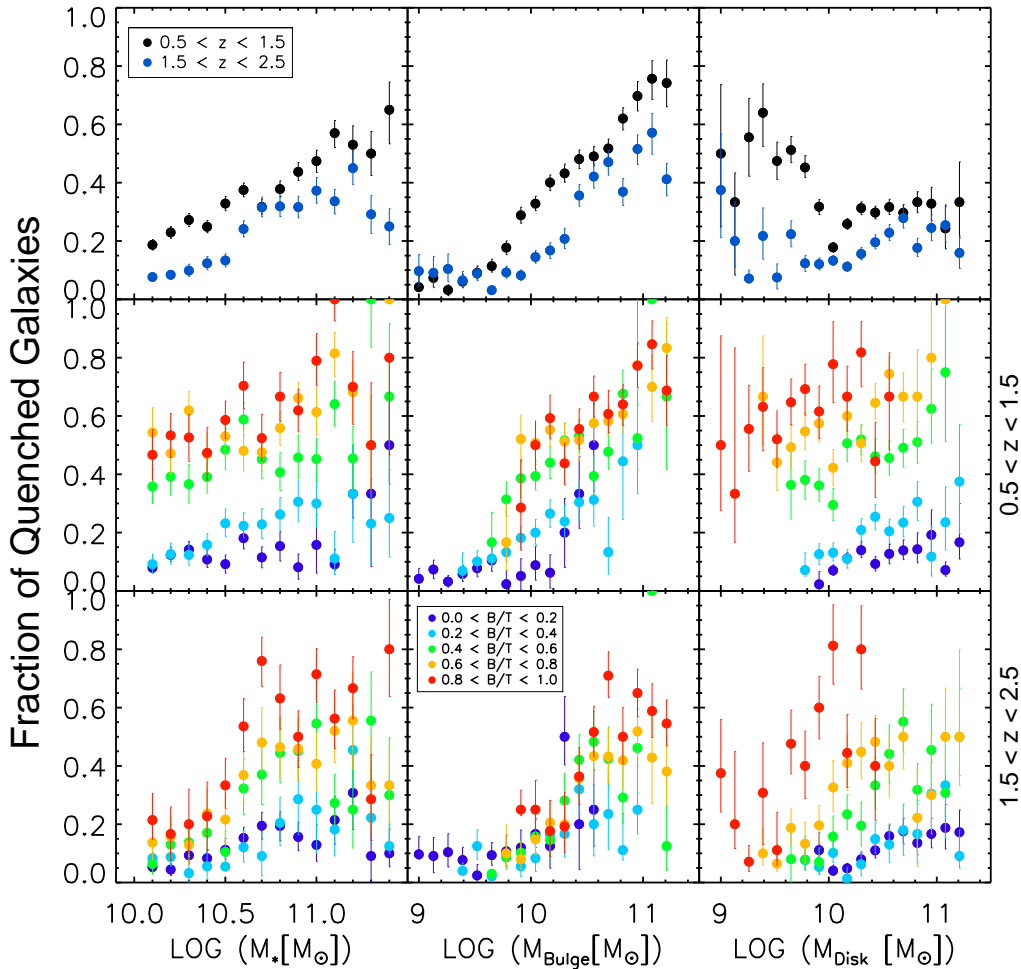


Figure 2.7: Fraction of massive galaxies ($M_* > 10^{10} M_\odot$) that are quiescent (f_{quench}) as a function of total stellar mass (left columns), bulge mass (middle columns) and disk mass (right columns) for $z \sim 1$ and $z \sim 2$. Galaxies with $sSFR < 1/(3 \cdot t_{Hubble})$ are assigned as quiescent, the others as star-forming. In the middle and bottom rows, we split the galaxy sample in bins of B/T for the two redshift bins. Uncertainties are derived from bootstrapping, and include sample variance as well as measurement uncertainties. A positive trend of f_{quench} is seen with total stellar mass, with this trend becoming stronger when correlating f_{quench} with the bulge mass, whereas f_{quench} shows no positive correlation with the mass of the disk component. At a given galaxy mass, f_{quench} is increasing significantly with increasing B/T ratio. The scatter in f_{quench} among the different B/T bins is largely reduced when correlating against the bulge mass, implying that the mass within a bulge of a galaxy is correlating best with quiescence. This trend is qualitatively similar for both redshift ranges, with overall quenched fractions being lower at $z \sim 2$ than at $z \sim 1$.

The uncertainties in f_{quench} are derived via a bootstrapping method and represent the 68% confidence levels. They include both sample variance and the typical measurement errors on B/T , which are derived as described in Section 2.3.2. For the bootstrapping, we computed f_{quench} for 1000 samples, which are randomly drawn from the original sample, with replacement. For each bootstrap iteration, we displace the B/T values for each galaxy by the typical measurement error in B/T , given the galaxy’s magnitude, size and measured profile shape.

The top left panel of Figure 2.7 illustrates that the fraction of quenched galaxies increases with increasing mass, from ~ 0.1 at around $10^{10} M_{\odot}$ to ~ 0.5 at $2 \cdot 10^{11} M_{\odot}$. A second conclusion is that the fraction of quenched galaxies is overall higher for the lower redshift bin, by a factor of ~ 2 on average. Both of these results are well established in the literature. The rising mass function of quiescent galaxies over cosmic time has most recently been quantified on a firm statistical footing by Muzzin et al. (2013) and Ilbert et al. (2013), both of which exploit the wide-area UltraVISTA survey. What CANDELS lacks in number statistics compared to UltraVISTA, it adds in depth and high resolution. Exploiting these key strengths, we now turn to the dependence of the quenched fraction on galaxy sub-components: the mass of their bulge (middle panel) and disk (right-hand panel). Clearly, the dependence of f_{quench} on the bulge mass is much stronger than on the disk mass, which does not show any significant correlation with f_{quench} above $\log(M_{Disk}) \sim 9.5$. Towards lower disk masses, f_{quench} increases rapidly, but we point out that this trend is entirely driven by the (total) stellar mass limit of our sample ($\log(M_*) > 10$, i.e., the galaxies occupying the lowest M_{Disk} bins are necessarily heavily bulge-dominated systems, that tend to form relatively few stars). If lower mass galaxies were to be included, less massive, disk-dominated SFGs would likely outnumber these massive spheroids with small residual disks in the low M_{Disk} bins, producing a flat relation of f_{quench} with M_{Disk} over the full range probed. Above respective masses of $10^{10} M_{\odot}$, f_{quench} increases more rapidly with bulge mass than with total stellar mass in both redshift ranges (~ 0.35 per dex of M_{Bulge} compared to ~ 0.3 per dex M_* , or ~ 0.1 per dex of M_{Disk}).

With the bulge-to-disk decompositions in hand, we next split the galaxy sample in bins of B/T , and explore second parameter dependencies. Considering first the dependence of f_{quench} on the total stellar mass, it is apparent that, at a given total mass, f_{quench} is increasing significantly with increasing B/T ratio. The middle panels of Figure 2.7 illustrate that, when considering the dependence of f_{quench} on bulge mass, the different B/T bins align along a much tighter locus. In contrast, a large spread is seen as a function of disk mass (right-hand panels of Figure 2.7). In order to quantify these trends, we compute the Spearman’s rank correlation coefficient (r_s) for the relations of f_{quench} with $\log(M_*)$, $\log(M_{Disk})$, and $\log(M_{Bulge})$ for respective masses $\log(M_*) > 10$. We find that r_s is indeed significantly higher for the relation f_{quench} vs. $\log(M_{Bulge})$ ($r_s \sim 0.68$) than for both f_{quench} vs. $\log(M_*)$ ($r_s \sim 0.32$) and f_{quench} vs. $\log(M_{Disk})$ ($r_s \sim -0.05$), as measured for $z \sim 1$. Consistent results are found for $z \sim 2$.

We investigated the impact of defining quiescence based on a UVJ color-color criterion

instead of a sSFR cut. When applying a UVJ - based selection of quiescent galaxies, we find an overall good agreement with the trends presented in Figure 2.7. Quantitatively, small changes occur, with f_{quench} increasing by $\sim 7\%$ for the entire $0.5 < z < 2.5$ sample integrated over all masses. The good agreement is not surprising, since the precise threshold in sSFR used to select quiescent galaxies ($sSFR < 1/(3 \cdot t_{Hubble})$) was chosen to yield maximum overlap with the UVJ selection criterion.

Taken together, this demonstrates that the build-up of a bulge seems to play a critical role in the quenching process of galaxies, whereas the disk does not. The amount of stars in the disk component of a galaxy has little to no predictive power regarding its star-forming or quenched state, unless also B/T (and hence the bulge mass) is known. We find a qualitatively similar behavior at $z \sim 2$ as at $z \sim 1$, but note that the cosmic evolution in the quiescent fraction cannot solely be attributed to continuing bulge growth over time, as galaxies in the same M_* and B/T bin at $z \sim 1$ are more likely to be quenched than those at $z \sim 2$. Section 2.6 illustrates how the equivalent diagrams composed from fits to the H -band surface brightness rather than the stellar mass distribution exhibit a larger spread from low to high B/T bins. This generic behavior can be understood from a physical picture where the disk component has a relatively larger weight in light than in mass.

Our work is in agreement with, and takes the next step beyond previous reports that the inner stellar mass density is better related to the star formation history than the total stellar mass (Franx et al. 2008; Bell et al. 2012), as inferred from rest-optical imaging of smaller samples of high-redshift galaxies (see Kauffmann et al. 2003 and Fang et al. 2013 for a local universe reference, and Cheung et al. 2012 for intermediate redshifts $z < 0.8$)

Importantly, the same behavior explored here over the redshift range $0.5 < z < 2.5$ extends in a strikingly similar fashion all the way to the present day, as demonstrated by Bluck et al. (2014) who exploit the large number statistics of SDSS.

2.5 Comparison with SAMs

2.5.1 The Somerville model

Semi-analytic models (SAMs) have a rich history of trying to reproduce galaxy scaling relations and abundances, with the goal of guiding our interpretation of the observational results. Here, we focus specifically on the SAM developed by Somerville et al. (2008) and further updated by Somerville et al. (2012) and Porter et al. (2014), which is rooted in the Bolshoi cosmological dark matter simulation (Klypin et al. 2011).⁷ As is generic to all SAMs, the model relies on simplified analytic prescriptions for the dynamical and astrophysical processes down from entire galaxy scales, rather than on kiloparsec to parsec scales (the resolution below which state-of-the-art cosmological and zoom-in hydro-simulations resort to subgrid physics, respectively). This limitation, however, yields the enhanced flexibility

⁷Hereafter, we refer to this model as the Somerville et al. SAM.

of a relatively inexpensive runtime, allowing the straightforward generation of statistically significant model galaxy populations, and the tuning of parameters to observational constraints such as mass functions and scaling relations (only empirical constraints from the nearby universe were used in tuning the parameters of the model considered here). The fact that SAMs conceptually are formulated in units of bulge and disk components furthermore makes them suitable for a direct and meaningful comparison to the diagnostics explored in this chapter.

A detailed description of the prescriptions for cooling, star formation, feedback, and structural growth is provided by Somerville et al. (2008, 2012), with extensions and applications to the CANDELS data set presented by Porter et al. (2014). The input to and output from the model is further contrasted to that of other SAMs by Lu et al. (2014).

For a detailed discussion of the physical recipes of this SAM and the resulting output in the context of a larger set of SAMs, we refer the reader to Lu et al. (2014). For the sake of the comparison presented here, we emphasize that none of the relations investigated in this analysis formed part of the set of observational constraints to which the model parameters were tuned. The model parameters of the SAM were tuned to (approximately) match observed properties of local galaxies. Those include the global stellar mass function, the stellar mass function of early- and late-type galaxies, the gas fraction as a function of stellar mass for disks, and the mass-metallicity relation for stars.

Also of particular relevance is the fact that, in the model, stars form either in the disk following a Kennicutt-Schmidt law (Kennicutt 1998), where the disk scalelength is set by a similar methodology as Mo, Mao & White (1998), or, in the event of a merger, during a starburst. Bulge formation as well as feeding of the central supermassive black hole can happen through two channels: mergers or disk instabilities (see Porter et al. 2014). The starburst, black hole accretion and morphological transformation induced by mergers depends on the mass ratio and gas fraction, as calibrated using a large suite of binary merger simulations (Somerville et al. 2008; Hopkins et al. 2009; Somerville et al. 2012). Star formation is moderated through heating of gas by supernovae as well as through AGN feedback. In addition to the quasar mode, during which AGN can drive powerful outflows, black holes also grow more gradually over longer timespans through the so-called radio mode (i.e., suppression of cooling via radio jets). No explicit connection between the bulge mass and quenching (as may for example be expected from the Toomre Q stability criterion in a gravitational quenching scenario, see Section 2.7.2) was built into the model.

2.5.2 Fraction of Quenched Galaxies in the SAM

In Figure 2.8, we show the model equivalent of Figure 2.7, describing how the fraction of galaxies that are quenched depends on the total stellar mass, the mass of stars in the bulge, and the mass of stars in the disk component respectively. As for the observations, we define the threshold for a galaxy to be quenched with a ruler moving with redshift: $sSFR < 1/(3 \cdot t_{Hubble})$. This definition, rather than an application of the *UVJ* diagnostic,

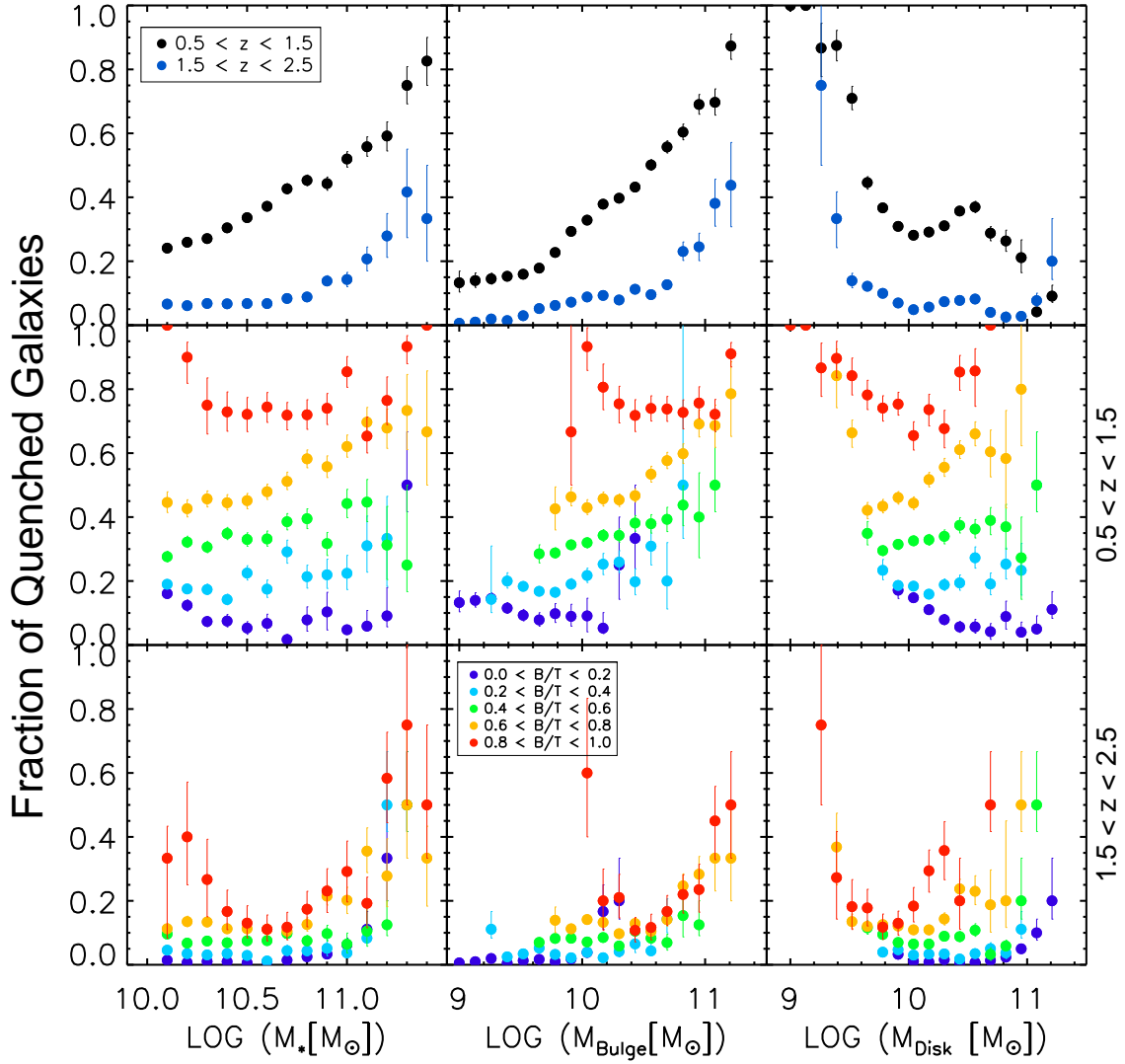


Figure 2.8: Same as Figure 2.7 using galaxies from the Somerville et al. SAM. Galaxies with $sSFR > 1/(3 \cdot t_{Hubble})$ are assigned as star-forming, the others as quiescent. Uncertainties are derived via bootstrapping to reflect the sample variance.

remains closer to the direct output of the SAM, avoiding a translation to mock spectral energy distributions, which would introduce additional assumptions and uncertainties⁸.

At first glance, the SAM features several of the characteristic trends noted earlier for the CANDELS galaxies: f_{quench} rises towards later cosmic times, increases with the total stellar mass, more steeply so with bulge mass, and shows no appreciable correlation with disk mass above $\log(M_{Disk}) = 9.5$. In the interval $9 \lesssim \log(M_{Disk}) \lesssim 9.5$, a sharp drop with increasing M_{Disk} is noted, as also seen in the observations. Given the $M_* > 10^{10} M_\odot$ threshold of our sample selection, the latter objects are necessarily heavily bulge-dominated. Without imposing such a mass limit, less massive, disk-dominated SFGs would outnumber massive early-type galaxies with small residual disks in the lower M_{Disk} bins. Despite the qualitative success, quantitative differences in the quenched fractions of model galaxies with respect to those observed are clearly present. The discrepancy is most severe at $z \sim 2$, where modeled f_{quench} values are, on average over the whole displayed mass range, of order a factor $\sim 2 - 3$ short of observed, hinting at an underestimated quenching rate and/or inefficiency to prevent quiescent systems from rejuvenating⁹.

When splitting the SAM galaxies at each M_* , M_{Bulge} , and M_{Disk} in bins of B/T (middle and bottom panels of Figure 2.8), we reproduce a similar behavior as found for the real universe in Section 2.4.3. Namely, the total stellar mass acts as a poorer predictor of the quenched state of a galaxy. This situation can be remedied if in addition to M_* also B/T (and hence M_{Bulge}) is known. Quantitatively, the correlation between f_{quench} and M_{Bulge} is measured to be the strongest ($r_s \sim 0.46$), whereas M_* and M_{Disk} only show weak correlation with f_{quench} ($r_s \sim 0.21$ and $r_s \sim -0.1$, respectively). The quoted values of r_s are measured for respective masses of $\log(M_*) > 10$ and at $z \sim 1$. The values for r_s at $z \sim 2$ are similar, with the correlation between f_{quench} and $\log(M_*)$ as well as between f_{quench} and $\log(M_{Disk})$ being somewhat stronger. At $0.5 < z < 1.5$, less than 20% of all massive galaxies with $B/T < 0.2$ are classified as quiescent. Conversely, the majority of galaxies in the upper B/T bin (with $B/T > 0.8$) have low sSFR. These inferences are in common between the SAM and the observations. Also in agreement, is the fact that M_{Bulge} serves as a better predictor of f_{quench} than the total stellar mass, with different B/T bins being more (albeit not perfectly) aligned along a single locus in the f_{quench} versus M_{Bulge} diagram.

At $1.5 < z < 2.5$, the model predictions are skewed towards too low f_{quench} values, as noted earlier. However, in relative terms the same generic behavior as a function of bulge prominence is notable.

We note that most of the trends in Figure 2.8 are driven by physical prescriptions in the SAM affecting central galaxies rather than satellites, as centrals account for 80% (90%) of

⁸It should be noted that equivalent assumptions and uncertainties associated with the conversion from light to physical properties enters upon SED modeling of the observed galaxies. The choice of how far to take the models to the observations or visa versa therefore remains somewhat arbitrary.

⁹See also Ciambur et al. 2013 for a discussion on the quenched fraction in the Garching semi-analytic models.

the model galaxy population above $\log(M_*) = 10$ (11). Those massive galaxies classified as satellites are further subjected to additional environmental quenching processes, resulting in a higher $f_{quench}(M_*, M_{Bulge})$ for this particular subpopulation.

2.5.3 The agent of quenching

Given the qualitative agreement between model and observations, we can now pose the question how, in the context of the Somerville SAM, the relation between structure and stellar populations could be interpreted. To this end, we consider the dependence of f_{quench} on two physical properties of galaxies in the SAM that are not observationally accessible for our CANDELS sample: the halo mass M_{Halo} and the mass of the central supermassive black hole M_{BH} . The top panels of Figure 2.9 illustrate that the probability of a galaxy being quenched increases towards high M_{Halo} and high M_{BH} . In detail, however, the dependencies on the two look different. The increase in f_{quench} with M_{Halo} is gradual over nearly two orders of magnitude. In contrast, a much sharper upturn of f_{quench} emerges above $\log(M_{BH}) = 7.5$. This behavior is especially notable at $z \sim 1$, but a rise above the same threshold is present in the $z \sim 2$ population as well. Breaking the model galaxy population down by its structural properties, we find a wide spread in f_{quench} for different B/T at a given M_{Halo} . Naively, a different, less scattered behavior would be expected if halo mass quenching were the sole and dominant mechanism (Birnboim et al. 2007; Dekel & Birnboim 2008; Dekel et al. 2009). As a function of M_{BH} , on the other hand, a similar upturn in f_{quench} is present for all B/T bins equally above $\log(M_{BH}) = 7.5$.

The increased scatter in the relation between f_{quench} and M_{Bulge} compared to the tight correlation of f_{quench} and M_{BH} can be explained by the SAM's $M_{BH} - M_{Bulge}$ relation. For a given B/T bin, the scatter in the $M_{BH} - M_{Bulge}$ relation is significant compared to the dynamic range in the bulge masses plotted. At a given bulge mass, the scatter stems in part from an anti-correlation between the black hole mass and the level of star formation activity (sSFR).

Our analysis illustrates that in the Somerville model, which includes feedback from both supernovae and AGN, the central supermassive black hole acts as the primary agent of quenching in massive galaxies, and its accumulated mass (i.e., the integral over past accretion activity) is tightly related to the probability of finding a galaxy in a quenched state. Since the physical processes giving rise to bulge and black hole growth are the same in the SAM (mergers and disk instabilities), the stronger relation of f_{quench} with M_{Bulge} than with M_* , present in both observations and model predictions, is not surprising.

We stress that in the Somerville model, no direct causal link between the presence of a bulge and quenching is implemented. The bulge is simply the accessible observable that correlates most tightly with the actual agent of quenching in this particular model: the supermassive black hole. Observationally, there is increasing evidence for AGN-driven outflows of massive $z \sim 1 - 3$ galaxies (e.g. Nesvadba et al. 2011; Cano-Díaz et al. 2012; Harrison et al. 2012; Förster Schreiber et al. 2014; Genzel et al 2014b). Given the shortcomings of

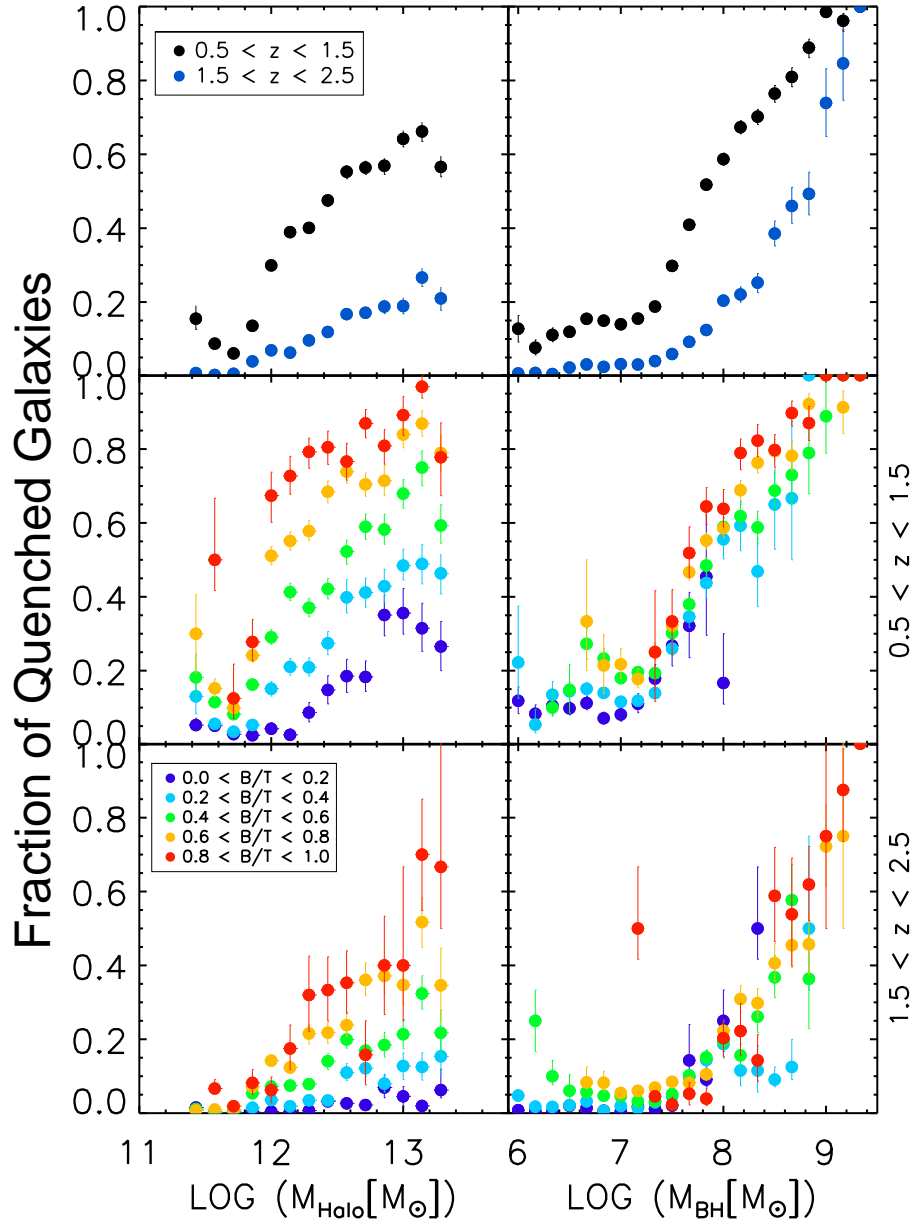


Figure 2.9: f_{quench} as a function of halo and black hole mass using galaxies from the Somerville et al. SAM. In the middle and bottom rows, the galaxy sample has been split in bins of B/T . Galaxies with $sSFR > 1/(3 \cdot t_{Hubble})$ are assigned as star-forming, the others as quiescent. Uncertainties are derived via bootstrapping to reflect the sample variance.

the SAM in a quantitative sense, notably its underprediction of the quiescent population at $z \sim 2$, additional or other quenching processes may be at play in the real universe. One such process, that is causally linked to the presence of a bulge, could be morphological quenching (Martig et al. 2009; Genzel et al. 2014a). In such a scenario, the high central stellar density provided by a bulge stabilizes the gas disk and prevents it from forming stars. While plausibly only a temporary measure (as no gas is expelled, nor stopped from accreting through this mechanism), it could potentially contribute to suppressing star formation in $z \sim 2$ galaxies more efficiently and/or preventing them from returning to the star-forming branch in the SAM. In the local universe, star formation efficiencies of bulge-dominated systems are reduced by factors of $\sim 2 - 3$ compared to disk-dominated galaxies (Saintonge et al. 2012; Martig et al. 2013).

2.6 Comparison with Measurements on H-band

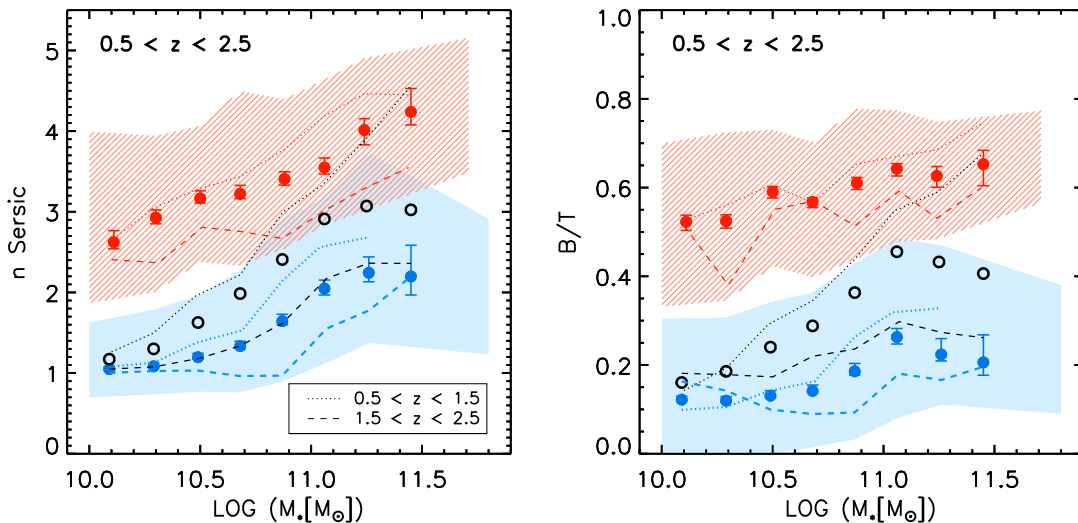


Figure 2.10: Equivalent of Figures 2.5 using the results of structural measurements on the H -band light images.

Here, we investigate how the results of our structural analysis change when conducting the measurements on the H -band light images rather than on the stellar mass maps. To this end, we present in Figure 2.10 the same figures as discussed in Section 2.4, now using the Sérsic index and B/T values as inferred from the CANDELS H -band imaging. Likewise, we compute the bulge and disk mass as $(B/T)_H M_*$ and $(1 - (B/T)_H) M_*$, respectively.

Overall, our analysis reveals a qualitatively similar mass dependence of n and B/T , and distinction between SFGs and quiescent galaxies as inferred from the mass maps. In detail, however, modest changes in n and B/T are notable. While the median $z \sim 1$ (2)

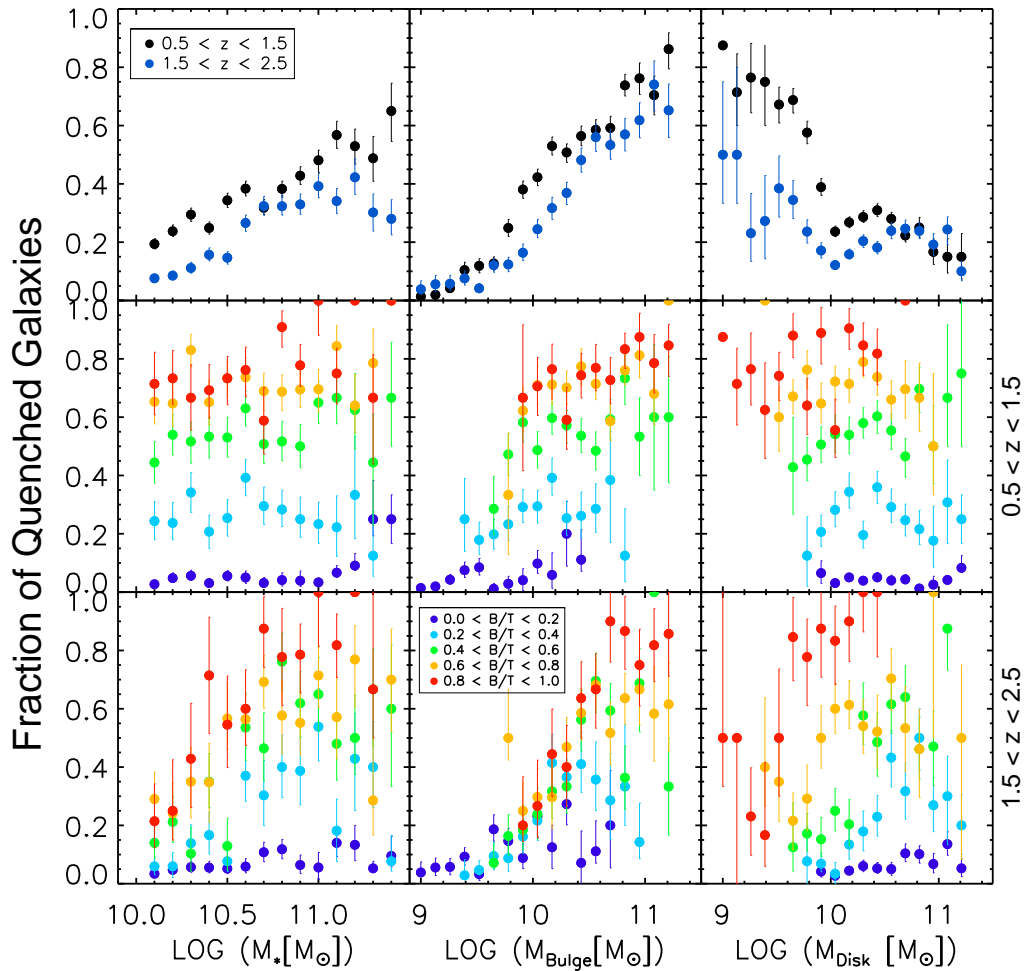


Figure 2.11: Equivalent of Figures 2.7 (right) using the results of structural measurements on the H -band light images.

SFG has $(B/T)_H \lesssim 0.25$ (0.20), the typical bulge fractions increase to above 20%, and reach up to $\sim 40 - 50\%$ at the massive end, once spatial M_*/L variations are corrected for. Likewise, the corresponding Sérsic indices measured on H -band imaging for SFGs below $\log(M_*) = 10.8$ are consistent with exponential disk profiles (see also Wuyts et al. 2011b), but are slightly cuspier when quantified on mass maps. This is in line with findings based on smaller subsets of CANDELS data by Wuyts et al. (2012) and Guo et al. (2012).

The central 50th percentile intervals marked by the red and blue polygons are somewhat less confined in the plots based on stellar mass maps compared to the H -band results. We interpret this to be due to an additional source of random uncertainty introduced by the resolved stellar population modeling. The resolved stellar population modeling itself was motivated by the need to reduce the systematic biases associated with spatial M_*/L ratio variations.

Focussing on Figure 2.11, the qualitative trends of f_{quench} with total stellar mass, bulge and disk mass are very similar. However, the lower two rows of Figure 2.11 compared to Figure 2.7 show that the bins of lowest and highest B/T are more separated from each other in f_{quench} in light than in mass. This observation too is in line with the disks of SFGs being dominating by a younger stellar population than that of the bulge, shifting SFGs to lower B/T . The middle panels of Figure 2.11 show a larger scatter than the corresponding panels in Figure 2.7.

2.7 Discussion

2.7.1 Structural change

In order to study the morphological differences between SFGs and quiescent galaxies, and to draw conclusions on the possible structural changes of star-forming galaxies as they move along the MS, we first examined the mass dependence of the profile shape of SFGs and quiescent galaxies as traced by the Sérsic index and B/T ratio. We have shown that quiescent galaxies are structurally distinct from the star-forming population as seen by overall higher Sérsic indices and B/T ratios at a given stellar mass. SFGs show rising trends of their median Sérsic index and B/T ratio with increasing stellar mass, with the latter rising up to $\sim 40 - 50\%$ above $10^{11} M_\odot$. These findings give insights about the link between the structural evolution of SFGs and the quenching process as they move along the MS.

Analyzing the Schechter functional forms of the SFG and QG mass function as a function of redshift, Peng et al. (2010) conclude that the quenching rate of galaxies climbing the MS rises proportionally to the SFR (and given the near-linear MS slope therefore also proportionally to the stellar mass, hence their terminology 'mass quenching'). This corresponds to a survival probability on the MS that drops exponentially with mass, implying that, while nearly all low-mass SFGs are destined to continue growing along the MS, toward the high-mass end the MS becomes progressively more dominated by near-to-be-dead SFGs. In fact, the sub-unity slope of the MS, and possible flattening at the high-mass end (Whitaker et

al. 2012), may well be interpreted in this context: the typical SFG above $10^{11} M_{\odot}$ is already undergoing some level of quenching, thereby deviating from the projected path along a SFR-Mass relation of slope unity, that could be expected from cosmological accretion rates in the absence of quenching. Tying in our observational results on galaxy structure, the deviation toward high median n and B/T at the massive end reflects the typical structure of soon-to-be-dead star-formers that account for the bulk of SFGs above $10^{11} M_{\odot}$. The fact that they are structurally distinct implies that the morphological transition happens first, to be followed later by the departure from the MS. Bulge growth precedes quiescence. Such a morphological change prior to quenching is in line with qualitative predictions based on a toy model by Dekel & Burkert (2013). In the latter study, about half of the star-forming disk galaxies at $z \sim 2$ are predicted to evolve into compact star-forming 'blue nuggets' due to violent disk instabilities before they are quenched into compact quiescent galaxies ('red nuggets'). An observed population of 'blue nuggets' has been proposed by Barro et al. (2013a,b) to represent an evolutionary link, originating from extended disk galaxies, and evolving into compact quiescent systems.

This does not refute that galaxies also undergo further structural evolution after they are quenched. At least part of the size growth (Cassata et al. 2013; van der Wel et al. 2014a) and evolution toward rounder axial ratios (Chang et al. 2013) has been attributed to (minor and/or major) dry mergers, and it is conceivable that similar processes contribute to the observed trend of increasing B/T toward the massive end for the quiescent population.

2.7.2 AGN as the driver of quenching ?

We have demonstrated that the bulge mass of a system is well correlated with its quenched state and has a stronger predictive power of quiescence than the total stellar mass. The observed trends of f_{quench} with total stellar mass, bulge mass and disk mass as viewed among galaxies in different B/T bins are in good qualitative agreement with predictions from the Somerville et al. SAM. In the context of this model, the growth of the central supermassive black hole, which is the primary quenching agent for massive galaxies in this SAM, is tightly coupled with the growth of bulges through both merging and disk instabilities.

If a black hole - bulge scaling relation is in place during the peak of cosmic star formation as it is in the present-day universe (Häring & Rix 2004), our observational results together with the model comparison could therefore hint at the bulge not being the causal link to quenching, but rather the most accessible observational proxy for the AGN acting as the quenching agent¹⁰. In detail, however, there are quantitative differences between the SAM and our observations, most severely in the highest redshift bin ($1.5 < z < 2.5$), where the observed quenched fraction exceeds the value predicted by the SAM by a factor of ~ 3.5 . The latter difference could hint at a need for more frequent, efficient, or lasting quenching,

¹⁰We note that Rosario et al. (2013) find X-ray signatures of AGN activity at these high redshifts to be most prominent among the star-forming population, most notably at the high-mass end, precisely where we see an upturn in the bulge fraction among SFGs.

a possible mechanism we speculate about below. We also note that the same behavior is not necessarily a generic feature to all SAMs (see Appendix B of this thesis).

It is tempting to draw connections between the emerging bulges in massive MS galaxies out to $z \sim 2.5$ revealed by our analysis, and recent observational results based on deep AO-assisted integral field data sets and grism spectroscopy over the same redshift range. Förster Schreiber et al. (2014) and Genzel et al. (2014b) found a high prevalence of powerful nuclear outflows in $\log(M_*) > 11$ galaxies possibly driven by AGN, which appear to be absent in galaxies at lower masses. Along with star formation driven winds in the outer parts of the galaxies, such outflows could efficiently remove gas out of galaxies and, in this way, contribute to the quenching process.

Meanwhile, the 3D-HST and CANDELS legacy programs have yielded evidence for nuclear depressions in the $H\alpha$ equivalent width in $z \sim 1$ SFGs (Nelson et al. 2012, 2013; Wuyts et al. 2013). At the highest stellar surface mass densities, star formation no longer appears to proceed in lockstep with the assembled stellar mass. Likewise, Genzel et al. (2014a) report on ring-shaped $H\alpha$ distributions in massive $z \sim 2$ SFGs, surrounding a more quiescent center where the dynamically inferred Toomre Q parameter significantly exceeds unity, owing to the emergence of a stellar bulge. As such, the Toomre stability criterion is satisfied in the central galaxy regions, which consequently could prevent the gas reservoir, if present there, from fragmenting and forming stars. While this result suggests that some causal connection between bulge growth and quenching may be at play, it should be noted (as is done also by Genzel et al. 2014a) that gravitational quenching by itself does not expel the gas present, neither does it stop the accumulation of a larger gas reservoir by continuing cosmological accretion. Additional maintenance mode might be required for a long-term shut-down of further gas supply.

2.8 Conclusions

In this chapter, we analyzed the structural properties of a sample of 6764 massive ($> 10^{10} M_\odot$) galaxies in the redshift range $0.5 < z < 2.5$, by exploiting the multi-wavelength CANDELS HST imaging data set in all five CANDELS/3D-HST fields, to shed light on the connection between galaxy structure and quenching at high redshift. We carried out single-component (Sérsic) fits and two-component (bulge + disk) decompositions, on stellar mass maps reconstructed from a resolved panchromatic SED modeling technique (Wuyts et al. 2012, 2013), as well as on images of the H -band surface brightness distribution. In addition, we compared our findings to predictions by the state-of-the-art semi-analytic model from Somerville et al. (2008, 2012, with extensions including disk instabilities presented by Porter et al. 2014). The main results are the following:

- At fixed stellar mass, quiescent galaxies have overall higher Sérsic indices and B/T ratios than SFGs as measured on their mass maps, in line with previous findings using monochromatic observations. We find an increase of Sérsic indices among SFGs with

increasing total stellar mass, with the median mass profiles increasing from $n \sim 1.3$ at $10^{10} M_{\odot}$, to $n \gtrsim 2$ above $10^{11} M_{\odot}$. Two-component bulge-disk decompositions confirm that the same rising trend is present when considering the median B/T ratio of SFGs, which is rising up to $\sim 40 - 50\%$ above $10^{11} M_{\odot}$. The same characteristic behavior is seen at $z \sim 1$ and $z \sim 2$.

- Quantifying the same trends on the H -band light profiles rather than the mass maps, the Sérsic indices and B/T fractions are overall lower for SFGs, confirming previous non-parametric measurements for a subset of our sample (Wuyts et al. 2012). The emergence of bulges above $10^{11} M_{\odot}$ in SFGs appears to be also slightly less prominent when viewed in light, consistent with the steepest color gradients (blue disks with red central bulges) being found among massive SFGs.
- The likelihood of a galaxy being quenched, as traced by the fraction of quiescent galaxies, is better correlated with the bulge mass than the total stellar mass and further shows no appreciable correlation with the amount of stellar mass in the disk component. The quenched fraction at redshift 1 is on average higher by a factor ~ 2 than at redshift 2.
- At a given total stellar mass, the quenched fraction exhibits a strong positive correlation with B/T , while different B/T bins are confined to a significantly tighter locus in a diagram of f_{quench} versus M_{Bulge} . These findings imply that the bulge mass of a system is the single observable parameter with the most predictive power regarding its quenched state, although a somewhat tighter constraint on the probability of quiescence can be obtained if in addition also the total stellar mass is known. The same trend is seen over the full redshift range probed, with the distinction that quenched fractions are lower at higher lookback times.
- We find a good qualitative agreement between the semi-analytic model by Somerville et al. and our observational findings. Since bulge and black hole growth are tightly coupled in the SAM, the strong dependence of f_{quench} on bulge mass follows rather naturally in this model. Our observational results can in the context of this model therefore be interpreted as the bulge being the closest observable proxy to the underlying agent of quenching: the black hole. Quantitatively, the largest discrepancy between model and observations is found in the highest redshift bin ($1.5 < z < 2.5$), where the observed quenched fraction is larger by a factor of ~ 3.5 than predicted by the SAM. We note that the same behavior is not necessarily a generic feature to all SAMs.

Chapter 3

Outer disk kinematics of high-redshift star-forming galaxies

In this chapter I will turn to the baryonic content of star-forming galaxies at high redshift as probed by their ionized gas kinematics. The available IFU datasets from the KMOS^{3D} and SINS/zc-SINF AO surveys will be the basis for deriving a representative rotation curve (RC) for disk galaxies at high redshift, which will give us for the first time important insights into kinematics and baryonic vs. dark matter contributions in the outer regions. I begin in Section 3.1 with stating the aims and motivation for this analysis in the context of open questions in galaxy formation at high redshift. In Section 3.2, I will give an overview of the observations and the sample this analysis is based on. Then I will describe the methodology applied in determining a rotation curve via stacking in Section 3.3, including the extraction and normalization of individual rotation curves for our sample, and an alternative method of normalizing rotation curves with the aid of effective size measurements. I examine the properties of the sample representing the parts of the stacked rotation curve at different radii. Section 3.4 will present the resulting stacked rotation curve and compare its shape with predictions of models that include the rotation of baryonic and dark matter arranged in a disk and halo, respectively. I will discuss the implications of this comparison on the relative baryonic content of high-z disk galaxies and I will demonstrate that the conclusions made are largely independent of model assumptions such as concentration index of the halo or the presence or absence of a central stellar bulge component within the disk. The results of this analysis are summarized in Section 3.5.

3.1 Aims

As discussed in the introductory Chapter, the baryonic versus dark matter components in the outer parts of galaxies are most successfully probed by extended rotation curves reaching beyond the radius R_{turn} (at which pure baryonic disk models expect a turnover in velocity), which is, however, not yet available for galaxies at higher redshift. The surface brightness

limitations inherent to observations of most individual galaxies at higher redshifts currently only allow to trace the RCs based on ionized gas kinematics within $\sim 1 R_{turn}$. However, current studies on the basis of IFU kinematics indicate high baryonic fractions of high- z star-forming disks in their inner parts, in line with findings from abundance matching on scales of the virial radius (e.g. Förster Schreiber et al. 2009; Burkert et al. 2015; Price et al. 2015; Wuyts et al. 2016). The high baryonic fractions of disk galaxies at high redshift likely leave an imprint on their rotation curves. Beyond R_{turn} , where local disk galaxies show *flat* rotation curves due to the dominance of dark matter, high- z disks possibly reveal a different behavior. Indeed, few individual galaxies with very deep integrations from the SINS/zc-SINF AO survey exhibit *dropping* rotation curves beyond R_{turn} (Förster Schreiber et al. 2006; Genzel et al. 2008, 2014a). In this context, the aim of this analysis is to further test if such a behavior is typical for star-forming galaxies at high redshift. Due to the sharply dropping $H\alpha$ surface brightness with galactocentric radius of high- z disks, we approach this by stacking the extensive set of available IFU data from the combined deep SINS/zc-SINF AO and the more recently started KMOS^{3D} survey. The combination of those datasets provides a unique combination of data quality and sample size, suitable for constraining the outer disk kinematics of galaxies with a good coverage of the $SFR - M_*$ plane at $0.7 < z < 2.6$. Based on our stacked rotation curve, we explore implications on dark matter fractions of high-redshift disks at unprecedented radii. This novel approach serves as an independent probe of the relative baryonic distribution, largely independent of light-to-mass conversions and assumptions on the IMF.

3.2 Data and sample selection

3.2.1 The KMOS^{3D} and SINS/zc-SINF datasets

The basis of this analysis is IFU spectroscopic observations of $H\alpha$ of 101 SFGs at $0.7 < z < 2.6$, representative of the main sequence (MS) population at high redshift. The sample is culled to a large extent from the KMOS^{3D} survey (Wisnioski et al. 2015) and the SINS/zCOSMOS (zC)-SINF survey (Förster Schreiber et al. 2009; Mancini et al. 2011), briefly described in the following.

The KMOS^{3D} survey is an ongoing program to observe galaxies at $0.7 < z < 2.7$ using the multiplexed IFU instrument KMOS on the VLT (Sharples et al. 2012). The targets are mass-selected galaxies from the 3D-HST Treasury Survey with the Hubble Space Telescope (Brammer et al. 2012; Skelton et al. 2014; Momcheva et al. 2015). The targets for KMOS^{3D} are furthermore selected based on magnitude cuts and the avoidance of night sky line contamination around the wavelengths of the redshifted $H\alpha$ emission. The baseline integration times for galaxies at different redshifts are adapted to account for the decreasing surface brightness with increasing redshift such that the S/N reached stays roughly at constant level. For redshift $\sim 1, 1.5$ and 2 , these baseline integrations times are ~ 4 hrs, ~ 6 hrs,

and ~ 10 hrs. Longer integrations (up to ~ 20 hrs) are spent for galaxies with fainter line fluxes, such as high-mass objects well below the MS. KMOS has a Field Of View (FOV) of $2''.8 \times 2''.8$ in size, sampled by $0''.2$ per spaxel. Observations are done in natural seeing yielding a typical value for the Full Width Half Maximum (FWHM) resolution of $0''.4 - 0''.6$. The spectral resolution depends on the redshift of the observed target and lies between ~ 60 and $\sim 110 \text{ km s}^{-1}$ in FWHM. The observations are done using either the YJ , H or K band grating. Within the first two years of ongoing observations, ~ 460 targets were observed, of which $\sim 79\%$ are detected, and $\sim 70\%$ are detected and spatially resolved. The analysis of this work includes data from KMOS^{3D} (including the selected sample and all stated numbers) observed until October 2015.

The SINS/zC-SINF survey (Förster Schreiber et al. 2009; Mancini et al. 2011) is a program using the IFU instrument SINFONI (Eisenhauer et al. 2003; Bonnet et al. 2004) at the Very Large Telescope (VLT), targeting ~ 110 star-forming galaxies at $z \sim 2$. A subset of 35 targets have been observed in adaptive optics-assisted mode, which is referred to as the SINS/zC-SINF AO sample below. The targets for SINS/zC-SINF are drawn from spectroscopic surveys and are mainly selected based on their magnitude and/or colors. The sample probes well the $z \sim 2$ main sequence population of SFGs. The FWHM of the spatial PSF is $\sim 0''.6$ in natural seeing mode, and ranges between $0''.15$ and $0''.25$ in AO mode, with a spectral resolution between ~ 80 and $\sim 120 \text{ km s}^{-1}$ in FWHM. The AO observations with SINFONI used in this analysis were done using spatial sampling of $0''.05$ per spaxel, yielding a FOV of $3''.2 \times 3''.2$ in size. To ensure an appropriate subtraction of sky signal, an 'on-source dithering' pattern was employed for most of the targets, in which the FOV in different exposures was shifted by around half its size. This results in an 'effective FOV', which is significantly reduced in size along one spatial direction. However, for larger targets ($> 1''.5$), the sky exposures were obtained at positions well away from the target, yielding an effective FOV that is not reduced in size.

3.2.2 Ancillary data

In addition to the IFU datasets presented, we make use of the available wealth of ancillary providing information on integrated and resolved properties of our galaxy sample. Integrated stellar masses and SFRs for the entire sample are derived by identical procedures as described for the CANDELS dataset in Chapter 2, employing a SED modeling technique with Bruzual & Charlot (2003) models, and the ladder of SFRs from Wuyts et al. (2011a). Molecular gas masses for our sample are computed using the scaling relation of Genzel et al. (2015) based on the combined CO + dust calibration of the gas depletion time scales.

We also use the available high-resolution panchromatic HST imaging in the COSMOS, GOODS-S and UDS fields observed within the CANDELS survey, and the derived morphological parameters from the H -band Sérsic profile fitting described in Chapter 2 of this

thesis, supplemented by identical measurements from van der Wel et al. (2012). In addition, we use available H -band WFC3 imaging for our SINS/zC-SINF targets (Tacchella et al. 2015). Information on redshift, stellar masses and SFRs for the underlying 3D-HST population plotted in Figure 3.1 and 3.8 are taken from the 3D-HST version 4.1 catalogs (Skelton et al. 2014).

Although reconstructed stellar mass maps are available for our galaxies sample, we choose to use the parameters derived on H -band images, (i.e. covering the rest-frame NIR, $\sim 8000 \text{ \AA}$ at $z \sim 1$, to optical regime, $\sim 5300 \text{ \AA}$ at $z \sim 2$). The mass maps are well representative for the stellar mass distribution in galaxies and show more concentrated profiles than the H -band light due to M_*/L gradients within galaxies. However, for our analysis it is important to quantify the structure of the *baryonic* distribution (i.e. stellar and gas) for our sample. Resolved distributions of gas within SFGs at high redshift (for the spatial scales probed from the HST imaging) are currently not yet systematically studied and are generally available through indirect methods that are connected to substantial uncertainties. Studies that analyzed the morphology of $H\alpha$ emission in massive SFGs have shown that the distribution of star formation and thus the inferred distribution of molecular gas (by inverting the Kennicutt Schmidt law, Kennicutt 1998) is less centrally concentrated than the stellar component and also exhibits ‘ring-like’ morphologies for the most massive systems (Wuyts et al. 2013; Genzel et al. 2014a). Although the (possibly) spatially varying extinction is a significant caveat for these observations and hamper a robust interpretation, the current findings suggest that the gas component within massive SFGs is more spatially extended than the stellar component. Therefore, given the significant gas fractions of SFGs at $z \sim 1 - 2.5$, the expected baryonic mass is more spatially extended than the stellar mass distribution. Since we are currently not able to derive robust extinction-corrected SFR and gas distributions for our sample, and also given that total gas mass estimations in individual galaxies can only be inferred from gas-mass scaling relations, resulting in further uncertainties in the gas fraction f_{gas} , we use the H -band morphology as a best proxy for the baryonic distributions for our galaxy sample.

3.2.3 The stacking sample

From the pool of available targets from both KMOS^{3D} and the SINS/zC-SINF AO sample that are detected and spatially resolved, we specifically select targets that are suitable for our science goals and therefore apply several selection criteria. Those are the following:

1. First, we select targets that represent the subset of rotationally supported disk galaxies. We therefore require galaxies to exhibit an overall smooth disk-like velocity field and a disk-like morphology judged by their rest-frame optical HST morphology. Galaxies with signatures of mergers either apparent in their velocity field or from the HST imaging are rejected.

2. Next, we require the individual extracted rotation curve of a galaxy to have the quality such that it exhibits a significant flattening in velocity or even a turnover within the extent it can be reliably determined. This constraint removes galaxies from our sample that are too extended such the flattening falls outside the FOV, although we demonstrate below that this is not a significant effect, even at redshift ~ 1 where galaxy sizes are larger than at ~ 2 . Galaxies for which the rotation curve can only be constrained in their very inner parts due to the limiting S/N , are also excluded.
3. Furthermore, galaxies with strong contamination of OH sky lines within the wavelength region of $H\alpha$ are discarded.

After applying Criterion 1, a fraction of $\sim 77\%$ targets remain, similar to disk fractions found within the first-year KMOS^{3D} survey (Wisnioski et al. 2015). We note that the fraction of galaxies with signs of mergers is relatively small ($\sim 3\%$ of the total sample). After applying Criterion 1 and 2, we stay with $\sim 40\%$ of the total sample, implying that Criterion 2 removes the largest portion of the total sample among our selection criteria. We dedicate a detailed analysis on potential effects connected with our selection that may bias our results by using simulated rotation curves, presented in Section 3.3.5. In short, we find that the rejection of galaxies according to Criterion 2 is mainly driven by the variations of S/N among the observed data and *does not* yield to significant biases in our stacking results. Finally, with all criteria applied, the final sample consists of 101 targets (92 from KMOS^{3D} and 9 from the SINS/zC-SINF AO sample, representing $\sim 32\%$ of the total sample) to be used in our stacking analysis.

In the following, we will compare the properties of the sample selected for stacking (henceforth referred to as the 'stacking sample') with the combined KMOS^{3D} and SINS/zC-SINF AO targets representing the parent sample for selection as a reference. In the latter, we only include galaxies which are detected and spatially resolved.

Figure 3.1 displays the coverage of the stacking sample (blue symbols) compared to the full KMOS^{3D} and SINS/zC-SINF AO samples of detected and resolved galaxies in the $SFR - M_*$ and $R_e - M_*$ planes (combined blue and red symbols), together with the underlying 3D-HST parent sample (grey points). The respective samples are shown in the two redshift bins $0.7 < z < 1.2$ and $1.2 < z < 2.7$ (i.e. targets observed with the YJ and H/K grating). The effective radii (R_e) shown in the right panels are derived from fits to the rest-frame optical HST images and serve as a measure of the size of the baryonic distribution. As can be seen by Figure 3.1, the stacking sample shows a fairly uniform overlap with the full KMOS^{3D} and SINS/zC-SINF AO samples in the $SFR - M_*$ plane for both redshift ranges and appears to overlap well with the main sequence population of SFGs above $M_* \gtrsim 10^{10} M_\odot$. A similar statement can be made considering the $R_e - M_*$ plane and the size-mass relation for late-type galaxies shown by the solid lines in the right panels of Figure 3.1. As apparent for the high redshift panel, the stacking sample is mildly offset towards larger radii. In the following, we will present the properties of the stacking sample

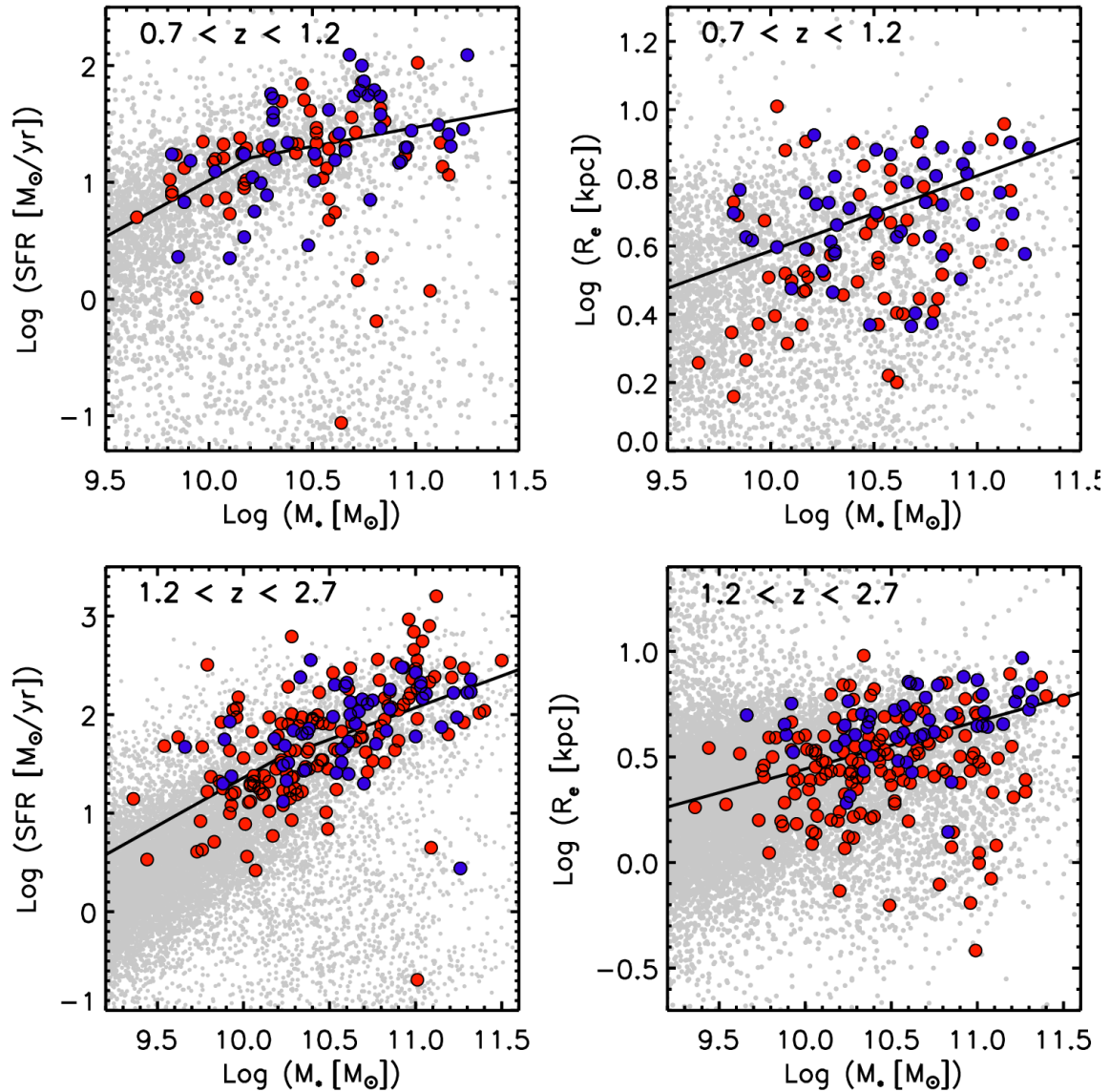


Figure 3.1: Properties of our sample of stacked galaxies (blue symbols) compared to all detected and resolved KMOS^{3D} and SINS/zc-SINF AO galaxies (combined blue and red symbols), plotted in the $SFR - M_*$ plane (left), and in the $R_e - M_*$ plane (right). Effective radii are measured on H -band light distributions. The grey points show the 3D-HST background population in the respective redshift ranges. The solid lines in the left panels represent the broken-power law parametrization of the main sequence by Whitaker et al. (2014) for the corresponding redshifts. The solid lines in the middle panels represent the size-mass relation for late-type galaxies as derived by van der Wel et al. (2014a).

and the underlying full KMOS^{3D} and SINS/zc-SINF AO sample and quantify their overlap in more detail. For this purpose, we also determine the overlap of each galaxy with the main sequence by computing the logarithmic main sequence offset $\Delta(\text{MS})$ in sSFR given by

$$\Delta(\text{MS}) = \log(s\text{SFR}/s\text{SFR}_{\text{MS}}(z, M_*)), \quad (3.1)$$

where $s\text{SFR}_{\text{MS}}(z, M_*)$ is the expected sSFR on the main sequence given a galaxy's redshift z and stellar mass M_* . In order to compute $s\text{SFR}_{\text{MS}}(z, M_*)$, we adopt Equations 5 and 6 from Wisnioski et al. (2015), who use the parametrization of the main sequence as measured by Whitaker et al. (2014).

The properties of both stacking sample and the full KMOS^{3D} + SINS/zc-SINF AO sample of detected and resolved galaxies are displayed in Table 3.1. Shown are the ranges, mean, and median averages of their distribution in stellar mass M_* , SFRs, intrinsic effective Radii R_e , main sequence offset $\Delta(\text{MS})$, and Sérsic index n . The respective distributions are displayed in Figure 3.2. To further facilitate a statistical comparison between properties of the stacking sample and the full KMOS^{3D} + SINS/zc-SINF AO sample, we perform two-sided Kolmogorov - Smirnov (K-S) tests on the distributions of the various parameters. The resulting probability values ('p-values', p) are indicated for each panel in Figure 3.2.

Property		Stacking sample			Full KMOS ^{3D} + SINS/zc-SINF AO		
		Range	Median	Mean	Range	Median	Mean
$\log(M_*)$	$z < 1.3$	[9.82,11.25]	10.61	10.56	[9.65,11.25]	10.52	10.48
	$z > 1.3$	[9.66,11.32]	10.61	10.62	[9.36,11.50]	10.46	10.48
$\log(\text{SFR})$	$z < 1.3$	[0.35,2.09]	1.31	1.50	[-1.06,2.09]	1.27	1.41
	$z > 1.3$	[0.44,2.55]	1.91	2.03	[-0.69,3.2]	1.79	2.05
R_e	$z < 1.3$	[2.32,8.58]	4.98	5.12	[1.44,10.22]	4.23	4.61
	$z > 1.3$	[1.40,9.30]	4.52	4.74	[0.38,9.54]	3.30	3.61
$\Delta(\text{MS})$	$z < 1.3$	[-0.67,0.93]	0.14	0.13	[-2.24,0.93]	0.11	0.04
	$z > 1.3$	[-1.52,0.77]	0.08	0.04	[-2.93,1.45]	0.04	0.01
n	$z < 1.3$	[0.2,8.0]*	1.26	1.78	[0.2,8.0]*	1.35	1.82
	$z > 1.3$	[0.2,7.9]	0.68	1.31	[0.2,8.0]*	0.97	1.49

Table 3.1: Properties of the stacking sample and the full KMOS^{3D} + SINS/zc-SINF AO sample of detected and resolved galaxies. Stellar masses M_* , SFRs and intrinsic effective Radii R_e are given in units of M_\odot , M_\odot/yr and in kpc, respectively.

*: These boundaries are set within the Sérsic profile fitting; for details see Chapter 2 of this thesis and van der Wel et al. (2012).

Figures 3.1 and 3.2, as well as the numbers in Table 3.1 show that the stacking sample yields overall fair representation of the star-forming main sequence population within the

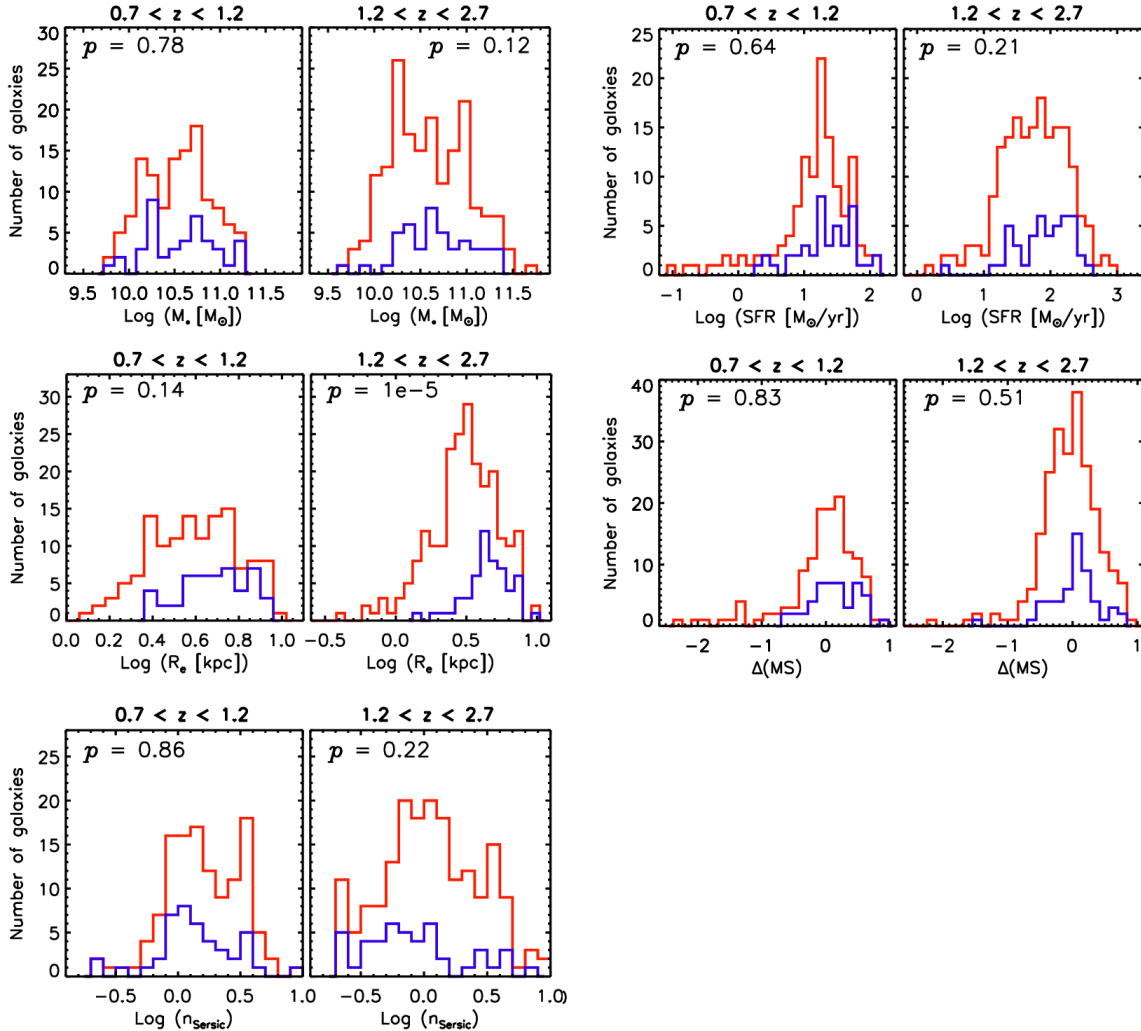


Figure 3.2: Distributions of Stellar masses M_* , SFRs, intrinsic effective Radii R_e , main sequence offsets $\Delta(\text{MS})$, and Sérsic indices n of the stacking sample (blue) and the full KMOS^{3D} + SINS/zc-SINF AO sample of detected and resolved galaxies (red). The distributions are shown in two redshift bins. The p-value from the K-S test on both respective distributions are furthermore indicated in each panel.

full redshift range probed. Although we significantly reduce the number of galaxies when selecting the sample of stacked galaxies, we find no or little bias in the average galaxy properties between the stacking sample and the full KMOS^{3D} + SINS/zc-SINF AO sample of detected and resolved galaxies (with exception for size distributions as discussed below). Considering the individual galaxy properties examined here, we conclude the following:

- The stacking sample shows a uniform coverage in stellar mass compared to the full KMOS^{3D} + SINS/zc-SINF AO sample as their probed ranges and averages are very similar, albeit at $z > 1.2$, the stellar mass range probed by the stacking sample is slightly narrower. The K-S test confirms that both samples follow the same distribution in stellar mass at $z < 1.2$, and they are only marginally different (at $\sim 1.5\sigma$ - level) at $z > 1.2$.
- Considering the coverage in SFR, both stacking sample and the full KMOS^{3D} + SINS/zc-SINF AO sample have very similar average values probed for both redshift ranges. The ranges in SFR probed by the stacking sample are slightly smaller, since in particular the SFRs do not extend to the low values well below the MS. The K-S test shows that we do not find any statistical significant differences in the distribution of SFRs probed by both samples.
- Our stacking sample overlaps well with the main sequence in both redshift ranges as indicated by the average main sequence offset $\Delta(\text{MS})$. At $z < 1.2$, the stacking sample has a small positive offset, which is however, only moderate compared to the 0.2 - 0.3 dex scatter of the MS (Whitaker et al. 2012; Speagle et al. 2014). The above numbers point out that the KMOS^{3D} plus SINS/zc-SINF AO parent sample extends to somewhat lower sSFRs into the regime well below the MS, compared to our stacking sample. Given that our selection criterion requires tracing the H α kinematics at least out to radii where the rotation curve flattens out, we thus are not able to include targets with low H α surface brightness well below the MS. We confirm that both the stacking and full KMOS^{3D} plus SINS/zc-SINF AO parent samples have MS offset distributions which are not different on a statistically significant level.
- Turning to the size distributions, we note that our stacking sample overlaps well with both the underlying size distribution of late-type galaxies at redshifts $z < 1.2$ as indicated by the right upper panel of Figure 3.1. However, we find that the average size of our stacking sample is slightly larger than for the full KMOS^{3D} plus SINS/zc-SINF AO parent sample. The K-S test confirms that the size distribution at $z < 1.2$ of the two samples are different at a $\sim 1.5\sigma$ - level, indicating that our selection causes a mild bias towards larger systems. We observe that this effect is even stronger at $z > 1.2$, where the average sizes between both samples differ significantly, also seen by the bias between the stacking sample and the size distribution of late-type galaxies in the lower right panel of Figure 3.1.

The K-S test confirms that the distributions in R_e of the stacking and full KMOS^{3D} plus SINS/zc-SINF AO parent samples are indeed different on a statistically significant level (with a p-value of < 0.01). Again, the selection criterion of being able to constrain the RC of a galaxy out to R_{turn} requires sufficient S/N in the outer regions of a galaxy which is more difficult to achieve for smaller targets due to the more severe impact of spatial beam smearing. Especially at $z > 1.3$, where effective sizes are smaller than at $z < 1.2$, this effect is strongest and most likely leads to the bias against smaller galaxies at $z > 1.2$. The average integration times for galaxies with sizes below $\log(R_e) \lesssim 0.35$ are ~ 16 hrs, which substantiate this conclusion. Deep observations are therefore required to include more galaxies that lie in the locus below the average $R_e - M_*$ relation at $z > 1.2$.

- The distribution of Sérsic indices as measured on the rest-frame optical light distributions for our stacking sample and for the full KMOS^{3D} plus SINS/zc-SINF AO parent sample are very similar, albeit we find a marginal trend (at $\sim 1.2\sigma$ - level) towards lower Sérsic indices for our stacking sample at $z > 1.2$. We also find that the rest-frame optical light distributions for our stacking sample are well in agreement with being exponential as the average mean (median) Sérsic index within the entire redshift range is 1.58 (1.15) with a logarithmic scatter of ~ 0.36 dex.

For further comparison of our results with modeled rotation curves presented in Section 3.4, we compute the median average baryonic mass of the stacking sample over the entire redshift range, taking into account the amount of molecular gas for each galaxy, and find a value of $\log(M_{baryonic}) = 10.96$. Also, we compute a median average R_e for our stacking sample over the entire redshift range and find a value of $R_e = 4.6$ kpc.

3.3 Methodology

3.3.1 Extraction and normalization of RCs

As a first step, we generate rotation curves for each galaxy in our sample as follows. We extract spectra from our data cubes within apertures placed along the kinematic major axis determined from the $H\alpha$ velocity field over the pixels with sufficient S/N . For details on how the kinematic maps are computed, see Förster Schreiber et al. (2009), Mancini et al. (2011), Wisnioski et al. (2015). In order to optimize the signal in the spectral extraction along the kinematic axis, we use the following method. We sum the spectra of individual pixels over apertures with a fixed radial diameter corresponding to the spatial PSF FWHM, such that the velocity field in the radial direction is not artificially smoothed. The size of the apertures in the perpendicular direction is increasing radially towards the fainter regions

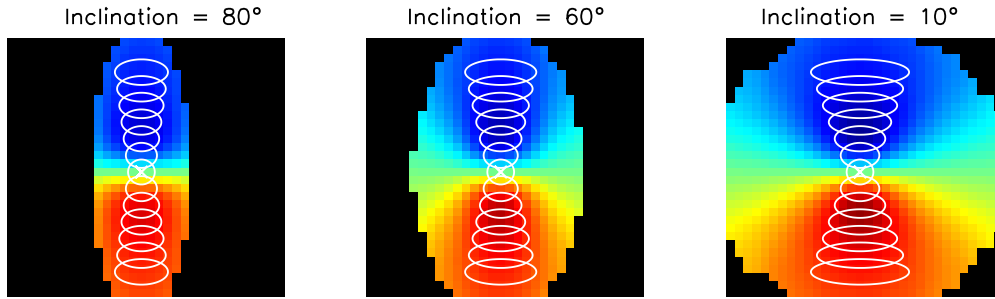


Figure 3.3: Apertures used for extraction plotted over model velocity fields for different adopted inclinations.

such that the signal in a given aperture is optimized due to the increased number of summed spaxels in it, also without additionally smoothing the velocity profile. The rate at which the size of the elliptical apertures increases with radius is dependent on the inclination angle of the galaxy. We gauge the size of the ellipses as a function of inclination by simulating artificial velocity maps of mock galaxies. The effective size and mass of the mock galaxies as well as the spatial PSF FWHM are adopted to represent our average sample properties. Figure 3.3 outlines the increasing elliptical apertures which are plotted over modeled velocity fields with identical spatial sampling and resolution as the real data, shown for 3 different inclinations. As apparent in Figure 3.3, the size of the ellipses are increasing with decreasing inclination. Figure 3.4 exemplifies the extraction of spectra for three galaxies at different redshifts. The left panels display the observed-frame IJJ color composite to show the rest-frame optical morphology. In the middle panels, the apertures used for extraction are plotted over velocity fields.

In order to generate the rotation curves for each galaxy, we determine the observed $H\alpha$ velocity as a function of galactocentric radius. The velocity is measured from fitting a single Gaussian profile to the extracted spectrum accounting for the instrumental spectral resolution derived from nearby sky lines, using the IDL LINEFIT code (Förster Schreiber et al. 2009; Davies et al. 2011). In the fitting process, the continuum is determined as the mean between the 40th and 60th percentile of the flux level around the $H\alpha$ and [NII] emission lines. The fits are performed with Gaussian weighting based on an input noise cube, and errors are computed based on Monte-Carlo(MC) techniques. Once we have constructed a rotation curve for each galaxy, we determine its observed amplitude and extent by fitting each rotation curve with a Freeman exponential disk model of the form:

$$v_{disk}(r) = \sqrt{4\pi G \Sigma_0 r_d x [I_0(x)K_0(x) - I_1(x)K_1(x)]}, \quad (3.2)$$

with $x = r/(2r_d)$, where r_d the radial scale-length of the exponential disk, corresponding to $r_d \sim R_e/1.68$. Σ_0 is the central stellar surface density of the disk, and I_n and K_n

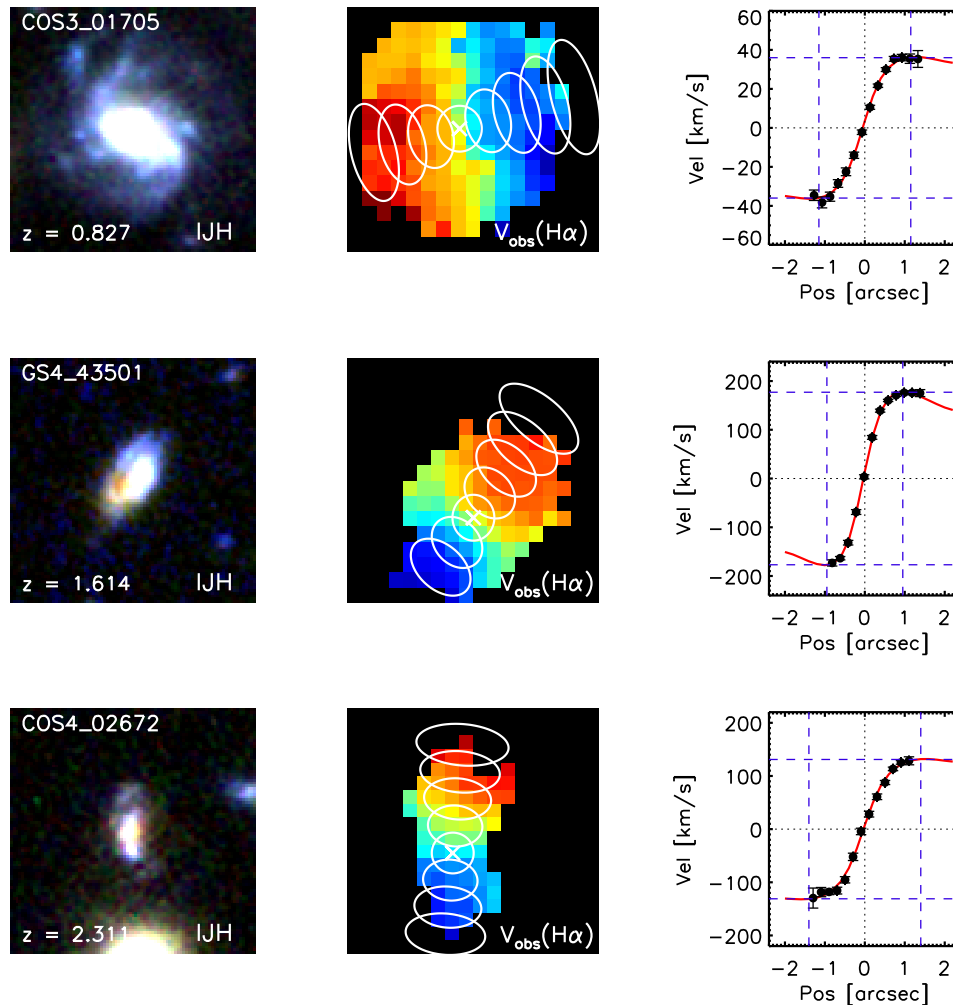


Figure 3.4: Examples of the extraction of spectra and the normalization of rotation curves for three targets with different redshifts. Left panels: *IJH* color composite from CANDELS/HST imaging. Middle: H α velocity field with overlapped apertures used for spectral extraction along the kinematic major axis. Right: Extracted rotation curve shown as black data points, together with the fitted exponential disk models shown in red.

denote the modified Bessel functions of the first and second kind (Freeman 1970). Within the fitting, we leave r_d and Σ_0 as free parameters. After the fit has converged, we determine the maximum observed velocity (V_{max}) and the radius of the peak (R_{turn}) from the model. Before fitting, the Freeman disk model is convolved with a 1D Gaussian of FWHM corresponding to the PSF associated with each galaxy. In the right panels of Figure 3.4, rotation curves of three examples are shown together with the respective fit. The maximum observed velocity does not correspond to the intrinsic rotation velocity (V_{rot}) since it is not further corrected for inclination, which is not necessary for our stacking methodology. We note that even when selecting galaxies with significant flattening towards the outer regions, a judgment whether this flattening results in a flat outer rotation curve or an actual turnover is typically not possible given the $H\alpha$ surface brightness limits of our data. However, we use the above Freeman disk model to quantify R_{turn} as the radius where a turnover of velocity would be expected. We refer to this turnover radius as quantified on the observed rotation curves as ' R_{turn}^{meas} '.

The model represented by Equation 3.2 is a correct description of a disk with infinitely small scale height h . As disks at higher redshift are found to be geometrically thick based on their shape and kinematics (e.g. Förster Schreiber et al. 2009, Kassin et al. 2012, Wisnioski et al. 2015, van der Wel et al. 2014b), we furthermore test the above normalization by using model rotation curves that take into account finite scale heights (Noordermeer 2008). Assuming a thickness parameter (i.e. ratio of scale height to scale length) of 0.2, we find that our V_{max} and R_{turn}^{meas} parameters do not change more than $\sim 1\%$ compared to the infinitely thin disk case.

The fit to determine R_{turn}^{meas} and V_{max} relies on the assumption that the shape of the baryonic mass profile is exponential. We find that on average this is justified for our sample, since the average Sérsic index as measured in H -band is ~ 1.1 . However, it is known that the shape of the inner rotation curve of galaxies, and in particular the position of the turnover relative to the intrinsic R_e , depends on details of the mass distribution (e.g. Kent 1986; Corradi & Capaccioli 1990; Noordermeer et al. 2007; Noordermeer 2008). Furthermore, the measurement of R_{turn}^{meas} based on the individual rotation curves might be less constrained in the regime where the rotation curves flatten out due to low S/N in the outer regions of the galaxies. Moreover, the presence of a possibly significant dark matter component might alter the shape of the outer rotation curve and therefore the position of R_{turn}^{meas} .

Due to the above reasons, and to validate the normalization of our rotation curves by R_{turn}^{meas} , we employ a second alternative method to determine R_{turn} . This technique converts a measurement of the intrinsic effective radius R_e to a turnover radius (hereafter referred to as ' R_{turn}^{morph} '), taking into account the Sérsic index and inclination of the galaxy as well as the amount of beam smearing that affects the observed rotation curve. Values for R_e , the Sérsic index and the inclination are determined based on the available H -band HST imaging assuming that those represent the extent and shape of the baryonic distribution (see Section 3.2.2). The details of this conversion and the resulting R_{turn}^{morph} are explained in Section 3.3.3.

In short, our sample shows good correspondence between the R_{turn}^{meas} and R_{turn}^{morph} , demonstrating the robustness of our R_{turn}^{meas} determination using the Freeman disk model. Also in Section 3.4, when the resulting stacked rotation curves are presented, the impact of using the R_{turn}^{morph} in the stacking process on the final results are presented.

As a next step, we create position-velocity (pv) diagrams for each object which are normalized in spectral and radial direction. In order to do so, the extracted spectra are re-sampled onto a common spatial and spectral grid using linear interpolation. The grid is designed in such way that each normalized pv diagram has a fixed pixel scale of $0.15 \cdot V_{max}$ in spectral and $0.16 \cdot R_{turn}$ in spatial direction, corresponding to an oversampling factor of ~ 1.8 and ~ 2.3 compared to the data cubes, respectively. We choose these pixel scales as a best compromise between accuracy in the alignment of normalized pv diagrams and resulting S/N . Next, we ensure that the signal of each galaxy contributes to the same amount to the outer disk region in the stack. This is done by scaling each pv diagram by the peak $H\alpha$ intensity at R_{turn} determined from the pv diagram itself. We therefore fit a gaussian profile to the spectrum in each pv diagram (i.e. the cut of a pv diagram along the velocity axis) at R_{turn} . We chose to derive the flux normalization at R_{turn} , since at larger radii it is not anymore possible to constrain the intensity for all targets due to the increasing noise. Through statistical tests as explained below, it is ensured that this scheme of flux normalization does not lead to a single object dominating the stack at large radii.

3.3.2 Final stacking and error estimation

As a last step, all normalized (in radius, velocity and surface brightness) pvs are averaged into a stacked pv from which the stacked rotation curve is then determined. The averaging is performed by computing the mean of all normalized pv diagrams. Before averaging, pixels that severely suffer from contamination of OH skylines or other sources of noise are masked out and discarded. Figure 3.5 plots the final stacked pv diagram, with the wavelength (or velocity) axis in horizontal and radial axis in vertical direction. The color coding indicates the surface brightness of $H\alpha$. The black lines indicate the center in radial position and velocity. The horizontal lines denote the radial position of 1 and 2 times the turnover radius for scale.

In order to furthermore increase the signal of the final stacked rotation curve, both sides of the stacked pv (i.e. the region above and below the horizontal line of zero radius in Figure 3.5) are combined by folding together the stacked pv diagram around the central spatial and spectral axis. On this folded pv diagram, the final stacked rotation curve is then derived by performing Gaussian fits with the LINEFIT code determining the centroid on the averaged $H\alpha$ emission line in the spectra at different radial positions. At each radius, the spectra of two spatial bins are summed up prior to extracting the velocities. This serves to enhance the S/N of the stacked rotation curve and still yields a sufficient spatial sampling of the resulting rotation curve. Prior to fitting, the spectra are median-filtered with a kernel of

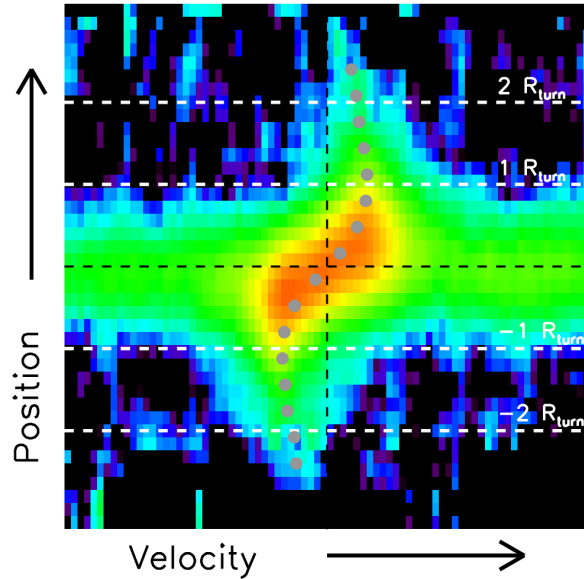


Figure 3.5: Final stacked pv diagram shown in logarithmic color scaling. The zero position in velocity and radius are marked as black lines, and the radial position of $1R_{turn}$ and $2R_{turn}$ are marked as white dashed horizontal lines. The grey symbols represent the best-fit velocity determined from Gaussian fits to the extracted spectrum at a given position to outline the shape of the two-sided stacked rotation curve before folding both sides together.

five normalized spectral pixels. This is done since wiggles in the resulting $H\alpha$ line profile originating from stacking emission lines with slightly different centroid positions should be smoothed out and to further enhance the S/N of the spectrum since the RMS pixel-to-pixel noise is diminished due to smoothing. Before folding both sides of the pv diagram together, we also derive a rotation curve from the pv diagram, which is indicated as grey symbols in Figure 3.5. We verify that both re-sampling the pv into radial bins of two pixels prior to extraction as well as additional spectral median-filtering do not change the shape and inferred slopes of the outer stacks on a level significant compared to the uncertainties. However, omitting either of these two steps leads to slightly larger uncertainties (up to $\sim 20\%$) in the inferred outer slopes.

We furthermore note that we refrained from including the galaxy Zc406690 in the stacking process due to its ring-like $H\alpha$ morphology, which leads to it strongly dominating the flux in the outer parts of the stack beyond R_{turn}^{meas} . This effect cannot be captured by our normalization of $H\alpha$ surface brightness on the basis of the individual pv diagrams. However, as presented in Figure 3.12 below, the rotation curve of Zc406690 closely resembles our stacked rotation curve and thus is not expected to cause significant changes when included.

The errors in velocity of the stacked RC are derived in the following way. To encompass both sample variance (e.g. different intrinsic shapes of the individual rotation curves of our sample) and statistical pixel-to-pixel RMS in the spectra, a bootstrapping technique is em-

ployed, in which the stacking and fitting is iteratively repeated 300 times, each time drawing a random sample from the original dataset allowing for replacement. At each bootstrap iteration, we perturb each pv by its pixel-to-pixel noise before stacking. The 68 % scatter in the distribution of all bootstrapped iterations is taken as the error in the stacked RC. S The number of galaxies contributing to the averaged pv diagram drops significantly in the outer parts due to the normalization of each pv diagram in radial direction (depending on the size of the FOV relative to the turnover radius) and masking out of pixels affected by noise or OH skyline contamination. We therefore additionally employ a jackknifing technique where we repeat the stacking, each time removing one galaxy from the sample, and verify that the stack in the outer part is not dominated by a single object. We find that this holds for galactocentric radii $\lesssim 2.4R_{turn}$, where the number of contributing galaxies is larger than 10. Also judged by the quality of the respective spectra and gaussian fits, we find the maximum radius at which the stack can be robustly determined is $2.4R_{turn}$.

We note that due to the radial normalization of each individual pv diagram to the same fiducial grid, adjacent radial velocity bins in the final stacked rotation curve are correlated. This effect is caused by galaxies that have individual rotation curves with small R_{turn}^{meas} where the original data is spatially undersampled compared to the fiducial grid of the normalized stacked pv diagram. This effect is not reflected by errorbars of the radial velocity bins of our stacked rotation curve presented below, but the derivation of an outer slope and its uncertainty of our stacked rotation curve via bootstrapping techniques takes the correlation of adjacent bins into account.

3.3.3 Using R_e to calibrate R_{turn}

As discussed in Section 3.3.1, the measurements of R_{turn}^{meas} are based on the assumption of exponential mass distributions and are possibly affected by low S/N in the outer parts of individual rotation curves as well as possibly dominant outer dark matter components. To validate our measured R_{turn}^{meas} , we employ an alternative approach to derive R_{turn} independently of the parametrization and fit of the observed rotation curve, taking into account deviations from exponential profiles.

Thus we aim to convert a measurement of intrinsic baryonic size, R_e , provided by the Sérsic profile parametrization of the rest-frame optical morphology, into an observed turnover radius also using information on the Sérsic index n and inclination (given by the measured axial ratio b/a). The resulting turnover radii are referred to as ' R_{turn}^{morph} ', in contrast to the turnover radii determined from the individual rotation curves (R_{turn}^{meas}).

The theoretical relationship for an infinitely thin disk with a purely exponential mass distribution is : $R_{turn} \simeq 1.15R_e$ (Binney & Tremaine 2008). However, there are additional effects acting on changing the relation between R_{turn}^{morph} and R_e present in our observed rotation curves. These effects include significant beam smearing of the rotation curve due to the limited spatial resolution, deviations from an exponential mass distribution caused by e.g. the presence of stellar bulges, and a finite disk thickness. In order to derive a conversion

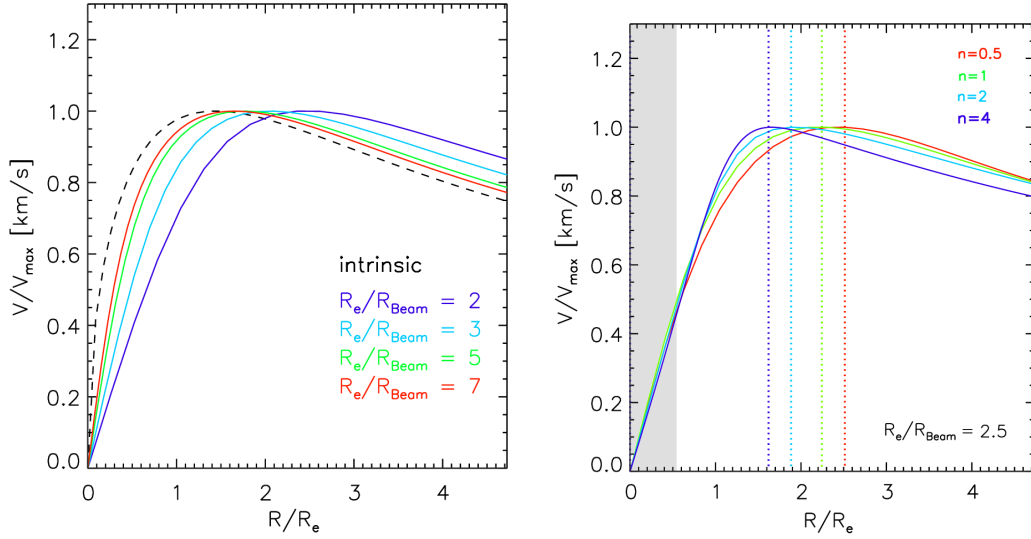


Figure 3.6: Left: Modeled and normalized observed -frame rotation curves with identical galaxy parameters but adopting different beam sizes (i.e. different R_e/R_{beam} ratios, shown as solid colored lines). For comparison, the intrinsic model without applied beam smearing is shown as dashed black line. Right: Same modeled curves with $R_e/R_{\text{beam}} = 2.5$ adopting different Sérsic indices shown as colored lines. The dotted vertical lines indicate the peak position of the respective rotation curve, and the grey shaded area marks the effective size of the spatial PSF (R_{beam}) used to convolve the modeled curves for $R_e/R_{\text{beam}} = 2.5$.

between a given $R_{\text{turn}}^{\text{morph}}$ and the R_e that can be applied to our sample, we use rotation curves of simulated galaxies. We construct noise-free mock data cubes using the DYSMAL code (Davies et al. 2011) with a range of Sérsic indices, sizes and inclinations. This methodology is similar to the one used for beam smearing corrections discussed in Chapter 4 of this thesis. We refer the reader to Chapter 4 for a more thorough description of the DYSMAL code. Within the modeling, we consider a finite thickness of the disk with $q = 0.2$, using the recipe in Noordermeer (2008) to calculate the corresponding rotation curves in DYSMAL. For each model rotation curve, we measure $R_{\text{turn}}^{\text{morph}}$ as the peak position of the rotation curve to compute the ratio $R_{\text{turn}}^{\text{morph}}/R_e$.

In Figure 3.6 we show a few examples of modeled rotation curves. The left panel displays normalized rotation curves all derived from identical galaxy parameters but with increasing beam size, along with an intrinsic curve with no beam smearing applied. The effect of increasing beam size (quoted as the effective half-light size ' R_{beam} ') at fixed effective radius of the modeled galaxy (thus decreasing R_e/R_{beam}) is reflected in a shift of turnover radius outwards with respect to the intrinsic case. In the right panel of Figure 3.6, simulated rotation curves are shown where the Sérsic index is varied. Evidently, the observed peak of velocity is shifted significantly inwards when increasing the Sérsic index due to a more centrally concentrated mass distribution.

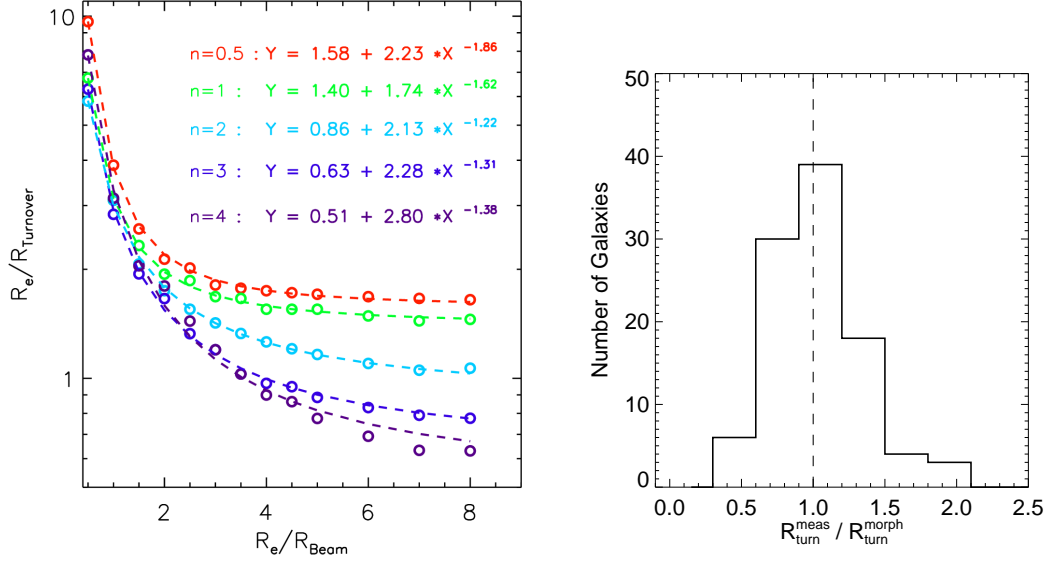


Figure 3.7: Left: The ratio between the $R_{\text{turn}}^{\text{morph}}$ and intrinsic effective radius R_e as a function of R_e/R_{beam} derived from modeled mock galaxies. The points are color-coded by Sérsic index. The fits are shown as dashed lines, and their parameterizations are also shown. Right: Distribution of calibrated versus observed turnover radii of the stacked galaxy sample. The dashed line indicates a ratio of 1.

$R_{\text{turn}}^{\text{morph}}/R_e$ shows a dependence on the intrinsic galaxy size compared to the size of the beam (R_e/R_{beam}) and the Sérsic index, but very little on inclination. The left panel in Figure 3.7 illustrates these dependencies by showing the ratio $R_{\text{turn}}^{\text{morph}}/R_e$ as a function of R_e/R_{beam} , plotted for different adopted Sérsic indices in different colors. The adopted inclination is 60 degrees. As expected, $R_{\text{turn}}^{\text{morph}}/R_e$ is strongly anti-correlated with R_e/R_{beam} since more severe beam smearing will shift the peak velocity of a rotation curve out to larger radii. In order to implement this conversion from R_e to $R_{\text{turn}}^{\text{morph}}$ for our sample, we derive conversion factors based on our grid of models, which are then applied on a galaxy-to-galaxy basis. For this purpose, we derive fits to $R_{\text{turn}}^{\text{morph}}/R_e$ as a function of R_e/R_{beam} , Sérsic index, and inclination. The ratio between $R_{\text{turn}}^{\text{morph}}$ and $R_{\text{turn}}^{\text{meas}}$ for our sample galaxies is displayed in the right panel in Figure 3.7. Overall, the data show good correspondence between $R_{\text{turn}}^{\text{morph}}$ and $R_{\text{turn}}^{\text{meas}}$ with a mean (median) ratio between $R_{\text{turn}}^{\text{meas}}$ and $R_{\text{turn}}^{\text{morph}}$ of 1.05 (1.02). The scatter in the distribution is ~ 0.35 and stems likely from uncertainties in the determination of n , a/b , and R_e from fits to the H -band light profiles as well as uncertainties in the measurement of $R_{\text{turn}}^{\text{meas}}$.

3.3.4 Sample properties at different radii

Due to the pv normalization in radial direction and the masking of pixels affected by noise or OH skyline contamination, each normalized pv diagram extends to a different radius

(relative to the normalized turnover radius) depending on the position of the turnover radius relative to the size of the FOV. This translates into a dropping number of galaxies that contribute to the final stack with increasing distance from the central position. We count a galaxy as contributing to our folded stack at a given position if at least one side of its pv diagram extends to the respective galactocentric radius. The masking of contaminating noisy pixels before stacking causes the effective number of galaxies that are averaged into our stack to be lower than the total number of galaxies in our sample, and is depending mostly on wavelength. We include this effect in the Figures displaying the 'effective number of galaxies' contributing as a function of radius in the next sections by only counting galaxies where more than 50 percent of the spectrum is not masked out within the wavelength region we use to constrain the gaussian fits to derive the velocity measurements on the stack.

Next, we explore whether there are biases in average galaxy parameters (potentially connected to the outer dark matter contribution) with increasing radius. We split our entire galaxy sample into different groups depending on the maximum radius they are contributing to and examine their location in the $SFR - M_*$ and $R_e - M_*$, which is illustrated in Figure 3.8. Galaxies that contribute to radii $r > 0$, $> 1.5 R_{turn}^{meas}$ and $r > 2 R_{turn}^{meas}$ are color-coded in red, green and blue, respectively. The panels display the $SFR - M_*$ and $R_e - M_*$ planes and are split into redshift ranges of $0.7 < z < 1.2$ and $1.2 < z < 2.6$. The different groups are plotted over the grey points which are the underlying 3D-HST population at the respective redshift. In addition to the colored points representing the sample galaxies, the underlying colored lines represent the running medians. Note that in Figure 3.8, galaxies contributing to radii $r > 0$ are represented by the combined green, red and blue symbols. Similarly, galaxies contributing to radii $r > 1.5 R_{turn}^{meas}$ are represented by the combined green and blue symbols. Thus, the running medians shown as the red solid lines, are computed using all colored symbols, and the green solid lines take into account green and blue symbols. The solid lines in the $SFR - M_*$ planes represent the broken power law parametrization of the main sequence from Whitaker (2014), the lines in the $R_e - M_*$ planes come from the H -band measurements from van der Wel et al. (2014a) for late-type galaxies.

Considering the $SFR - M_*$ plane, galaxies that contribute to the middle and outer regions of the stack still cover homogeneously the main sequence over the entire redshift range. As indicated by the underlying colored lines representing the running median for the respective groups, the median SFR at a given stellar mass shows good overlap among the different subsets of our sample with respect to the full sample within the scatter. At $z < 1.2$, the median SFRs of the blue points are offset by $\sim 0.2 - 0.3$ dex with respect to the full stacking sample, which is, however, smaller than the scatter among the blue points (~ 0.4 dex). Furthermore, the position of the blue points seems to indicate slightly higher median SFRs of galaxies contributing to the outermost radii of our stack compared to the full stacking sample at $z > 1.2$. The largest offset between the blue running median and the full sample at $\log(M_*) \sim 10.4$ is ~ 0.4 dex, comparable to the 1σ scatter among the points. However, we conclude that galaxies probing the middle and outer parts of the stack are still representative of the MS population over our entire redshift range.

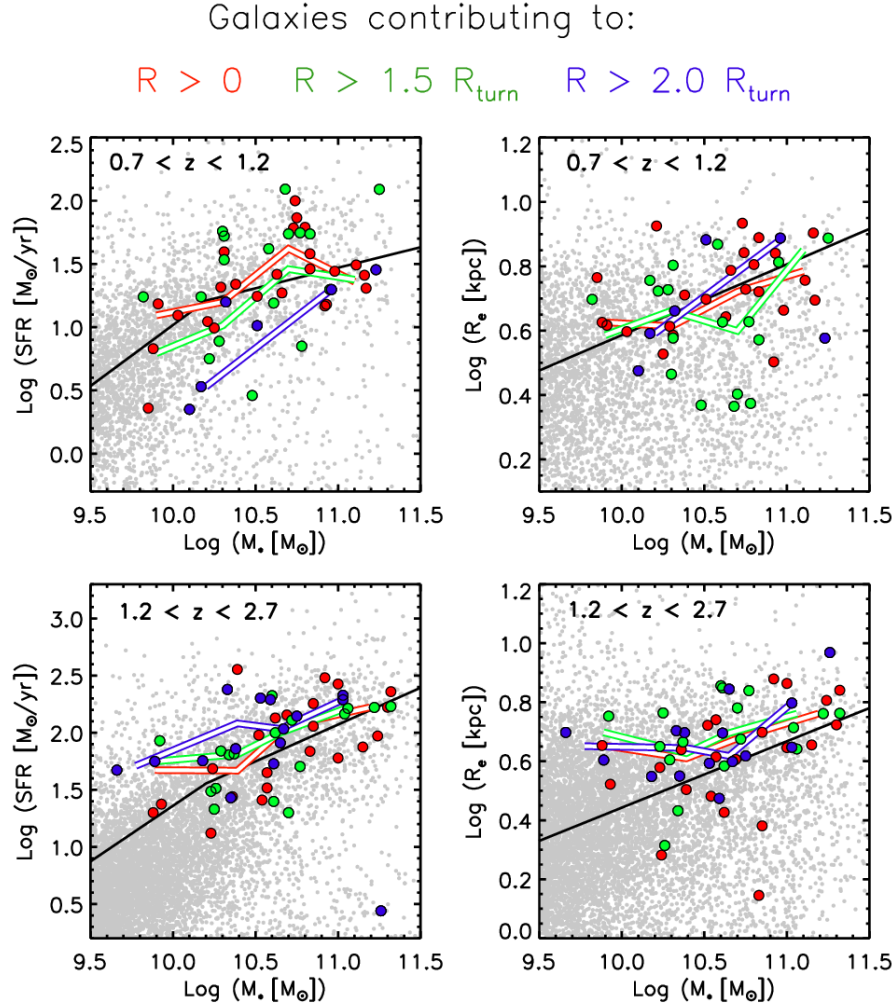


Figure 3.8: Properties of the stacked galaxy sample in the $SFR - M_*$ plane (left) and $R_e - M_*$ plane (right). In each panel, the colored symbols represent galaxies that contribute to the stack at all radii, and galaxies contributing out to radii $> 1.5 R_{\text{turn}}^{\text{meas}}$ and $> 2 R_{\text{turn}}^{\text{meas}}$ are overplotted in green and blue, respectively. Galaxies thus contributing to radii > 0 are represented by the combined green, red and blue symbols. Similarly, galaxies contributing to radii $> 1.5 R_{\text{turn}}^{\text{meas}}$ are represented by the combined green and blue symbols. Running medians shown as the red solid lines are computed using all colored symbols, the green solid lines show the running medians for the green and blue symbols, and the blue lines represent the running median for the blue symbols. The top panels show the sample at $0.7 < z < 1.2$ and the bottom panels show the one at $1.2 < z < 2.5$, with grey points showing the 3D-HST background population. The black solid lines in the left panels represent the broken-power law parametrization of the main sequence by Whitaker et al. (2014) for the corresponding redshifts. The solid lines in the right panels represent the size-mass relation of late-type galaxies derived from van der Wel et al. (2014a).

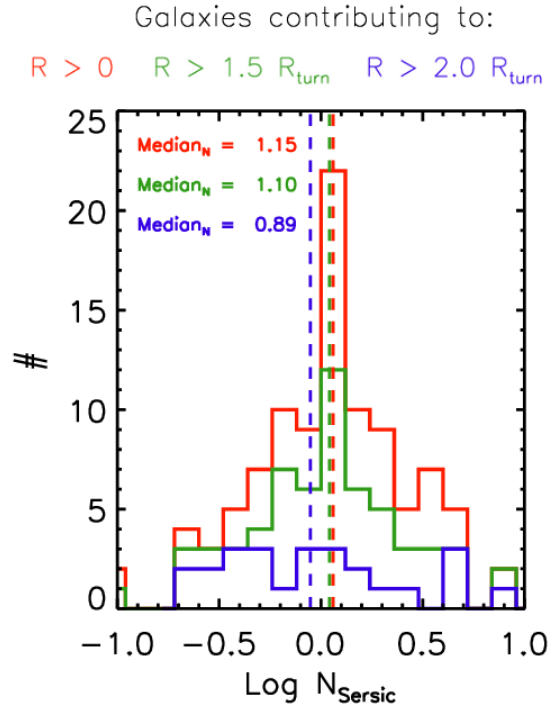


Figure 3.9: Distribution of H -band Sérsic indices. In each panel, the colored histograms represent galaxies that contribute to the stack at all radii (red), at radii $> 1.5 R_{\text{turn}}^{\text{meas}}$ (green) and $> 2 R_{\text{turn}}^{\text{meas}}$ (blue).

Turning to the size distributions shown in the right panels, we also find good overlap among galaxies contributing to the middle and outer parts of the stack compared to entire stacking sample. The size distributions of galaxies among the different subsets in the high redshift regime show a good overlap. The elevated average size of our stacking sample compared to the underlying 3D-HST distribution of star-forming galaxies is discussed in Section 3.2. The distribution of measured Sérsic indices for galaxies displayed in Figure 3.9 at all radii is in a good agreement with the baryonic distribution being exponential at all radii in the stack.

3.3.5 Potential biases due to sample selection and normalization

In this subsection, we will explore how the selection of galaxies for the stacking sample as well as the normalization of individual RCs with an exponential disk model could potentially affect the results on our stacked rotation curve presented in the next Section. In summary, we will address the following two questions:

1. Does the selection of galaxies for stacking according to Criterion 2 (discussed in Section 3.2.3) bias our stacking sample towards galaxies with outer *falling* rotation curves

as might be expected for DM-poor galaxies?

2. Under the assumption that the average outer rotation curves of massive SFGs at high redshift were *rising* as expected for DM-dominated galaxies, could the resulting *positive* outer slope be recovered by our stacking technique?

Question 1 is important since Criterion 2 discussed in Section 3.2.3 removes a large portion of targets from the available pool of rotating disks in the KMOS^{3D} and SINS/zC-SINF datasets. In particular, we require individual RCs to show a sufficient change of slope, which is indeed expected for baryonic disks, and still so for DM-poor galaxies. However, outer RCs of DM-dominated galaxies with outer rising profiles may exhibit much less of outer flattening and therefore may be rejected more frequently, leading to a potential bias towards low dark matter fractions in our stacking sample. In Section 3.2.3, we already demonstrated that the stacking sample shows little to no bias in the average galaxy properties such as stellar mass, SFR, $\Delta(\text{MS})$, and Sérsic index compared to the full KMOS^{3D} plus SINS/zC-SINF AO sample (with exception for larger R_e in our stacking sample). However, there might exist additional galaxy properties connected to the dark matter fraction or the outer slope of RCs that are not examined here.

We raise Question 2 since the pure exponential disk model (without the contribution of dark matter) used to normalize our individual RCs provides a good description for *inner* rotation curves until R_{turn} , but does not reflect the outer *rising* RCs for galaxies with significant DM components and thus potentially fails to recover rising outer slopes in our normalized stack.

We base the method to approach the above questions on simulated 1D rotation curves that include a rotating exponential baryonic disk and an added dark matter NFW halo for a range of sizes, masses and dark matter fractions. The simulated rotation curves are derived analytically assuming axisymmetry, identical to the method presented in Section 3.4.3. For the combined disk+halo mock-RCs, we vary the effective size of the disk, R_e , and the disk-to-dark matter halo mass fraction inside the halo, m_d . Pressure support and adiabatic contraction are neglected. Mock-RCs are created for a grid of R_e ranging from 2 to 5 kpc, and for m_d in the range of 1 (no dark matter) to 0.01 (strongly dark matter dominated), setting the baryonic disk mass to the average of our stacking sample.

At each given grid point $[R_e, m_d]$ we create 25 observed-frame realizations of the rotation curve by applying a random inclination (i.e. scaling the RC by $\sin i$) and perturbation by typical uncertainties in velocity. Furthermore, each realization is cut at a maximum galactocentric radius, R_{obs} (simulating that individual *observed* RCs are traceable to a limiting radius) and the Sérsic index n of the disk is varied. The values of R_{obs} , n , and the typical uncertainty in velocity for each realization are determined by randomly drawing from gaussian distributions. The mean and scatter of those distributions are determined from the observed sample of detected and resolved KMOS^{3D} and SINS/zC-SINF galaxies. Then, each observed-frame rotation curve realization is convolved with a 1D Gaussian PSF of

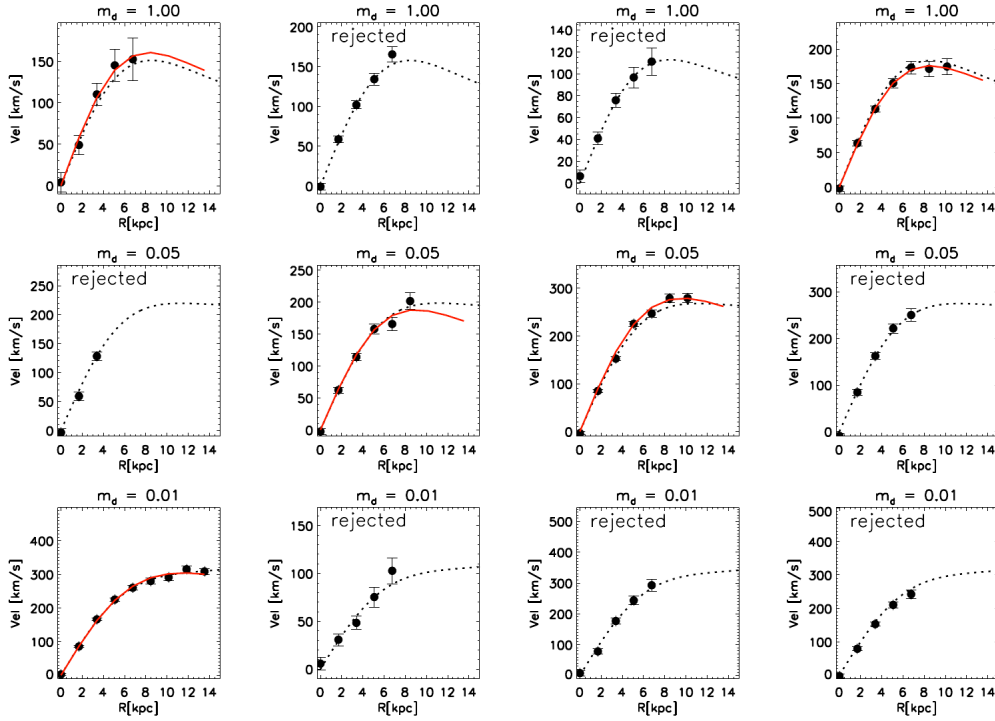


Figure 3.10: Simulated observed-frame and corresponding noise-free mock rotation curves, shown as circles and dashed lines, respectively. The different row plot models with decreasing m_d from 1 to 0.01. The four columns present different observed-frame realizations of the same rotation curve. The adopted R_e for all models shown is 2 kpc. Fitted exponential disk models are overplotted in red, in case the respective realization did not get rejected.

FWHM typical for our dataset, and the RC is sampled according to the pixel scale provided by the observed datacubes.

Then, we fit each of the simulated observed-frame RC-realizations with an exponential disk model as done with the real data, and we also apply the same selection (i.e. Criterion 2) to include galaxies for stacking or not. After selection, we average the noise-free theoretical RCs at a given $[R_e, m_d]$ according to their normalization, accounting for the typical FOV limitations in our data. Finally, we measure the outer slope on this average for a given $[R_e, m_d]$ within similar radii as done for the stacked rotation curve discussed in Section 3.4.1.

Figure 3.10 plots a few observed-frame mock-RC examples, showing four realizations for different adopted m_d , with an indication of whether a RC has gotten rejected or not. As apparent from Figure 3.10, the outer slope of a simulated RC strongly correlates with m_d . In cases of strong dark matter dominance ($m_d = 0.01$), a significant outer flattening is still present in the outer observed mock-RC (in cases where R_{obs} is sufficiently large), which can be reasonably well recovered by the exponential disk model shown in red. We also ascertain

that the decision on whether to reject an observed mock-RC in our analysis here is mainly driven by the radius out to which it is traceable (i.e. R_{obs}).

To approach the above Question 1 we first examine the fraction of observed-frame mock-RCs we selected for stacking as a function of m_d , displayed in the left panel of Figure 3.11. Overall, the fraction of selected galaxies over the entire range of m_d is $\sim 40 - 60\%$ and shows a mild trend with m_d as indicated by the dotted line. The fraction of galaxies selected for stacking from the KMOS^{3D} and SINS/zC-SINF samples presented in Section 3.2.3, are in good agreement with the numbers found here. Since we found that the variation of R_{obs} in the mock-RC realizations is the dominating factor for determining whether a galaxy gets rejected or not, we conclude that the main effect setting the selected fraction of galaxies for stacking out of the full KMOS^{3D} plus SINS/zC-SINF sample is the S/N level (setting R_{obs}) and its variation among the data. However, as revealed by our analysis here, a trend of the selection fraction and m_d remains, implying that dark matter poor galaxies will be preferentially selected. To test the effect arising from this trend on our results, we do the following exercise:

First we consider a large sample of galaxies with an underlying log-normal distribution of m_d with 0.4 dex scatter and apply the selection function shown in the left panel of Figure 3.11 to the distribution of m_d . Then we determine the resulting average m_d by again randomly drawing from the distribution. We find that the resulting bias in m_d is small, such that the selection function in Figure 3.11 changes the average m_d by $\sim 10\%$ at most over the entire range of m_d values tested. Albeit this test is very simplified, it indicates that even when rejecting a large number of galaxies when selecting for stacking, this does not bias the average m_d of galaxies in the selected sample significantly.

Next, we turn to answering the above Question 2 by examining the outer slopes measured on our simulated mock rotation curves. The right panel of Figure 3.11 displays the recovered outer slopes determined from the selected, normalized and averaged mock-RCs in the full grid of $[R_e, m_d]$, shown as circles. In addition, the outer slopes determined from the noise-free rotation curves with a given $[R_e, m_d]$ are shown as dashed lines (i.e. which have *not* been perturbed by noise, normalized, selected, and averaged). All slopes are shown in units of observed normalized coordinates V/V_{max} and R/R_{turn} , in analogy to the analysis of our results in Chapter 3.4. As expected, the theoretical outer slope of the mock-RCs is a strong function of m_d . It is negative for pure baryonic disks and gets positive for DM-dominated galaxies ($m_d < 0.04$). The method of selection, normalizing and averaging our mock-RCs can reproduce those outer slopes even in the regime of rising rotation curves. This shows that the stacking process is able to reproduce rising rotation curves in case our typical high- z SFG would be dark matter dominated. The differences between the theoretical and recovered values are small, considering the uncertainty in the normalized slope of our stack ($\sim 0.1[V/V_{max}, R/R_{turn}]$). Since the dashed lines consider all 25 realizations for a given $[R_e, m_d]$, the difference between the circles and the dashed lines also encompasses

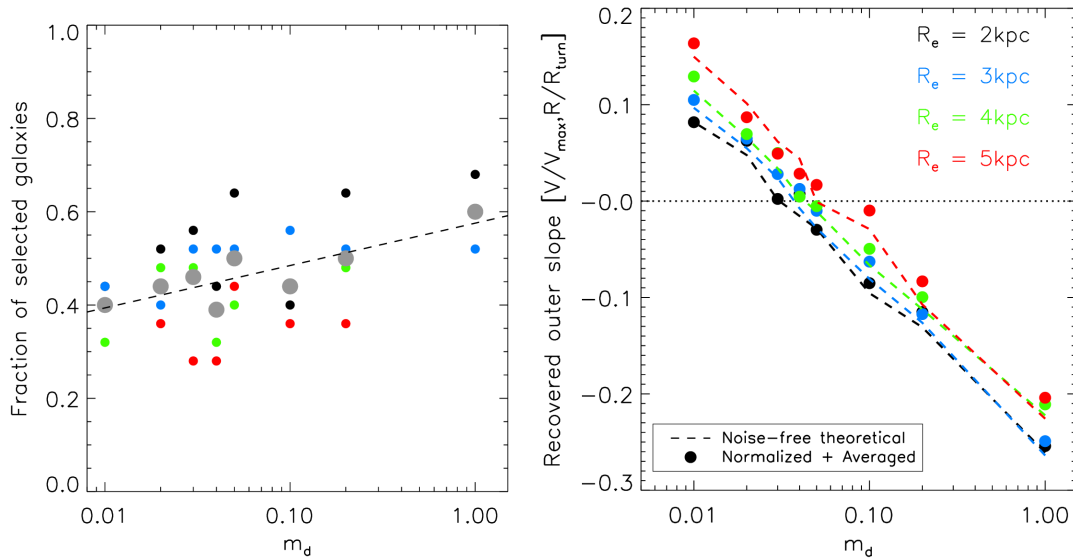


Figure 3.11: Left: Fraction of non-rejected mock RCs selected for stacking as a function of m_d . The colored symbols plot values for different adopted R_e , while the grey circles represent the average over all R_e for a given m_d . The dashed line indicates the linear fit to all grey circles. Right: Recovered outer slopes obtained from the noise-free RCs (dashed lines) as well as from the selected, normalized, and averaged mock-RCs (colored symbols). The slopes are shown in units of our normalized coordinate frame $[V/V_{max}, R/R_{turn}]$, in analogy to the results presented in Section 3.4.

the bias in slope due to selection of galaxies discussed above, further substantiating that this bias is small.

To investigate in possible mass dependencies, we repeat our entire analysis changing the baryonic mass of the disk by ± 0.5 dex and find that this does not influence our conclusion made here. In particular, we find that the overall selection fractions vary by $\sim 10\%$ at most. When decreasing the total mass, the scatter of the recovered slopes from averaging our mock-RCs with respect to their theoretical value slightly increases to at most $\sim 0.03[V/V_{max}, R/R_{turn}]$. This can most be likely attributed to larger *relative* uncertainties in the observed-frame mock-RCs for lower-mass systems.

Albeit the analysis presented here is solely based on 1D-profiles and thus provides only a simplified view on our full stacking methodology, it outlines the robustness of our stacking technique and sample selection. Regarding the above Question 1, our analysis revealed that the selection of our stacking sample out of the full KMOS^{3D} plus SINS/zC-SINF sample is unlikely to cause significant biases in m_d . We find that the selection of galaxies for our stacking is mostly driven by the radius out to which individual RCs can be constrained, i.e.

given by the available S/N ratio for a given galaxy.

Concerning Question 2, we can show that our stacking technique is, in the context of our mock-simulations here, able to recover a wide range of expected outer slopes. Although the model we use to normalize individual RCs intrinsically falls-off in rotation velocity after the turn-over, we are still able to reproduce *positive* outer slopes in our stack in case massive SFGs at high redshift are genuinely more dark matter dominated.

3.4 Results

In this section, we will present the shape of the resulting stacked rotation curve, followed by a comparison with models and discussion.

3.4.1 Shape of the stacked rotation curve

Figure 3.12 displays the best-fit velocity measurements on the stacked and folded pv diagram plotted as black symbols, shown in the normalized coordinate frame of observed units $[V/V_{max}, R/R_{turn}]$. The uncertainties on the stack indicated by the vertical errorbars are derived using the aforementioned bootstrapping technique. Note that the errorbars do not take into account the correlation between adjacent radial bins. The number of galaxies that contribute to each velocity bin of the stack is indicated in the lower panel of Figure 3.12. In addition, we show in Figure 3.13 the spectra that are used for the velocity measurements for all radial positions shown in Figure 3.12. The actual data is plotted in cyan, and the respective gaussian fit is overplotted in red. The solid and dashed vertical lines denote the wavelength corresponding to a velocity V/V_{max} of 0 and 1, respectively.

Despite the rapidly dropping number of galaxies contributing to the stack beyond the turnover radius, we are able to robustly constrain our stacked rotation curve out to $\sim 2.4R_{turn}$, corresponding roughly to several effective radii in intrinsic size. The stacked rotation curve shows an inner rising part and peaks at a position in agreement with the normalization. Beyond the turnover, the velocity decreases monotonically down to $\sim 0.65V_{max}$ at $\sim 2.4R_{turn}$. The last velocity measurement shown in Figure 3.12 still contains enough galaxies to determine a representative average as discussed in the previous section. The behavior of dropping rotation curves at this level could only be seen on the level of individual rotation curves for our highest S/N galaxies from the deep SINFONI + AO integrations, which are indicated as the colored lines in Figure 3.12. By employing our stacking approach, we are able to confirm the drop of rotation velocity beyond $\sim 2R_{turn}$ and show that this is a coherent behavior at least for a subsample of ~ 25 galaxies that effectively contribute to the stack out to these radii.

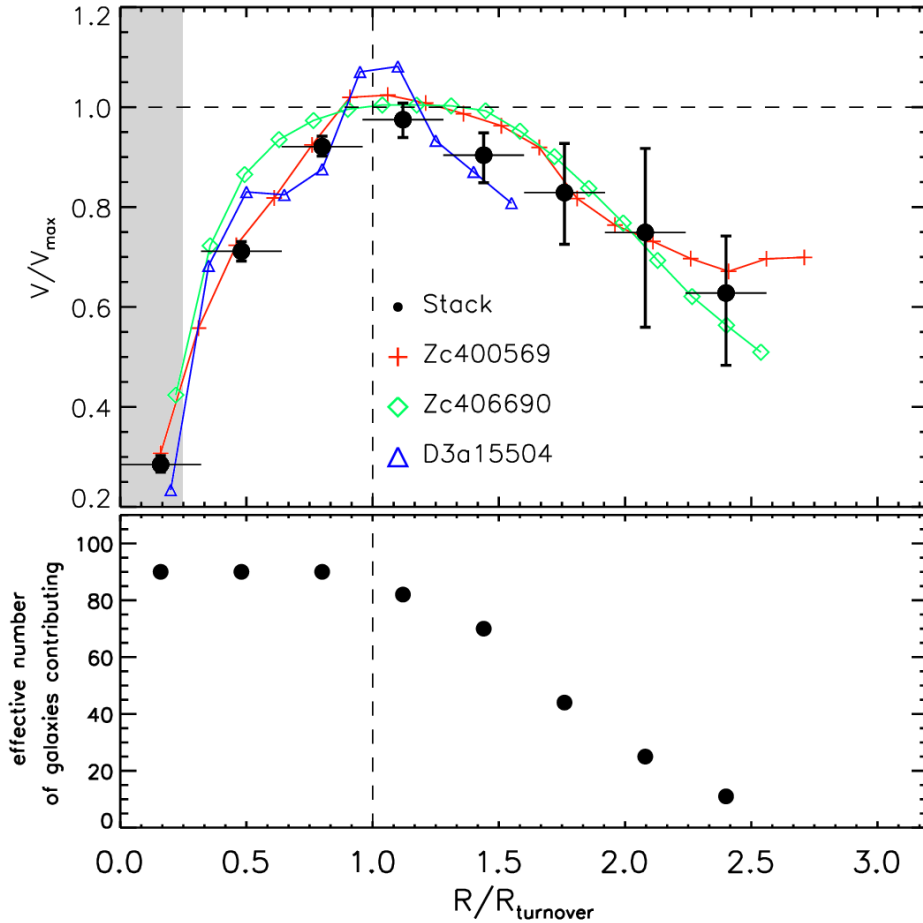


Figure 3.12: Top: Stacked rotation curve (black dots) plotted in units of observed normalized velocity (V/V_{max}) and observed normalized radius ($R/R_{turnover}$). The errors are derived from bootstrapping and include both sample variance as well as RMS noise in the spectra. Overplotted are individual normalized rotation curves for our highest S/N galaxies. The shaded area marks the half-light beam size of the average PSF observed for our sample. The stack as well as individual galaxies show a decrease beyond the turnover. Bottom: Effective number of galaxies contributing to the stack, accounting for masking out noisy pixels in the pv diagrams. The decrease in the number of contributing galaxies with increasing radius is driven by FOV limitations.

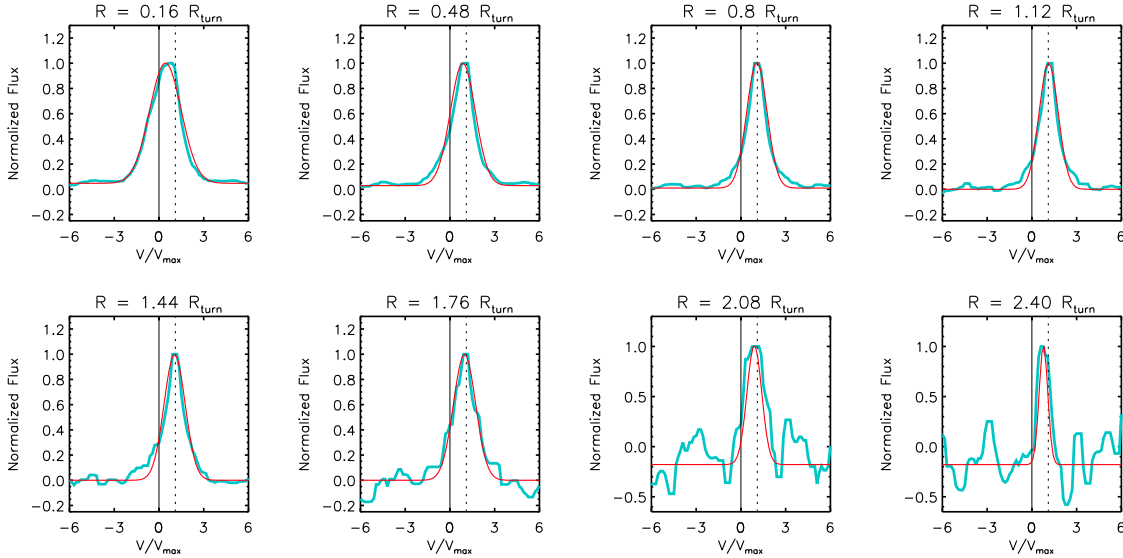


Figure 3.13: Spectra (cyan) and gaussian fits (red) of the stack in normalized units of flux and velocity for the different radial bins shown in Figure 3.12. The solid and dashed line represent a V/V_{max} of 0 and 1, respectively.

In order to evaluate the significance of the drop in velocity beyond R_{turn} and to quantify the shape of our outer stacked rotation curve we derive a linear slope fitting the five outer velocity bins of the stack weighted by their respective errors. Our approach is also motivated by studies of extended local rotation curves which have used measurements of linear slopes on outer local rotation curves (e.g. Vogt et al. 2004), also by rotation curve parameterizations by the ‘Polyex model’ (Giovanelli & Haynes 2002; see also Catinella et al. 2006), in which the outer rotation curve is approximated with a linear function. The method of parameterizing the outer shape of our rotation curve has as well the advantage that the correlation between the different radial bins in Figure 3.12 can be taken into account when computing uncertainties by employing bootstrapping techniques.

We derive an outer slope of $\Delta V/\Delta R = -0.25_{-0.11}^{+0.10}$, where the quantities ΔV and ΔR are computed in units of normalized coordinates V/V_{max} and R/R_{turn} , respectively. In the remainder of this Chapter, we quote all outer slopes $\Delta V/\Delta R$ in this normalized unit, which we refer to as ‘ $[V/V_{max}, R/R_{turn}]$ ’. The uncertainty represents the scatter of slopes determined from the bootstrapping technique discussed in Section 3.3, and accounts for possible correlations among radial bins. We find that these uncertainties are roughly to equal extent driven by statistical RMS noise in the stacked spectra and by the sample variance.

The quoted outer slopes of our stacked rotation curve are affected by the spatial beam smearing of our observed data, which complicates an appropriate quantitative comparison to local rotation curves (where beam smearing is less severe). We compute expected outer slopes from simple axisymmetric models (including a thin exponential Freeman disk model

and a Keplerian fall-off) that take into account spatial convolution with a gaussian PSF of FWHM similar to our data, as well as the radial range sampled by our data, facilitating an appropriate comparison of expected slopes. We find that the slope a pure baryonic disk as approximated by a Freeman model, as well as a Keplerian fall-off assuming a point-like central mass distribution predict $\Delta V/\Delta R \sim -0.24 [V/V_{max}, R/R_{turn}]$. This slope is strikingly similar to the outer slope of our stacked rotation curve and thus demonstrates that our average rotation curve for massive SFGs at high redshift is well represented by a pure baryonic exponential disk, with only a weak or no imprint of an additional dark matter component within the radial range probed here. However, there are additional mechanisms such as pressure support to the outer disks which need to be considered, and which are discussed together with a more detailed comparison of our stacked rotation curve to modeled rotation curves including baryons and dark matter in the remainder of this Chapter.

As discussed in the previous section, we repeat our stacking process using R_{turn}^{morph} for each galaxy in our sample as represented in Section 3.3.3. The resulting stacked rotation curve is displayed in Figure 3.14 as red symbols and compared to the stack as presented in Figure 3.12 as black symbols. As apparent in the Figure 3.14, both stacks show a turnover at the same location, which is expected from the good overall concordance between R_{turn}^{meas} and R_{turn}^{morph} as presented in Figure 3.7. However, the distribution of R_{turn}^{morph}/R_e exhibits considerable scatter, which is potentially imprinted as larger uncertainties in the R_{turn}^{morph} -normalized stacked rotation curve. Also, the number of galaxies as a function of radius is lower at $r > 1.5 \cdot R_{turn}$, which likely contributes to the larger uncertainties of outer bins of the velocity curve due to a lower signal. The outermost bin at $r = 2.4 R_{turn}$ is not plotted for the R_{turn}^{morph} -normalized stack since only few (< 10) galaxies contribute hampering a representative velocity measurement at this radius. Despite the larger uncertainties of the R_{turn}^{morph} -normalized stack, we measure an outer slope of $\Delta V/\Delta R = -0.27_{-0.18}^{+0.15} [V/V_{max}, R/R_{turn}]$, consistent with the outer slope of our nominal stack in Figure 3.12 within the uncertainties. In the remainder of this chapter, we will adopt the stacked rotation curve presented in Figure 3.12 as the fiducial rotation curve, which we will compare to models.

In this section we have shown that our stacking approach can for the first time constrain an extended representative rotation curve reaching out to $\sim 2.4 R_{turn}$. We observe a rapid fall-off in our stack with a negative outer slope of $\Delta V/\Delta R = -0.25_{-0.11}^{+0.10} [V/V_{max}, R/R_{turn}]$. By applying the alternative calibration of the turn-over radii using R_{turn}^{morph} determined from the size measurements on rest-frame optical HST imaging, we obtain a stack that shows similar behavior with a consistent (negative) outer slope, albeit with larger uncertainties.

The following Section 3.4.2 presents a first comparison of our stack to rotation curves expected for local disk galaxies of similar mass. In Section 3.4.3, we will make a more detailed comparison of our stack with expected rotation curves calculated from combined

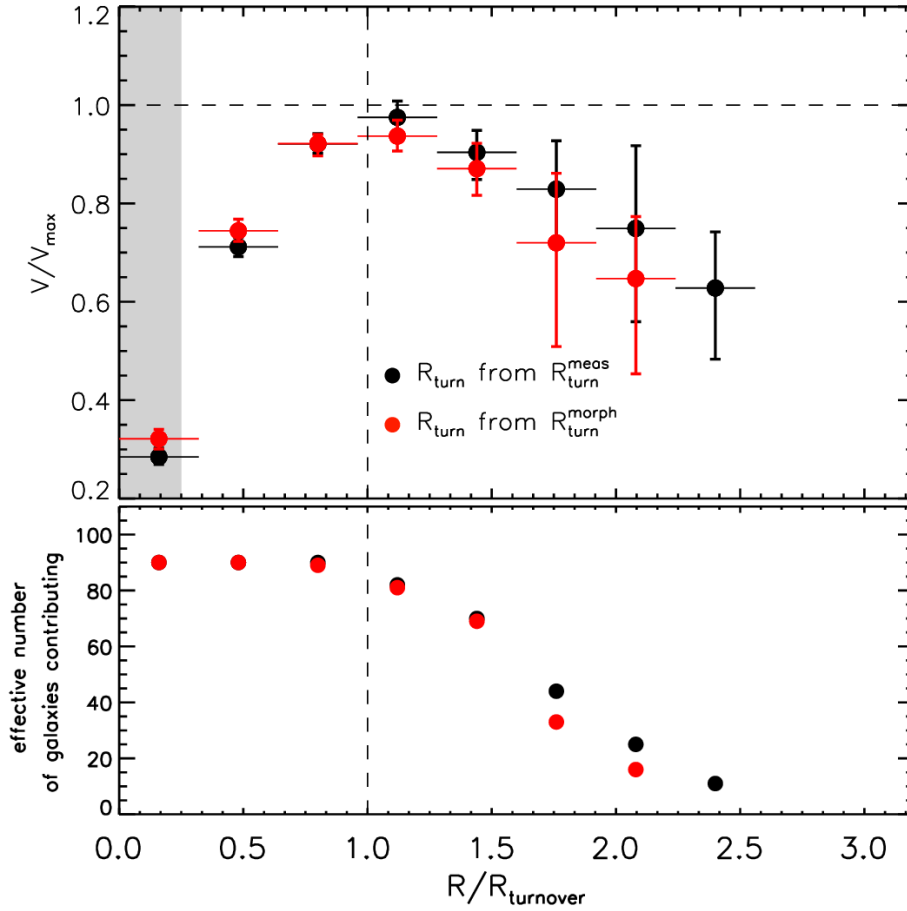


Figure 3.14: Stacked rotation shown in Figure 3.12 (black symbols) together with an alternative stacked rotation curve derived using $R_{\text{turn}}^{\text{morph}}$ derived from R_e (red symbols). The shaded area marks the half-light beam size of the average PSF observed for our sample.

baryonic and dark matter components to interpret our findings in view of relative baryonic fractions of massive high- z SFGs. Section 3.4.4 expands this comparison to models including the effect of pressure support to the outer disk as a consequence of elevated velocity dispersions observed in star-forming galaxies at high redshift. Next, we examine the possible effect of adiabatic contraction of the halo as a response to the disk potential and discuss the resulting imprint on our models in Section 3.4.5. This is followed in Section 3.4.6 by an analysis of how the modeled rotation curves change when challenging the assumption on exponential disks, considering scenarios of combined central bulge and disk profiles. Finally, we test our results against variations in the assumed concentration parameter outlined in Section 3.4.7.

3.4.2 Comparison to local rotation curves

The measurement of an outer slope (and its uncertainty) of our stacked rotation curve also allows a first quantitative comparison to local rotation curves and to judge the significance of the observed outer fall-off. As a basis, we use the compilation of template rotation curves from Catinella et al. (2006), who determined averaged rotation curves of a large sample of ~ 2200 low-redshift disks, based on long-slit $H\alpha$ observations. Their template averages are parameterized in bins of absolute I -band magnitude and are sampled at galactocentric radii comparable to our stack. To conduct an appropriate comparison with our stacked rotation curve, we perform the following exercise:

First, we create low- z template RCs as a function of R/r_d for each bin in absolute I -band magnitude using the Polyex parametrization as found in Table 1 in Catinella et al. (2006). Those are shown in the left panel of Figure 3.15, color-coded by absolute I -band magnitude. We convolve each RC with the a gaussian beam of FWHM representative for our sample to bring the low- z template RCs to the same spatial resolution as our stacked RC, since the template RCs in Catinella et al. (2006) are well resolved (i.e with a ratio of spatial beam size to angular size of r_d at least a few times higher than our data). The smeared rotation curves are converted into same frame of observed normalized coordinates $[V/V_{max}, R/R_{turn}]$. Since no peak (i.e. turnover) in the template rotation curves is observed as those are all rising monotonically, we estimate the observed turnover radius as expected from a pure baryonic disk on the same intrinsic spatial scale (peaking intrinsically at $2.15 r_d$), where the same beam smearing has been applied. Finally, we determine the linear outer slope on the convolved, normalized template rotation curves at galactocentric radii out to $\sim 2.4R_{turn}$ as in the case of our stack. The convolved and normalized template rotation curves are presented in right panel of Figure 3.15, plotted in the same fiducial coordinate frame as our stacked presented in Figure 3.12. The linear outer slopes are indicated as dashed lines. Depending on absolute I -band magnitude, we find positive outer slopes ranging from $\Delta V/\Delta R = 0.075$ to $\Delta V/\Delta R = 0.342$, quoted in units of normalized coordinates $[V/V_{max}, R/R_{turn}]$.

To choose an appropriate comparison template corresponding to a massive disk with the baryonic mass equal to our stacked sample ($\log M_{baryonic} = 10.96$), we compute the expected I -band magnitude for such a disk at low-redshift. Assuming a $(M_*/L)_I \sim 1$, based on population synthesis models from Bell & de Jong (2001) and average galaxy colors of disks ($B-V \sim 0.5$, e.g. Buta et al. 1994), we find that the average template rotation curve of $Mag_I = -23.4$ yields a good low- z comparison case to our data at the same *baryonic* mass. The measured outer slope for the corresponding normalized template RC gives a positive value of $\Delta V/\Delta R = 0.062 [V/V_{max}, R/R_{turn}]$. This value deviates from our *falling* stacked rotation curve on a $\sim 3.3\sigma$ level. If we select a low- z template rotation curve corresponding to a disk with the same *stellar* mass as our stack ($\log M_* = 10.61$), we would choose the $Mag_I \sim -22.6$ bin, yielding an outer slope of $\Delta V/\Delta R = 0.098 [V/V_{max}, R/R_{turn}]$. This would give a larger difference to our stacked, on a $\sim 3.7\sigma$ level.

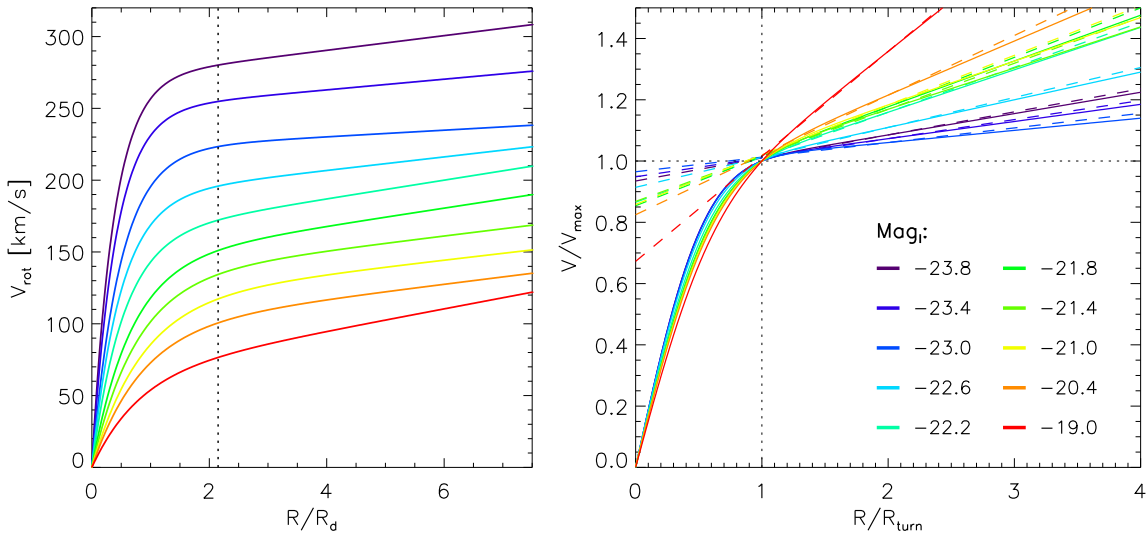


Figure 3.15: Low redshift template rotation curves from Catinella et al. (2006) in different bins of absolute I -band magnitude. The left panel plots the rotation curves in units of disk scale lengths r_d using the Polyex parameterization coefficients from Table 1 in Catinella et al. (2006). The right panel shows the same rotation curves which have been beam smeared and normalized in radius and velocity, plotted in the same normalized coordinate frame as Figure 3.12. Fitted outer slopes are overplotted as dashed lines for each I -band magnitude bin.

In summary, this comparison shows that rotation curves representative for local analogues to our massive disks at high redshift show an outer rising profile in comparison to our dropping rotation curve. Choosing an appropriate template RC for local disks at a baryonic mass similar to our sample, we find that the outer slope of our stack deviates from the one of local rotation curves least on a $\sim 3.3\sigma$ level given the uncertainties in our data.

3.4.3 Comparison to baryonic plus dark matter rotation curves

In this section, we will compare our stacked RC with models including the contribution from baryons plus dark matter to constrain their relative contribution in the outer disk. In order to compare our stacked RC with models, we simulate a rotating baryonic disk embedded in a DM halo. For this purpose, we assume the form of the baryonic distribution to be an exponential disk with a thickness of 0.2 appropriate for high redshift disks (see discussion in Section 3.3.1). The assumption on exponential mass profiles is based on the observed average Sérsic index measured on rest-frame optical light distributions for our sample which is close to unity. The expected rotation curve for such a disk, $v_{\text{disk}}(r)$, is computed by

following the Equations 13-14 from Noordermeer (2008). We note that the resulting rotation curve with a finite thickness has a peak rotation velocity $\sim 10\%$ lower than what would be expected for an infinitely thin disk given by Equation 3.2. The effective radius and total baryonic mass of the exponential disk model is set by the median average properties of our sample ($R_e \sim 4.6$ kpc, $\log(M_{baryonic}) \sim 10.96$). Furthermore, we set $z = 1.5$ in the calculations below as this is the average redshift for sample.

The dark matter halo is assumed to have the form of a Navarro-Frenk-White profile with the density distribution (Navarro et al. 1997)

$$\rho(r) = \frac{\rho_0}{(r/r_s)(1 + r/r_s)^2}, \quad (3.3)$$

where ρ_0 is the central density of the halo, and r_s is the scale radius. It is related to the halo's virial radius, r_{200} via $r_s = r_{200}/c$ where c is the concentration parameter.

The rotation curve of such a dark matter halo is then given by

$$\frac{v_{DM}^2(r)}{V_{200}^2} = \frac{r_{200}}{r} \frac{\ln(1 + r/r_s) - (r/r_s)(1 + r/r_s)}{\ln(1 + c) - c/(1 + c)}. \quad (3.4)$$

The halo's virial velocity V_{200} and virial mass (M_{200}) are connected through r_{200} in the following way (Mo et al. 1998):

$$r_{200}(z) = \frac{V_{200}(z)}{10H(z)}, M_{200} = \frac{V_{200}^3(z)}{10GH(z)}. \quad (3.5)$$

For a flat Λ CDM universe, the Hubble parameter $H(z)$ is connected to H_0 via

$$H = H_0 \sqrt{\Omega_{\Lambda,0} + \Omega_m \cdot (1 + z)^3}. \quad (3.6)$$

Given these relations, the rotation curve of a NFW halo is completely defined by setting a virial mass, concentration parameter and redshift. To set those parameters such that they represent a dark matter halo appropriate for our galaxy sample, we compute the DM halo mass by setting m_d , the mass fraction of the baryonic disk over the halo within r_{200} , given by $m_d = \frac{M_d}{M_{200}}$. The final model rotation curve is then given by the circular velocity $v_{circ}(r)$, computed by combining the baryonic plus dark matter component :

$$v_{circ}^2(r) = v_{disk}^2(r) + v_{DM}^2(r). \quad (3.7)$$

In order to make appropriate comparisons of our modeled rotation curves with the data, we convolve our model with a Gaussian PSF of FWHM that corresponds to the average of our sample. After the model is convolved, it is scaled in velocity and radius such that the turnover in the model is [1,1] in the normalized coordinate frame of $[R/R_{turn}, V/V_{max}]$.

Numerical simulations show that the concentration of halos, c , is anti-correlated with halo mass and decreases with redshift (e.g. Bullock et al. 2001; Zhao et al 2009; Prada et

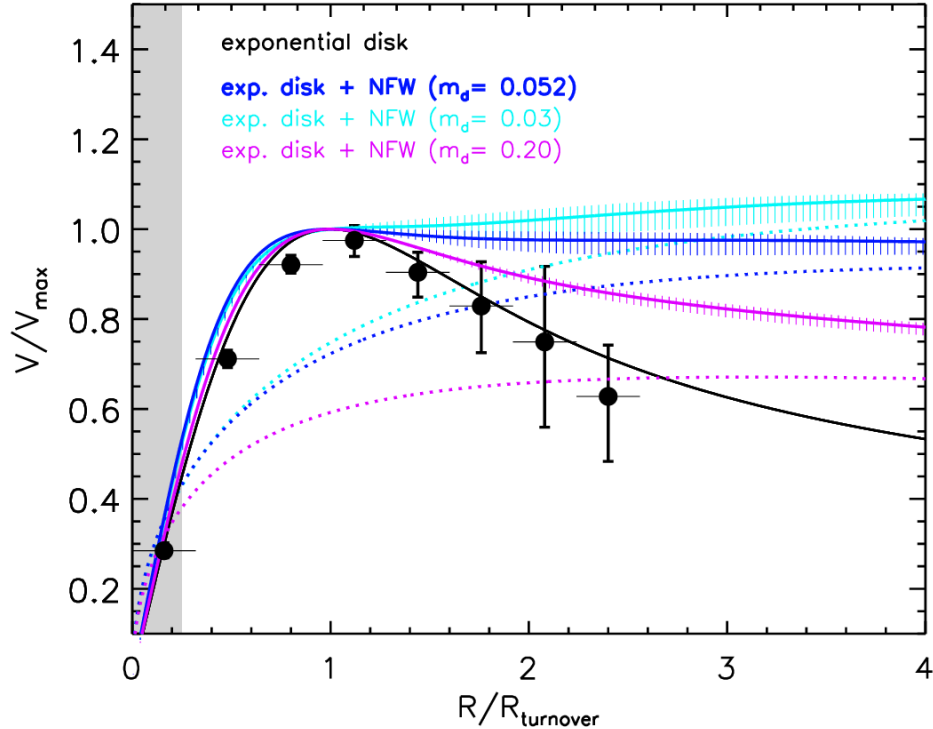


Figure 3.16: Normalized stacked rotation curve (black circles) shown together with a baryonic-only Freeman exponential disk model (black lines), and models with added dark matter halo components for different baryonic mass fraction in the disk, m_d (colored lines). Each model is convolved with a PSF of the representative average FWHM (the shaded area represents the average $R_{beam} = \text{FWHM}/2$) of the sample before normalization. Errors on the models resulting from changing the disk mass by 0.3 dex are furthermore indicated

. The dotted curves display the velocity for the dark matter component only.

al. 2012). For our comparison we compute c on the basis of the parametrization given by Bullock et al. (2001):

$$c = 9\mu^{-0.13}, \quad (3.8)$$

where $\mu = M_{200}/M_*$, with $M_* = 1.5 \cdot 10^{13} h^{-1} M_\odot$. This equation is valid for $z = 0$, and c has a redshift dependence of $c \propto (z + 1)^{-1}$. Due to the mass dependence, we compute c for each modeled rotation curve depending on halo mass (resulting from setting the m_d parameter discussed below). For the range of halo masses considered here, we find that c varies roughly from 4 to 7. However, we verify that further variations in the concentration parameter only marginally affect our models presented below by exploring a large range of c from 2 to 12, discussed in Section 3.4.7.

In our modeling, we also fold in uncertainties in baryonic mass as those are a signifi-

cant limitation in interpreting RCs of disk galaxies in view of baryonic fractions. We adopt an ~ 0.3 dex scatter in the baryonic disk mass reflecting the systematic errors in population synthesis modeling (with the most dominant error source arising from assumptions on the IMF, causing uncertainties in stellar mass by a factor of two, e.g. Kauffmann et al. 2013a). Note that changing the total mass in our models considering a pure baryonic disk solely scales its peak velocity but does not alter its shape, and thus the resulting *normalized* modeled RC (as presented below) remains unchanged. This is, however, not the case for combined baryonic disk + dark matter models, where, e.g. the dependence of virial radius on virial mass leads to variations in the profile shape of $v_{circ}(r)$ when changing the baryonic mass of the disk at given m_d .

Since one of our goals is to constrain the amount of baryons relative to that of dark matter, we will at first explore models with different baryonic disk mass fractions m_d . In Figure 3.16 we plot the stacked RC together with a normalized pure exponential disk model as black solid line together with additional baryonic plus dark matter models with a range of baryonic disk fractions m_d as solid colored lines. The mere dark matter halo velocity profile is furthermore plotted as dotted lines for the respective models to indicate the relative contribution to the total rotation curves. As apparent in Figure 3.16, decreasing the value of m_d increases the rotation velocity of the dark matter halo due to increased dark matter halo mass, which leads to an increase of outer slope of the summed total rotation curve. The error bars on the modeled RCs shown in Figure 3.16 are small enough compared to the uncertainties of our stack beyond R_{turn} to not affect our conclusions made in this section.

In order to consider a fiducial model appropriate for high redshift disk galaxies, we adopt $m_d = 0.052$ from Burkert et al. (2015). These authors have measured m_d by modeling DM halos of a large sample of ~ 360 massive ($\log(M_*) \sim 9.3 - 11.8$) SFGs galaxies at $0.8 < z < 2.6$ based on resolved H α kinematics, including our entire stacking sample used here. Albeit affected by significant uncertainties, their estimate on m_d is currently the most representative measurement for high redshift star-forming disks. As discussed in the Introduction of this thesis, the value of $m_d = 0.052$ as the *baryonic* mass fraction inside the halo includes the significant amount of gas. The corresponding *stellar* mass fraction is $m_d = 0.022$ and shows good agreement with abundance matching results: It is 35 % larger than predicted by Moster et al. (2013) and comparable to estimates of Behroozi et al. (2013a). The model with $m_d = 0.052$ predicts a velocity profile that features a turnover of velocity with an overall flat behavior beyond the turnover radius. The strong fall-off of our stack appears to be inconsistent with this flat behavior.

Next, we consider a model adopting a baryonic mass fraction appropriate for *local* massive disk galaxies. At $z \sim 0$, abundance matching results estimate as stellar mass fraction between $m_d \cong 0.025$ (Behroozi et al. 2013a) and $m_d \cong 0.035$ (Moster et al. 2013). Neglecting the amount of gas in massive local spiral galaxies, we thus set $m_d = 0.03$ as a *baryonic* mass fraction. The corresponding model predicts a similar behavior with a slightly more positive

outer slope, which is yet more inconsistent with our data.

We furthermore test an extreme situation in which all baryons in the dark matter halo are confined within the disk by setting $m_d = 0.2$, representing the cosmic baryon fraction relative to that of the dark matter (Ω_b/Ω_{DM}). Although this assumption represents an upper limit on m_d , the corresponding model still predicts a rotation curve that does not fall off as rapidly as our stack indicates. Despite the discrepancies between our stacked rotation curve and the discussed models, there are further mechanisms that act to change and especially lower the predicted outer RC slopes, which we will discuss in the next sections.

3.4.4 The effects of pressure support to outer disk rotation

In this section we will continue the comparisons of our stack with models that include the effect of pressure support in the disk. This is motivated by the elevated level of gas turbulence reflected by high gas velocity dispersions that are observed in high- z disk galaxies.

For each stable orbit in the mid-plane of a pressurized gas disk in hydrostatic equilibrium the following balance of radial forces must be fulfilled:

$$\frac{v_{rot}^2(r)}{r} = f_{grav}(r) + \frac{1}{\rho} \frac{\partial p}{\partial r}. \quad (3.9)$$

The term on the left side represents the force due to centripetal acceleration, where r is the distance from to the center of the galaxy and $v_{rot}(r)$ the resulting (observed) rotation velocity for the orbit. On the right side, the force due to gravitation, f_{grav} , is summed with the force due to radial pressure gradients in the disk. In order to calculate the latter term, we assume that turbulent motions dominate the gas pressure whereas pressure due to thermal processes can be neglected as the sound speed is in general much lower than the velocity due to turbulent motions. The local gas pressure is then

$$P = \rho_{gas} \sigma^2, \quad (3.10)$$

where σ is the isotropic velocity dispersion in the disk. Setting $f_{grav} = \frac{v_{circ}^2(r)}{r}$, equation 3.9 then becomes

$$v_{rot}^2(r) = v_{circ}^2(r) + \frac{r}{\rho} \frac{\partial p}{\partial r} = v_{circ}^2(r) + \frac{1}{\rho} \frac{\partial}{\partial \ln r} \rho \sigma^2 = v_{circ}^2(r) + \sigma^2 \frac{\partial \ln \rho}{\partial \ln r} \quad (3.11)$$

where the velocity $v_{circ}(r)$ is the circular velocity, i.e. the rotation velocity in the case of no pressure support and $v_{rot}(r)$ is the observed rotation velocity. Equation 3.11 demonstrates that the presence of negative pressure gradients can lower the rotation velocity.

For a disk where the velocity dispersion is independent of the distance to the equatorial plane and assuming an exponential disk profile as discussed in the previous section, equation 3.11 leads to (Burkert et al. 2010):

$$v_{rot}^2(r) = v_{circ}^2(r) + 2\sigma_0^2 \frac{\partial \ln \Sigma}{\partial \ln r} = v_{circ}^2(r) - 2\sigma_0^2 \left(\frac{r}{r_d} \right), \quad (3.12)$$

where r_d is the exponential scale length of the disk. If the exponential mass distribution $\Sigma(r)$ is replaced by a Sérsic profile $\Sigma(r) = \Sigma_0 \exp(-b_n (\frac{r}{R_e})^{1/n})$, Equation 3.12 becomes

$$v_{rot}^2(r) = v_{circ}^2(r) - 2\sigma_0^2 b_n \left(\frac{r}{R_e} \right)^{1/n}. \quad (3.13)$$

For systems with non-negligible σ_0 compared to V_{rot} , $v_{rot}(r)$ is reduced significantly beyond R_{turn} , which can lead to a decline of rotation velocity steeper than Keplerian ($v(r) \sim \sqrt{1/r}$) in the outer disk.

In order to assign a value for the velocity dispersion for our model comparison, we use an average σ_0 of our sample. Measurements of velocity dispersions for our sample galaxies have been done using gaussian fits to the $H\alpha$ emission line profiles in the outer disks where the rotation curves flatten out (e.g. Förster Schreiber et al. 2009; Genzel et al. 2014a, Wisnioski et al. 2015). At these radii, the influence of unresolved rotation in the center to the measured velocity dispersion is minimal, such that the extracted line width can be used for a measurement of σ_0 . In addition, we correct the remaining level of beam smeared rotation based on beam smearing correction factors applied on a galaxy-to-galaxy basis. The detailed derivation of these corrections is explained in Chapter 4 of this thesis. The resulting average estimate of σ_0 for our sample is $\sim 35 \text{ km s}^{-1}$. We adopt this as value for the characteristic dispersion throughout the disk since our best AO- IFU datasets currently available suggest a radially constant velocity dispersion within the disk to first order (Genzel et al. 2011; 2014a, Wisnioski et al. 2015, Förster Schreiber et al. 2016 in preparation).

As in the previous section, we derive uncertainties in the models with pressure support by changing the assumed baryonic disk mass by 0.3 dex. Changing the total mass of the model has the consequence of a change in V_{rot} of the model and implies a significant change of slope as V_{rot}/σ_0 determines the amount of pressure support. For the shown uncertainties computed here, we keep V_{rot}/σ_0 in the models *constant*, such that we scale the assumed value of $\sigma_0 = 35 \text{ km s}^{-1}$ when changing the total mass of the disk.

Adopting equation 3.12, we compare the same models but turning on the effects turbulent gas pressure in the disk. Figure 3.17 shows the same models as discussed in Section 3.4.3, adding models accounting for $\sigma_0 = 35 \text{ km s}^{-1}$. As apparent in the Figure, the effect of pressure support strongly decreases the rotation velocity of the baryonic disk at large radii, leading to a finite truncation of the disk where $v_{rot}(r) = 0$. The resulting models with added dark matter halo thus also show a faster decrease in velocity within the truncation radius. The case of pressure support now increases the overlap between our fiducial model of $m_d = 0.052$ and the stack significantly, such that a baryonic disk fraction of $m_d = 0.052$ is in better agreement with our stack within the uncertainties. Increasing the baryon fractions up to $m_d = 0.2$ brings the model to even better agreement with our observations, hinting at possibly higher baryonic fractions at least for our sample. Burkert et al. (2015) find that this is indeed predicted when including the effect of adiabatic contraction in their Mo, Mao & White (1998) (MMW) modeling, which we will discuss in the next subsection. Also here, the uncertainties on the modeled curves including pressure effects are small compared to the amount of fall-off and the uncertainties on the data and thus do not influence the conclusions made.

In order to further substantiate our conclusion that the drop in the outer stack is partly driven by pressure effects, we split our sample into two bins according to their amount of velocity dispersion relative to the rotation velocity (V_{rot}/σ_0) and repeat the stacking process for each bin. V_{rot} is the inclination corrected intrinsic peak rotation velocity measured on the rotation curves of the galaxies in our sample, corrected for beam smearing for each galaxy

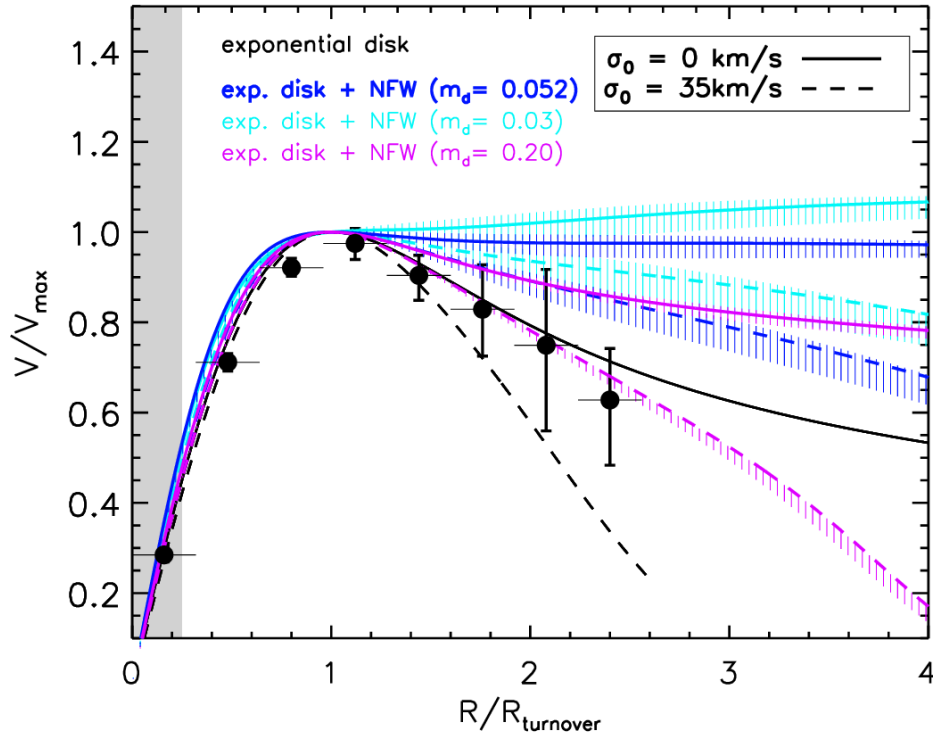


Figure 3.17: Same as Figure 3.16, but now including models with accounting pressure support in the disk with $\sigma_0 = 35 \text{ km s}^{-1}$ as dashed lines. Errors on the models resulting from changing the disk mass by 0.3 dex are furthermore indicated.

individually as described in Chapter 4. The sample is divided around the median V_{rot}/σ_0 of 6.4 such that each bin contains an equal number of galaxies. The resulting stacked rotation curves of high and low V_{rot}/σ_0 - galaxies are displayed in Figure 3.18 as black and red symbols, respectively. As seen in Figure 3.18, they indeed show a different behavior beyond the turnover radius despite the larger uncertainties due to decreased number of galaxies in each bin. The stack of galaxies with $V_{rot}/\sigma_0 > 6.4$ exhibit a fairly flat behavior with an outer slope of $\Delta V/\Delta R = -0.09_{-0.17}^{+0.14} [V_{max}/R_{turn}]$, compared to the lower V_{rot}/σ_0 stack with a slope of $\Delta V/\Delta R = -0.46_{-0.23}^{+0.22} [V_{max}/R_{turn}]$. This behavior is indeed expected according to equation 3.12, since the amount of pressure effects on the rotation curve of galaxy increases with decreasing V_{rot}/σ_0 . The behavior of the two stacks in Figure 3.18 as seen by their differing slopes, albeit with large uncertainties, are in agreement with this prediction and therefore support the conclusion that at least a significant part of the drop seen in the stacked rotation curve is driven by pressure effects in the outer disk.

We also derive the average galaxy properties of the two V_{rot}/σ_0 bins shown in Figure 3.18 due to possible correlations of V_{rot}/σ_0 with other galaxy properties. Most significantly, we find that the mean (median) redshift are different: ~ 1.8 (~ 2.2) and ~ 1.3 (~ 0.9) for the low and high V_{rot}/σ_0 bin, respectively, with a scatter of ~ 0.6 . Employing

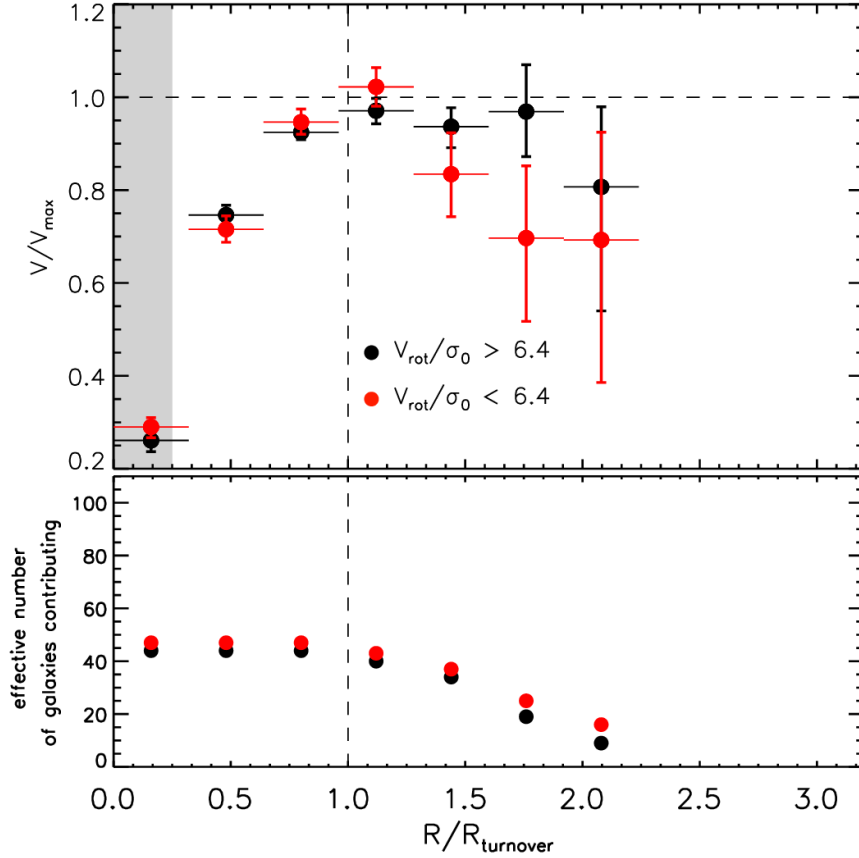


Figure 3.18: Stacked rotation curves for galaxies with $V_{\text{rot}}/\sigma_0 > 6.4$ (black symbols) and for galaxies with $V_{\text{rot}}/\sigma_0 < 6.4$ (red symbols). The shaded area marks the half-light beam size of the average PSF observed for our sample.

an K-S test, we confirm that the redshift distributions of both bins are different on a statistically significant level (yielding a p-value of $< 0.1\%$). This finding might be unsurprising due to the known increasing σ_0 with increasing redshift (e.g. Kassin et al. 2012, Wisnioski et al. 2015), resulting in a negative correlation between redshift and V_{rot}/σ_0 . However, as discussed below, we do not find any significant difference in shape of our stacked RC within the uncertainties when splitting our sample in bins of redshift only. We also find that the galaxies in the low V_{rot}/σ_0 bin have on average lower stellar mass (with a mean and median $\log(M_*)$ of 10.5 and 10.4) than the high low V_{rot}/σ_0 bin (with a mean and median $\log(M_*)$ of 10.7), albeit with moderate difference. The K-S yields a significance of $\sim 99\%$ that both stellar mass distributions are statistically different. Correlations of V_{rot}/σ_0 with stellar mass among the KMOS^{3D} and SINS/zC-SINF AO samples have been observed previously (Newman et al. 2013; Wisnioski et al. 2015), in line with our findings here. Among other galaxy properties such as R_e , Sérsic index or $\Delta(\text{MS})$, we do not find statistical significant ($> 1\sigma$ significance level) differences in their distributions between the low V_{rot}/σ_0 and high

V_{rot}/σ_0 bin, using the K-S test.

The above presented models that include the effect of pressure support in the outer disks are based on a radially constant velocity dispersion and therefore rest on the assumption that σ_0 stays at a significant level out to at least $\sim 2.4 R_{turn}$. However, measurements of σ_0 on *individual* SFGs are only available out to $\sim 2 - 2.5 R_e$ and thus do not reach out to the radii probed by our stack. Therefore, our above assumption remains still to be confirmed. Interestingly, a constant level of dispersion for a hydrostatic pressurized gas disk predicts that the scale height h increases exponentially with radius (Burkert et al. 2010):

$$h = \frac{\sigma^2}{\pi G \Sigma_0} \exp\left(\frac{r}{r_d}\right), \quad (3.14)$$

which can in principle be tested by observations. However, we note that such rapidly increasing scale heights of high- z disk galaxies in the outer regions are so far not observed based on the currently available HST imaging, although surface brightness limitations severely hamper scale height measurements in the outer disk out to several effective radii.

Another consequence of an outer constant σ_0 profile is a pressure-driven truncation of the disk where Equation 3.12 predicts $v_{rot}(r) = 0$. As in the case of local spirals (see e.g. van der Kruit & Freeman 2011 and references therein), such outer radial truncations might be frequent among high- z SFGs. Although observations at high redshift still lack the sensitivity to trace light profiles out to radii expected for truncations (i.e. $R \gtrsim 2.4 R_{turn}$, see Figure 3.17), they can potentially be probed by future observation.

Alternatively, assuming a constant scale-height throughout the disk in our models would lead to σ_0 decreasing exponentially with radius, which would lead to a negligible effect of pressure support beyond the turnover that our stack does not support. Other assumptions such as a more moderate decrease of velocity dispersion (assuming a more modest increase of the scale height) beyond the turnover radius are possible and need to be constrained by further observations.

We also explore possible trends of our stacked RC with redshift, since the cosmic evolution of σ_0 and disk sizes of SFGs might lead to an imprint on the outer rotation curve. Furthermore, the m_d parameter shows a possibly significant evolution with redshift, since the increasing molecular gas fractions in disks with increasing redshift lead to higher concentrations of baryons within the disks of SFGs. Splitting our sample around the median redshift of ~ 1.5 , we do *not* find a significant difference in the outer slope within the uncertainties.

3.4.5 Effect of adiabatic contraction

The scenario of adiabatic contraction has been proposed as a simple prescription of how the dark matter halo reacts to the infall and condensation of baryons onto its central region. Blumenthal et al. (1986) suggested a simple model in which the baryonic disk forms in the

center of a dark matter halo so slowly that the orbital period of a dark matter particle is short compared to the build-up time of the disk. Assuming that the dark matter particles move along circular orbits, the adiabatic response of the halo to the disk can be expressed such that the so called 'adiabatic invariant' $M(r)r$ is conserved. On this basis, and given that one knows the final baryonic disk distribution, $M_{disk}(r)$, one can construct the final dark matter distribution after contraction, $M_f(r)$, via

$$r_i M_i(r_i) = r [M_f(r) + M_{disk}(r)], \quad (3.15)$$

where $M_i(r_i)$ is the initial dark matter distribution from, e.g. a NFW halo profile, and r_i is the initial radius of a dark matter particle. This relation is only valid if the dark matter distribution is spherical and the orbits do not cross.

Other recipes for adiabatic contraction exist, where the general assumption of pure spherical orbits is challenged. Introducing radial motions of the dark matter particles, Gnedin et al. (2004) suggest another prescription which effectively reduces the contraction effect compared to Blumenthal et al. (1986). However, it remains an open question how the infall of baryons act on the structure of dark matter halos. Testing the impact of adiabatic contraction on rotation curves yielded mixed results in studies of different galaxy types in the local universe (Dutton et al. 2005; Kassin et al. 2006; Schulz et al. 2010; Auger et al. 2010; Puglielli et al. 2011). At higher redshifts, based on the resolved H α kinematics from the SINS survey, Burkert et al. (2010) argues for a suppressed halo contraction during the disk formation phase since it would lead to rotation velocities in excess of what is observed.

In order to test and include adiabatic contraction in our models, we adopt the Blumenthal et al. (1986) prescription, which can be re-arranged to yield the implicit equations (Burkert et al. 2010):

$$v_{circ}^2(r) = v_{disk}^2(r) + v_{DM}^2(r'), \quad (3.16)$$

where

$$r' = r \left(1 + \frac{r \cdot v_{disk}^2(r)}{r' \cdot v_{DM}^2(r')} \right). \quad (3.17)$$

We solve these equations numerically and replace in the following discussion equation 3.7 with equation 3.17 to include adiabatic contraction. Figure 3.19 displays the effect of the dark halo contraction on the inner rotation curves in the case of our fiducial rotation model with $m_d = 0.052$ without accounting for pressure effects. As seen in the Figure, the dark matter halo rotation in the contracted case is elevated compared to non-contracted case, yielding a higher rotation velocity, but a very similar shape.

Figure 3.20 plots the resulting models equivalent to the ones discussed in the previous sections, adopting a range of m_d ratios and a concentration parameter of 4. As obvious in the top panel of Figure 3.20, the impact of adiabatic contraction on the normalized modeled

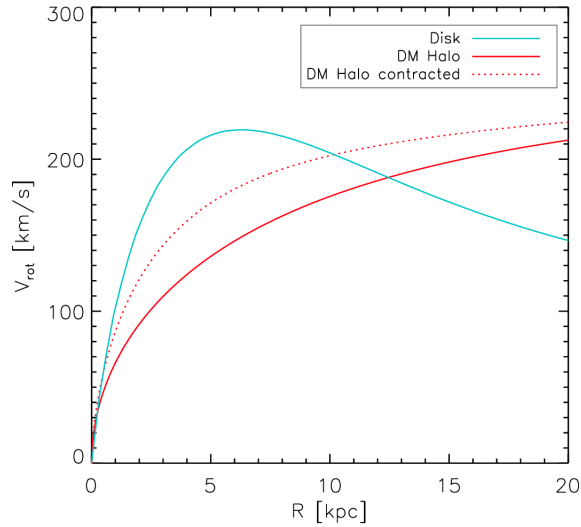


Figure 3.19: Intrinsic disk and dark matter rotation curves extracted from the models with $m_d = 0.052$ and no pressure support (solid lines). The mere dark halo rotation curve for the same model but including adiabatic contraction is plotted as dotted line.

rotation curves is small for a given value of m_d compared to the uncertainties of our data, leading to slightly decreased normalized outer velocity. We thus conclude that the imprint of adiabatic contraction cannot be tested by our stacked rotation curve since the shape of the rotation curve normalized in velocity hardly changes. In the bottom panel of Figure 3.20 we plot models incorporating adiabatic contraction and the effect of pressure support, also including an additional model with an increased baryon fraction of $m_d = 0.1$. This is the result of the MMW modeling from Burkert et al. (2015), finding that an increase in the baryonic fraction from 0.05 to 0.1 is needed to explain the higher rotation velocities of contracted halos. The resulting model of $m_d = 0.1$ does fit the observed stacked rotation curve better than the fiducial $m_d = 0.052$ model adopted previously in Figure 3.14. We conclude that even when accounting for adiabatic contraction, our observed stacked rotation curve can be reconciled with our models within the $1 - \sigma$ uncertainties when accounting for pressure support in the outer disk ($\sim 35 \text{ km s}^{-1}$) and a high baryonic disk fraction $m_d \gtrsim 0.05$. However, the value of $m_d = 0.1$ resulting from the analysis of Burkert et al. (2015) when switching on adiabatic contraction in their analysis, yields a better fit to our stacked rotation curve.

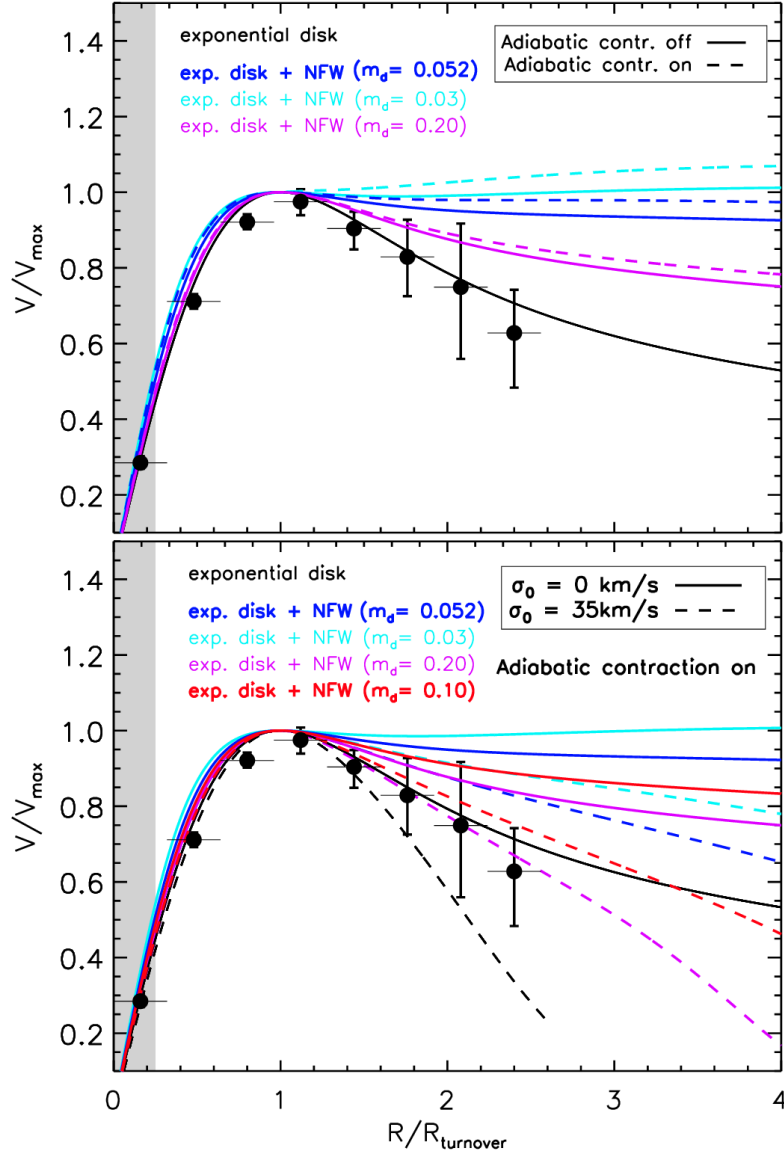


Figure 3.20: Same as Figure 3.16 but including adiabatic contraction of the NFW halo. Top: Comparison between models with (dashed lines) and without (solid lines) adiabatic contraction. Bottom: Model rotation curves with adiabatic contraction turned on (solid lines), also including the effect of pressure support (dashed lines). A model adopting $m_d = 0.10$ is plotted additionally as red lines.

3.4.6 Impact of deviations from exponential distributions

In this section, we explore how possible deviations of the inner baryonic distribution from being exponential change our results. As demonstrated in Section 3.2, the surface density distribution of the baryons as approximated by H -band light Sérsic profiles is on average exponential. As already demonstrated in Section 3.3.3, the shape of observed rotation curves around R_{turn} changes when varying the Sérsic index given the spatial resolution of our data. Also the outer slope of rotation curves beyond the turnover radius is sensitive to the surface density distribution. Based on the study of local samples, galaxies of high central surface brightness or total luminosity such as bulge-dominated early-type disks or early-type galaxies are found to exhibit slightly decreasing outer rotation curves (e.g. Kent 1988; Casertano & van Gorkum 1991; Noordermeer et al. 2007). Recently, van Dokkum et al. (2015) found that the reconstructed RC inferred from galaxy-integrated emission line widths of 10 compact massive star-forming galaxies at $2 < z < 2.5$ are in agreement with a declining rotation curve. However, such measurements solely based on line widths only provide indirect evidence compared to a direct measure of rotation velocity based on our stacked RC.

Here we want to test how the presence of a significant central stellar bulge (thus galaxies with profiles $n > 1$) is reflected on the expected outer rotation curves in the context of our models. We generate a set of additional model rotation curves similar to the ones discussed before but with an extra central bulge component:

$$v_{circ}^2(r) = v_{disk}^2(r) + v_{bulge}^2(r) + v_{DM}^2(r), \quad (3.18)$$

where we calculate $v_{bulge}(r)$ using the Noordermeer (2008) prescription for a spherical body (i.e. with a thickness parameter of 1), assuming a Sérsic law with $n = 4$. We set $R_{e,bulge}$ to be 1 kpc, as found by the bulge-disk decomposition in Chapter 2 of this thesis as an average size for stellar bulges at $0.5 < z < 2.5$. For a given bulge-to-total (B/T) ratio for the models presented below, we scale the mass of disk and bulge such that the total baryonic mass of the two components remains unchanged and corresponds to the assumed value given above. In order to properly incorporate the effect of pressure support in the combined bulge+disk models, we adopt Equation 3.13. The Sérsic index needed for Equation 3.13 is determined from Appendix B in Lang et al. (2014), providing the relationship between B/T , $R_{e,bulge}/R_{e,disk}$ for a bulge+disk model and n for a corresponding single-Sérsic profile.

Figure 3.21 displays our fiducial model with $m_d = 0.052$, and with added bulge components of different mass relative to the disk expressed by the B/T ratio. We test a range of B/T up to 0.6 as observed for the highest mass star-forming galaxies (see Chapter 2 of this thesis). As seen in Figure 3.21, the models including a central bulge component within the range of $0.2 < B/T < 0.6$ show overall only small differences compared to a pure disk model. It appears that the models with more significant bulges predict outer slopes

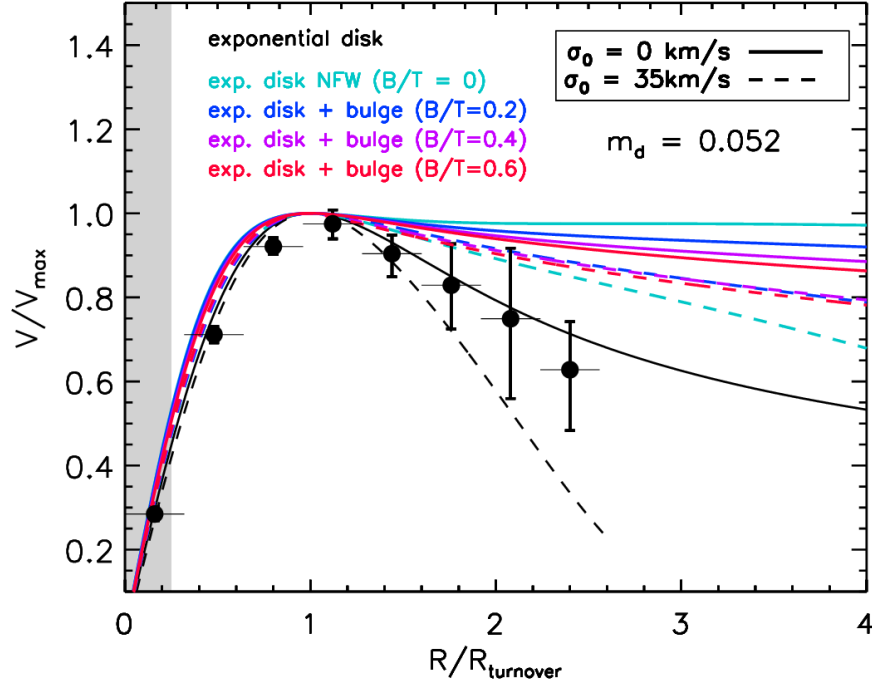


Figure 3.21: Same as Figure 3.16 but including a central bulge in the modeled rotation curves. All colored lines represent our fiducial model for high- z disks with $m_d = 0.052$.

with a slightly steeper fall-off compared to the fairly flat model without bulge. This is naturally explained since the intrinsic rotation curve of the bulge component alone ($v_{bulge}(r)$) is strongly centrally peaked around $R_e = 1$ kpc and falls off rapidly in the outer regions. However, due to the significant spatial beam smearing applied, the imprint of this effect is small such that the expected RC of a (heavy) bulge-dominated galaxy with added dark matter component is hardly indistinguishable from the same model without a bulge contribution, given the uncertainties of our data. We observe the same behavior when considering our models with pressure support, where the additional effect of adopting Equation 3.13 might lead to only small differences between a bulge-dominated model and a model with $B/T = 0$.

We thus conclude that a possibly significant central stellar bulge present within the galaxies in our sample does not affect our conclusion made in this Chapter.

3.4.7 Exploring variations in the concentration parameter

In this section we discuss the dependencies of our modeled rotation curves on the assumed concentration parameter of the underlying dark matter halo. For the above models, we adopted the scaling relation of c with halo mass and redshift from Bullock et al. (2001). Here we want to explore how further variations in the concentration parameter are reflected by the modeled rotation curves, especially since dark matter halos at lower redshift are ex-

pected to be more concentrated (with $c \sim 12$ at $z = 0$ and $M_{200} \sim 2 \cdot 10^{12} M_{sun}$, e.g. Bullock et al. 2001, Zhao et al. 2009).

To test the impact of changing c on our models discussed above, we explore lower and higher values of c (albeit the former is not observed in current N-body simulations). We therefore generate models adopting $m_d = 0.052$, varying c from 2 to 12. The corresponding models are plotted in Figure 3.22 as the colored lines. As seen from the Figure, the impact of changing c on the normalized rotation curve is only marginal compared to the uncertainties throughout the region we probe with our stack. Note that this behavior is partly, as in the case of adiabatic contraction, due to the normalization of our model in velocity. I.e. increasing c at a given m_d does produce a dark matter halo rotation profile with a overall higher rotation velocity, but this does not significantly alter the normalized shape in our models. We conclude that our results are largely independent on our choice of the concentration parameter of the halo component.

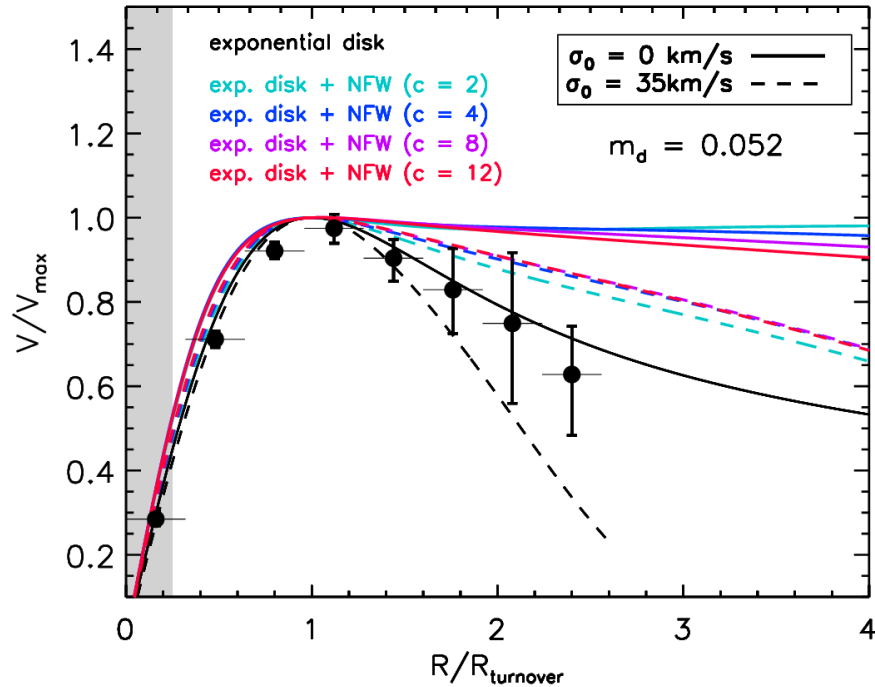


Figure 3.22: Same as Figure 3.16 but with varying concentration parameters c of the NFW halo component in the modeled rotation curves. All colored lines represent our fiducial model for high- z disks with $m_d = 0.052$.

3.5 Conclusions

In this Chapter we have presented an analysis aiming to constrain the outer disk rotation profiles of disk galaxies at high redshift to shed light on the structure and baryonic fractions of the outer disk regions. We have combined resolved $H\alpha$ kinematic data for a sample of 101 massive star forming galaxies at $0.7 < z < 2.6$ based on the large seeing limited KMOS^{3D} dataset with additional targets from the SINS/zc-SINF AO survey. We have derived a stacked rotation curve representative for the kinematics of massive ($\sim 10^9 - 10^{11} M_\odot$) high- z disk galaxies and compared the resulting stack with modeled rotation curves to constrain the relative baryonic fractions and kinematical properties in the outer disk regions. Our main results are the following:

- Through stacking we were able to constrain a representative rotation curve for our sample out to $\sim 2.5R_{turn}$, revealing an unprecedented view on outer disk kinematics at $z \sim 1 - 2.6$. Our stacked rotation curve exhibits a decrease in rotation velocity beyond the turnover down to ~ 0.65 times the normalized rotation velocity, confirming the drop seen in few individual galaxies as a representative feature for our sample of high- z disk galaxies. The drop seen in our stacked rotation curve deviates from the average rotation curves of local analogues at same baryonic mass at a $\sim 3.3\sigma$ level.
- The comparison with models shows that the falling stacked rotation curve can be explained by a high baryonic to dark matter fraction m_d (0.05 - 0.1), in combination with a significant level of pressure support in the outer disk ($\sigma_0 = 35 \text{ km s}^{-1}$). These results are in good agreement with recent studies demonstrating that star forming disks at high redshift are strongly baryon dominated at least in their inner parts (Burkert et al. 2015; Wuyts et al. 2016). This also independently confirms the presence of high gas velocity dispersions in high redshift star-forming disks and furthermore suggests that those persist to the outer disk regions, possibly causing a disk truncation at larger radii.
- We demonstrate that these results are largely independent of our model assumptions such as the absence or presence of a central stellar bulge, the halo concentration parameter and the possible effect of adiabatic contraction at fixed m_d .

Chapter 4

Beam smearing corrections

In this chapter I will describe and discuss corrections for kinematic measurements on high-redshift IFU datasets that are affected by beam smearing. Systematic beam smearing corrections are important to derive the intrinsic rotation velocity and intrinsic velocity dispersion from their measured values extracted from observed data cubes. In Section 4.1, I begin with describing the motivations and need for beam smearing correction factors on the basis of currently available IFU datasets. Then I follow with a discussion on the properties of the simulations and their set ups used to derive the corrections in Section 4.2. I present the derived correction factors for velocity and velocity dispersion and their dependencies on galaxy parameters in Section 4.3. The analysis of this Chapter is finally summarized in Section 4.4.

A major part of the content of this Chapter has been published in Burkert et al. (2015). Tables 4.1 and 4.2 are copied directly from the paper, and Figures 4.3 - 4.5 are modified versions of figures in the paper. As a co-author of Burkert et al. (2015), I had the leading role in deriving the beam smearing corrections presented in the paper and in this Chapter.

4.1 Aims

The intrinsic rotation velocity of a galaxy is the peak of the one-dimensional intrinsic rotation curve along the kinematic major axis. In the following, we will refer to this as V_{rot} . Due to spatial beam smearing, a rotation curve is observed as a smoothed or convolved version, leading to a decrease of V_{rot} and a shift of the peak to larger radii. For large PSF sizes with respect to the angular size of the observed galaxy, such as for seeing-limited observations at high redshift, this can lead to a severe underestimate of V_{rot} , even when the observed rotation curve is well constrained in the case of high S/N data.

The intrinsic velocity dispersion, σ_0 is also affected by spatial beam smearing. An observed dispersion profile, $\sigma(r)$, of a galaxy extracted along the kinematic axis results from the intrinsic velocity dispersion floor combined with beam-smear rotation of the galaxy, which is strongest in the center. This implies that a reliable measurement of σ_0 should be

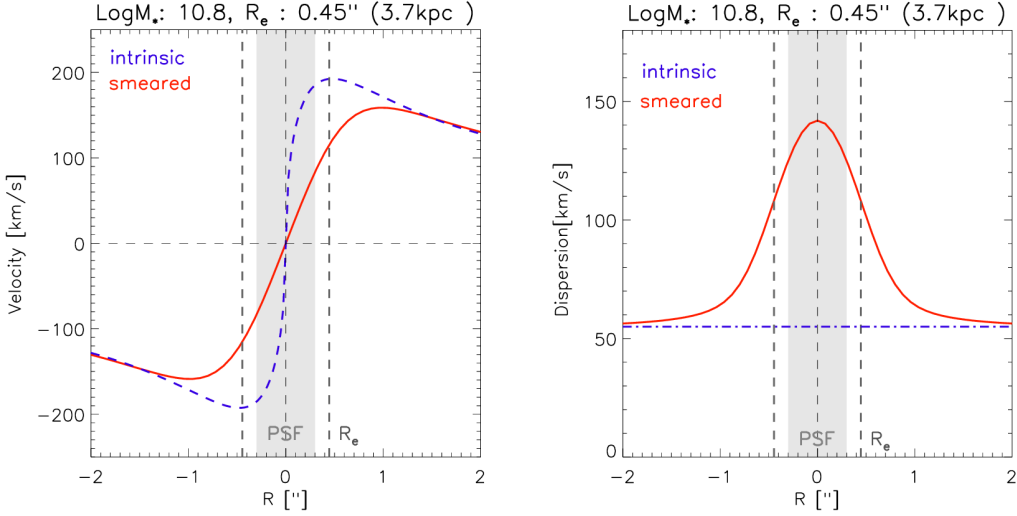


Figure 4.1: Simulated profiles of velocity (left) and velocity dispersion (right) to illustrate the impact of spatial beam smearing. The blue-dashed curves plot the intrinsic profiles as expected from a modeled data cube, whereas the red solid curves display the same model that has been spatially convolved by a Gaussian beam corresponding to a typical seeing FWHM. For the shown models, we adopt the following parameters $\log(M) = 10.8$, $R_e = 3.7$ kpc, an inclination of 60 degrees, and a PSF FWHM of $0''.6$, representing the average galaxy properties and seeing conditions of the KMOS^{3D} sample at $z \sim 2$. The shown velocity profile is corrected for inclination.

extracted as far out as possible in regions where the dispersion profile is asymptotically reaching σ_0 , but an overestimate of σ_0 without further correction still remains.

Figure 4.1 illustrates the effect of beam smearing on the rotation curve and velocity dispersion profile, on the basis of a simulation described below. The galaxy properties associated with the velocity and dispersion profiles shown are representative for seeing-limited observations with KMOS at redshift ~ 2 . As mentioned, the observed rotation curve is significantly smoothed due to beam smearing, leading to a decreased amplitude and to a shift of the peak from $r \sim 1R_e$ to $\sim 2R_e$. The resulting observed dispersion profile is centrally peaked and closely approaches the dispersion floor σ_0 at radii $\gtrsim 2R_e$, where R_e is the intrinsic effective radius of a galaxy.

In the analysis of high-redshift IFU datasets, the correction for beam smearing has been approached by modeling rotation curves and dispersion profiles individually accounting for the convolution with a known PSF (Genzel et al. 2006, 2008, 2011, 2014a; Cresci 2009; Wuyts et al. 2016 in preparation). Using this method, full intrinsic rotation curves can be constructed. Also, dispersion and velocity profiles of a galaxy can be fitted simultaneously yielding more constraining power, albeit prior assumptions on the intrinsic geometry and/or mass distribution are needed to robustly recover intrinsic kinematic profiles. However, for

the use of corrections applied to bigger compilations of IFU data, we derive scaling relations in the form of correction factors to recover the intrinsic rotation velocity V_{rot} from an observed measurement, V_{obs} , as well as the intrinsic velocity dispersion σ_0 from an observed σ_{obs} . Note that for our corrections we assume that the measurements of σ_{obs} extracted from dispersion profiles have been already corrected for instrumental resolution. The correction factors can then be easily applied on a galaxy-to-galaxy basis even for large datasets. In the following, we discuss the derivation of those correction factors for V_{rot} and σ_0 calibrated on the basis of simulations that mimic observed IFU data cubes, spanning a sufficient range in observed galaxy parameters such as size, inclination, mass, and redshift.

4.2 Simulations and setup

The basis for the derivation of the beam smearing corrections are mock data cubes created using the IDL DYSMAL code. A detailed description of the code can be found in Cresci et al. (2009) and Davies et al. (2011), here we will present a short description. Based on input parameters, DYSMAL creates a three dimensional data cube (with two spatial directions and one wavelength direction). At first, a face-on axisymmetric galaxy model with a given input mass distribution and thickness is produced. The model is then rotated according to an input inclination angle and then convolved with a spatial beam of given FWHM. The size of spatial pixels in the model is chosen to yield sufficient spatial sampling, ensuring that the modeled galaxies are sampled by at least ~ 3 spatial pixels. The model is furthermore spectrally convolved by creating a spectral Gaussian emission line profile with adjustable FWHM. Since we aim at correcting measurements of velocity dispersion that have already been corrected for instrumental resolution, we set the FWHM of the spectral emission line profiles in the models such that they correspond to typical values of intrinsic galaxy velocity dispersions σ_0 . We find that the resulting corrections for velocity are largely independent on the choice of the spectral line emission FWHM, but the corrections for velocity dispersion do depend on this choice, which is discussed in Section 4.3.2. The spectral sampling in the models is chosen such that the FWHM of the Gaussian line profiles are sufficiently sampled (by at least 3.5 spectral pixels).

Then, the resulting projected line-of-sight velocity and dispersion profiles are determined along the kinematic major axis resulting in 'observed' rotation and dispersion profiles appropriate for the set of given input parameters. DYSMAL computes the rotation curve $v(r)$ from the input mass distribution via $v^2(r) = \frac{GM(r)}{r}$. The geometry of the disk in the models is set to be very thin (i.e. $h/R_e \ll 1$). Then, based on the resulting observed rotation curve and dispersion profile for a given model, beam smearing correction factors are computed. The correction factor for velocity is computed as the ratio between the peak of the intrinsic (i.e. unconvolved but inclined) rotation curve, V_{rot} , and the observed rotation curve at radius R_{obs} , $V_{obs}(R_{obs})$. R_{obs} is chosen to be 1, 1.5, 2, and 2.5 times the intrinsic effective radius of the galaxy. This choice is motivated by the fact that measurements

of velocity (and dispersion) on real data cubes are made at radii different from galaxy to galaxy, depending on the available S/N ratio. The correction factor for the velocity dispersion is computed to be the ratio between the intrinsic σ_0 and the observed dispersion profile at radius R_{obs} . The mass profiles in the simulations are assumed to be exponential, as motivated in Chapter 3 of this thesis. In order to explore the parameter space in observed galaxy properties, we run the simulations for a range in inclination, total dynamical masses (from $10^9 - 10^{11} M_*$) and sizes.

We derive correction factors for both seeing limited and AO-assisted observations, by using a single Gaussian and double-Gaussian PSF kernel for the spatial convolution in the models. The choice of the latter is motivated by the fact that the spatial PSFs for AO-assisted observations in the SINS/zc-SINF sample are well characterized by a narrow Gaussian core (with FWHM $\sim 0''.16$) and a second broad underlying Gaussian component (with FWHM $\sim 0''.5$). The relative flux contribution of the narrow and broad component in the average AO - assisted observations are found to be 40 and 60 %, respectively. In the following we use the quantity ' R_{beam} ' as the half-light size of the Gaussian PSF kernel used (i.e. $R_{beam} = FWHM/2$). In case of the corrections for AO observations using the double-Gaussian PSF kernels, R_{beam} refers to the half-light size of the narrow Gaussian component.

4.3 Results

4.3.1 Corrections for velocity

The resulting correction factors for the rotation velocity are presented in Figure 4.2. Correction factors are plotted for both a Gaussian beam in case of seeing limited data and for double-component PSFs appropriate for AO observations, as a function of the intrinsic size of the galaxy versus the beam size, R_e/R_{beam} . The different panels display the corrections for different radii R_{obs} , at which the velocity measurement on the simulated 'observed' rotation curve is extracted. The correction factor shows the strongest dependence on R_e/R_{beam} as well as on R_{obs} , and only negligible dependencies on stellar mass and inclination angle within the accuracy of our models. The AO corrections yield higher values compared to a single Gaussian of FWHM equal to that of the 2-component PSF core at a given R_e/R_{beam} , due to the broad underlying component of the double-Gaussian PSF kernel.

In order to easily apply these corrections, we parametrize the correction factors as a function of R_e/R_{beam} and R_{obs} in the following way:

$$Correction = V_{rot}/V_{obs}(R_{obs}) = 1 + A(B + X)^C, \quad (4.1)$$

where $X = R_e/R_{beam}$. The parameters A, B and C are dependent on R_{obs} and on the choice of the used beam shape. Tables 4.1 and 4.2 list the parameters for the range of R_{obs} , and for both Gaussian and double-component AO PSF.

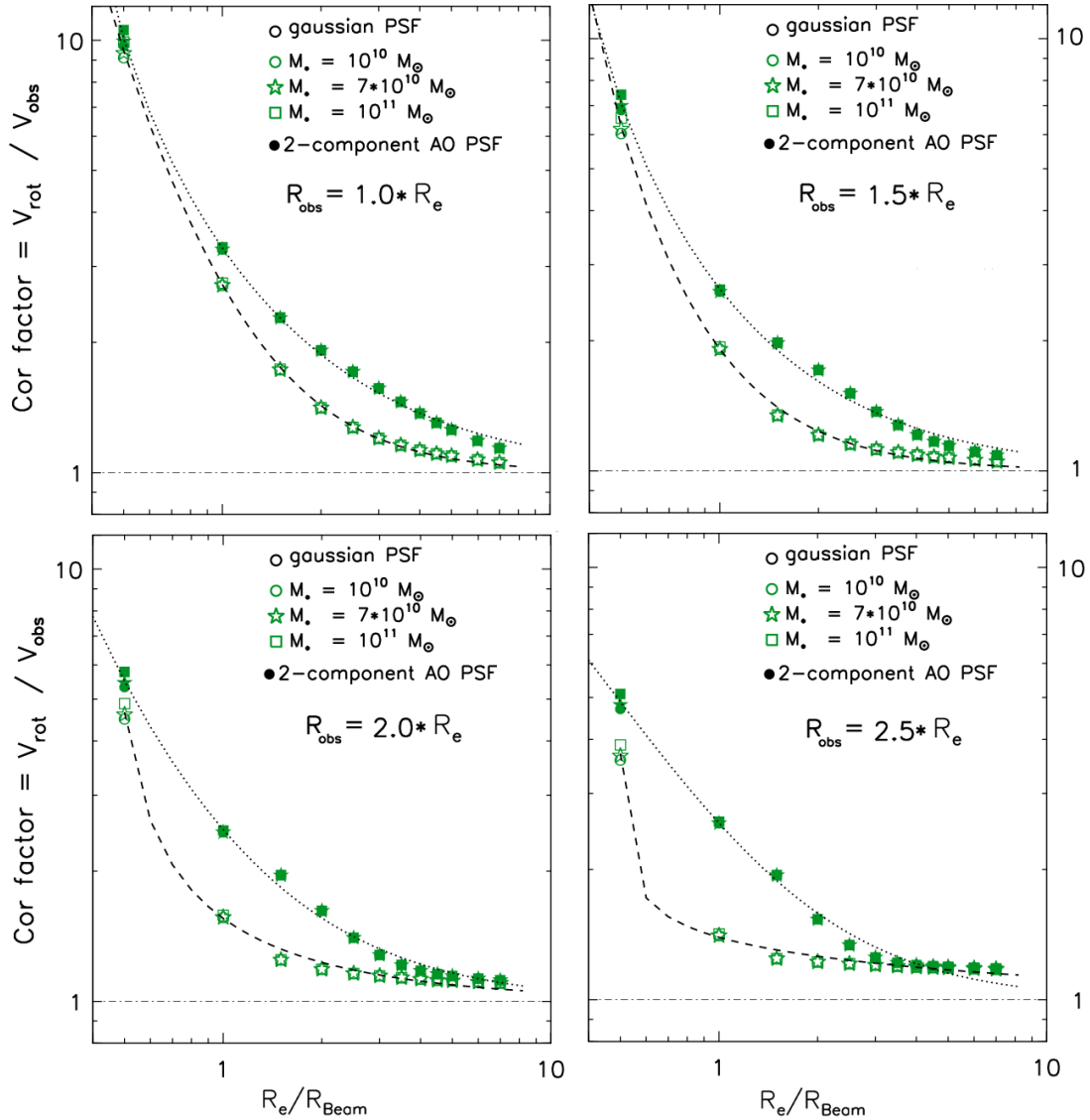


Figure 4.2: Beam smearing correction factors between the intrinsic maximum rotation velocity and the observed maximum rotation velocity measured at $1R_e$ (upper left), $1.5R_e$ (upper right), $2R_e$ (lower left), and $2.5R_e$ (lower right). Open symbols show the corrections for single Gaussian PSFs appropriate for seeing-limited data, whereas corrections derived with double-component Gaussian PSFs for AO-observations are plotted by filled symbols. The corrections are mostly dependent on the intrinsic size of the galaxy versus the beam size, R_e/R_{beam} , and are well fit by a parametric function which is also plotted. Within the explored range in dynamical masses as illustrated by different symbols, the correction factors vary only marginally. As seen by the difference between panels, the corrections change significantly with the radius at which the observed velocity was extracted (R_{obs}).

$R_{obs} [R_e]$	A	B	C
1	1.28	-0.15	-1.78
1.5	0.58	-0.25	-1.60
2	0.34	-0.44	-0.86
2.5	0.3	-0.50	-0.40

Table 4.1: Parameters for the fits to the correction factors for a single Gaussian PSF. This table has been published in Appendix A2.3 in Burkert et al. (2015)

$R_{obs} [R_e]$	A	B	C
1	1.56	-0.30	-1.10
1.5	1.15	-0.27	-1.15
2	1.25	-0.13	-1.29
2.5	1.96	0.15	-1.60

Table 4.2: Parameters for the fits to the correction factors for a double component AO PSF with a core and wing FWHM of $0.''16$ and $0.''5$, and respective relative flux contributions of 40 and 60 %. This table has been published in Appendix A2.3 in Burkert et al. (2015)

4.3.2 Corrections for velocity dispersion

The resulting corrections for dispersion also show a strong dependence on R_e/R_{beam} and R_{obs} , as in the case of velocity, but there are also significant secondary dependencies on adopted dynamical mass and inclination angle. The former is strongest and comes from the fact that a higher dynamical mass (at fixed galaxy properties) implies a steeper velocity gradient and more unresolved rotation, thus a higher observed dispersion profile. The dependence on inclination is such that more highly inclined objects show higher dispersion profiles and thus a higher correction as well, which comes from extra smeared rotation along the line of sight through the simulated disk. Figure 4.3 displays the correction factors as a function of R_e/R_{beam} , for different inclination angles and adopted dynamical masses, as well as for single Gaussian PSFs and double-Gaussian AO-PSFs. The panels show the corrections at different radii R_{obs} to illustrate that an extraction of σ_0 at larger radii implies lower corrections at fixed galaxy parameters, due to the asymptotic behavior of the dispersion profiles. As in the case of velocity, adopting a double-component AO PSF yields higher corrections at given R_e/R_{beam} due to the effects of the underlying broad Gaussian component.

Another dependence is the assumed value of intrinsic σ_0 itself, since a level of dispersion (or equivalently a Gaussian FWHM of the spectral line profile assumed) has to be assumed for a given model. In order to set a sensible value for σ_0 in our models, we assume an intrinsic dispersion corresponding to measurements obtained from the set of KMOS^{3D} data cubes, that have not been corrected for beam smearing yet. Thus we assume a σ_0 level of 25, 35 and 55 kms^{-1} which represent the average measured velocity dispersions for the

redshifts ~ 1 , ~ 1.5 , and ~ 2 from the first year of the KMOS^{3D} survey (see Wisnioski et al. 2015). To illustrate the difference in corrections within the explored redshift range, Figure 4.4 and 4.5 display the correction factors in the same fashion as Figure 4.3, but with a assumed σ_0 of 35 and 25 kms^{-1} , respectively. As apparent in the Figures, the corrections are higher for lower assumed values of σ_0 . Unfortunately we are here not able to mitigate for the dependency of the dispersion corrections on the assumption of σ_0 itself. Additional deep observations of disk kinematics at high redshift will be potentially helpful to constrain dispersion profiles more accurately which can help to gauge the assumptions on σ_0 in the models more precisely.

The velocity dispersion corrections can be applied to any observed galaxy by interpolating our grids presented in Figures 4.3 -4.5, given that the needed parameters (inclination angle, total dynamical mass, intrinsic R_e/R_{beam} , and R_{obs}) are known and lie within the range of our models. An example for the application of the corrections is the sample of resolved disk galaxies from the KMOS^{3D} survey that targets ~ 600 galaxies on the main sequence at $0.7 < z < 2.7$, focusing on stellar masses $M > 10^{10} M_\odot$. Since KMOS^{3D} profits from the rich available ancillary data from ground-based and space-based photometry as well as the high-resolution HST imaging from the CANDELS survey, measurements of intrinsic effective sizes and inclination angles are available, alongside with SED-derived integrated stellar masses. Using estimates of R_e and a/b from the HST optical rest-frame imaging, and estimates of the dynamical mass based on the inferred integrated stellar + gas masses, typical corrections for the resolved KMOS^{3D} disks are ~ 0.5 , ~ 0.6 and ~ 0.6 at redshift ~ 1 , ~ 1.5 , ~ 2 . Thus these corrections are significant for seeing-limited galaxy observations at high redshift, even though individual dispersion profiles can be traced out to $R_{obs} = 2 - 2.5R_e$.

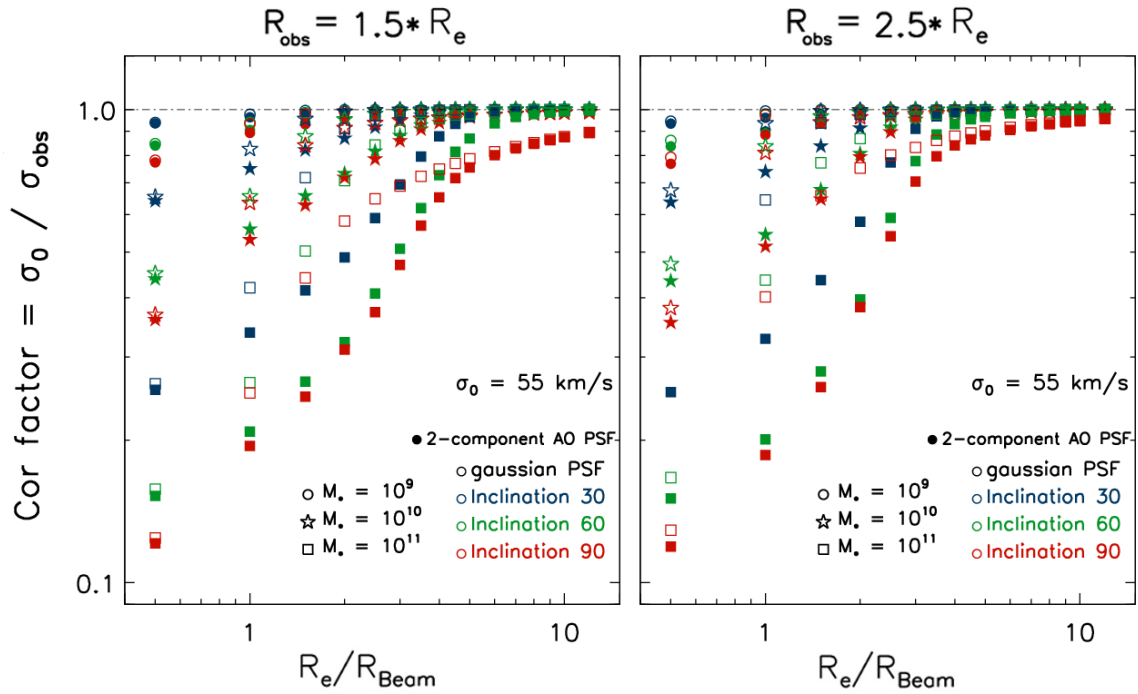


Figure 4.3: Beam smearing correction factors between the intrinsic velocity dispersion and the observed velocity dispersion measured at $1.5R_e$ (left), $2.5R_e$ (right), as example cases. Open symbols show the corrections for single Gaussian PSFs appropriate for seeing-limited data, whereas corrections derived with double-component Gaussian PSFs for AO-observations are plotted by filled symbols. Different symbols are shown for different adopted masses, and the color-coding indicates three different inclination angles. The assumed intrinsic velocity dispersion in the models are here $\sigma_0 = 55 \text{ km s}^{-1}$, thus are appropriate for $z \sim 2$. As in the case for rotation velocity, the corrections are strongly dependent on R_e / R_{beam} , but also show dependencies on inclination and adopted dynamical mass. As seen by the difference between the left and right panel, the corrections change significantly with the radius at which the observed velocity dispersion was extracted (R_{obs}).

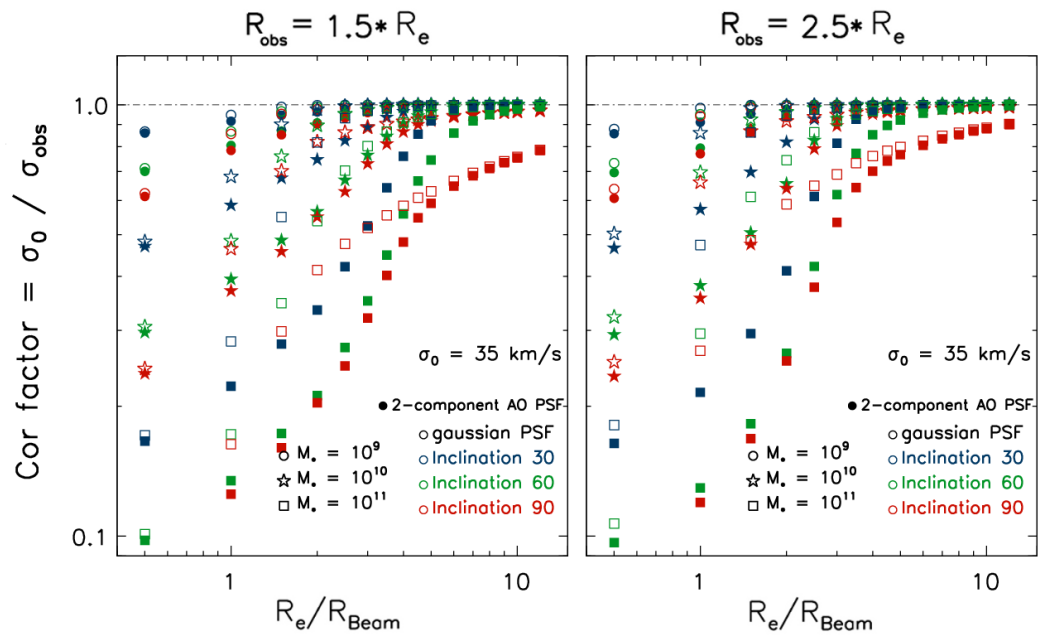


Figure 4.4: Same as Figure 4.3 but adopting $\sigma_0 = 35 \text{ km s}^{-1}$ appropriate for $z \sim 1.5$.

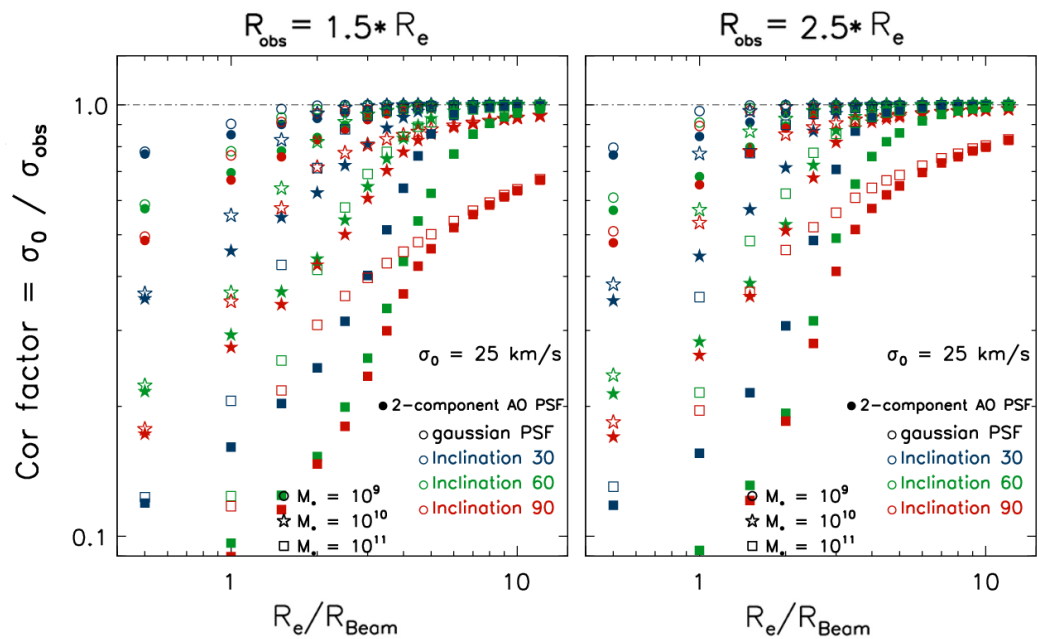


Figure 4.5: Same as Figure 4.3 but adopting $\sigma_0 = 25 \text{ km s}^{-1}$ appropriate for $z \sim 1$.

4.4 Summary

In this Chapter we have determined beam smearing corrections for high redshift IFU datasets to recover intrinsic values of the rotation velocity V_{rot} and velocity dispersion σ_0 from observed rotation curves and dispersion profiles. The correction factors are derived from simulated mock datacubes spanning a wide range of galaxy parameters, using both Gaussian PSF kernels as well as 2-component Gaussian kernels appropriate for seeing-limited and AO-assisted observations, respectively. Our main results are the following:

- The correction factors for velocity V_{rot} show a strong dependence on the effective size of the galaxy versus the size of the instrumental spatial PSF, R_e/R_{beam} , with only marginal dependencies on other galaxy parameters within our model accuracies. Also, the corrections depend on the radius at which the observed velocity is extracted from an observed rotation curve (R_{obs}). In order to make our corrections easily applicable to IFU datasets, we provide fitting functions to derive the correction factors given R_e/R_{beam} and R_{obs} , for both seeing-limited and AO-assisted observations.
- The correction factors for velocity dispersion σ_0 also show a strong dependence on R_e/R_{beam} and R_{obs} , but also significant secondary dependencies on inclination angle, dynamical mass and the assumed level of σ_0 itself. To mitigate the latter, we assume a σ_0 in the models of 25, 35 and 55 kms^{-1} for redshift ~ 1 , ~ 1.5 , and ~ 2 , respectively. To facilitate an application for the velocity dispersion correction, we create a grid of correction factors spanning a wide range in galaxy parameters (inclination, dynamical mass: $M = 10^9 - 10^{11} M_\odot$) which can be used to derive a correction factor for any observed galaxy by interpolation.

Chapter 5

Conclusions and outlook

5.1 Summary of this work

In this thesis work we have investigated open questions on the assembly and shutdown of disk galaxies at high redshift by analyzing their detailed baryonic structure. The main results of this work are the following:

- In the first part of this work, we focused on the stellar morphology of both star-forming and quiescent galaxies on the basis of the deep panchromatic high-resolution imaging dataset from the CANDELS survey in conjunction with accurate redshift information from 3D-HST. We have performed single Sérsic fits as well as bulge-disk decompositions on the light and mass distributions of a sample of 6764 galaxies above $10^{10} M_*$ in the redshift range $0.5 < z < 2.5$. In order to overcome M_*/L gradients within galaxies, we followed an approach to reconstruct resolved stellar mass distributions from SED modeling.

Our results show that the quiescent galaxies have on average higher Sérsic indices and bulge-to-total ratios (B/T) than their star-forming counterparts at the same stellar mass, confirming these results previously found in rest-frame optical light. Moreover, the B/T amongst star-forming galaxies is increasing with stellar mass, up to 40–50% for the most massive systems above $10^{11} M_*$. These findings hint at efficient bulge growth within the disk of galaxies as they evolve along the main sequence before they are getting quenched. We find that these trends are present both at $z \sim 1$ and $z \sim 2$. Viewing the results from fits to the H -band light profiles instead of mass maps, we find that B/T ratios and Sérsic indices are lower on average, with the above mentioned trends being less significant. The latter result naturally follows from the existence of significant M_*/L gradients within galaxies which are strongest among the most massive star-forming galaxies (SFGs). By viewing the fraction of quiescent galaxies as a function of stellar, bulge and disk mass, we find that, amongst those, the bulge mass shows the best correlation with the quenched fraction. Moreover, this

correlation even holds when splitting the sample into different bins of the B/T ratio, implying that the bulge mass of a galaxy is the parameter with the most predictive power in determining the probability of a galaxy being quenched. However, additional knowledge on the total stellar mass yields a tighter probability constraint. A further comparison between our findings and predictions from a recent Semi-Analytic Model (SAM) by Somerville et al. revealed that the inferred trends are, in the context of this model, consistent with AGN feedback being the agent of quenching, assuming that bulge and black hole growth are in reality related at high redshift as found to be locally.

- In the second part of this thesis, we focused on the outer kinematics of disk galaxies at high redshift. The extended shape of a rotation curve provides important information on the dark matter fractions and disk structure, largely independent of uncertainties in the light-to-mass conversions for the baryonic components. To boost the signal received from the outer faint disk regions, we employ a stacking approach combining the IFU KMOS^{3D} and SINS/zc-SINF AO datasets building a firm basis of sufficient depth and sample size for this analysis. By stacking the signal of 101 disks at $0.7 < z < 2.6$, we are for the first time able to constrain a representative rotation curve that extends out to several effective radii. Our stacked rotation curve exhibits a turnover of rotation velocity and moreover a decrease in rotation velocity in the outer regions, resulting in a slope that is different on a 3.3σ -level compared to the mildly positive outer RCs of local disks at the same mass. This result confirms the fall-off that had so far only been seen in a few individual galaxies with best quality and S/N data, and suggest it is common among massive high- z disks. Through a comparison with models including a rotating baryonic disk embedded in a dark matter halo, we show that the falling outer rotation curve can be explained by a high disk-to-dark matter mass fraction in the halo, m_d , of 5 to 10 percent, in combination with a significant level of pressure support in the outer disk (given by $\sigma_0 = 35 \text{ km s}^{-1}$). These results are in good agreement with recent studies finding that star forming disks at high redshift are strongly baryon dominated in their inner parts and exhibit high gas velocity dispersions. Our results therefore independently confirm elevated velocity dispersions in high redshift star-forming disks and furthermore suggests that those persist to the outer disk regions, possibly causing a disk truncation at larger radii. We furthermore demonstrate that these results are largely independent on our model assumptions such as the absence or presence of a central stellar bulge, the halo concentration parameter and the effect of adiabatic contraction of the halo at fixed m_d .
- In the final part of this work we quantified beam smearing corrections that can be applied to kinematics measurements on IFU datasets at high redshift in order to recover the intrinsic rotation velocity V_{rot} and velocity dispersion σ_0 given their observed values. We follow this approach by deriving correction factors that are handy to be applied to large seeing-limited or AO datasets without the need of fitting individual

rotation curves and velocity dispersion profiles. The methodology of deriving those correction factors is based on creating mock-data cubes that are artificially smeared to mimic real datasets. The resulting correction factors on rotation velocity only depend on the size of the galaxy versus the size of the instrumental spatial PSF considering the model accuracies, and we present fitting functions to be made easily applicable on data. We furthermore find that the corrections for velocity dispersion depend on several additional intrinsic galaxy parameters, such as the inclination angle, total dynamical mass and the assumed level of σ_0 itself. In order to facilitate the application of those corrections on single measurements, we create a grid of correction factors spanning a wide range in intrinsic galaxy parameters. On the basis of this grid, velocity dispersion corrections can be computed via interpolation for any source given that the needed galaxy parameters such as inclination angle, total dynamical mass, and intrinsic size vs. beam size, are known and lie within the range of our model parameters.

5.2 Future work

Both of the approaches pursued in this work yielded important insights into the baryonic structure of high redshift galaxies at different radii. However, there are still many open questions remaining about the interpretation of the findings in the context of galaxy evolution.

The correlation of inner stellar structure with quiescence of galaxies as found in this work is demonstrated to be significant, but from these correlations it is currently not possible to infer a causal link constraining a physical quenching mechanism. Also, the comparison presented with SAM predictions is not a necessary proof that AGN feedback is the actual quenching agent, but it implies a close connection between bulge growth and possible quenching processes.

Based on the analysis of high redshift IFU datasets, there is growing evidence that AGN feedback is a common phenomenon amongst high-mass SFGs (see e.g. Förster Schreiber et al. 2014; Genzel et al. 2014b). Both the KMOS^{3D} and SINS/zc-SINF datasets have played an important role in determining the properties of nuclear outflows and quantifying their incidence depending on galaxy parameters. The broad nuclear outflows show spectral properties associated with originating from AGN, and appear to be able to drive powerful winds with mass ejection rates comparable to the SFR of the host galaxy. Moreover, their incidence rapidly increases towards high stellar masses, such that 50-90 % of SFGs above $\log(M_*) > 10.9$ show this phenomenon. These properties hint at AGN feedback being a likely mechanism for quenching massive SFGs at high redshift, but it is not an ultimate proof for AGN quenching since it is yet not clear if outflows driven by AGN provide the energy and momentum to expel all gas in the entire galaxy and potentially maintain a quiescent stage over longer timescales. More spectroscopic studies at high redshift also involving long-slit

spectroscopic observation with e.g. MOSIFRE on Keck yielding more sample statistics will help to map out the dependence on other galaxy parameters in order to help to understand the connection between AGN feedback and quenching.

Another step towards further characterizing and understanding such feedback mechanisms involves tracing those outflows by the molecular gas component. Prominent outflows of molecular gas associated with feedback from AGN have been observed in nearby galaxies (Feruglio et al. 2010; Sturm et al. 2011; Veilleux et al. 2013; Cicone et al. 2013). At redshifts $z > 1$, tracing those outflows has so far only been successful in few bright QSOs using the e.g. [CII] transition (Maiolino et al. 2012). Planned follow-up observations in CO emission with the ALMA interferometer for galaxies from KMOS^{3D} and SINS/zc-SINF, where broad outflows in H α have been detected, provides a promising avenue in this direction. Also, more systematic observations of local AGN as well as simulations are needed to provide further insights on how AGN are fueled and act to drive large-scale outflows. Simulations might improve our understanding on how the energy and momentum output of AGNs interact with the ISM through radiation, momentum and cosmic rays. In this respect, hydrodynamical cosmological simulations such as Illustris (Vogelsberger et al. 2014; Genel et al. 2014) present an excellent avenue to study the impact of implemented AGN feedback mechanisms on evolving galaxy populations.

The role of morphological quenching seems at least to partly play a role as found through studies of determining central disk (in)stabilities of massive SFGs at high redshift (Genzel et al. 2014a). These results are in agreement with findings that the central equivalent width (EW) of H α as a proxy for specific Star Formation Rate (sSFR) seems to be suppressed in the central regions of massive SFGs (see also e.g. Wuyts et al. 2013; Nelson et al. 2015; Tacchella et al. 2015), implying that the quenching process happens inside-out. Unfortunately, the (potentially) spatially varying extinction in high redshift SFGs hampers a robust recovery of resolved SFRs from the observation tracers such as H α or UV emission (e.g. Nelson et al. 2016). A future possibility to mitigate this problem is expanding the observed wavelength from the NIR range to longer wavelengths into the extinction-free regime using future space-based facilities such as the James-Web-Telescope (JWST), or using local analogues for high redshift galaxies, which is further discussed below. Further support for morphological quenching comes from enhanced depletion timescales in local ETGs (e.g. Saintonge et al. 2012; Crocker et al. 2012). However, reliable measurements of depletion time scales for ETGs are still rare and further observations will help to constrain the deficiency of star formation in those systems.

A promising avenue for shedding further light on quenching at high redshift is the study of 'freshly' quenched galaxies that lie below the main sequence, representing the immediate descendants of SFGs. Their properties regarding gas content and kinematics may encode information on how they were undergoing quenching processes. Observationally constraining their kinematical properties, their distribution of star formation and determining their gas content is currently very challenging. Pushing towards the locus of compact quiescent galaxies well below the main sequence with very deep integrations, few targets

within KMOS^{3D} have been identified as rotation-dominated disks (Wisnioski et al. 2016 in preparation). Interestingly, there are few galaxies among the KMOS^{3D} sample that show a massive dense core containing most of the stellar mass and an extended, rotation-dominated star-forming disks. Proposed observations with the X-Shooter instrument on the Very Large Telescope (VLT) constraining e.g. radial metallicity gradients will help to elucidate if those systems are normal SFGs experiencing ongoing quenching or if they represent rejuvenated disks around an evolved dense core.

The analysis presented in this thesis also revealed that main sequence SFGs at high redshift are experiencing significant bulge growth along the main sequence with increasing stellar mass. However, it remains still unclear which processes might lead to internal bulge growth. On the one hand, mergers are expected to leave an imprint on the inner structure in galaxies, but it is on the other hand also tantalizing to conclude that star-forming clumps frequently found in gas rich high- z disks are driving the build-up of bulges through radial migrations (e.g. Dekel et al. 2009; Bournaud et al. 2011). Studies of the extracted photometric properties of clumps revealed radial trends of clumps in optical colors and inferred ages (Förster Schreiber et al. 2011; Guo et al. 2012). However, the unknown impact of spatially varying extinction, the limited spatial resolution and the limited wavelength range available for those systems still hamper a conclusive interpretation of these radial trends. Furthermore, as proposed in the local universe, the structure and kinematics of the central bulge might hint at different formation mechanisms either connected to galaxy mergers or slower secular evolution processes (see e.g. Kormendy & Kennicutt 2004). Unfortunately, radial structures of bulges at high redshift cannot be measured due to the limited spatial resolution even for current space-based telescopes.

A possibility to overcome the limitations and to expand the aforementioned studies at high redshift are future high-resolution facilities operating in the infrared. For instance, the MICADO instrument on the 40-meter class European Extremely Large Telescope (E-ELT), equipped with adaptive optics, is designed to provide diffraction-limited NIR imaging with a superior resolution ($0''.06 - 0''.01$ FWHM in the J-K bands), which will enable the resolved study of clumps and bulges at high redshift. Also future space-based telescopes such as the James Web Space Telescope (JWST) will be equipped with instruments providing imaging and spectroscopy with a higher angular resolution than current HST imaging due to its larger mirror diameter, albeit not surpassing the spatial resolution capabilities of future E-ELT instruments. The key advantage of JWST will be the extension to longer wavelengths (although with decreasing spatial resolution), reaching up to $\sim 30\mu m$. This will enable covering the rest-frame NIR part of the spectrum of galaxies at $z \sim 2$ which encodes information on the bulk of older stellar population particularly important to constrain stellar ages, and is also less affected by extinction.

Another approach to shed further light on the properties of high-redshift SFGs galaxies in more detail is studying their local analogues. In this respect, the DYNAMO IFU survey (Green et al. 2014) represents an excellent sample of ~ 70 local star-forming galaxies at $10^9 - 10^{11} M_{\odot}$, containing a subset of rare $H\alpha$ luminous galaxies observed at $\sim 1 - 3$

kpc resolution. Samples such as DYNAMO are particularly promising since their targets can be observed at rest-frame wavelength ranges not accessible at high redshift. Thus, their Spectral Energy Distributions (SEDs) can be probed over a wider wavelength range which increases the accuracy of recovering stellar properties from photometric and spectroscopic observations. Early results on the basis of DYNAMO also including high-resolution follow-up observations have confirmed that the sample contains galaxies with clumpy features and turbulent disks (Green et al. 2014). Early observations of the CO emission line of the DYNAMO sample have confirmed that those are indeed gas-rich (Fisher et al. 2014). The study of the morphology of those galaxies utilizing future high-resolution follow-up observations will enable the investigation of photometric properties of clumps to constrain clump migration models and understand the build-up of bulges in such galaxies. Also other properties such as the angular momentum will help to understand the origin of the clumpy nature of high- z galaxies and potentially the regulation of star-formation in those systems.

The rotation curve (RC) stacking approach presented in this thesis improved the signal of individual galaxies strikingly and increased the available rotation signal out to large unexplored radii. We have demonstrated that the applied selection of stacked galaxies out of the bigger pool of available rotating disks among the KMOS^{3D} and SINS/zC-SINF samples is unlikely to cause a bias in dark matter fraction representative for the average stack. Moreover, our stacking methodology seems to be able to robustly recover a wide range of outer slopes. However, there are still caveats and limitations to the analysis arising from the normalization and averaging over many galaxies. Although we have shown that we still select 'normal' SFGs on the MS, a bias against smaller galaxies with lower surface brightness still remains. Deeper integrations on these more compact sources extending individual RCs (albeit observationally expensive) will help to mitigate for this bias.

Although the current stacking includes a significant number of 101 galaxies, our conclusions are based on the outer (negative) slope of the stacked rotation curve which is different from the ones of local disks of same mass at a $\sim 3.3\sigma$ level. This demonstrates the challenges of this analysis given by the faint surface brightness levels of $H\alpha$ in the outer disk. The ongoing observations within KMOS^{3D} (reaching a final sample size of ~ 600 galaxies) will help to further increase the signal in the outer stack by adding more galaxies, further constraining the outer slope of the stacked RC. With a firmer statistical sample in hand, dependencies of the shape of the stack with galaxy properties such as V_{rot}/σ_0 or redshift can be further explored providing further insights into the origin of the outer falloff.

Furthermore, very deep observations of several KMOS^{3D} targets with SINFONI in seeing-limited mode, with integrations times of ~ 5 h per target will soon be obtained (PI: R. Genzel) and will help to access the outer parts of rotation curves in individual galaxies that can be interpreted without making normalizations. Long-slit observations of galaxies with a known velocity field using LUCI on the Large Binocular Telescope (LBT), specifically on edge-on systems, are also ongoing and will provide additional suitable data.

Regarding the outer structure and kinematics of disk galaxies at high redshift, also open questions remain. The outer slope of our falling stacked rotation curve implies that the ve-

locity dispersion persist at a high level to the outer disk regions. As a consequence, the outer (exponential) disks are required to be truncated at the radius where the rotation velocity reaches zero. While the outer velocity dispersion levels could potentially be explored with very deep integrations on individual galaxies, the radial structure of the stellar disk might be independently determined with the aid of HST imaging and/or spectroscopy. Nelson et al. (2015) uses a stacking approach with the WFC3 grism spectroscopic data from the 3D-HST survey for ~ 3000 galaxies at $z \sim 1$ to derive extended radial profiles of $H\alpha$ and optical continuum emission. The authors find that the resulting (outer) profiles are well in agreement with being exponential until $\sim 5r_d$, where truncations in local disks are observed. Also deep high-resolution surveys such as CANDELS may provide the necessary data quality and sample sizes to explore further stacking approaches reaching to the faint levels of the (exponential) disks potentially revealing systematic radial truncations. An analysis may also provide information on the scale height in e.g. edge-on systems, which is connected to the expected outer dispersion profiles.

Moreover, the aforementioned DYNAMO sample also provides an excellent opportunity to study outer disk kinematics in a similar fashion as done within this work. The sample size offered by DYNAMO as well as the spatial coverage of single galaxies reaching to their outer regions is well suited to potentially probe the outer disk kinematics by exploring such a stacking approach. Thus, an imprint of the elevated level of velocity dispersions among DYNAMO galaxies on their outer kinematics could be confirmed. Moreover, the sampled range in galaxy properties by DYNAMO is also suited for exploring tentative trends of such stacks by e.g. construction a control sample of galaxies with more moderate velocity dispersion compared to 'normal' local star-forming galaxies.

DYNAMO represents one of the ongoing IFU surveys studying the properties of local galaxy kinematics systematically with substantial sample sizes covering a wide range in galaxy parameters. Recent IFU surveys include for instance the CALIFA survey with the PMAS/PPAK IFUs on the 3.5m Calar Alto Telescope, targeting a sample of ~ 600 galaxies selected from SDSS to include a wide range of colors and morphologies, covering a wavelength range of $3700 - 7000 \text{ \AA}$. Moreover, SAMI is an IFU survey with the SAMI instrument on the Anglo Australian Telescope (AAT) targeting a larger sample of ~ 3400 galaxies selected from the Galaxy Mass Assembly Survey (GAMA) and contains galaxies with $10^7 - 10^{12} M_\odot$. The MANGA survey is an ongoing program with the MANGA IFU on the Sloan Foundation 2.5m Telescope that will observe an even larger mass-selected sample of $\sim 10,000$ galaxies with $M > 10^9 M_\odot$ selected from SDSS, covering the wavelength range $6000 - 10300 \text{ \AA}$. Those extensive surveys will help us to study systematic galaxy kinematics for a wide range of galaxy types in synergy with existing ancillary data which will help to elucidate the assembly history and shutdown processes in galaxies.

Appendix A

The meaning of a Sérsic index measurement

The text and the figure of this Section have been published in Lang et al. (2014).

The combination of our one and two-component fits on the mass maps enables us to examine empirically how the Sérsic index relates the amplitude of the bulge (as parametrized by B/T) on the one hand, and the relative size-ratio to the bulge and disk component ($R_{e,B}/R_{e,D}$) on the other hand. Figure A.1 illustrates that, while B/T shows a clear correlation with the Sérsic index n , there is no unique one-to-one translation between the two. Instead, the best-fit n to a composite bulge+disk system additionally depends on the size ratio of the two components. In other words, a galaxy's Sersic index could be increased by placing more material in the bulge, but also by growing the disk at fixed bulge size. The observed CANDELS galaxies occupy a surface in this three-parameter space (n , B/T , $R_{e,B}/R_{e,D}$) that is in good agreement with what would be anticipated from Sersic fits to idealized, noise-free bulge ($n = 4$) plus disk ($n = 1$) profiles (squares and curves in the left- and right-hand panels of Figure A.1, respectively). Evidently, for systems with B/T close to 0 or 1, the size ratio of the two components is ill-constrained as one of them contains barely any mass. The galaxies in our full $0.5 < z < 2.5$ sample span the full range of B/T values, and are located predominantly around bulge-to-disk size ratios of $R_{e,B}/R_{e,D} \sim 0.2$.

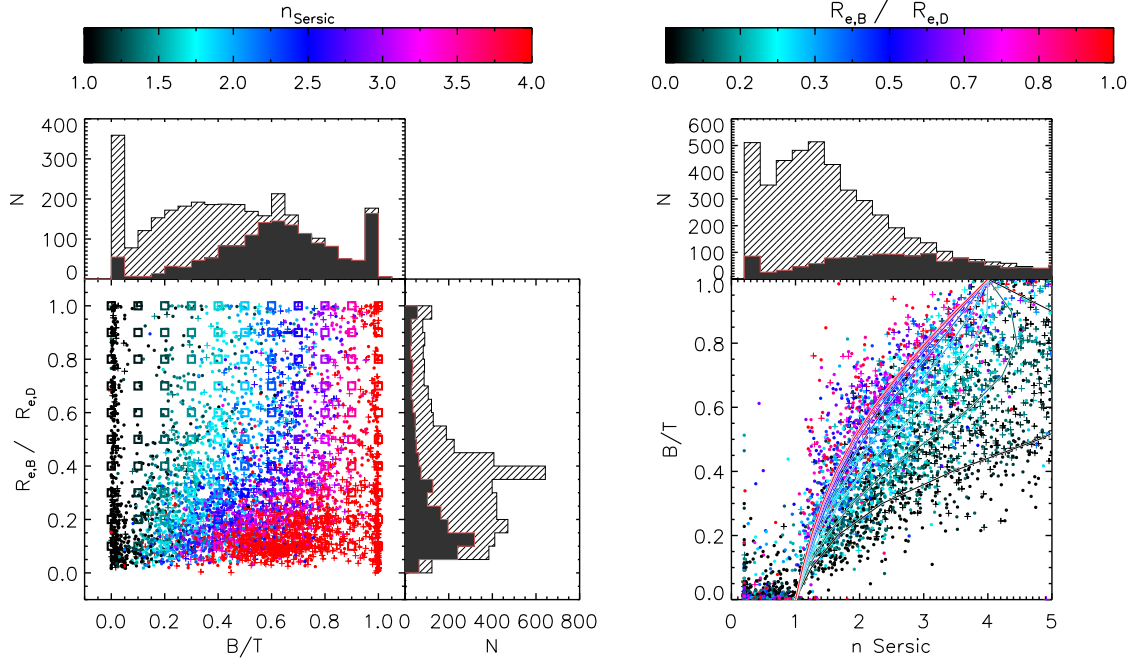


Figure A.1: Left: Size ratio between bulge and disk component ($R_{e,B}/R_{e,D}$) vs. B/T for the whole galaxy sample as measured in mass. The color indicates the measured Sérsic index. Quiescent galaxies are shown as a plus (+), SFGs are shown as dots. Right: Measured B/T values against Sérsic indices as seen in mass. The histograms show the respective measured distributions of B/T , $R_{e,B}/R_{e,D}$ and n among the sample for quiescent galaxies (solid black areas) and SFGs (hatched areas). The relationship between the Sérsic index and B/T is not unique, but rather crucially depends on $R_{e,B}/R_{e,D}$. The squares (left) and curved lines (right) illustrate the relation between $(B/T, R_{e,B}/R_{e,D})$ and n as inferred from noise free idealized bulge + disk toy models, consistent with the trends seen for our observed galaxy samples.

Appendix B

Comparison to the Guo et al. (2013) Semi-analytic model

The text and the figures of this Section have been published in Lang et al. (2014).

In order to evaluate to which extent the characteristic trends of the Somerville et al. SAM, as presented in Section 2.5, are generic to all semi-analytic models, we considered an independent semi-analytic model by Guo et al. (2013). The Guo et al. (2013) model is rooted in the dark matter backbone of the Millennium Simulation (Springel et al. 2005), and its output tables with galaxy properties for snapshots of different lookback times are publicly available on the Virgo Millennium Database (G. Lemson & the Virgo Consortium 2006). We present the equivalent plots of Figure 2.8 and 2.9 in Figure B.1 and Figure B.2. As in the Somerville model, quenched fractions are rising with increasing mass, increasing bulge mass, and decreasing redshift, but broken down in bins of B/T , significant differences are notable. Specifically, f_{quench} does not monotonically increase with increasing B/T at a given stellar mass.

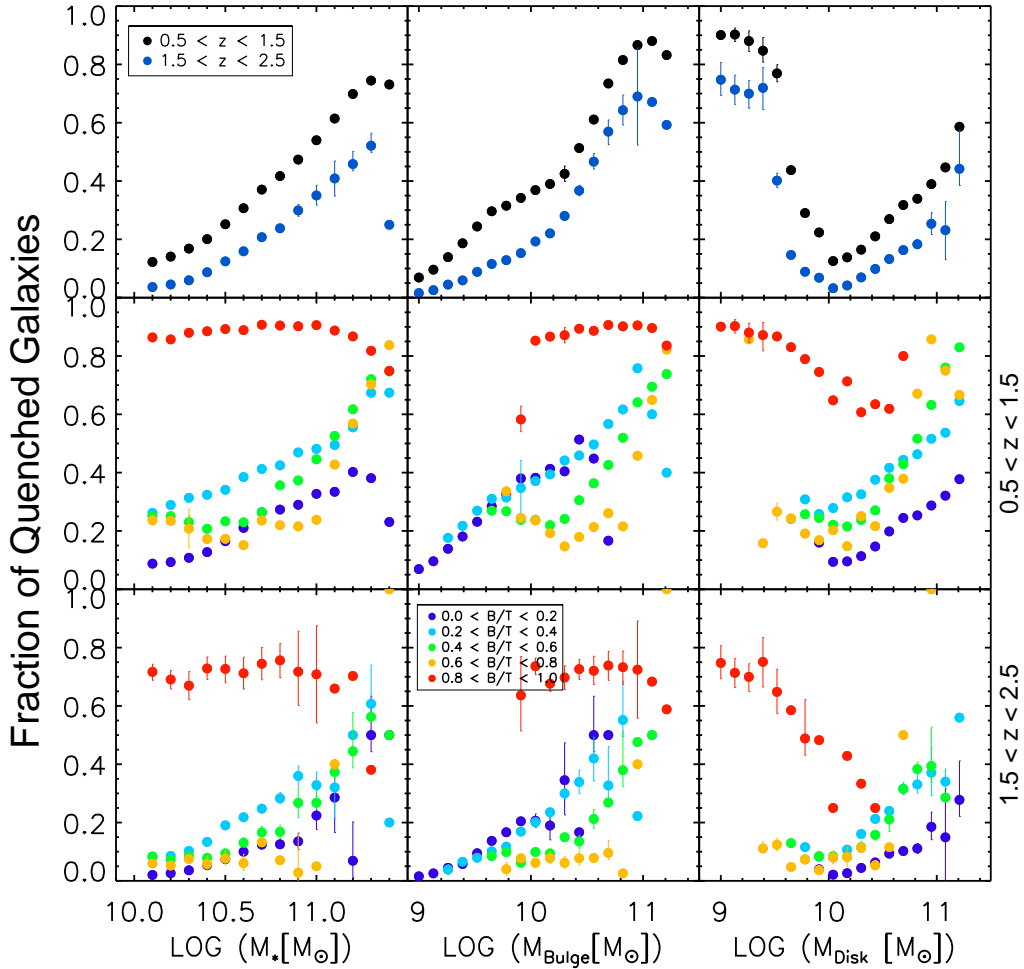


Figure B.1: Fraction of massive galaxies ($M_* > 10^{10} M_\odot$) that are quiescent in the SAM of Guo et al. (2013), as a function of total stellar mass, stellar mass in the bulge and disk separately. The bottom two rows show the results split by bulge-to-total ratio, for the $z \sim 1$ and $z \sim 2$ bins respectively.

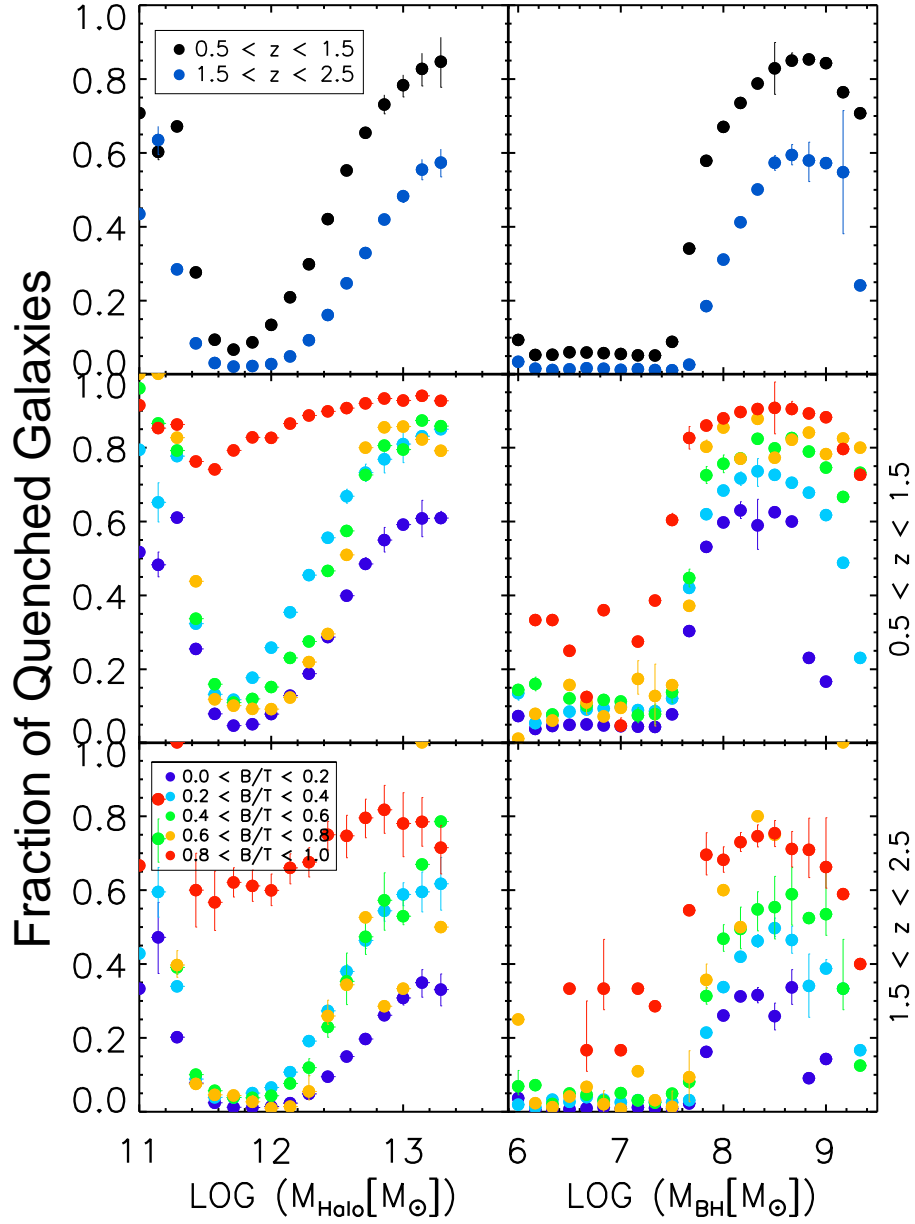


Figure B.2: Fraction of massive galaxies ($M_* > 10^{10} M_\odot$) that are quiescent in the SAM of Guo et al. (2013), as a function of halo and black hole mass. The bottom two rows show the results split by bulge-to-total ratio, for the $z \sim 1$ and $z \sim 2$ bins respectively.

Bibliography

- (Abraham *et al.* 1996) R. G. Abraham, N. R. Tanvir, B. X. Santiago, R. S. Ellis, K. Glazebrook, & S. van den Bergh, *Galaxy morphology to $I=25$ mag in the Hubble Deep Field*, MNRAS **279**, L47 (1996).
- (Abramson *et al.* 2014) L. E. Abramson, D. D. Kelson, A. Dressler, B. Poggianti, M. D. Gladders, A. Oemler, Jr., & B. Vulcani, *The Mass-independence of Specific Star Formation Rates in Galactic Disks*, ApJL **785**, L36 (2014).
- (Andredakis *et al.* 1995) Y. C. Andredakis, R. F. Peletier, & M. Balcells, *The Shape of the Luminosity Profiles of Bulges of Spiral Galaxies*, MNRAS **275**, 874 (1995).
- (Auger *et al.* 2010) M. W. Auger, T. Treu, A. S. Bolton, R. Gavazzi, L. V. E. Koopmans, P. J. Marshall, L. A. Moustakas, & S. Burles, *The Sloan Lens ACS Survey. X. Stellar, Dynamical, and Total Mass Correlations of Massive Early-type Galaxies*, ApJ **724**, 511 (2010).
- (Babcock 1939) H. W. Babcock, *The rotation of the Andromeda Nebula*, Lick Observatory Bulletin **19**, 41 (1939).
- (Balogh *et al.* 2001) M. L. Balogh, D. Christlein, A. I. Zabludoff, & D. Zaritsky, *The Environmental Dependence of the Infrared Luminosity and Stellar Mass Functions*, ApJ **557**, 117 (2001).
- (Barnabè *et al.* 2012) M. Barnabè, A. A. Dutton, P. J. Marshall, *et al.*, *The SWELLS survey - IV. Precision measurements of the stellar and dark matter distributions in a spiral lens galaxy*, MNRAS **423**, 1073 (2012).
- (Barro *et al.* 2014) G. Barro, S. M. Faber, P. G. Pérez-González, *et al.*, *CANDELS+3D-HST: Compact SFGs at $z \sim 2 - 3$, the Progenitors of the First Quiescent Galaxies*, ApJ **791**, 52 (2014).
- (Barro *et al.* 2013) G. Barro, S. M. Faber, P. G. Pérez-González, *et al.*, *CANDELS: The Progenitors of Compact Quiescent Galaxies at $z \sim 2$* , ApJ **765**, 104 (2013).
- (Behroozi *et al.* 2013) P. S. Behroozi, R. H. Wechsler, & C. Conroy, *On the Lack of Evolution in Galaxy Star Formation Efficiency*, ApJL **762**, L31 (2013).

- (Bell 2008) E. F. Bell, *Galaxy Bulges and their Black Holes: a Requirement for the Quenching of Star Formation*, ApJ **682**, 355 (2008).
- (Bell & de Jong 2001) E. F. Bell & R. S. de Jong, *Stellar Mass-to-Light Ratios and the Tully-Fisher Relation*, ApJ **550**, 212 (2001).
- (Bell *et al.* 2004) E. F. Bell, C. Wolf, K. Meisenheimer, *et al.*, *Nearly 5000 Distant Early-Type Galaxies in COMBO-17: A Red Sequence and Its Evolution since $z \sim 1$* , ApJ **608**, 752 (2004).
- (Bell *et al.* 2012) E. F. Bell, A. van der Wel, C. Papovich, *et al.*, *What Turns Galaxies Off? The Different Morphologies of Star-forming and Quiescent Galaxies since $z \sim 2$ from CANDELS*, ApJ **753**, 167 (2012).
- (Bershady *et al.* 2010) M. A. Bershady, M. A. W. Verheijen, R. A. Swaters, D. R. Andersen, K. B. Westfall, & T. Martinsson, *The DiskMass Survey. I. Overview*, ApJ **716**, 198 (2010).
- (Bershady *et al.* 2011) M. A. Bershady, T. P. K. Martinsson, M. A. W. Verheijen, K. B. Westfall, D. R. Andersen, & R. A. Swaters, *Galaxy Disks are Submaximal*, ApJL **739**, L47 (2011).
- (Bigiel *et al.* 2008) F. Bigiel, A. Leroy, F. Waleer, E. Brinks, W. J. G. de Blok, B. Madore, & M. D. Thornley, *The Star Formation Law in Nearby Galaxies on Sub-Kpc Scales*, ApJ **136**, 2846 (2008).
- (Binney & Tremaine 2008) J. Binney & S. Tremaine, *Galactic Dynamics: Second Edition*, by James Binney and Scott Tremaine. ISBN 978-0-691-13026-2 (HB). Published by Princeton University Press, Princeton, NJ USA, 2008. (Princeton University Press, 2008).
- (Birnboim & Dekel 2003) Y. Birnboim & A. Dekel, *Virial shocks in galactic haloes?*, MNRAS **345**, 349 (2003).
- (Birnboim *et al.* 2007) Y. Birnboim, A. Dekel, & E. Neistein, *Bursting and quenching in massive galaxies without major mergers or AGNs*, MNRAS **380**, 339 (2007).
- (Bluck *et al.* 2014) A. F. L. Bluck, J. T. Mendel, S. L. Ellison, J. Moreno, L. Simard, D. R. Patton, & E. Starkeburg, *Bulge mass is king: the dominant role of the bulge in determining the fraction of passive galaxies in the Sloan Digital Sky Survey*, MNRAS **441**, 599 (2014).
- (Blumenthal *et al.* 1986) G. R. Blumenthal, S. M. Faber, R. Flores, & J. R. Primack, *Contraction of dark matter galactic halos due to baryonic infall*, ApJ **301**, 27 (1986).
- (Boada *et al.* 2015) S. Boada, V. Tilvi, C. Papovich, *et al.*, *The Role of Bulge Formation in the Homogenization of Stellar Populations at $z \sim 2$ as revealed by Internal Color Dispersion in CANDELS*, ApJ **803**, 104 (2015).

- (Bonnet *et al.* 2004) H. Bonnet, R. Abuter, A. Baker, *et al.*, *First light of SINFONI at the VLT*, *The Messenger* **117**, 17 (2004).
- (Bournaud *et al.* 2011) F. Bournaud, A. Dekel, R. Teyssier, M. Cacciato, E. Daddi, S. Juneau, & F. Shankar, *Black Hole Growth and Active Galactic Nuclei Obscuration by Instability-driven Inflows in High-redshift Disk Galaxies Fed by Cold Streams*, *ApJL* **741**, L33 (2011).
- (Bovy & Rix 2013) J. Bovy & H.-W. Rix, *A Direct Dynamical Measurement of the Milky Way's Disk Surface Density Profile, Disk Scale Length, and Dark Matter Profile at $4 \text{ kpc} \lesssim R \lesssim 9 \text{ kpc}$* , *ApJ* **779**, 115 (2013).
- (Brammer *et al.* 2011) G. B. Brammer, K. E. Whitaker, P. G. van Dokkum, *et al.*, *The Number Density and Mass Density of Star-forming and Quiescent Galaxies at $0.4 \leq z \leq 2.2$* , *ApJ* **739**, 24 (2011).
- (Brammer *et al.* 2012) G. B. Brammer, P. G. van Dokkum, M. Franx, *et al.*, *3D-HST: A Wide-field Grism Spectroscopic Survey with the Hubble Space Telescope*, *ApJ* **200**, 13 (2012).
- (Bruce *et al.* 2012) V. A. Bruce, J. S. Dunlop, M. Cirasuolo, *et al.*, *The morphologies of massive galaxies at $1 \leq z \leq 3$ in the CANDELS-UDS field: compact bulges, and the rise and fall of massive discs*, *MNRAS* **427**, 1666 (2012).
- (Bruzual & Charlot 2003) G. Bruzual & S. Charlot, *Stellar population synthesis at the resolution of 2003*, *MNRAS* **344**, 1000 (2003).
- (Burkert 1995) A. Burkert, *The Structure of Dark Matter Halos in Dwarf Galaxies*, *ApJL* **447**, L25 (1995).
- (Burkert *et al.* 2010) A. Burkert, R. Genzel, N. Bouché, *et al.*, *High-redshift Star-forming Galaxies: Angular Momentum and Baryon Fraction, Turbulent Pressure Effects, and the Origin of Turbulence*, *ApJ* **725**, 2324 (2010).
- (Burkert *et al.* 2015) A. Burkert, N. M. Förster Schreiber, R. Genzel, *et al.*, *The angular momentum distribution and baryon content of star forming galaxies at $z \sim 1 - 3$* , *ArXiv e-prints* (2015), arXiv:1510.03262.
- (Buta *et al.* 1994) R. Buta, S. Mitra, G. de Vaucouleurs, & H. G. Corwin, Jr., *Mean morphological types of bright galaxies*, *ApJ* **107**, 118 (1994).
- (Cacciato *et al.* 2012) M. Cacciato, A. Dekel, & S. Genel, *Evolution of violent gravitational disc instability in galaxies: late stabilization by transition from gas to stellar dominance*, *MNRAS* **421**, 818 (2012).

- (Calzetti *et al.* 2000) D. Calzetti, L. Armus, R. C. Bohlin, A. L. Kinney, J. Koornneef, & T. Storchi-Bergmann, *The Dust Content and Opacity of Actively Star-forming Galaxies*, *ApJ* **533**, 682 (2000).
- (Cano-Díaz *et al.* 2012) M. Cano-Díaz, R. Maiolino, A. Marconi, H. Netzer, O. Shemmer, & G. Cresci, *Observational evidence of quasar feedback quenching star formation at high redshift*, *AAP* **537**, L8 (2012).
- (Cappellari & Copin 2003) M. Cappellari & Y. Copin, *Adaptive spatial binning of integral-field spectroscopic data using Voronoi tessellations*, *MNRAS* **342**, 345 (2003).
- (Cappellari *et al.* 2013) M. Cappellari, N. Scott, K. Alatalo, *et al.*, *The ATLAS^{3D} project - XV. Benchmark for early-type galaxies scaling relations from 260 dynamical models: mass-to-light ratio, dark matter, Fundamental Plane and Mass Plane*, *MNRAS* **432**, 1709 (2013).
- (Cappellari *et al.* 2011) M. Cappellari, E. Emsellem, D. Krajnović, *et al.*, *The ATLAS^{3D} project - VII. A new look at the morphology of nearby galaxies: the kinematic morphology-density relation*, *MNRAS* **416**, 1680 (2011).
- (Carignan & Freeman 1985) C. Carignan & K. C. Freeman, *Basic parameters of dark halos in late-type spirals*, *ApJ* **294**, 494 (1985).
- (Casertano 1983) S. Casertano, *Rotation curve of the edge-on spiral galaxy NGC 5907: disc and halo masses*, *MNRAS* **203**, 735 (1983).
- (Casertano & van Gorkom 1991) S. Casertano & J. H. van Gorkom, *Declining rotation curves - The end of a conspiracy?*, *ApJ* **101**, 1231 (1991).
- (Cassata *et al.* 2013) P. Cassata, M. Giavalisco, C. C. Williams, *et al.*, *Constraining the Assembly of Normal and Compact Passively Evolving Galaxies from Redshift $z = 3$ to the Present with CANDELS*, *ApJ* **775**, 106 (2013).
- (Catinella *et al.* 2006) B. Catinella, R. Giovanelli, & M. P. Haynes, *Template Rotation Curves for Disk Galaxies*, *ApJ* **640**, 751 (2006).
- (Chabrier 2003) G. Chabrier, *The Galactic Disk Mass Function: Reconciliation of the Hubble Space Telescope and Nearby Determinations*, *ApJL* **586**, L133 (2003).
- (Chang *et al.* 2013) Y.-Y. Chang, A. van der Wel, H.-W. Rix, *et al.*, *Structural Evolution of Early-type Galaxies to $z = 2.5$ in CANDELS*, *ApJ* **773**, 149 (2013).
- (Cheung *et al.* 2012) E. Cheung, S. M. Faber, D. C. Koo, *et al.*, *The Dependence of Quenching upon the Inner Structure of Galaxies at $0.5 \leq z \leq 0.8$ in the DEEP2/AEGIS Survey*, *ApJ* **760**, 131 (2012).

- (Cibinel *et al.* 2013) A. Cibinel, C. M. Carollo, S. J. Lilly, *et al.*, *The Zurich Environmental Study (ZENS) of Galaxies in Groups along the Cosmic Web. II. Galaxy Structural Measurements and the Concentration of Morphologically Classified Satellites in Diverse Environments*, *ApJ* **776**, 72 (2013).
- (Cicone *et al.* 2014) C. Cicone, R. Maiolino, E. Sturm, *et al.*, *Massive molecular outflows and evidence for AGN feedback from CO observations*, *AAP* **562**, A21 (2014).
- (Clowe *et al.* 2004) D. Clowe, A. Gonzalez, & M. Markevitch, *Weak-Lensing Mass Reconstruction of the Interacting Cluster 1E 0657-558: Direct Evidence for the Existence of Dark Matter*, *ApJ* **604**, 596 (2004).
- (Cole *et al.* 2001) S. Cole, P. Norberg, C. M. Baugh, *et al.*, *The 2dF galaxy redshift survey: near-infrared galaxy luminosity functions*, *MNRAS* **326**, 255 (2001).
- (Conroy 2013) C. Conroy, *Modeling the Panchromatic Spectral Energy Distributions of Galaxies*, *ARAA* **51**, 393 (2013).
- (Conselice *et al.* 2009) C. J. Conselice, C. Yang, & A. F. L. Bluck, *The structures of distant galaxies - III. The merger history of over 20000 massive galaxies at $z \leq 1.2$* , *MNRAS* **394**, 1956 (2009).
- (Contini *et al.* 2012) T. Contini, B. Garilli, O. Le Fèvre, *et al.*, *MASSIV: Mass Assembly Survey with SINFONI in VVDS. I. Survey description and global properties of the $0.9 \leq z \leq 1.8$ galaxy sample*, *AAP* **539**, A91 (2012).
- (Corradi & Capaccioli 1990) R. L. M. Corradi & M. Capaccioli, *Does the dark component influence the shape of the inner rotation curves of spiral galaxies?*, *AAP* **237**, 36 (1990).
- (Courteau & Dutton 2015) S. Courteau & A. A. Dutton, *On the Global Mass Distribution in Disk Galaxies*, *ApJL* **801**, L20 (2015).
- (Courteau *et al.* 2007) S. Courteau, A. A. Dutton, F. C. van den Bosch, L. A. MacArthur, A. Dekel, D. H. McIntosh, & D. A. Dale, *Scaling Relations of Spiral Galaxies*, *ApJ* **671**, 203 (2007).
- (Courteau *et al.* 2014) S. Courteau, M. Cappellari, R. S. de Jong, *et al.*, *Galaxy masses*, *Reviews of Modern Physics* **86**, 47 (2014).
- (Cresci *et al.* 2009) G. Cresci, E. K. S. Hicks, R. Genzel, *et al.*, *The SINS Survey: Modeling the Dynamics of $z \sim 2$ Galaxies and the High- z Tully-Fisher Relation*, *ApJ* **697**, 115 (2009).
- (Crocker *et al.* 2012) A. Crocker, M. Krips, M. Bureau, *et al.*, *The ATLAS^{3D} project - XI. Dense molecular gas properties of CO-luminous early-type galaxies*, *MNRAS* **421**, 1298 (2012).

- (Croton *et al.* 2006) D. J. Croton, V. Springel, S. D. M. White, *et al.*, *The many lives of active galactic nuclei: cooling flows, black holes and the luminosities and colours of galaxies*, MNRAS **365**, 11 (2006).
- (Daddi *et al.* 2010) E. Daddi, F. Bournaud, F. Walter, *et al.*, *Very High Gas Fractions and Extended Gas Reservoirs in $z = 1.5$ Disk Galaxies*, ApJ **713**, 686 (2010).
- (Daddi *et al.* 2007) E. Daddi, M. Dickinson, G. Morrison, *et al.*, *Multiwavelength Study of Massive Galaxies at $z \sim 2$. I. Star Formation and Galaxy Growth*, ApJ **670**, 156 (2007).
- (Davies *et al.* 2011) R. Davies, N. M. Förster Schreiber, G. Cresci, *et al.*, *How Well Can We Measure the Intrinsic Velocity Dispersion of Distant Disk Galaxies?*, ApJ **741**, 69 (2011).
- (Davis *et al.* 2007) M. Davis, P. Guhathakurta, N. P. Konidaris, *et al.*, *The All-Wavelength Extended Groth Strip International Survey (AEGIS) Data Sets*, ApJL **660**, L1 (2007).
- (de Jong *et al.* 2004) R. S. de Jong, L. Simard, R. L. Davies, R. P. Saglia, D. Burstein, M. Colless, R. McMahan, & G. Wegner, *Structural properties of discs and bulges of early-type galaxies*, MNRAS **355**, 1155 (2004).
- (de Jong *et al.* 2007) R. S. de Jong, A. C. Seth, D. J. Radburn-Smith, *et al.*, *Stellar Populations across the NGC 4244 Truncated Galactic Disk*, ApJL **667**, L49 (2007).
- (de Vaucouleurs 1948) G. de Vaucouleurs, *Recherches sur les Nebuleuses Extragalactiques*, Annales d'Astrophysique **11**, 247 (1948).
- (Dekel & Birnboim 2008) A. Dekel & Y. Birnboim, *Gravitational quenching in massive galaxies and clusters by clumpy accretion*, MNRAS **383**, 119 (2008).
- (Dekel & Burkert 2014) A. Dekel & A. Burkert, *Wet disc contraction to galactic blue nuggets and quenching to red nuggets*, MNRAS **438**, 1870 (2014).
- (Dekel & Birnboim 2006) A. Dekel & Y. Birnboim, *Galaxy bimodality due to cold flows and shock heating*, MNRAS **368**, 2 (2006).
- (Dekel *et al.* 2009) A. Dekel, Y. Birnboim, G. Engel, *et al.*, *Cold streams in early massive hot haloes as the main mode of galaxy formation*, Nature **457**, 451 (2009).
- (Dib *et al.* 2006) S. Dib, E. Bell, & A. Burkert, *The Supernova Rate-Velocity Dispersion Relation in the Interstellar Medium*, ApJ **638**, 797 (2006).
- (Dickinson 2000) M. Dickinson, *The first galaxies: structure and stellar populations*, in *Astronomy, physics and chemistry of H^+* , Philosophical Transactions of the Royal Society of London Series A, Vol. 358 (2000) p. 2001.

- (Dunkley *et al.* 2009) J. Dunkley, E. Komatsu, M. R.olta, *et al.*, *Five-Year Wilkinson Microwave Anisotropy Probe Observations: Likelihoods and Parameters from the WMAP Data*, *ApJ* **180**, 306 (2009).
- (Dutton *et al.* 2005) A. A. Dutton, S. Courteau, R. de Jong, & C. Carignan, *Mass Modeling of Disk Galaxies: Degeneracies, Constraints, and Adiabatic Contraction*, *ApJ* **619**, 218 (2005).
- (Dutton *et al.* 2007) A. A. Dutton, F. C. van den Bosch, A. Dekel, & S. Courteau, *A Revised Model for the Formation of Disk Galaxies: Low Spin and Dark Halo Expansion*, *ApJ* **654**, 27 (2007).
- (Einstein 1916) A. Einstein, *Die Grundlage der allgemeinen Relativitätstheorie*, *Annalen der Physik* **354**, 769 (1916).
- (Eisenhauer *et al.* 2003) F. Eisenhauer, R. Abuter, K. Bickert, *et al.*, *SINFONI - Integral field spectroscopy at 50 milli-arcsecond resolution with the ESO VLT*, in *Instrument Design and Performance for Optical/Infrared Ground-based Telescopes*, Society of Photo-Optical Instrumentation Engineers (SPIE) Conference Series, Vol. 4841, edited by M. Iye & A. F. M. Moorwood (2003) pp. 1548–1561.
- (Elbaz *et al.* 2007) D. Elbaz, E. Daddi, D. Le Borgne, *et al.*, *The reversal of the star formation-density relation in the distant universe*, *AAP* **468**, 33 (2007).
- (Elmegreen *et al.* 2004a) B. G. Elmegreen, D. M. Elmegreen, & A. C. Hirst, *A Constant Bar Fraction out to Redshift $z \sim 1$ in the Advanced Camera for Surveys Field of the Tadpole Galaxy*, *ApJ* **612**, 191 (2004a).
- (Elmegreen *et al.* 2009) B. G. Elmegreen, D. M. Elmegreen, M. X. Fernandez, & J. J. Lemoias, *Bulge and Clump Evolution in Hubble Ultra Deep Field Clump Clusters, Chains and Spiral Galaxies*, *ApJ* **692**, 12 (2009).
- (Elmegreen *et al.* 2004b) D. M. Elmegreen, B. G. Elmegreen, & C. M. Sheets, *Chain Galaxies in the Tadpole Advanced Camera for Surveys Field*, *ApJ* **603**, 74 (2004b).
- (Elmegreen *et al.* 2004c) D. M. Elmegreen, B. G. Elmegreen, & A. C. Hirst, *Discovery of Face-on Counterparts of Chain Galaxies in the Tadpole Advanced Camera for Surveys Field*, *ApJL* **604**, L21 (2004c).
- (Elmegreen *et al.* 2005) D. M. Elmegreen, B. G. Elmegreen, D. S. Rubin, & M. A. Schaffer, *Galaxy Morphologies in the Hubble Ultra Deep Field: Dominance of Linear Structures at the Detection Limit*, *ApJ* **631**, 85 (2005).

- (Epinat *et al.* 2010) B. Epinat, P. Amram, C. Balkowski, & M. Marcelin, *Evidence for strong dynamical evolution in disc galaxies through the last 11 Gyr. GHASP VIII - a local reference sample of rotating disc galaxies for high-redshift studies*, MNRAS **401**, 2113 (2010).
- (Epinat *et al.* 2009) B. Epinat, T. Contini, O. Le Fèvre, *et al.*, *Integral field spectroscopy with SINFONI of VVDS galaxies. I. Galaxy dynamics and mass assembly at $1.2 \leq z \leq 1.6$* , AAP **504**, 789 (2009).
- (Epinat *et al.* 2012) B. Epinat, L. Tasca, P. Amram, *et al.*, *MASSIV: Mass Assembly Survey with SINFONI in VVDS. II. Kinematics and close environment classification*, AAP **539**, A92 (2012).
- (Erb *et al.* 2004) D. K. Erb, C. C. Steidel, A. E. Shapley, M. Pettini, & K. L. Adelberger, *The Kinematics of Morphologically Selected $z \sim 2$ Galaxies in the GOODS-North Field*, ApJ **612**, 122 (2004).
- (Erb *et al.* 2003) D. K. Erb, A. E. Shapley, C. C. Steidel, M. Pettini, K. L. Adelberger, M. P. Hunt, A. F. M. Moorwood, & J.-G. Cuby, *H α Spectroscopy of Galaxies at $z \lesssim 2$: Kinematics and Star Formation*, ApJ **591**, 101 (2003).
- (Erwin *et al.* 2008) P. Erwin, M. Pohlen, & J. E. Beckman, *The Outer Disks of Early-Type Galaxies. I. Surface-Brightness Profiles of Barred Galaxies*, ApJ **135**, 20 (2008).
- (Faber *et al.* 2007) S. M. Faber, C. N. A. Willmer, C. Wolf, *et al.*, *Galaxy Luminosity Functions to $z \sim 1$ from DEEP2 and COMBO-17: Implications for Red Galaxy Formation*, ApJ **665**, 265 (2007).
- (Fall & Efstathiou 1980) S. M. Fall & G. Efstathiou, *Formation and rotation of disc galaxies with haloes*, MNRAS **193**, 189 (1980).
- (Fan *et al.* 2001) X. Fan, M. A. Strauss, D. P. Schneider, *et al.*, *High-Redshift Quasars Found in Sloan Digital Sky Survey Commissioning Data. IV. Luminosity Function from the Fall Equatorial Stripe Sample*, ApJ **121**, 54 (2001).
- (Fang *et al.* 2013) J. J. Fang, S. M. Faber, D. C. Koo, & A. Dekel, *A Link between Star Formation Quenching and Inner Stellar Mass Density in Sloan Digital Sky Survey Central Galaxies*, ApJ **776**, 63 (2013).
- (Ferrarese *et al.* 1994) L. Ferrarese, F. C. van den Bosch, H. C. Ford, W. Jaffe, & R. W. O'Connell, *Hubble Space Telescope photometry of the central regions of Virgo cluster elliptical galaxies. 3: Brightness profiles*, ApJ **108**, 1598 (1994).
- (Feruglio *et al.* 2010) C. Feruglio, R. Maiolino, E. Piconcelli, N. Menci, H. Aussel, A. Lamastra, & F. Fiore, *Quasar feedback revealed by giant molecular outflows*, AAP **518**, L155 (2010).

- (Fisher *et al.* 2014) D. B. Fisher, K. Glazebrook, A. Bolatto, *et al.*, *Extreme Gas Fractions in Clumpy, Turbulent Disk Galaxies at $z \sim 0.1$* , *ApJL* **790**, L30 (2014).
- (Florido *et al.* 2006) E. Florido, E. Battaner, A. Guijarro, F. Garzón, & A. Castillo-Morales, *Truncated stellar disks in the near infrared. I. Observations*, *AAP* **455**, 467 (2006).
- (Förster Schreiber *et al.* 2011a) N. M. Förster Schreiber, A. E. Shapley, D. K. Erb, R. Genzel, C. C. Steidel, N. Bouché, G. Cresci, & R. Davies, *Constraints on the Assembly and Dynamics of Galaxies. I. Detailed Rest-frame Optical Morphologies on Kiloparsec Scale of $z \sim 2$ Star-forming Galaxies*, *ApJ* **731**, 65 (2011a).
- (Förster Schreiber *et al.* 2006) N. M. Förster Schreiber, R. Genzel, M. D. Lehnert, *et al.*, *SINFONI Integral Field Spectroscopy of $z \sim 2$ UV-selected Galaxies: Rotation Curves and Dynamical Evolution*, *ApJ* **645**, 1062 (2006).
- (Förster Schreiber *et al.* 2009) N. M. Förster Schreiber, R. Genzel, N. Bouché, *et al.*, *The SINS Survey: SINFONI Integral Field Spectroscopy of $z \sim 2$ Star-forming Galaxies*, *ApJ* **706**, 1364 (2009).
- (Förster Schreiber *et al.* 2011b) N. M. Förster Schreiber, A. E. Shapley, R. Genzel, *et al.*, *Constraints on the Assembly and Dynamics of Galaxies. II. Properties of Kiloparsec-scale Clumps in Rest-frame Optical Emission of $z \sim 2$ Star-forming Galaxies*, *ApJ* **739**, 45 (2011b).
- (Förster Schreiber *et al.* 2014) N. M. Förster Schreiber, R. Genzel, S. F. Newman, *et al.*, *The Sins/zC-Sinf Survey of $z \sim 2$ Galaxy Kinematics: Evidence for Powerful Active Galactic Nucleus-Driven Nuclear Outflows in Massive Star-Forming Galaxies*, *ApJ* **787**, 38 (2014).
- (Franx *et al.* 2008) M. Franx, P. G. van Dokkum, N. M. F. Schreiber, S. Wuyts, I. Labbé, & S. Toft, *Structure and Star Formation in Galaxies out to $z = 3$: Evidence for Surface Density Dependent Evolution and Upsizing*, *ApJ* **688**, 770 (2008).
- (Freeman 1970) K. C. Freeman, *On the Disks of Spiral and so Galaxies*, *ApJ* **160**, 811 (1970).
- (Friedmann 1922) A. Friedmann, *Über die Krümmung des Raumes*, *Zeitschrift für Physik* **10**, 377 (1922).
- (Genel *et al.* 2014) S. Genel, M. Vogelsberger, V. Springel, *et al.*, *Introducing the Illustris project: the evolution of galaxy populations across cosmic time*, *MNRAS* **445**, 175 (2014).
- (Genzel *et al.* 2006) R. Genzel, L. J. Tacconi, F. Eisenhauer, *et al.*, *The rapid formation of a large rotating disk galaxy three billion years after the Big Bang*, *Nature* **442**, 786 (2006).

- (Genzel *et al.* 2008) R. Genzel, A. Burkert, N. Bouché, *et al.*, *From Rings to Bulges: Evidence for Rapid Secular Galaxy Evolution at $z \sim 2$ from Integral Field Spectroscopy in the SINS Survey*, *ApJ* **687**, 59 (2008).
- (Genzel *et al.* 2011) R. Genzel, S. Newman, T. Jones, *et al.*, *The Sins Survey of $z \sim 2$ Galaxy Kinematics: Properties of the Giant Star-forming Clumps*, *ApJ* **733**, 101 (2011).
- (Genzel *et al.* 2014a) R. Genzel, N. M. Förster Schreiber, P. Lang, *et al.*, *The SINS/zC-SINF Survey of $z \sim 2$ Galaxy Kinematics: Evidence for Gravitational Quenching*, *ApJ* **785**, 75 (2014a).
- (Genzel *et al.* 2015) R. Genzel, L. J. Tacconi, D. Lutz, *et al.*, *Combined CO and Dust Scaling Relations of Depletion Time and Molecular Gas Fractions with Cosmic Time, Specific Star-formation Rate, and Stellar Mass*, *ApJ* **800**, 20 (2015).
- (Genzel *et al.* 2014b) R. Genzel, N. M. Förster Schreiber, D. Rosario, *et al.*, *Evidence for Wide-spread Active Galactic Nucleus-driven Outflows in the Most Massive $z \sim 1 - 2$ Star-forming Galaxies*, *ApJ* **796**, 7 (2014b).
- (Giavalisco *et al.* 2004) M. Giavalisco, H. C. Ferguson, A. M. Koekemoer, *et al.*, *The Great Observatories Origins Deep Survey: Initial Results from Optical and Near-Infrared Imaging*, *ApJL* **600**, L93 (2004).
- (Gnedin & Zhao 2002) O. Y. Gnedin & H. Zhao, *Maximum feedback and dark matter profiles of dwarf galaxies*, *MNRAS* **333**, 299 (2002).
- (Gnedin *et al.* 2004) O. Y. Gnedin, A. V. Kravtsov, A. A. Klypin, & D. Nagai, *Response of Dark Matter Halos to Condensation of Baryons: Cosmological Simulations and Improved Adiabatic Contraction Model*, *ApJ* **616**, 16 (2004).
- (Gnerucci *et al.* 2011) A. Gnerucci, A. Marconi, G. Cresci, *et al.*, *Dynamical properties of AMAZE and LSD galaxies from gas kinematics and the Tully-Fisher relation at $z \sim 3$* , *AAP* **528**, A88 (2011).
- (Green *et al.* 2010) A. W. Green, K. Glazebrook, P. J. McGregor, *et al.*, *High star formation rates as the origin of turbulence in early and modern disk galaxies*, *Nature* **467**, 684 (2010).
- (Green *et al.* 2014) A. W. Green, K. Glazebrook, P. J. McGregor, *et al.*, *DYNAMO - I. A sample of $H\alpha$ -luminous galaxies with resolved kinematics*, *MNRAS* **437**, 1070 (2014).
- (Grogin *et al.* 2011) N. A. Grogin, D. D. Kocevski, S. M. Faber, *et al.*, *CANDELS: The Cosmic Assembly Near-infrared Deep Extragalactic Legacy Survey*, *ApJ* **197**, 35 (2011).

- (Guo *et al.* 2013) Q. Guo, S. White, R. E. Angulo, B. Henriques, G. Lemson, M. Boylan-Kolchin, P. Thomas, & C. Short, *Galaxy formation in WMAP1 and WMAP7 cosmologies*, MNRAS **428**, 1351 (2013).
- (Guo *et al.* 2012) Y. Guo, M. Giavalisco, H. C. Ferguson, P. Cassata, & A. M. Koekemoer, *Mulei-wavelength View of Kiloparsec-scale Clumps in Star-forming Galaxies at $z \sim 2$* , ApJ **757**, 120 (2012).
- (Guo *et al.* 2011) Y. Guo, M. Giavalisco, P. Cassata, *et al.*, *Color and Stellar Population Gradients in Passively Evolving Galaxies at $z \sim 2$ from HST/WFC3 Deep Imaging in the Hubble Ultra Deep Field*, ApJ **735**, 18 (2011).
- (Guo *et al.* 2015) Y. Guo, H. C. Ferguson, E. F. Bell, *et al.*, *Clumpy Galaxies in CANDELS. I. The Definition of UV Clumps and the Fraction of Clumpy Galaxies at $0.5 \leq z \leq 3$* , ApJ **800**, 39 (2015).
- (Häring & Rix 2004) N. Häring & H.-W. Rix, *On the Black Hole Mass-Bulge Mass Relation*, ApJL **604**, L89 (2004).
- (Harrison *et al.* 2012) C. M. Harrison, D. M. Alexander, A. M. Swinbank, *et al.*, *Energetic galaxy-wide outflows in high-redshift uleraluminous infrared galaxies hosting AGN activity*, MNRAS **426**, 1073 (2012).
- (Hopkins *et al.* 2006) P. F. Hopkins, L. Hernquist, T. J. Cox, T. Di Matteo, B. Robertson, & V. Springel, *A Unified, Merger-driven Model of the Origin of Starbursts, Quasars, the Cosmic X-Ray Background, Supermassive Black Holes, and Galaxy Spheroids*, ApJ **163**, 1 (2006).
- (Hopkins *et al.* 2009) P. F. Hopkins, R. S. Somerville, T. J. Cox, *et al.*, *The effects of gas on morphological transformation in mergers: implications for bulge and disc demographics*, MNRAS **397**, 802 (2009).
- (Hoyle 1951) F. Hoyle, *The Origin of the Rotations of the Galaxies*, in *Problems of Cosmical Aerodynamics* (1951) p. 195.
- (Hubble 1929) E. Hubble, *A Relation between Distance and Radial Velocity among Extragalactic Nebulae*, Proceedings of the National Academy of Science **15**, 168 (1929).
- (Hubble 1926) E. P. Hubble, *Extragalactic nebulae.*, ApJ **64** (1926), 10.1086/143018.
- (Ilbert *et al.* 2013) O. Ilbert, H. J. McCracken, O. Le Fèvre, *et al.*, *Mass assembly in quiescent and star-forming galaxies since $z \lesssim 4$ from UleraVISTA*, AAP **556**, A55 (2013).
- (Iocco *et al.* 2009) F. Iocco, G. Mangano, G. Miele, O. Pisanti, & P. D. Serpico, *Primordial nucleosynthesis: From precision cosmology to fundamental physics*, Phys Rep **472**, 1 (2009).

- (Jaffe *et al.* 1994) W. Jaffe, H. C. Ford, R. W. O'Connell, F. C. van den Bosch, & L. Ferrarese, *Hubble Space Telescope photometry of the central regions of Virgo Cluster elliptical galaxies. I: Observations, discussion, and conclusions*, ApJ **108**, 1567 (1994).
- (Kartaltepe *et al.* 2007) J. S. Kartaltepe, D. B. Sanders, N. Z. Scoville, *et al.*, *Evolution of the Frequency of Luminous ($\geq L^*_V$) Close Galaxy Pairs at $z \leq 1.2$ in the COSMOS Field*, ApJ **172**, 320 (2007).
- (Kassin *et al.* 2006) S. A. Kassin, R. S. de Jong, & B. J. Weiner, *Dark and Baryonic Matter in Bright Spiral Galaxies. II. Radial Distributions for 34 Galaxies*, ApJ **643**, 804 (2006).
- (Kauffmann *et al.* 2006) G. Kauffmann, T. M. Heckman, G. De Lucia, J. Brinchmann, S. Charlot, C. Tremonti, S. D. M. White, & J. Brinkmann, *Gas infall and stochastic star formation in galaxies in the local universe*, MNRAS **367**, 1394 (2006).
- (Kauffmann *et al.* 2003a) G. Kauffmann, T. M. Heckman, S. D. M. White, *et al.*, *The dependence of star formation history and internal structure on stellar mass for 10^5 low-redshift galaxies*, MNRAS **341**, 54 (2003a).
- (Kauffmann *et al.* 2003b) G. Kauffmann, T. M. Heckman, S. D. M. White, *et al.*, *Stellar masses and star formation histories for 10^5 galaxies from the Sloan Digital Sky Survey*, MNRAS **341**, 33 (2003b).
- (Kautsch 2009) S. J. Kautsch, *The Edge-On Perspective of Bulgeless, Simple Disk Galaxies*, PASP **121**, 1297 (2009).
- (Kennicutt 1998) R. C. Kennicutt, Jr., *The Global Schmidt Law in Star-forming Galaxies*, ApJ **498**, 541 (1998).
- (Kent 1986) S. M. Kent, *Dark matter in spiral galaxies. I - Galaxies with optical rotation curves*, ApJ **91**, 1301 (1986).
- (Kent 1988) S. M. Kent, *Dark matter in spiral galaxies. III - The SA galaxies*, ApJ **96**, 514 (1988).
- (Kereš *et al.* 2005) D. Kereš, N. Katz, D. H. Weinberg, & R. Davé, *How do galaxies get their gas?*, MNRAS **363**, 2 (2005).
- (Klypin *et al.* 2011) A. A. Klypin, S. Trujillo-Gomez, & J. Primack, *Dark Matter Halos in the Standard Cosmological Model: Results from the Bolshoi Simulation*, ApJ **740**, 102 (2011).
- (Koekemoer *et al.* 2007) A. M. Koekemoer, H. Aussel, D. Calzetti, *et al.*, *The COSMOS Survey: Hubble Space Telescope Advanced Camera for Surveys Observations and Data Processing*, ApJ **172**, 196 (2007).

- (Koekemoer *et al.* 2011) A. M. Koekemoer, S. M. Faber, H. C. Ferguson, *et al.*, *CANDELS: The Cosmic Assembly Near-infrared Deep Extragalactic Legacy Survey—The Hubble Space Telescope Observations, Imaging Data Products, and Mosaics*, *ApJ* **197**, 36 (2011).
- (Koo *et al.* 2005) D. C. Koo, L. Simard, C. N. A. Willmer, *et al.*, *The DEEP Groth Strip Survey. VIII. The Evolution of Luminous Field Bulges at Redshift $z \sim 1$* , *ApJ* **157**, 175 (2005).
- (Kormendy & Kennicutt 2004) J. Kormendy & R. C. Kennicutt, Jr., *Secular Evolution and the Formation of Pseudobulges in Disk Galaxies*, *ARAA* **42**, 603 (2004).
- (Kregel & van der Kruit 2004) M. Kregel & P. C. van der Kruit, *Radial truncations in stellar discs in galaxies*, *MNRAS* **355**, 143 (2004).
- (Kregel *et al.* 2005) M. Kregel, P. C. van der Kruit, & K. C. Freeman, *Structure and kinematics of edge-on galaxy discs - V. The dynamics of stellar discs*, *MNRAS* **358**, 503 (2005).
- (Kregel *et al.* 2002) M. Kregel, P. C. van der Kruit, & R. de Grijs, *Flattening and truncation of stellar discs in edge-on spiral galaxies*, *MNRAS* **334**, 646 (2002).
- (Kriek *et al.* 2009) M. Kriek, P. G. van Dokkum, M. Franx, G. D. Illingworth, & D. K. Magee, *The Hubble Sequence Beyond $z = 2$ for Massive Galaxies: Contrasting Large Star-forming and Compact Quiescent Galaxies*, *ApJL* **705**, L71 (2009).
- (Krist 1995) J. Krist, *Simulation of HST PSFs using Tiny Tim*, in *Astronomical Data Analysis Software and Systems IV*, Astronomical Society of the Pacific Conference Series, Vol. 77, edited by R. A. Shaw, H. E. Payne, & J. J. E. Hayes (1995) p. 349.
- (Krumholz & McKee 2005) M. R. Krumholz & C. F. McKee, *A General Theory of Turbulence-regulated Star Formation, from Spirals to Uleraluminous Infrared Galaxies*, *ApJ* **630**, 250 (2005).
- (Lang *et al.* 2014) P. Lang, S. Wuyts, R. S. Somerville, *et al.*, *Bulge Growth and Quenching since $z = 2.5$ in CANDELS/3D-HST*, *ApJ* **788**, 11 (2014).
- (Lanyon-Foster *et al.* 2012) M. M. Lanyon-Foster, C. J. Conselice, & M. R. Merrifield, *The structures of distant galaxies - V. The evolution of galaxy structure in stellar mass at $z \leq 1$* , *MNRAS* **424**, 1852 (2012).
- (Larson 1976) R. B. Larson, *Models for the formation of disc galaxies*, *MNRAS* **176**, 31 (1976).
- (Law *et al.* 2012) D. R. Law, C. C. Steidel, A. E. Shapley, S. R. Nagy, N. A. Reddy, & D. K. Erb, *An HST/WFC3-IR Morphological Survey of Galaxies at $z = 1.5-3.6$. I. Survey Description and Morphological Properties of Star-forming Galaxies*, *ApJ* **745**, 85 (2012).

- (Law *et al.* 2009) D. R. Law, C. C. Steidel, D. K. Erb, J. E. Larkin, M. Pettini, A. E. Shapley, & S. A. Wright, *The Kiloparsec-scale Kinematics of High-redshift Star-forming Galaxies*, *ApJ* **697**, 2057 (2009).
- (Lemson & Virgo Consortium 2006) G. Lemson & t. Virgo Consortium, *Halo and Galaxy Formation Histories from the Millennium Simulation: Public release of a VO-oriented and SQL-queryable database for studying the evolution of galaxies in the LambdaCDM cosmogony*, *ArXiv Astrophysics e-prints* (2006).
- (Leroy *et al.* 2008) A. K. Leroy, F. Walter, E. Brinks, F. Bigiel, W. J. G. de Blok, B. Madore, & M. D. Thornley, *The Star Formation Efficiency in Nearby Galaxies: Measuring Where Gas Forms Stars Effectively*, *ApJ* **136**, 2782 (2008).
- (Leroy *et al.* 2009) A. K. Leroy, F. Walter, F. Bigiel, *et al.*, *Heracles: The HERA CO Line Extragalactic Survey*, *ApJ* **137**, 4670 (2009).
- (Lilly *et al.* 2013) S. J. Lilly, C. M. Carollo, A. Pipino, A. Renzini, & Y. Peng, *Gas Regulation of Galaxies: The Evolution of the Cosmic Specific Star Formation Rate, the Metallicity-Mass-Star-formation Rate Relation, and the Stellar Content of Halos*, *ApJ* **772**, 119 (2013).
- (Lotz *et al.* 2011) J. M. Lotz, P. Jonsson, T. J. Cox, D. Croton, J. R. Primack, R. S. Somerville, & K. Stewart, *The Major and Minor Galaxy Merger Rates at $z \leq 1.5$* , *ApJ* **742**, 103 (2011).
- (Lu *et al.* 2014) Y. Lu, R. H. Wechsler, R. S. Somerville, *et al.*, *Semi-analytic Models for the CANDELS Survey: Comparison of Predictions for Intrinsic Galaxy Properties*, *ApJ* **795**, 123 (2014).
- (Lutz *et al.* 2011) D. Lutz, A. Poglitsch, B. Aleieri, *et al.*, *PACS Evolutionary Probe (PEP) - A Herschel key program*, *AAP* **532**, A90 (2011).
- (Madau & Dickinson 2014) P. Madau & M. Dickinson, *Cosmic Star-Formation History*, *ARAA* **52**, 415 (2014).
- (Magdis *et al.* 2010) G. E. Magdis, D. Rigopoulou, J.-S. Huang, & G. G. Fazio, *On the stellar masses of IRAC detected Lyman Break Galaxies at $z \sim 3$* , *MNRAS* **401**, 1521 (2010).
- (Magnelli *et al.* 2013) B. Magnelli, P. Popesso, S. Berta, *et al.*, *The deepest Herschel-PACS far-infrared survey: number counts and infrared luminosity functions from combined PEP/GOODS-H observations*, *AAP* **553**, A132 (2013).
- (Magorrian *et al.* 1998) J. Magorrian, S. Tremaine, D. Richstone, *et al.*, *The Demography of Massive Dark Objects in Galaxy Centers*, *ApJ* **115**, 2285 (1998).

- (Maiolino *et al.* 2012) R. Maiolino, S. Gallerani, R. Neri, *et al.*, *Evidence of strong quasar feedback in the early Universe*, MNRAS **425**, L66 (2012).
- (Mancini *et al.* 2011) C. Mancini, N. M. Förster Schreiber, A. Renzini, *et al.*, *The zCOSMOS-SINFONI Project. I. Sample Selection and Natural-seeing Observations*, ApJ **743**, 86 (2011).
- (Maraston *et al.* 2010) C. Maraston, J. Pforr, A. Renzini, E. Daddi, M. Dickinson, A. Cimatti, & C. Tonini, *Star formation rates and masses of $z \sim 2$ galaxies from multi-colour photometry*, MNRAS **407**, 830 (2010).
- (Markevitch *et al.* 2004) M. Markevitch, A. H. Gonzalez, D. Clowe, A. Vikhlinin, W. Forman, C. Jones, S. Murray, & W. Tucker, *Direct Constraints on the Dark Matter Self-Interaction Cross Section from the Merging Galaxy Cluster 1E 0657-56*, ApJ **606**, 819 (2004).
- (Martig *et al.* 2009) M. Martig, F. Bournaud, R. Teyssier, & A. Dekel, *Morphological Quenching of Star Formation: Making Early-Type Galaxies Red*, ApJ **707**, 250 (2009).
- (Martig *et al.* 2013) M. Martig, A. F. Crocker, F. Bournaud, *et al.*, *The ATLAS^{3D} project - XXII. Low-efficiency star formation in early-type galaxies: hydrodynamic models and observations*, MNRAS **432**, 1914 (2013).
- (Martinsson *et al.* 2013) T. P. K. Martinsson, M. A. W. Verheijen, K. B. Westfall, M. A. Bershadsky, D. R. Andersen, & R. A. Swaters, *The DiskMass Survey. VII. The distribution of luminous and dark matter in spiral galaxies*, AAP **557**, A131 (2013).
- (Milgrom 1983) M. Milgrom, *A modification of the Newtonian dynamics as a possible alternative to the hidden mass hypothesis*, ApJ **270**, 365 (1983).
- (Mo *et al.* 1998) H. J. Mo, S. Mao, & S. D. M. White, *The formation of galactic discs*, MNRAS **295**, 319 (1998).
- (Mo *et al.* 2010) H. Mo, F. C. van den Bosch, & S. White, *Galaxy Formation and Evolution*, by Houjun Mo, Frank van den Bosch, Simon White, Cambridge, UK: Cambridge University Press, 2010 (2010).
- (Momcheva *et al.* 2015) I. G. Momcheva, G. B. Brammer, P. G. van Dokkum, *et al.*, *The 3D-HST Survey: Hubble Space Telescope WFC3/G141 grism spectra, redshifts, and emission line measurements for $\sim 100,000$ galaxies*, ArXiv e-prints (2015), arXiv:1510.02106.
- (Moorwood *et al.* 2000) A. F. M. Moorwood, P. P. van der Werf, J. G. Cuby, & E. Oliva, *H α emitting galaxies and the cosmic star formation rate at $z \sim 2.2$* , AAP **362**, 9 (2000).

- (Moster *et al.* 2013) B. P. Moster, T. Naab, & S. D. M. White, *Galactic star formation and accretion histories from matching galaxies to dark matter haloes*, MNRAS **428**, 3121 (2013).
- (Muzzin *et al.* 2013) A. Muzzin, D. Marchesini, M. Stefanon, *et al.*, *The Evolution of the Stellar Mass Functions of Star-forming and Quiescent Galaxies to $z = 4$ from the COSMOS/UltraVISTA Survey*, ApJ **777**, 18 (2013).
- (Navarro *et al.* 1996) J. F. Navarro, V. R. Eke, & C. S. Frenk, *The cores of dwarf galaxy haloes*, MNRAS **283**, L72 (1996).
- (Navarro *et al.* 1997) J. F. Navarro, C. S. Frenk, & S. D. M. White, *A Universal Density Profile from Hierarchical Clustering*, ApJ **490**, 493 (1997).
- (Nelson *et al.* 2016) E. J. Nelson, P. G. van Dokkum, I. G. Momcheva, *et al.*, *Spatially Resolved Dust Maps from Balmer Decrements in Galaxies at $z \sim 1.4$* , ApJL **817**, L9 (2016).
- (Nelson *et al.* 2012) E. J. Nelson, P. G. van Dokkum, G. Brammer, *et al.*, *Spatially Resolved $H\alpha$ Maps and Sizes of 57 Strongly Star-forming Galaxies at $z \sim 1$ from 3D-HST: Evidence for Rapid Inside-out Assembly of Disk Galaxies*, ApJL **747**, L28 (2012).
- (Nelson *et al.* 2013) E. J. Nelson, P. G. van Dokkum, I. Momcheva, *et al.*, *The Radial Distribution of Star Formation in Galaxies at $z \sim 1$ from the 3D-HST Survey*, ApJL **763**, L16 (2013).
- (Nelson *et al.* 2015) E. J. Nelson, P. G. van Dokkum, N. M. Förster Schreiber, *et al.*, *Where stars form: inside-out growth and coherent star formation from HST H α maps of 2676 galaxies across the main sequence at $z \sim 1$* , ArXiv e-prints (2015), arXiv:1507.03999.
- (Nesvadba *et al.* 2011) N. P. H. Nesvadba, M. Polletta, M. D. Lehnert, J. Bergeron, C. De Breuck, G. Lagache, & A. Omont, *The dynamics of the ionized and molecular interstellar medium in powerful obscured quasars at $z \geq 3.5$* , MNRAS **415**, 2359 (2011).
- (Neto *et al.* 2007) A. F. Neto, L. Gao, P. Bett, *et al.*, *The statistics of Λ CDM halo concentrations*, MNRAS **381**, 1450 (2007).
- (Newman *et al.* 2013) S. F. Newman, R. Genzel, N. M. Förster Schreiber, *et al.*, *The SINS/ z C-SINF Survey of $z \sim 2$ Galaxy Kinematics: The Nature of Dispersion-dominated Galaxies*, ApJ **767**, 104 (2013).
- (Noeske *et al.* 2007) K. G. Noeske, B. J. Weiner, S. M. Faber, *et al.*, *Star Formation in AEGIS Field Galaxies since $z=1.1$: The Dominance of Gradually Declining Star Formation, and the Main Sequence of Star-forming Galaxies*, ApJL **660**, L43 (2007).
- (Noordermeer 2008) E. Noordermeer, *The rotation curves of flattened Sérsic bulges*, MNRAS **385**, 1359 (2008).

- (Noordermeer *et al.* 2007) E. Noordermeer, J. M. van der Hulst, R. Sancisi, R. S. Swaters, & T. S. van Albada, *The mass distribution in early-type disc galaxies: declining rotation curves and correlations with optical properties*, MNRAS **376**, 1513 (2007).
- (Oort 1940) J. H. Oort, *Some Problems Concerning the Structure and Dynamics of the Galactic System and the Elliptical Nebulae NGC 3115 and 4494.*, ApJ **91**, 273 (1940).
- (Padilla & Strauss 2008) N. D. Padilla & M. A. Strauss, *The shapes of galaxies in the Sloan Digital Sky Survey*, MNRAS **388**, 1321 (2008).
- (Papovich *et al.* 2001) C. Papovich, M. Dickinson, & H. C. Ferguson, *The Stellar Populations and Evolution of Lyman Break Galaxies*, ApJ **559**, 620 (2001).
- (Peebles 1969) P. J. E. Peebles, *Origin of the Angular Momentum of Galaxies*, ApJ **155**, 393 (1969).
- (Peng *et al.* 2010a) C. Y. Peng, L. C. Ho, C. D. Impey, & H.-W. Rix, *Detailed Decomposition of Galaxy Images. II. Beyond Axisymmetric Models*, ApJ **139**, 2097 (2010a).
- (Peng *et al.* 2010b) Y.-j. Peng, S. J. Lilly, K. Kovač, *et al.*, *Mass and Environment as Drivers of Galaxy Evolution in SDSS and zCOSMOS and the Origin of the Schechter Function*, ApJ **721**, 193 (2010b).
- (Penzias & Wilson 1965) A. A. Penzias & R. W. Wilson, *A Measurement of Excess Antenna Temperature at 4080 Mc/s.*, ApJ **142**, 419 (1965).
- (Perlmutter *et al.* 1999) S. Perlmutter, G. Aldering, G. Goldhaber, *et al.*, *Measurements of Ω and Λ from 42 High-Redshift Supernovae*, ApJ **517**, 565 (1999).
- (Pettini *et al.* 2001) M. Pettini, A. E. Shapley, C. C. Steidel, J.-G. Cuby, M. Dickinson, A. F. M. Moorwood, K. L. Adelberger, & M. Giavalisco, *The Rest-Frame Optical Spectra of Lyman Break Galaxies: Star Formation, Extinction, Abundances, and Kinematics*, ApJ **554**, 981 (2001).
- (Planck Collaboration *et al.* 2014) Planck Collaboration, P. A. R. Ade, N. Aghanim, *et al.*, *Planck 2013 results. XVI. Cosmological parameters*, AAP **571**, A16 (2014).
- (Pohlen & Trujillo 2006) M. Pohlen & I. Trujillo, *The structure of galactic disks. Studying late-type spiral galaxies using SDSS*, AAP **454**, 759 (2006).
- (Porter *et al.* 2014) L. A. Porter, R. S. Somerville, J. R. Primack, & P. H. Johansson, *Understanding the structural scaling relations of early-type galaxies*, MNRAS **444**, 942 (2014).
- (Prada *et al.* 2012) F. Prada, A. A. Klypin, A. J. Cuesta, J. E. Betancort-Rijo, & J. Primack, *Halo concentrations in the standard Λ cold dark matter cosmology*, MNRAS **423**, 3018 (2012).

- (Price *et al.* 2015) S. H. Price, M. Kriek, A. E. Shapley, *et al.*, *The MOSDEF Survey: Dynamical and Baryonic Masses and Kinematic Structures of Star-Forming Galaxies at $1.4 \leq z \leq 2.6$* , ArXiv e-prints (2015), arXiv:1511.03272.
- (Puglielli 2011) D. Puglielli, *Detecting Adiabatic Contraction in Rotation Curves*, ApJ **739**, 32 (2011).
- (Read & Gilmore 2005) J. I. Read & G. Gilmore, *Mass loss from dwarf spheroidal galaxies: the origins of shallow dark matter cores and exponential surface brightness profiles*, MNRAS **356**, 107 (2005).
- (Rees & Ostriker 1977) M. J. Rees & J. P. Ostriker, *Cooling, dynamics and fragmentation of massive gas clouds - Clues to the masses and radii of galaxies and clusters*, MNRAS **179**, 541 (1977).
- (Riess *et al.* 1998) A. G. Riess, A. V. Filippenko, P. Challis, *et al.*, *Observational Evidence from Supernovae for an Accelerating Universe and a Cosmological Constant*, ApJ **116**, 1009 (1998).
- (Roberts & Whitehurst 1975) M. S. Roberts & R. N. Whitehurst, *The rotation curve and geometry of M31 at large galactocentric distances.*, ApJ **201**, 327 (1975).
- (Rosario *et al.* 2013) D. J. Rosario, P. Santini, D. Lutz, *et al.*, *Nuclear Activity is More Prevalent in Star-forming Galaxies*, ApJ **771**, 63 (2013).
- (Rubin & Ford 1970) V. C. Rubin & W. K. Ford, Jr., *Rotation of the Andromeda Nebula from a Spectroscopic Survey of Emission Regions*, ApJ **159**, 379 (1970).
- (Ruphy *et al.* 1996) S. Ruphy, A. C. Robin, N. Epchtein, E. Copet, E. Bertin, P. Fouque, & F. Guglielmo, *New determination of the disc scale length and the radial cutoff in the anticenter with DENIS data.*, AAP **313**, L21 (1996).
- (Saintonge *et al.* 2012) A. Saintonge, L. J. Tacconi, S. Fabello, *et al.*, *The Impact of Interactions, Bars, Bulges, and Active Galactic Nuclei on Star Formation Efficiency in Local Massive Galaxies*, ApJ **758**, 73 (2012).
- (Salucci & Persic 1999) P. Salucci & M. Persic, *The baryonic mass function of spiral galaxies: clues to galaxy formation*, MNRAS **309**, 923 (1999).
- (Schade *et al.* 1995) D. Schade, S. J. Lilly, D. Crampton, F. Hammer, O. Le Fevre, & L. Tresse, *Canada-France Redshift Survey: Hubble Space Telescope Imaging of High-Redshift Field Galaxies*, ApJL **451**, L1 (1995).
- (Schaye 2004) J. Schaye, *Star Formation Thresholds and Galaxy Edges: Why and Where*, ApJ **609**, 667 (2004).

- (Schechter 1976) P. Schechter, *An analytic expression for the luminosity function for galaxies.*, ApJ **203**, 297 (1976).
- (Schiminovich *et al.* 2007) D. Schiminovich, T. K. Wyder, D. C. Martin, *et al.*, *The UV-Optical Color Magnitude Diagram. II. Physical Properties and Morphological Evolution On and Off of a Star-forming Sequence*, ApJ **173**, 315 (2007).
- (Schulz *et al.* 2010) A. E. Schulz, R. Mandelbaum, & N. Padmanabhan, *Testing adiabatic contraction with Sloan Digital Sky Survey elliptical galaxies*, MNRAS **408**, 1463 (2010).
- (Sersic 1968) J. L. Sersic, *Cordoba, Argentina: Observatorio Astronomico, 1968* (1968).
- (Shapley *et al.* 2005) A. E. Shapley, C. C. Steidel, D. K. Erb, N. A. Reddy, K. L. Adelberger, M. Pettini, P. Barmby, & J. Huang, *Ultraviolet to Mid-Infrared Observations of Star-forming Galaxies at $z \sim 2$: Stellar Masses and Stellar Populations*, ApJ **626**, 698 (2005).
- (Sharples *et al.* 2004) R. M. Sharples, R. Bender, M. D. Lehnert, *et al.*, *KMOS: an infrared multiple-object integral field spectrograph for the ESO VLT*, in *Ground-based Instrumentation for Astronomy*, SPIE, Vol. 5492, edited by A. F. M. Moorwood & M. Iye (2004) pp. 1179–1186.
- (Sharples *et al.* 2012) R. Sharples, R. Bender, A. Agudo Berbel, *et al.*, *Status of the KMOS multi-object near-infrared integral field spectrograph*, in *Society of Photo-Optical Instrumentation Engineers (SPIE) Conference Series*, Society of Photo-Optical Instrumentation Engineers (SPIE) Conference Series, Vol. 8446 (2012) p. 84460K.
- (Sharples *et al.* 2013) R. Sharples, R. Bender, A. Agudo Berbel, *et al.*, *First Light for the KMOS Multi-Object Integral-Field Spectrometer*, The Messenger **151**, 21 (2013).
- (Skeleon *et al.* 2014) R. E. Skeleon, K. E. Whitaker, I. G. Momcheva, *et al.*, *3D-HST WFC3-selected Photometric Catalogs in the Five CANDELS/3D-HST Fields: Photometry, Photometric Redshifts, and Stellar Masses*, ApJ **214**, 24 (2014).
- (Sofue & Rubin 2001) Y. Sofue & V. Rubin, *Rotation Curves of Spiral Galaxies*, ARAA **39**, 137 (2001).
- (Somerville *et al.* 2012) R. S. Somerville, R. C. Gilmore, J. R. Primack, & A. Domínguez, *Galaxy properties from the ultraviolet to the far-infrared: Λ cold dark matter models confront observations*, MNRAS **423**, 1992 (2012).
- (Somerville *et al.* 2008) R. S. Somerville, P. F. Hopkins, T. J. Cox, B. E. Robertson, & L. Hernquist, *A semi-analytic model for the co-evolution of galaxies, black holes and active galactic nuclei*, MNRAS **391**, 481 (2008).

- (Sturm *et al.* 2011) E. Sturm, E. González-Alfonso, S. Veilleux, *et al.*, *Massive Molecular Outflows and Negative Feedback in ULIRGs Observed by Herschel-PACS*, *ApJ* **733**, L16 (2011).
- (Swinbank *et al.* 2012) A. M. Swinbank, D. Sobral, I. Smail, J. E. Geach, P. N. Best, I. G. McCarthy, R. A. Crain, & T. Theuns, *The properties of the star-forming interstellar medium at $z = 0.84$ -2.23 from HiZELS: mapping the internal dynamics and metallicity gradients in high-redshift disc galaxies*, *MNRAS* **426**, 935 (2012).
- (Szomoru *et al.* 2013) D. Szomoru, M. Franx, P. G. van Dokkum, M. Trenti, G. D. Illingworth, I. Labbé, & P. Oesch, *The Stellar Mass Structure of Massive Galaxies from $z = 0$ to $z = 2.5$: Surface Density Profiles and Half-mass Radii*, *ApJ* **763**, 73 (2013).
- (Szomoru *et al.* 2010) D. Szomoru, M. Franx, P. G. van Dokkum, *et al.*, *Confirmation of the Compactness of a $z = 1.91$ Quiescent Galaxy with Hubble Space Telescope's Wide Field Camera 3*, *ApJ* **714**, L244 (2010).
- (Tacchella *et al.* 2015) S. Tacchella, P. Lang, C. M. Carollo, *et al.*, *SINS/zC-SINF Survey of $z \sim 2$ Galaxy Kinematics: Rest-frame Morphology, Structure, and Colors from Near-infrared Hubble Space Telescope Imaging*, *ApJ* **802**, 101 (2015).
- (Tacconi *et al.* 2006) L. J. Tacconi, R. Neri, S. C. Chapman, *et al.*, *High-Resolution Millimeter Imaging of Submillimeter Galaxies*, *ApJ* **640**, 228 (2006).
- (Tacconi *et al.* 2008) L. J. Tacconi, R. Genzel, I. Smail, *et al.*, *Submillimeter Galaxies at $z \sim 2$: Evidence for Major Mergers and Constraints on Lifetimes, IMF, and CO-H₂ Conversion Factor*, *ApJ* **680**, 246 (2008).
- (Tacconi *et al.* 2010) L. J. Tacconi, R. Genzel, R. Neri, *et al.*, *High molecular gas fractions in normal massive star-forming galaxies in the young Universe*, *Nature* **463**, 781 (2010).
- (Tacconi *et al.* 2013) L. J. Tacconi, R. Neri, R. Genzel, *et al.*, *Phibss: Molecular Gas Content and Scaling Relations in $z \sim 1 - 3$ Massive, Main-sequence Star-forming Galaxies*, *ApJ* **768**, 74 (2013).
- (Toft *et al.* 2009) S. Toft, M. Franx, P. van Dokkum, N. M. Förster Schreiber, I. Labbé, S. Wuyts, & D. Marchesini, *The Size-Star Formation Relation of Massive Galaxies at $1.5 \leq z \leq 2.5$* , *ApJ* **705**, 255 (2009).
- (Tomczak *et al.* 2014) A. R. Tomczak, R. F. Quadri, K.-V. H. Tran, *et al.*, *Galaxy Stellar Mass Functions from ZFOURGE/CANDELS: An Excess of Low-mass Galaxies since $z = 2$ and the Rapid Buildup of Quiescent Galaxies*, *ApJ* **783**, 85 (2014).
- (Toomre 1964) A. Toomre, *On the gravitational stability of a disk of stars*, *ApJ* **139**, 1217 (1964).

- (Tully & Fisher 1977) R. B. Tully & J. R. Fisher, *A new method of determining distances to galaxies*, AAP **54**, 661 (1977).
- (van Albada *et al.* 1985) T. S. van Albada, J. N. Bahcall, K. Begeman, & R. Sancisi, *Distribution of dark matter in the spiral galaxy NGC 3198*, ApJ **295**, 305 (1985).
- (van den Bosch *et al.* 1994) F. C. van den Bosch, L. Ferrarese, W. Jaffe, H. C. Ford, & R. W. O’Connell, *Hubble Space Telescope photometry of the central regions of Virgo cluster elliptical galaxies. II: Isophote shapes.*, ApJ **108**, 1579 (1994).
- (van der Kruit & Allen 1978) P. C. van der Kruit & R. J. Allen, *The kinematics of spiral and irregular galaxies*, ARAA **16**, 103 (1978).
- (van der Kruit & Searle 1981a) P. C. van der Kruit & L. Searle, *Surface photometry of edge-on spiral galaxies. I - A model for the three-dimensional distribution of light in galactic disks.*, AAP **95**, 105 (1981a).
- (van der Kruit & Searle 1981b) P. C. van der Kruit & L. Searle, *Surface Photometry of Edge-On Spiral Galaxies. II - the Distribution of Light and Colour in the Disk and Spheroid of NGC891*, AAP **95**, 116 (1981b).
- (van der Kruit & Freeman 2011) P. C. van der Kruit & K. C. Freeman, *Galaxy Disks*, ARAA **49**, 301 (2011).
- (van der Wel *et al.* 2011a) A. van der Wel, H.-W. Rix, S. Wuyts, *et al.*, *The Majority of Compact Massive Galaxies at $z \sim 2$ are Disk Dominated*, ApJ **730**, 38 (2011a).
- (van der Wel *et al.* 2012) A. van der Wel, E. F. Bell, B. Häussler, *et al.*, *Structural Parameters of Galaxies in CANDELS*, ApJ **203**, 24 (2012).
- (van der Wel *et al.* 2011b) A. van der Wel, A. N. Straughn, H.-W. Rix, *et al.*, *Extreme Emission-line Galaxies in CANDELS: Broadband-selected, Starbursting Dwarf Galaxies at $z \geq 1$* , ApJ **742**, 111 (2011b).
- (van der Wel *et al.* 2014a) A. van der Wel, M. Franx, P. G. van Dokkum, *et al.*, *3D-HST+CANDELS: The Evolution of the Galaxy Size-Mass Distribution since $z = 3$* , ApJ **788**, 28 (2014a).
- (van der Wel *et al.* 2014b) A. van der Wel, Y.-Y. Chang, E. F. Bell, *et al.*, *Geometry of Star-forming Galaxies from SDSS, 3D-HST, and CANDELS*, ApJL **792**, L6 (2014b).
- (van Dokkum *et al.* 2015) P. G. van Dokkum, E. J. Nelson, M. Franx, *et al.*, *Forming Compact Massive Galaxies*, ApJ **813**, 23 (2015).

- (van Dokkum *et al.* 2011) P. G. van Dokkum, G. Brammer, M. Fumagalli, *et al.*, *First Results from the 3D-HST Survey: The Striking Diversity of Massive Galaxies at $z \geq 1$* , *ApjL* **743**, L15 (2011).
- (Veilleux *et al.* 2013) S. Veilleux, M. Meléndez, E. Sturm, *et al.*, *Fast Molecular Outflows in Luminous Galaxy Mergers: Evidence for Quasar Feedback from Herschel*, *ApJ* **776**, 27 (2013).
- (Vergani *et al.* 2012) D. Vergani, B. Epinat, T. Contini, *et al.*, *MASSIV: Mass Assembly Survey with SINFONI in VVDS. IV. Fundamental relations of star-forming galaxies at $1 \leq z \leq 1.6$* , *AAP* **546**, A118 (2012).
- (Vogelsberger *et al.* 2014) M. Vogelsberger, S. Genel, V. Springel, *et al.*, *Introducing the Illustris Project: simulating the coevolution of dark and visible matter in the Universe*, *MNRAS* **444**, 1518 (2014).
- (Vogt *et al.* 1996) N. P. Vogt, D. A. Forbes, A. C. Phillips, C. Gronwall, S. M. Faber, G. D. Illingworth, & D. C. Koo, *Optical Rotation Curves of Distant Field Galaxies: Keck Results at Redshifts to Z approximately 1*, *ApjL* **465**, L15 (1996).
- (Vogt *et al.* 1997) N. P. Vogt, A. C. Phillips, S. M. Faber, *et al.*, *Optical Rotation Curves of Distant Field Galaxies: Sub- L^* Systems*, *ApjL* **479**, L121 (1997).
- (Walcher *et al.* 2011) J. Walcher, B. Groves, T. Budavári, & D. Dale, *Fitting the integrated spectral energy distributions of galaxies*, *APSS* **331**, 1 (2011).
- (Weiner *et al.* 2005) B. J. Weiner, A. C. Phillips, S. M. Faber, *et al.*, *The DEEP Groth Strip Galaxy Redshift Survey. III. Redshift Catalog and Properties of Galaxies*, *ApJ* **620**, 595 (2005).
- (Whitaker *et al.* 2012) K. E. Whitaker, P. G. van Dokkum, G. Brammer, & M. Franx, *The Star Formation Mass Sequence Out to $z = 2.5$* , *ApjL* **754**, L29 (2012).
- (Whitaker *et al.* 2014) K. E. Whitaker, M. Franx, J. Leja, *et al.*, *Constraining the Low-mass Slope of the Star Formation Sequence at $0.5 \leq z \leq 2.5$* , *ApJ* **795**, 104 (2014).
- (White 1984) S. D. M. White, *Angular momentum growth in protogalaxies*, *ApJ* **286**, 38 (1984).
- (Williams *et al.* 1996) R. E. Williams, B. Blacker, M. Dickinson, *et al.*, *The Hubble Deep Field: Observations, Data Reduction, and Galaxy Photometry*, *ApJ* **112**, 1335 (1996).
- (Williams *et al.* 2009) R. J. Williams, R. F. Quadri, M. Franx, P. van Dokkum, & I. Labbé, *Detection of Quiescent Galaxies in a Bicolor Sequence from $Z = 0-2$* , *ApJ* **691**, 1879 (2009).

- (Windhorst *et al.* 2011) R. A. Windhorst, S. H. Cohen, N. P. Hathi, *et al.*, *The Hubble Space Telescope Wide Field Camera 3 Early Release Science Data: Panchromatic Faint Object Counts for 0.2-2 μm Wavelength*, *ApJ* **193**, 27 (2011).
- (Wisnioski *et al.* 2015) E. Wisnioski, N. M. Förster Schreiber, S. Wuyts, *et al.*, *The KMOS^{3D} Survey: Design, First Results, and the Evolution of Galaxy Kinematics from $0.7 \leq z \leq 2.7$* , *ApJ* **799**, 209 (2015).
- (Wisnioski *et al.* 2011) E. Wisnioski, K. Glazebrook, C. Blake, *et al.*, *The WiggleZ Dark Energy Survey: high-resolution kinematics of luminous star-forming galaxies*, *MNRAS* **417**, 2601 (2011).
- (Woo *et al.* 2013) J. Woo, A. Dekel, S. M. Faber, *et al.*, *Dependence of galaxy quenching on halo mass and distance from its centre*, *MNRAS* **428**, 3306 (2013).
- (Wuyts *et al.* 2007) S. Wuyts, I. Labbé, M. Franx, *et al.*, *What Do We Learn from IRAC Observations of Galaxies at $2 \leq z \leq 3.5$?*, *ApJ* **655**, 51 (2007).
- (Wuyts *et al.* 2013) S. Wuyts, N. M. Förster Schreiber, E. J. Nelson, *et al.*, *A CANDELS-3D-HST synergy: Resolved Star Formation Patterns at $0.7 \leq z \leq 1.5$* , *ApJ* **779**, 135 (2013).
- (Wuyts *et al.* 2012) S. Wuyts, N. M. Förster Schreiber, R. Genzel, *et al.*, *Smooth(er) Stellar Mass Maps in CANDELS: Constraints on the Longevity of Clumps in High-redshift Star-forming Galaxies*, *ApJ* **753**, 114 (2012).
- (Wuyts *et al.* 2011a) S. Wuyts, N. M. Förster Schreiber, D. Lutz, *et al.*, *On Star Formation Rates and Star Formation Histories of Galaxies Out to $z \sim 3$* , *ApJ* **738**, 106 (2011a).
- (Wuyts *et al.* 2011b) S. Wuyts, N. M. Förster Schreiber, A. van der Wel, *et al.*, *Galaxy Structure and Mode of Star Formation in the SFR-Mass Plane from $z \sim 2.5$ to $z \sim 0.1$* , *ApJ* **742**, 96 (2011b).
- (Wuyts *et al.* 2016) S. Wuyts, N. M. Förster Schreiber, E. Wisnioski, *et al.*, *KMOS^{3D}: Dynamical constraints on the mass budget in early star-forming disks*, *ArXiv e-prints* (2016), arXiv:1603.03432.
- (Yang *et al.* 1984) J. Yang, M. S. Turner, D. N. Schramm, G. Steigman, & K. A. Olive, *Primordial nucleosynthesis - A critical comparison of theory and observation*, *ApJ* **281**, 493 (1984).
- (Yuma *et al.* 2012) S. Yuma, K. Ohta, & K. Yabe, *Intrinsic Shape of Star-forming BzK Galaxies. II. Rest-frame Ultraviolet and Optical Structures in GOODS-South and SXDS*, *ApJ* **761**, 19 (2012).

(Zhao *et al.* 2009) D. H. Zhao, Y. P. Jing, H. J. Mo, & G. Börner, *Accurate Universal Models for the Mass Accretion Histories and Concentrations of Dark Matter Halos*, *ApJ* **707**, 354 (2009).

(Zibetti *et al.* 2009) S. Zibetti, S. Charlot, & H.-W. Rix, *Resolved stellar mass maps of galaxies - I. Method and implications for global mass estimates*, *MNRAS* **400**, 1181 (2009).

(Zwicky 1933) F. Zwicky, *Die Rotverschiebung von extragalaktischen Nebeln*, *Helvetica Physica Acta* **6**, 110 (1933).

Acknowledgements

First of all I want to thank my advisors Natascha M. Förster Schreiber and Reinhard Genzel for giving me the opportunity to conduct exciting research at MPE and mentoring me on the challenging way I have been through during my PhD. Thank you for all the great support, for guiding me through my first steps in the field of high-z galaxy evolution, for sharing expertise and ideas with me and for giving me constant advice, but also for letting me develop my own ideas. Many thanks go to my co-advisor Stijn Wuyts, who has very closely and patiently guided my efforts and was giving me great support, also through answering all my endless questions.

I am grateful to Linda Tacconi and Jaron Kurk for being part of my thesis committee, supporting me and helping me to shape my research projects. I especially thank Jaron for advising me in my first observing experience at the LBT.

Many thanks go to Andreas Burkert, Dieter Lutz, Emily Wisnioski and Eva Wuyts for supporting my research with advice and scientific input. I want to thank the SINS and KMOS^{3D} teams at MPE for valuable scientific input during the meetings and particularly for putting all the work in the data which was the basis of my research.

I am also grateful to all other past and present members of the Infrared Group at MPE, who I have come to know, and I am glad for being able to work in such a nice environment. I am thankful for the fruitful science exchange and collaboration with Sandro Tacchella, Marcella Carollo and Simon Lilly at ETH Zürich. Also many thanks go to my former supervisor Polychronis Papaderos for keeping on being supportive, sharing ideas and being excited about my research.

My life at MPE would not have been as great as it was without my PhD colleges and close friends Michael Opitsch, Thomas Siebert and Jan Grieb. Thank you guys for all your scientific and personal support, for being around and bearing me throughout the last 4 years, and of course for a great distraction from work. During my PhD, I was lucky to work in an office with very nice people that made my day-to-day life at MPE enjoyable, so I want to thank Javier, Christina, Agatha, Anna, Yoshi and Hannah. Among my fellow PhD students and colleges, I also want to thank Pierre, Sergey, Taka, Manuel, and Annemieke for a great time together.

Last but not least, I am very thankful to my parents, my sister and also to Iulia for all their warmth, and for patiently supporting me in difficult times throughout my entire PhD journey!